THE UNIVERSITY OF CHICAGO

SEARCHING FOR TENSOR CURRENTS IN THE WEAK INTERACTION USING LITHIUM-8 β DECAY

A DISSERTATION SUBMITTED TO
THE FACULTY OF THE DIVISION OF THE PHYSICAL SCIENCES
IN CANDIDACY FOR THE DEGREE OF
DOCTOR OF PHILOSOPHY

DEPARTMENT OF PHYSICS

BY

MARY TERESE BURKEY

CHICAGO, ILLINOIS

MARCH 2019

Copyright © 2019 by Mary Terese Burkey

All Rights Reserved

"The phrase 'in the dark,' as I'm sure you know, can refer not only to one's shadowy surroundings, but also to the shadowy secrets of which one might be unaware. Every day, the sun goes down over all these secrets, and so everyone is in the dark in one way or another. If you are sunbathing in a park, for instance, but you do not know that a locked cabinet is buried fifty feet beneath your blanket, then you are in the dark even though you are not actually in the dark, whereas if you are on a midnight hike, knowing full well that several ballerinas are following close behind you, then you are not in the dark even if you are in fact in the dark. Of course, it is quite possible to be in the dark in the dark, as well as to be not in the dark not in the dark, but there are so many secrets in the world that it is likely that you are always in the dark about one thing or another, whether you are in the dark in the dark or in the dark not in the dark, although the sun can go down so quickly that you may be in the dark about being in the dark in the dark, only to look around and find yourself no longer in the dark about being in the dark in the dark, but in the dark in the dark nonetheless, not only because of the dark, but because of the ballerinas in the dark, who are not in the dark about the dark, but also not in the dark about the locked cabinet, and you may be in the dark about the ballerinas digging up the locked cabinet in the dark, even though you are no longer in the dark about being in the dark, and so you are in fact in the dark about being in the dark, even though you are not in the dark about being in the dark, and so you may fall into the hole that the ballerinas have dug, which is dark, in the dark, and in the park."

-Lemony Snicket, A Series of Unfortunate Events: The End

TABLE OF CONTENTS

LIST OF FIGURES

LIST OF TABLES

ACKNOWLEDGMENTS

Though I can put my name on the title page, the project described in this thesis was very much a team effort and would not have been possible without the help, support, and guidance of many mentors, fellow students, friends, and family. Hopefully I can do justice to all their contributions here.

First and foremost, I owe my deepest thanks to my adviser, Dr. Guy Savard, from whom I have learned so much. For someone who has an insurmountable mountain of things to do from all different spheres of work and life, he has never failed to be 100% ready to talk about my very specific technical problems with little-to-no notice. Furthermore, even during the busiest of times, he has always managed to keep himself available for questions. I am extremely lucky to have had him as a mentor.

Equally helpful in this endeavor has been Dr. Jason Clark. Without a beamline for this experiment, there would be no data, and if Jason were to ever go back to Canada, the beamline would undoubtedly self-destruct. His hard work and attention to detail keep the group running smoothly (and more recently, the entire building staff safe from radiation). He also deserves an extra thank you for being such a patient mentor during the internship that ultimately led me to joining this group in the first place. Either way, there is no one else I would rather be taking data with at 8 in the morning after an all-night shift.

Also, though he left the group several years prior, this work would have taken years longer if it had not been for Dr. Adrian Perez Galvan's thorough training and guidance. It was quite scary when he departed to begin a new job right before we were going to lead a big data-taking campaign, but it was equally gratifying to realize soon after that he had more than prepared me for carrying on without him. One of the most insightful mentors I've ever had, his most frequent advice to always anticipate what will go wrong will stay with me well after graduate school.

Throughout the analysis process, both in the realms of programming and actual science, Dr. Tsviki Hirsh and Dr. Aaron Gallant have been invaluable resources. All the puzzle

pieces that make up this project have either one or both of their fingerprints on them. As the analysis evolves, I hope to continue collaborating with them both and if I ever become half as proficient at coding as they are, I'll count myself successful.

Another ever-present source of wisdom at group meetings has been Dr. Nick Scielzo. A true veteran of beta-correlation analysis, he has read all the important papers and has the factor of 10 that you're missing. His guidance in working through all the theory for this analysis cannot be overstated. He, alongside Dr. Ralph Segel, kept us true to the physics even when technical difficulties were piled high.

Outside the realm of mentoring, I also owe deep thanks to all of my fellow students for their help in the daily grind of science. Dan Burdette and Jeff Klimes were wonderful companions in the grand process of hunting for noise and tuning way too many filters. Much aluminum foil was wasted. Many thanks go to Louis Varriano as well for showing up just in time to answer some key questions and take over filling the magnet. More thanks go to Jake Zappala for all the wonderful discussions we had in the process of consuming my stash of tea. But by far, the most thanks go to my consistent comrade in the G142 office, Rodney Orford. We began and ended this adventure at the same time, but he is unquestionably the senior graduate student [85]. He was always there to help with whatever strange hardware problem I was having and a significant portion of my data is a result of his tuning prowess. His ability to somehow radiate calmness alongside an unparalleled sense of humor made him literally the best office companion one could ask for, particularly during the mores stressful times.

In addition, it was a great privilege to have the assistance of the Physics Division's support staff whenever small disasters struck. Whether it be a stuck bolt, the data acquisition system crashing spectacularly, or just finding that the RF box had mysteriously broken, John Rohrer, Ken Teh, Tony Levand, and Bruce Nardi were all enormously helpful in setting the world right again.

And of course, I was fortunate to have the great support of all my friends and family

during the entirety of graduate school. Special thanks to my parents for always being supportive while not asking too many questions and making the trip up for my defense. Finally, for all the mornings where I left long before the sun had risen and came home late at night frustrated by traffic and slow progress, I owe deep thanks for the patience, love, and support of my fiancé, Gerwin Koolstra. Graduate school would not have been the same without him.

ABSTRACT

Nuclear physics remains a powerful tool to search for New Physics by testing the limits of the Standard Model. The electroweak interaction is well-predicted by a pure vector-axial vector structure. However, the beta-neutrino correlation coefficient, $a_{\beta\nu}$, which determines the weighting between emission directions of the β and ν ($W(\theta_{\beta\nu}) = 1 \mp a_{\beta\nu}(v/c)\cos(\theta_{\beta\nu})$) in β decay is sensitive to tensor and scalar currents. Thus, high-precision measurements of the $a_{\beta\nu}$, have long been used as a means to probe for New Physics. The beta decay of ^{8}Li is an ideal reaction for measuring $a_{\beta\nu}$ due to its high Q-value and delayed alpha emission of the daughter nucleus. By measuring the kinematics of stopped ^{8}Li ions in a Paul Trap surrounded with silicon strip detectors backed with plastic scintillators and comparing to simulation, we can set a limit on tensor contributions from $a_{\beta\nu}$. This work represents the analysis of a high-statistics ^{8}Li data set obtained in 2016 to extract a value of $a_{\beta\nu}$. The results indicated a value of $a_{\beta\nu} = -0.3346 \pm -0.0011_{stat} \pm 0.0024_{sys}$ at 1σ uncertainty, which is consistent with the Standard Model and is the most stringent tensor current limit yet achieved in the low energy regime.

CHAPTER 1

INTRODUCTION

As with any scientific endeavor, this story is woven into the grand epic of humanity's quest to understand the world they occupy. Not even a century ago, the chapters were told almost entirely in slow episodes with only a few main characters whose names are all well known today. Fortunately, with the advent of government-sponsored research, grand multinational collaborations, and eventually the internet, humans have managed to make astronomical progress in both observing the world's mechanisms and developing theories to describe. There is still much left to be discovered, but this work and anything newly introduced should build upon what we have already learned.

1.1 The Standard Model

According to our current state of knowledge, all of known physics in the universe can be divided into three different fundamental interactions. These regimes include: the gravitational interaction, which governs the long-range attraction between bodies of mass (such as planets and stars), the strong interaction, which explains how the particles in an atomic nucleus are bound, and the electroweak interaction [5], which is more easily distinguishable as the electromagnetic interaction, (covers the behavior of charged particles and light) and the weak interaction (relates to radioactive decay) at low energies. Gravity remains a bit of a mystery, but the final three interactions can be collectively described by a single theory in terms of discrete or "quantum" mathematical fields. This theory, known as the Standard Model of Particle Physics (SM) is the culmination of several decades of work from scientists around the world and has successfully predicted many experimental outcomes, classified all known fundamental particles and is currently the best theory mankind has for understanding elementary physics.

However, as was mentioned earlier, the SM is still very much incomplete. On top of the

glaring omission of gravity (which some hope will be solved by the discovery of a "graviton"), there is an abundance of phenomena that are either unexplained or present theoretical problems. Cosmological observations indicate that the ordinary matter we interact with only makes up about 5 percent of the universe's mass [79]. The rest is delegated to dark matter and dark energy, both of which are not addressed within the SM. Furthermore, the SM has trouble explaining even the distribution of its own matter. Why there is so much more matter than antimatter in the universe and why some of that matter is divided into multiple hierarchies remains a mystery. Since it was discovered via oscillations that neutrinos have masses, theorists have managed to add that previously unaccounted for fact into the SM, but the results are rather clunky. The list of similar issues goes on, but many physicists also voice complaints (which seem almost picky in comparison) that the SM is ugly and has too many arbitrary parameters that can be measured but not derived.

To address this fundamental problem, the global community of physicists has employed a two-pronged approach that directly reflects their natural division of labor. The theorists have devoted a figurative mountain of literature, developing extensions and alternatives to the SM, which grows ever higher every year. The equally-industrious experimentalists have similarly devoted many years of effort to a wide variety of ambitious (and sometimes expensive projects aimed at finding evidence of anything that contradicts the SM or corroborates one of the theoretical extensions.

At the moment, all particles described in the Standard Model can be summed up using the scheme in Figure 1. There are 4 gauge bosons (particles with integer spin) that act as mediators for the interactions that the SM describes: W and Z bosons (weak), photons (electromagnetic), and gluons (strong). The newly-observed Higgs boson has 0 spin and allocates mass to all other particles. Fermions (particles with half integer spin) consist of leptons and quarks, each with three different generations of matter. The higher generations, being more massive, only occur in high-energy conditions and subsequently decay to the first generation. Quarks participate in all interactions, while the leptons only participate in the

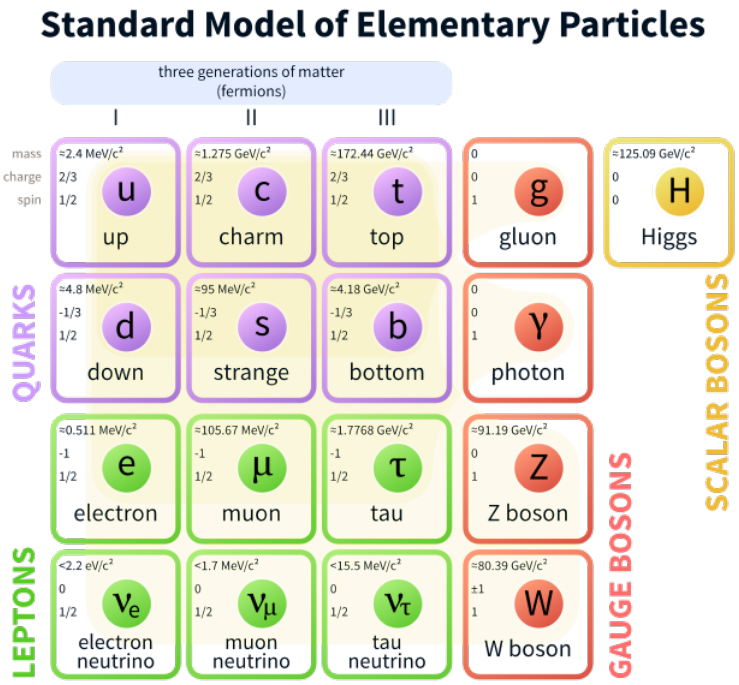

Figure 1.1: The fundamental particles of the Standard Model. All other particles that have been observed are combinations of these. [70]

weak and electromagnetic interactions (when charged). Of the particles pictured, the most commonly encountered are the up and down quarks that form the protons and neutrons within an atomic nucleus, along with the electron, which orbits around them.

Under some circumstances in the nucleus, an up or down quark can change flavor to the opposing first generation quark and emit a virtual W boson. Depending on which way the quarks change flavor, the W boson will decay into either an electron and an anti-neutrino or a positron and a neutrino. This work focuses on the former process, which is depicted in Figure 2. On an expanded scale, the quark flavor change would look like a neutron changing into a proton (or vice versa) within an atomic nucleus, resulting in a decay that changes the atom's properties. This entire process is known as beta decay.

Precision measurements of beta decay are often used as a "broad-band" test of physics beyond the SM (BSM) because the theoretical structure is sensitive to so many of the different favored SM extensions or alternative mechanisms. Any deviation from the behavior

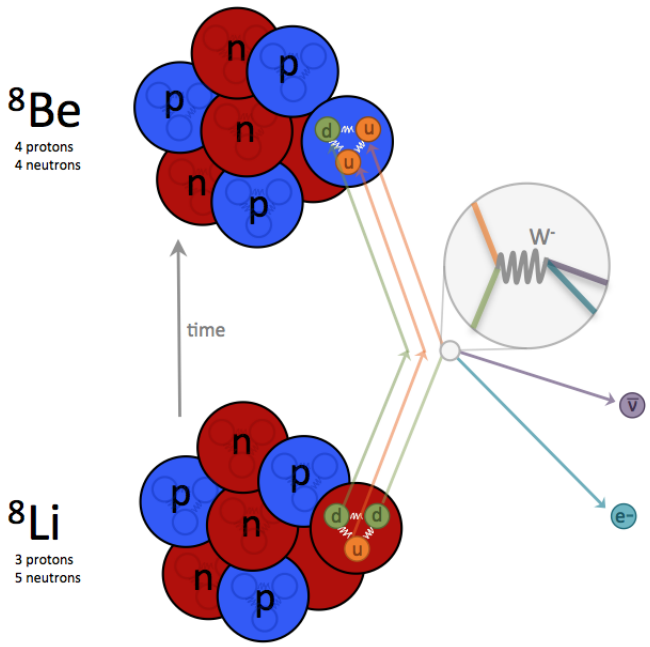

Figure 1.2: An example of beta decay in a lithium-8 atom to a beryllium-8 atom via the emission of a virtual W^- boson, which immediately decays into an electron and an antineutrino

that the SM predicts could be an indication of leptoquarks, charged Higgs bosons, composite models, [46] or even supersymmetry [80]. A brief review of the possible SM extensions or modifications scalar and tensor currents would indicate is in Table 1.2.1 in section 1.2.1. Alternatively, if no deviation is found, the same precision measurements can put powerful boundary conditions on potential contributions from BSM physics. This work presents an example of a beta-decay precision measurement using the correlation between the electron and anti-neutrino in lithium-8 beta decay.

1.2 Development of the Beta Decay theory

The history of Beta Decay and its eventual development into a facet of the Standard Model began well over a century ago in the late 1800's when Henri Becquerel and the Curies discovered that elements such as uranium, thorium, polonium, and radium all emitted particles. [4] In 1899, Ernest Rutherford's research partitioned the emitted particles from radioactive

decay into "alpha rays" and "beta rays." [17] Thus, the term "beta decay" was born. It was quickly established that the beta rays were effectively electrons (in the case of β^- decay) and that the process resulted in a different element one atomic number away from the parent. However, for the next 30 years, beta decay was a source of great anxiety for many physicists attempting to understand how it worked. Unlike their sister "alpha-rays" that were emitted in discrete energies accounted for by the difference in mass between the original and resulting nuclei, the beta-particle energies populated a broad continuum. Even more frustrating, the entire process resulted in energy, momentum, and angular momentum defying conservation laws.

Wolfgang Pauli finally shed some light in 1930 with a noteworthy letter to a physics meeting in Tübingen, Germany, [14] where he suggested that another neutral light particle contained in the nucleus is emitted alongside the β particle. A few years later in 1933, one of the most famous characters in the Story of Science; Enrico Fermi, dubbed this particle the "neutrino" and published his historical "Theory of Beta Decay" in various Italian and German physics journals after being rejected by the journal Nature (this should provide some solace to graduate students everywhere).[33] [34] [32].

Though not translated into English until several decades later [107], Fermi's theory (with Pauli's assistance) solved many of the problems that beta decay had introduced and correctly predicted a great deal more. The continuous energy spectra of the β particle could be explained by the neutrino also taking away some of the energy from the decay. If detected, the energy and mass of the two particles summed together would equal how much mass/energy had been lost in the decay, thus allowing energy and momentum to be conserved. In addition, the angular momentum between the initial and final states of the nucleus remained unchanged during beta decay since the number of total nucleons (protons and neutrons, each having intrinsic spin angular momentum 1/2) also remained unchanged. However, the β particle also comes away with a 1/2 unit of spin in one direction, which when coupled with a neutrino carrying a 1/2 unit of spin in the opposite direction would restore angular mo-

mentum conservation. This particular process would later be termed a "Fermi transition." Included in Fermi's theory was also the first Hamiltonian for beta decay:

$$\mathscr{H}_{\beta^-} = gC_V\left(\bar{\psi}_p\gamma_\mu\tau_+\psi_n\right)\left(\bar{\psi}_e\gamma_\mu\psi_\nu\right) \tag{1.1}$$

where ψ refers to the wave functions of the particles, γ_μ is the set of Dirac matrices, and τ_+ is the operator that turns a neutron into a proton (or vice versa). C_V is a constant that indicates the relative strength of the vector interaction, which the Fermi interaction requires (one of 5 available). This Hamiltonian could in turn be used to calculate the transition probability of a beta decay, which allowed experimentalists to compare their beta energy spectra to Fermi's new theory.

Fermi concluded his paper with a derivation of the aforementioned transition probability and a neutrino mass estimation of either zero or very small compared to the electron mass. [106] Shortly thereafter, in 1934, the other half of beta decay theory was experimentally confirmed by none other than Marie Curie's daughter, Iréne Joliot-Curie and her husband Frédéric. They observed a β^+ decay (a positron and neutrino emission) by bombarding aluminum with alpha particles to create radioactive phosphorus-30. This discovery won them the Nobel prize in chemistry in 1935 for producing the first artificially radioactive nucleus. [21]

Again, though slightly incomplete, Fermi and Pauli were largely correct in all their predictions concerning beta decay. Their theory was expanded a couple years later in 1936 by George Gamow and Edward Teller to include transitions where the neutrino and beta particle are emitted with their spins in the same direction with a net change of 1 unit of angular momentum. [36] This addition lengthened the beta decay Hamiltonian to include an axial vector interaction. That said, if one could be added, so could more, since the wave functions in the Hamiltonian can theoretically be multiplied via all five of the available interactions.

$$\mathscr{H}_\beta = \; g\big[C_S(\bar{\psi}_p\tau_\pm\psi_n)(\bar{\psi}_e\psi_\nu) \; + \qquad\qquad \text{(scalar interaction)}$$

$$C_V(\bar{\psi}_p\gamma_\mu\tau_\pm\psi_n)(\bar{\psi}_e\gamma_\mu\psi_\nu) \; + \qquad \text{(vector interaction)}$$

$$C_T(\bar{\psi}_p i\gamma_\mu\gamma_\lambda\tau_\pm\psi_n)(\bar{\psi}_e i\gamma_\mu\gamma_\lambda\psi_\nu) \; + \qquad \text{(tensor interaction)}$$

$$C_A(\bar{\psi}_p i\gamma_\mu\gamma_5\tau_\pm\psi_n)(\bar{\psi}_e i\gamma_\mu\gamma_5\psi_\nu) \; + \qquad \text{(axial vector interaction)}$$

$$C_P(\bar{\psi}_p\gamma_5\tau_\pm\psi_n)(\bar{\psi}_e\gamma_5\psi_\nu)\big] \; + \qquad \text{(pseudoscalar interaction)}$$

$$h.c \qquad \text{(Hermetian Conjugate)}$$

Following the second World War, fundamental research resumed with vigor in the 1940's as scientists rushed to make use of the nuclear reactors that had been previously developed for other purposes. With the rapid parallel development of various spectrometry methods and the shell model via Maria Goeppert-Mayer, this was a particularly fruitful time for beta decay. A plethora of previously unavailable beta decay spectra allowed for further confirmation of Fermi's beta decay model in addition to revealing less common "forbidden" transitions where more than 1 unit of total angular momentum change can occur in the center of mass system. It was these spectra that at the time led researchers to believe that beta decay was a scalar-tensor (ST) interaction based on the lack of energy dependence in allowed transitions and a sole measurement of helium-6. [82] It was also amidst all this new understanding that the next big question of beta decay was raised: Is parity conserved in the weak interaction?

By 1953, in the high-energy regime, the K-meson beta decay was beginning to hint that final states with different parities were possible [22]. This discovery caused quite some stress among those studying low-energy beta decay and in 1956 Tsung-Dao Lee and Chen Ning Yang published a detailed study of available experimental data in the strong, electromagnetic, and weak interactions as it applied to parity conservation. Their findings indicated that there was sound evidence of parity conservation in the first two interactions, but that nobody had actually looked into whether or not this was the case in the weak interaction.[61] They offered up some potential experiments to resolve the issue and in the next year, the landmark Cobalt-60 experiment was conducted by a team of scientists led by Chien Shiung Wu (Columbia

University) at the US National Bureau of Standards. The setup required cooled Cobalt-60 nuclei to be aligned in a magnetic field (so that all the spins point in the same direction) with means to detect the Cobalt-60 beta particle, and then 2 photons from the excited daughter nucleus. Since the electromagnetic interaction was known to adhere to parity conservation, if the beta particles were emitted in the same directions as the photons (and the spin of the nucleus), then parity would be conserved. To everyone's surprise, most of the beta particles were emitted in the opposite direction to the gamma rays and there was clear distinguishability between the "right-handed and left-handed" spin particles. The phenomenon in turn proved that parity was not only violated, but maximally violated. [110]

This discovery meant that the beta decay interaction Hamiltonian had to be updated once more to include parity violating interactions. It took the more general form of:

$$\begin{aligned}\mathscr{H}_\beta &= g\Big[\sum_i C_i(\bar{\psi}_p\Lambda_i\tau_\pm\psi_n)(\bar{\psi}_e\Lambda_i\psi_\nu) + \sum_i C_i'(\bar{\psi}_p\Lambda_i\tau_\pm\psi_n)(\bar{\psi}_e\Lambda_i\gamma_5\psi_\nu)\Big] + h.c \\ &= g\Big[\sum_i (\bar{\psi}_p\Lambda_i\tau_\pm\psi_n)\Big(\bar{\psi}_e\Lambda_i(C_i + C_i'\gamma_5)\psi_\nu\Big)\Big] + h.c \end{aligned} \tag{1.2}$$

where the summation is over the 5 different interactions and Λ_i refers to the corresponding operations. The original summation includes the "parity-even" interactions while the second term introduces "parity-odd" couplings (a pseudoscalar changes sign when space is inverted). Furthermore, parity violation allowed for two more developments to emerge. It was soon confirmed at various laboratories that the distinguishable spins of the beta particles were always longitudinally polarized a certain way. β^+ particles behave as "right-handed screws" when traveling and β^- particles behave as "left-handed screws" (the same for anti-neutrinos and neutrinos, respectively)[109]. This interesting detail prompted the same Lee and Yang from before (along with a few other theorists) to simplify the theory of the neutrino (assuming that the neutrino is massless). Since the spin of the neutrino is always parallel to the momentum, the 4 components that usually describe a wave function could be cut in half, resulting in what is known as the "2-component theory."[62]

Once the parity excitement was over, some researchers also returned to the process of confirming the interaction structure of beta decay. Then, as now, one of the most powerful methods of probing interactions was via beta-neutrino correlation. After a more robust measurement of helium-6 and argon-35 (Gamow-Teller and Fermi decay types, respectively) in 1957 at Argonne National Laboratory and the University of Illinois Cyclotron, each transition was found to be operated predominantly via axial vector and vector interactions, respectively. [47] [9] The same structure was then confirmed in electron capture via Europium-152 [39], the decay of a highly polarized neutron beam [18], and in π^+ β^+ decay [31]. Additionally, it was observed that the vector and axial vector interactions occur in opposite phase, finally solidifying what is now known as the V-A interaction. There have since been many similar measurements limiting scalar and tensor contributions (pseudoscalar terms vanish in a non-relativistic setting), this one included. However, by 1958, when all of these findings were being published, the theorists finally caught up with what was happening and updated the theory of beta decay once more (while pointing out many other positive points of V-A) in separate papers from Feynman and Gell-Mann[35], and Sudarshan and Marshak. [96]

Drawing from Feynman and Gell-Mann's paper, the two used Lee and Yang's 2-component theory to introduce operators that would transform 4-component spinors into 2-component spinors (either left or right-handed). These projection operators, defined as $a = \frac{1}{2}(1 - \gamma_5)$ (left-handed) and $\bar{a} = \frac{1}{2}(1 + \gamma_5)$ (right-handed), could be inserted into equation (1.2) where $\psi_L = a\psi$ and $\psi_R = \bar{a}\psi$[1]. In addition, if one assumes that parity is violated maximally and that the neutrinos are massless, $C_i = C_i'$ for a left-handed neutrino and $C_i = -C_i'$ for a right handed neutrino. The result for a β^- decay, when including the observed orientations

1. Formalism taken from Peskin and Schroeder [78]

specified earlier, is: [2]

$$\begin{aligned}\mathscr{H}_\beta &= g\Big[\sum_i(\bar{\psi}_p\Lambda_i\tau_\pm\psi_n)\Big(\bar{\psi}_{e,L}\Lambda_i(C_i+C_i'\gamma_5)\psi_{\nu,L}\Big)\Big]+h.c\\ &=g\Big[\sum_i(\bar{\psi}_p\Lambda_i\tau_\pm\psi_n)\Big(\bar{\psi}_e\frac{1}{2}(1+\gamma_5)\Lambda_i(C_i+C_i'\gamma_5)\frac{1}{2}(1-\gamma_5)\psi_\nu\Big)\Big]+h.c\\ &=\frac{1}{4}g\Big[\sum_i(\bar{\psi}_p\Lambda_i\tau_\pm\psi_n)C_i\big(\bar{\psi}_e(1+\gamma_5)\Lambda_i(1-\gamma_5)\psi_\nu+\bar{\psi}_e(1+\gamma_5)\Lambda_i\gamma_5(1-\gamma_5)\psi_\nu\Big)\Big]+h.c\end{aligned}$$

Of the 5 interactions, Λ_i and γ_5 commute in the case of S, T, and P ($\Lambda_i\gamma_5-\gamma_5\Lambda_i=0$) and anticommute in the case of A and V. ($\Lambda_i\gamma_5+\gamma_5\Lambda_i=0$). In addition, since $\gamma_5\gamma_5=1$, only the V and A interactions of both terms are nonzero. Thus, we have:

$$\begin{aligned}\mathscr{H}_\beta =&\frac{1}{4}g\Big[\sum_i(\bar{\psi}_p\Lambda_{V,A}\tau_\pm\psi_n)C_i\Big(\bar{\psi}_e2(\Lambda_{V,A}-\Lambda_{V,A}\gamma_5)\psi_\nu+\bar{\psi}_e2(\Lambda_{V,A}-\Lambda_{V,A}\gamma_5)\psi_\nu\Big)\Big]+h.c\\ =&\,g\Big[C_V(\bar{\psi}_p\gamma_\mu\tau_\pm\psi_n)\Big(\bar{\psi}_e(\gamma_\mu-\gamma_\mu\gamma_5)\psi_\nu\Big)+C_A(\bar{\psi}_p\gamma_\mu\gamma_5\tau_\pm\psi_n)\Big(\bar{\psi}_e(\gamma_\mu\gamma_5-\gamma_\mu)\psi_\nu\Big)\Big]+h.c\end{aligned}$$

Since the $\tau_\pm$ operator does not change the wave function of the final state[3], it can be dropped. Also, the two constants can effectively be combined since the interaction is the same for both terms. Thus the final beta decay Hamiltonian is:

$$\mathscr{H}_\beta = g_iC\big(\bar{\psi}_p\gamma_\mu(1-\gamma_5)\psi_n\big)\big(\bar{\psi}_e\gamma_\mu(1-\gamma_5)\psi_\nu\big)+h.c \tag{1.3}$$

The wave functions and Hamiltonian are discussed in greater detail in Appendix A.

There have since been many developments in the Standard Model that have contributed to the total weak interaction theory, including unification with the electromagnetic interaction at high energies, but we will not discuss them here. The final electroweak interaction Lagrangian (approximately equal to the Hamiltonian but better suited to the math required

2. The lepton wave functions are displayed in such a way that indicates the annihilation of a neutrino and the emission of an electron rather than the emission of an antineutrino and an electron

3. More details discussed in Appendix A.

in the SM) can have up to eight terms after dealing with neutrino masses and the Higgs field. However, the only term that concerns this work is the charged current, which deals with a transfer of charge via a W boson. For a standard β^- decay, the effective Lagrangian is: [78]

$$\Delta\mathscr{L}_{\beta^-} = \frac{g^2 V_{ud}}{8m_W^2}\Big[\Big(\bar{\psi}_e\gamma^\mu(1-\gamma^5)\psi_\nu\Big)\Big(\bar{\psi}_d\gamma^\mu(1-\gamma^5)\psi_u\Big)\Big] + h.c \quad \text{and} \quad \frac{G_F}{\sqrt{2}} = \frac{g^2}{8m_W^2} \tag{1.4}$$

where G_F is the Fermi Constant and is defined as the strength of the weak interaction at energies much less than m_W and V_{ud} is the up-down quark entry of the Cabibbo-Kobayashi-Maskawa (CKM) Matrix. Equations (1.3) and (1.4) are effectively the same.

Though the SM has written off by construction contributions from scalar, tensor, and pseudoscalar interactions, there are still many questions unanswered. As in the 1950's, beta-neutrino correlation measurements continue to be a powerful tool in limiting BSM physics.

1.2.1 Brief Review of Potential BSM Physics

Model	Via	S/T	Explanation
New particle/Various SM extensions	Higgs exchange	S	Though in the SM they are neutral, in many SM extensions, charged Higgs bosons are possible in a state of two charged doublets, which would form a "meson". In principle, a $H^{\pm}$ meson can take the place of any $W^{\pm}$ boson exchange, such as β-decay and produces S currents.[42][46] 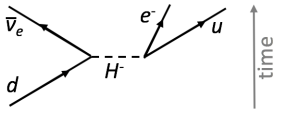
	Leptoquark exchange	S/T	Leptoquarks (LQs) are hypothetical heavy bosons that allow coupling between leptons and quarks. Their properties vary based on what SM extension is predicting them, but for β decay interactions, they can only have spin 0 or 1 and charge 2/3 or 1/3. Spin-0 LQ exchanges can result in S, P, and T interactions while spin-1 LQ exchanges only result in S and P interactions.[a] [46] 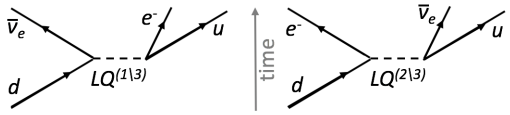
Composite model	Contact interaction	S/T	In composite models, quarks and leptons make up "composites" of the bound states in other fundamental particles. At mass-scales above 300 GeV, β-decay contact interactions can occur, for which the reaction Hamiltonian would contain couplings to S, P, and T currents.[a] [46] 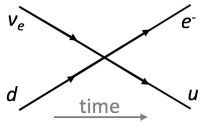
Minimal supersymmetric SM	Slepton exchange	S/T	In MSSM physics, Lepton and Baryon numbers need not be conserved and both left and right-handed (L,R) fields may be used. The addition of R-handed, spin-0 partner particles, such as squarks ($\tilde{d}$,$\tilde{u}$), sleptons ($\tilde{l}$), and neutralinos ($\tilde{\chi}$), results in L-R mixing which would add S and T currents to the interaction Hamiltonian. [80] 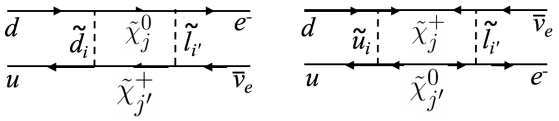

Table 1.1: Brief overview of BSM physics that would introduce scalar (S) and tensor (T) currents to the β-decay interaction.

a. Several more terms with exotic currents are possible if right-handed neutrinos are introduced

1.3 $\beta - \nu$ Correlation Measurements

If one follows Fermi's golden rule to derive a transition probability for an allowed beta decay with a non-oriented nucleus, the results would look something like the equation below (see Appendix A).

$$\Gamma(E_e)dE_e = (2\pi^3 c^5 \hbar^7)^{-1} pE_e(E_0 - E_e)^2 dE_e \xi \left(1 + a_{\beta\nu}\frac{(\boldsymbol{p}\cdot\boldsymbol{q})c^2}{|E_e||E_\nu|} + b_{fierz}\frac{mc^2}{|E_e|} + ...\right) \quad (1.5)$$

where $\boldsymbol{p}$ and $\boldsymbol{q}$ are the momentum of the β particle and neutrino, respectively. The constant $a_{\beta\nu}$ that determines the level of contribution from the cross term between $\boldsymbol{p}$ and $\boldsymbol{q}$ is known as the $\beta - \nu$ correlation coefficient or "little a" for short. The expansion of $a_{\beta\nu}$, taken from Jackson, Treiman and Wyld is below:[4][52]

$$a_{\beta\nu} = \frac{|M_F|^2\left(|C_V|^2 - |C_S|^2 + |C'_V|^2 - |C'_S|^2\right) + \frac{|M_{GT}|^2}{3}\left(|C_T|^2 - |C_A|^2 + |C'_T|^2 - |C'_A|^2\right)}{|M_F|^2\left(|C_S|^2 + |C_V|^2 + |C'_S|^2 + |C'_V|^2\right) + |M_{GT}|^2\left(|C_A|^2 + |C_T|^2 + |C'_A|^2 + |C'_T|^2\right)} \quad (1.6)$$

If we take the previous assumptions of maximal parity violation with left-handed and essentially massless neutrinos (from the 2-component theory), then $C_i = C'_i$. In addition, for a pure Fermi or Gamow-Teller allowed beta decay, $a_{\beta\nu}$ simplifies quite nicely:

$$\text{Fermi:}\ \ a_{\beta\nu} = \frac{|C_V|^2 - |C_S|^2}{|C_S|^2 + |C_V|^2}, \quad \text{Gamow-Teller:}\ \ a_{\beta\nu} = \frac{1}{3}\frac{|C_T|^2 - |C_A|^2}{|C_T|^2 + |C_A|^2} \quad (1.7)$$

The reader will probably notice that in both the case of pure Fermi and Gamow-Teller beta decay, if $a_{\beta\nu}$ is measured through the transition probability, it can be determined whether or not either scalar or tensor couplings are contributing to the decay.[5] Unsurprisingly, many physicists have also noticed this feature and have since designed experiments around it, though this is not the only way to limit exotic contributions to the electroweak

4. Fermi nuclear matrix element: $|M_F|^2 = \left|\int \mathbf{1}\right|^2$, Gamow-Teller nuclear matrix element: $|M_{GT}|^2 = \left|\int \boldsymbol{\sigma}\right|^2$

5. Many experiments measuring $a_{\beta\nu}$ construct an asymmetry ratio, as shown in Equation 1.7 using recoil spectra simulated from transition probabilities. In the Gamow-Teller instance, such a renormalization would

interaction.

In general, all experiments designed to detect scalar or tensor currents fall into one of two categories: high and low-energy. High-energy experiments at the LHC count events with high missing transverse energy (MET) to put bounds on new physics, or just search for new particles that would expand the SM, such as a right-handed W boson. Low-energy experiments use nuclear properties to put similar bounds on new physics. Though there are a plethora of ways to limit new physics in the low-energy regime (half-life measurements or using higher-order coefficients in the transition probability rate), I will only focus on experiments that use $a_{\beta\nu}$ and are directly comparable to this work. Figure 1.3 is a chart of various limits set by such low-energy experiments on $a_{\beta\nu}$. Each of them will be covered briefly and this section will conclude with a detailed explanation of my group's contribution using the beta decay of lithium-8. In addition, it is also worth delving into the tensor and scalar limits set at the LHC in the high-energy regime using a survey of their vast data sets. Their surveys have resulted in limits of relative uncertainty in the 0.1% range, though nucleus-based measurements are not far behind as they too are beginning to push below the 1% threshold.

1.3.1 High-energy limits of scalar and tensor currents at the LHC

The LHC combined with the experiments it hosts, the Compact Muon Solenoid (CMS) and A Toroidal LHC Apparatus (ATLAS), have two great strengths when it comes to making new discoveries or postulating on physics that already exists. These advantages are: ever-heightening particle collision energies and more data than anyone knows what to do with.

---

look like this:

$$a_{\beta\nu}(meas) = \frac{\int_{\delta\Omega}\int_{E_{min}}^{E_0} F(\pm ZE_e)p_e(E_0-E_e)^2 a_{\beta\nu}\frac{\boldsymbol{p}\cdot\boldsymbol{q}}{E_e E_\nu}dE_e d\Omega_e}{\int_{\delta\Omega}\int_{E_m in}^{E_0} F(\pm ZE_e)p_e(E_0-E_e)^2(1+b_{fierz}/E_e)dE_e d\Omega_e} = \frac{a_{\beta\nu}}{(1+b_{fierz}\langle\frac{m_e}{E_e}\rangle)}$$

where the positive and negative $\boldsymbol{p}\cdot\boldsymbol{q}$ terms add in the numerator and cancel in denominator (vice versa with 1 and b_{fierz})[103] The current high energy bounds on b_{fierz} for both Gamow-Teller and Fermi interactions are below 10^{-3} [74] with a similar constraint from low-energy measurements [44].

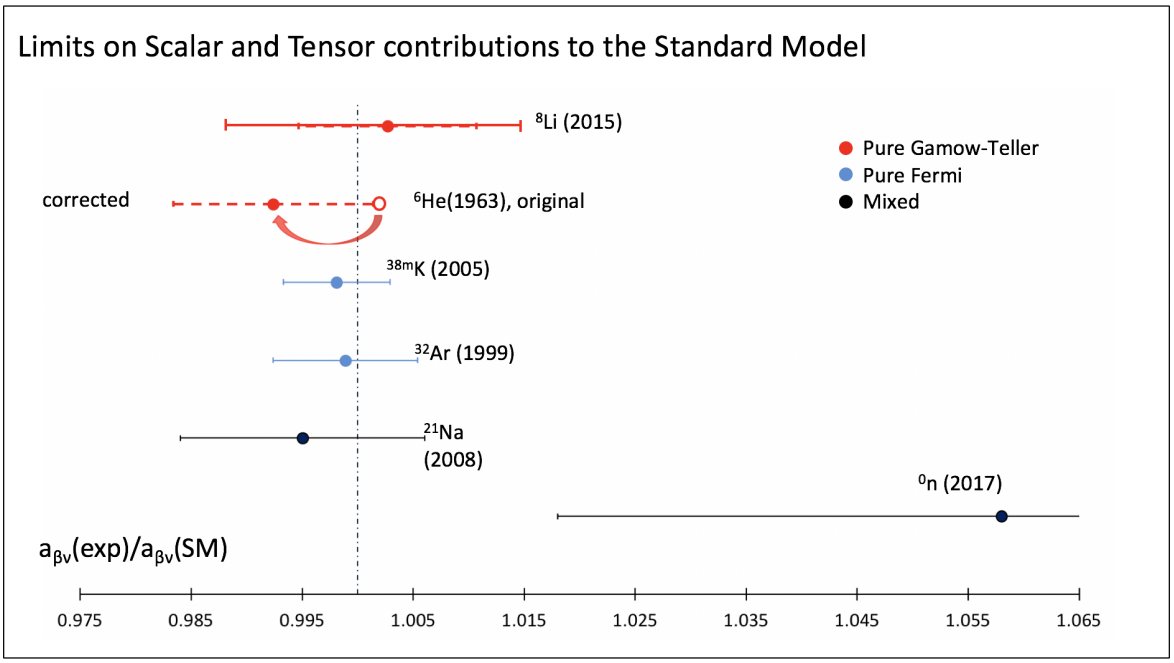

Figure 1.3: Comparison of experimental values of $a_{\beta\nu}$ determined via nuclear beta decay to the predicted SM values. Error bars represent uncertainty at 1σ. References include: n^0:[23], ^{21}Na:[102], ^{32}Ar:[7], ^{38m}Kr:[40], ^{6}He:[54], ^{8}Li:[94].

It is generally understood that new physics can be observed at higher energies (which is the motto of anyone trying to build a bigger and better collider). To that end, the LHC (or whatever high-energy collider comes after it) will continue to search for new physics that exist above the current maximum: 13 TeV. In the case of the electroweak interaction, the most interesting particle that could potentially be found is a right-handed W boson. If such a particle were found, it would overturn the assumption that the weak interaction only deals with left-handed particles and new physics would be introduced.

Conversely, given that the LHC has just finished an upgrade without finding any new interesting particles (yet), we can use their figurative mountain of data to limit new physics. Experimentalists at the CMS have used $pp \rightarrow e + MET + X$ reactions, which are similar to normal beta decay ($\bar{u}d \rightarrow e + \bar{\mu}$) to search for scalar and tensor interactions in the effective field theory regime. Their theory suggests that an MET in the TeV range would offset the extremely small new physics couplings. By counting such events, the corresponding limits

can be calculated. In the previous 8 TeV regime, using a luminosity of 20 fb^{-1}, the limits set for scalar and tensor couplings were below 5.8×10^{-3} and 1.3×10^{-3} at 90% confidence, respectively. In the new energy regime with 50 fb^{-1}, the collaboration anticipates that these limits can be cut in half.[74][19][29] Needless to say, these limits pose quite a challenge for the nuclear physicists working to make a complementary limit in their energy regime.

Though not cleanly within the realm of high-energy physics, another collaboration based in Switzerland is also posing extremely stringent limits on tensor contributions to the SM. Thus, by rule of proximity, they will be included in this section as well. Using a stopped pion beam and the PIBETA large-acceptance CsI calorimeter, they managed to limit tensor couplings to $\epsilon_T < 1.4 \times 10^{-36}$ at the 90% confidence level. [26] [74]

1.3.2 Neutron Decay (Mixed Fermi and Gamow-Teller)

Most early neutron $\beta - \nu$ correlation experiments used the recoil energy spectrum of the daughter proton to determine $a_{\beta\nu}$ and were systematically limited to about 5% relative uncertainty. However, since then, a new "wishbone" technique has been implemented by the aCORN collaboration (based at NIST), which resulted in the most precise measurement of $a_{\beta\nu}$ for the neutron to date. Their apparatus and the corresponding "wishbone" data are shown in Figure 1.4. When a neutron from the beam decays, the proton and electron are guided to opposite sides of the apparatus. The proton's time of flight is measured on one end and the beta's energy is measured on the other. By calculating the asymmetry between the branches (the antineutrino and electron's momentum were correlated so the daughter protons are faster and anticorrelated so the protons are slower), and comparing to Monte Carlo simulation, they established a value of $a_{\beta\nu}$ =-0.109 $\pm$ 0.0041 (1σ), (3.5% relative uncertainty) which examplifies a "mixed" Fermi and Gamow-Teller decay, and is in good agreement with the current accepted value. They plan to eventually bring their relative uncertainty down to the 1% range. [23]

6. ϵ_T is the high-energy formalism equivalent to C_T

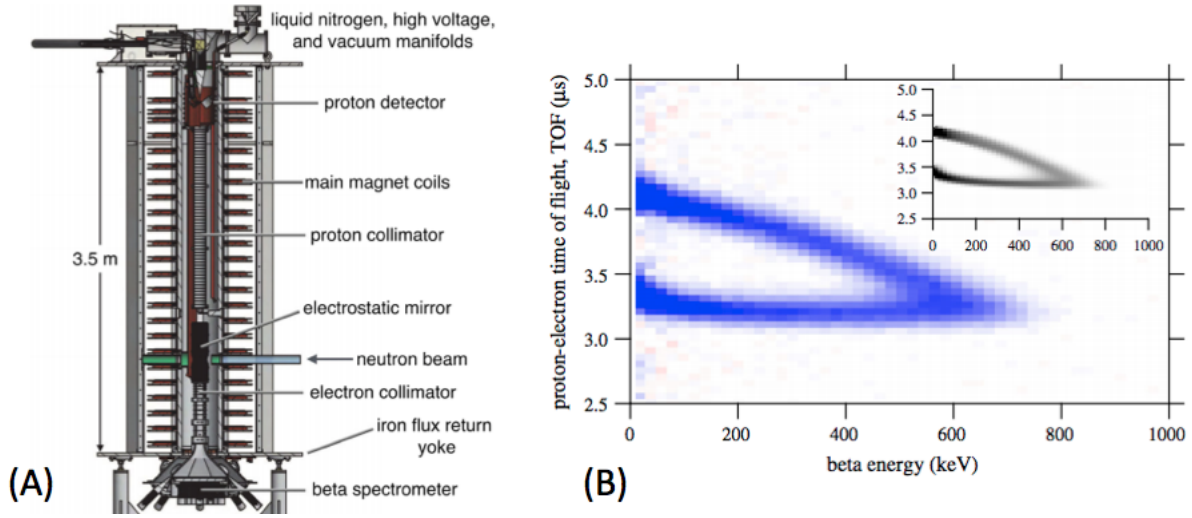

Figure 1.4: A) The apparatus aCORN used to measure the $a_{\beta\nu}$ of neutron decay. B) The "wishbone" plot for neutron decay compared to an inset Monte Carlo simulation. [23]

1.3.3 Sodium-21 Decay (Mixed Fermi and Gamow-Teller)

A 2008 measurement of sodium-21 mirror β^+ decay ($^{21}Na(3/2^+) \rightarrow {}^{21}Ne(3/2^+)$) confirmed the accepted value of $a_{\beta\nu}$ [102] after a previous experiment resulted in a 3.6σ discrepancy from the Standard Model due to molecular contamination [88]. The group obtained their ^{21}Na from the cyclotron at Lawrence Berkeley National Lab and used a magneto-optic trap (MOT) to hold ions in place while they decayed. The recoiled daughter nuclei and the shake-off electrons produced from the positron interacting with the electron cloud were both picked up using microchannel plate detector (MCP). The times of flight of the decay products were compared to a Monte Carlo simulation to infer $a_{\beta\nu}$ (as seen in Figure 1.5-A). The result, 0.5502 ± 0.006 (1σ) reflects a roughly 1% relative uncertainty measurement, though the group anticipates they could reduce it by an order of magnitude if they successfully addressed their chief sources of error, the highest of which was the size and location of the ion cloud. [102]

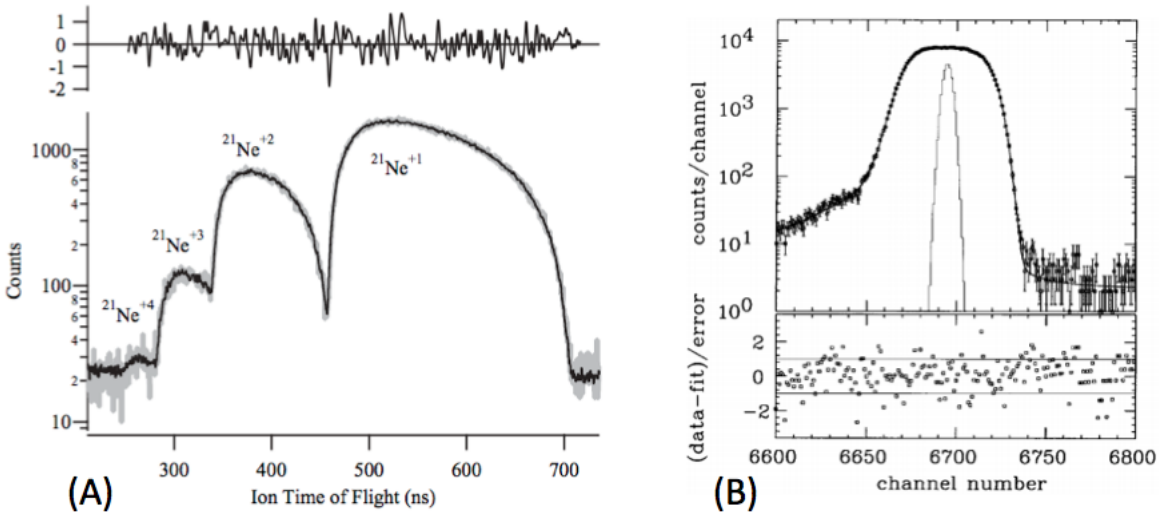

Figure 1.5: The analysis methods used to determine $a_{\beta\nu}$ in the ^{21}Na and the ^{32}Ar experiments, respectively. A) Time of flight spectrum of the recoiling ^{21}Ne daughter ion compared to a Monte Carlo simulation with residuals [102], B) Energy spectrum of the delayed proton emitted from ^{32}Ar fit to another Monte Carlo simulation with residuals. The narrow peak is from a pulser to demonstrate the energy resolution. [7]

1.3.4 Argon-32 Decay (Pure Fermi)

The first of the pure trasition measurements listed here, the β^+ decay of ^{32}Ar was performed at the Isotope mass Separator On-Line (ISOLDE) facility at CERN in 1999. The group's setup only required implanting ^{32}Ar from a general-purpose separator on a carbon foil. In turn, rather than tracking all the decay products, only the energies of the delayed protons emitted by the daughter nucleus were measured using p-i-n diode detectors while all the other products were deflected away using magnets. In the same manner as the two previously mentioned experiments, the energy spectra of the protons were compared to a Monte Carlo simulation to determine $a_{\beta\nu}$ (Figure 1.5-B). The final result produced a 0.7% relative uncertainty with $a_{\beta\nu}$=0.9989 $\pm$ 0.0065. The experiment itself only took 12 days (though the analysis took several years) and the error was dominated by statistical uncertainty and the errors attributed to the mass values of the parent, daughter, and proton.[7] If it were to be done again today, this experiment also has some merit for constraining $a_{\beta\nu}$ even further.

1.3.5 Potassium-38 Decay (Pure Fermi)

Another high-precision measurement of the pure Fermi $a_{\beta\nu}$ was conducted at Canada's TRIUMF facility's Isotope Separator and Accelerator (ISAC) in 2005 using $^{38}\mathrm{K}^{m}$. This particular setup used a combination of 2 MOT's (as used in the ^{21}Na experiment and shown in Figure 1.6-A) to reduce background from any other states of potassium-38. When held at rest, the ions were allowed to decay. The daughter nucleus was accelerated toward another MCP to measure the time of flight and energy. The positions and energies of shake-off electrons generated from the β^+ particle would be picked up by a silicon double-sided-strip-detector (DSSD) and backing plastic scintillator. $a_{\beta\nu}$ was determined using separately the time of flight of the recoiled daughter nucleus and by reconstructing the angle between the beta and neutrino while comparing to yet more Monte Carlo simulations (see Figure 1.6-B). Their results produced a 0.5% relative uncertainty measurement with $a_{\beta\nu}$=0.9981 $\pm$ 0.0048. As one of the most precise low-energy experiments to date, this one's largest weaknesses were their understanding of the electric field within their trap and the data calibration. [40] An upgrade is currently being conducted to further reduce the relative uncertainty to the 0.1% range.

1.3.6 Helium-6 Decay (Pure Gamow-Teller)

helium-6 is a very interesting isotope and is an equal to lithium-8 in terms of studying pure Gamow-Teller decays. Recently, there has been a surge of activity among a variety of collaborations to use its decay to measure $a_{\beta\nu}$. Currently, there are setups being developed and upgraded in Seattle at the University of Washington's Center for Experimental Nuclear Physics and Astrophysics (CENPA), at the Weizmann Institute of Science in Rehovot using the Soreq Applied Research Accelerator Facility, and at the Grand Accelerateur National d'Ions Lourds (GANIL) in France. However, as of yet, none of them have been able to match the limit set by a helium-6 measurement done in 1963 at Oak Ridge National Lab [54].

This particular experiment made use of an unusual apparatus pictured in Figure 1.7.A.

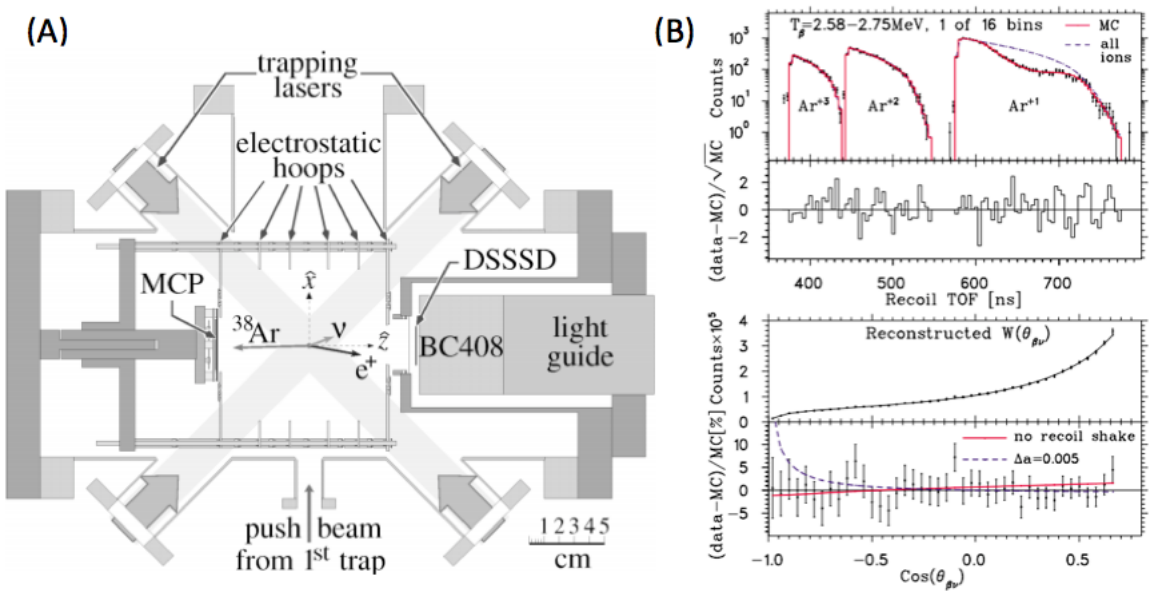

Figure 1.6: A) Double MOT system used at TRIUMF to measure ^{38m}K decay product kinematics. B) Top: Monte Carlo fit to the daugher Ar time of flight spectrum. Bottom: reconstructed angle between the β and ν, Monte Carlo fit, and residuals. [40]

After irradiating a fine BeO powder at the Oak Ridge Research Reactor, the resulting helium-6 was swept away using water vapor through various cold and hot volumes designed to remove the moisture. The then mostly-pure helium-6 was allowed to decay in a large conical volume. In turn, a small fraction of the recoiling daughter lithium-6 emerged through the tip of the cone to be eventually detected by a secondary-electron multiplier. Their counting rate and energy spectrum of the daughter ^{6}Li was compared to a derived counting rate and energy spectrum to obtain a final value.

The results of this experiment set $a_{\beta\nu}$ at -0.3343 ± 0.003, a 0.9% relative uncertainty measurement. The group cited their chief sources of error as "random variations in the spectra and efficiency curves", possibly from the 12 different data sets they used in combination to make their measurement. [54] However, in 1998, the experiment was revisited by a theorist: Glück, who took into account radiative corrections in the daughter recoil that had previously been unaccounted for. This adjustment pushed $a_{\beta\nu}$ a full 1σ higherthan the original measurement, to -0.3308 ± 0.003 now a 0.8% relative uncertainty measurement.[38] For its time, this experiment proved to be quite a landmark in precision. An even more

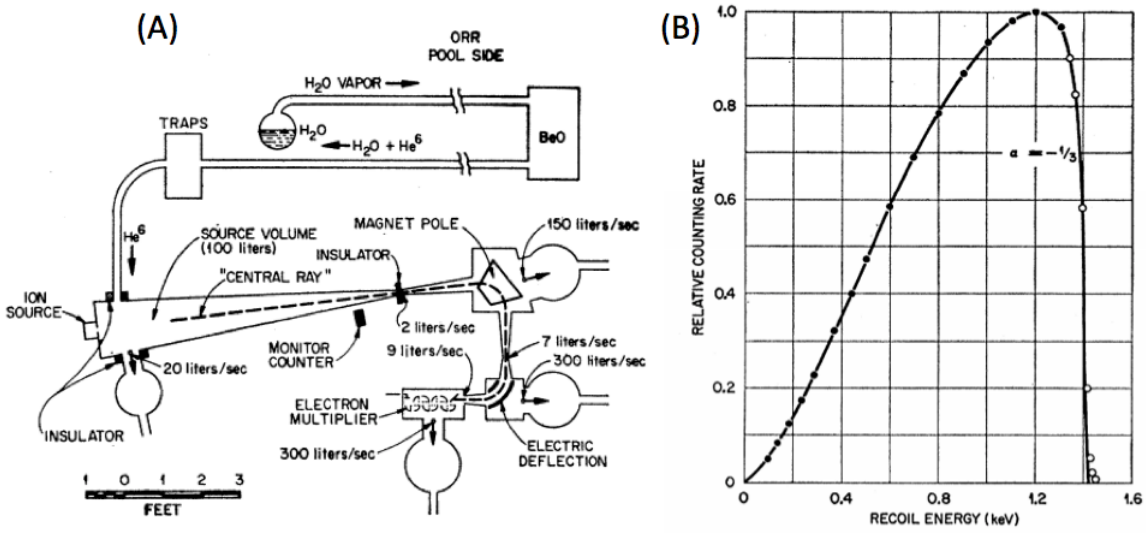

Figure 1.7: A) Apparatus used in the 1963 helium 6 $a_{\beta\nu}$ measurement. B) Comparison between measured recoiled ^{6}Li recoil energy spectrum (circles) vs the theoretically calculated spectrum for $a_{\beta\nu} = -\frac{1}{3}$ (line) [54]

precise measurement of $a_{\beta\nu}$ using helium-6 should not be so far away given the attention the isotope is currently receiving.

1.4 The Argonne Lithium-8 Experiment

This work represents the third iteration of the Argonne lithium-8 beta-neutrino correlation experiment. The first experiment was performed in 2010 and published in 2013 by Gang Li [64]. Much of the hardware, beam delivery system, and original development of the trap can be attributed to his work. With only 20,000 full "triple" events, Li was able to constrain the relative uncertainty to about 3% with $a_{\beta\nu} = -0.3307 \pm 0.009$. The second iteration comprised of data taken in 2011 (about 300,000 full events) and was published in 2015 by Matt Sternberg, who considerably reduced systematic sources of error and updated the detector-data acquisition system. The result of his efforts was an $a_{\beta\nu}$ value of -0.3342 $\pm$ 0.0039, a 1% relative uncertainty measurement.[94] Though the listed error bar on $a_{\beta\nu}$ itself for the 2015 paper was higher than the adjusted 1963 helium-6 experiment, Glück's corrections resulted in a higher sensitivity to tensor currents. Comparing the two $|C_T|^2/|C_A|^2$ ratios (what is

actually measured in the experiment and used to infer $a_{\beta\nu}$), at 1 sigma the lithium-8 experiment limited tensor currents to 0.6% compared to the helium-6's 0.8% [38], resulting in the first improvement on the low-energy limit to tensor currents in over 50 years. This work will further reduce that number.

1.4.1 The Decay of Lithium-8

The isotope lithium-8 itself can actually be credited a nontrivial portion of the success from the previous experiments given how many useful features it brings both in terms of convenience of measuring and theoretical sensitivity. Beginning in a 2+ ground state and decaying into a broad, low-lying 2+ excited state of beryllium-8, the isospin change from 1 to 0 requires a Gamow-Teller transition. The nearest 2+ ^{8}Be state that could produce a Fermi interaction is 13.3 MeV away, so mixing is very unlikely. Calculations performed in-house using the ab-initio Green's function Monte Carlo method by R. B. Wiringa and S. C. Pieper indicate that "very unlikely" means less than 10^{-4} intensity. [108] Thus, for all intents and purposes, lithium-8 decays purely via a Gamow-Teller transition. The Q-value of the original β decay to ^{8}Be* is on the order of 12 MeV, which results in daughter nucleus recoiling energies larger than in the previously listed experiments and thus easier to measure. In turn, almost instantaneously (approximately 1x10^{-21} s), the ^{8}Be* ion falls apart into two alpha particles, each with its own recoil energy of about 1.5 MeV. In addition, if both the β particle and the two α's are detected, they produce a "triple" event that is nearly impossible to arise from a background event. The full decay scheme is pictured in Figure 1.8.

1.4.2 $\beta - \alpha - \nu$ Correlation

With the addition of ^{8}Li's delayed alpha emission, the transition probability becomes a bit more complicated than the one given in equation 1.5 due to the correlations between each of the leptons and the additional alpha. A full expansion of the transition probability was done by Barry Holstein in 1974 [49]. The complete equation can be found in Appendix B

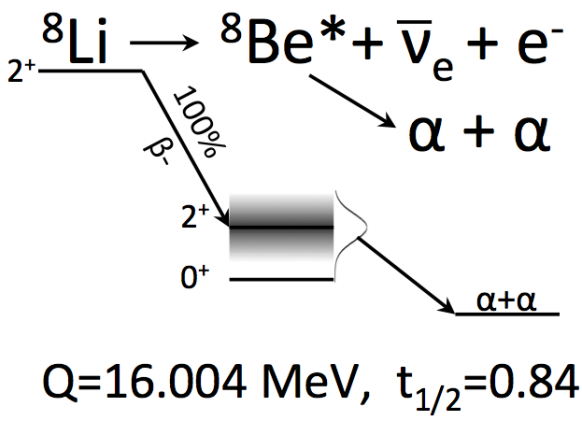

Figure 1.8: The lithium-8 decay schematic including total Q-value and half-life. The entire decay actually consists of two separate decays: $^8\text{Li} \rightarrow {}^8\text{Be}^* + \text{e}^- + \bar{\nu}$ and $^8\text{Be}^* \rightarrow \alpha + \alpha$.

along with more details about each of the terms, but the equation containing the largest contributions is:

$$\Gamma(E_e)dE_e \propto pE_e(E_0 - E_e)^2 dE_e \left(g_1 + g_2 \frac{(\boldsymbol{p}\cdot\boldsymbol{q})}{|E_e||E_\nu|} + g_{12}\left(\frac{(\boldsymbol{p}\cdot\boldsymbol{p_\alpha})(\boldsymbol{q}\cdot\boldsymbol{p_\alpha})}{|E_e||E_\nu|} - \frac{1}{3}\frac{(\boldsymbol{p}\cdot\boldsymbol{q})}{|E_e||E_\nu|} \right) + ... \right) \tag{1.8}$$

where g_1, g_2, and g_{12} are defined in Appendix B. In the events where one of the α's and the β particle are emitted in roughly the same direction, the g_{12} term can be approximated as a beta neutrino correlation term, except up to $2\times$ larger than g_2. In the case of ^{8}Li's transition from $2^+ \rightarrow 2^+ \rightarrow 0^+$, g_{12} can be written in terms of:

$$\frac{g_{12}}{g_1} = \frac{|C_T|^2 - |C_A|^2}{|C_T|^2 + |C_A|^2} = 3\frac{g_2}{g_1} = 3a_{\beta\nu} \tag{1.9}$$

In summary, thanks to the additional correlation terms introduced by beryllium-8's alpha emission, we have a factor of 3 higher sensitivity to $a_{\beta\nu}$ than other decays would. Again, for more details, see Appendix B.

1.4.3 Experimental implementation

Both of the lithium-8 experiments discussed previously were conducted at the Argonne Tandem Linac Accelerator System (ATLAS) Facility.[7] Using a neutron stripping reaction via lithium-7 provided by the accelerator and a deuterium gas target, lithium-8 was created and transferred to the Beta decay Paul Trap or "BPT" hereafter. The ^{8}Li ions that decayed while trapped were picked up by a set of silicon double-sided-strip-detectors (DSSD's, 16x16 strips in 2010 and 32x32 strips in 2011) and in the case of the 2011 experiment, backing plastic scintillator detectors (see Figure 1.9). Thus, if all the decay products were detected, a full kinematic reconstruction of the decay would be possible. In this way, an energy spectrum of the recoiling daughter alphas (see Figure 1.10 and the reconstructed angle between the beta and the neutrino (compared as in many other experiments to a Monte Carlo simulation) could be used to determine $a_{\beta\nu}$. Though the reconstructed $\theta_{\beta\nu}$ was never actually used to establish $|C_T|^2/|C_A|^2$, the recoil spectra were specifically chosen using beta particles that had hit the same detector as one of the alphas (relative angles between the two particles were less than 50 degrees). Thus, as was discussed in the previous section, sensitivities to $a_{\beta\nu}$ and the ^{8}Be* recoil energy were maximized .

1.5 Outline

The following chapters will roughly correspond to the chronology of this experiment, beginning with the production and transfer of the lithium-8 ions used for this measurement at the ATLAS facility. Chapter 3 will continue with a description of the BPT, our detectors, and the data acquisition system. Chapter 4 will cover my calibration and further data processing. Chapter 5 will address the simulations my group and I have developed for comparing to the data and how we calculate $a_{\beta\nu}$ from both. The remaining chapters will be populated with results, an analysis of our errors and systematics, followed by conclusions. The more adven-

7. The tandem has since been removed and they are searching for a new acronym. Contact Guy Savard if you have a good idea.

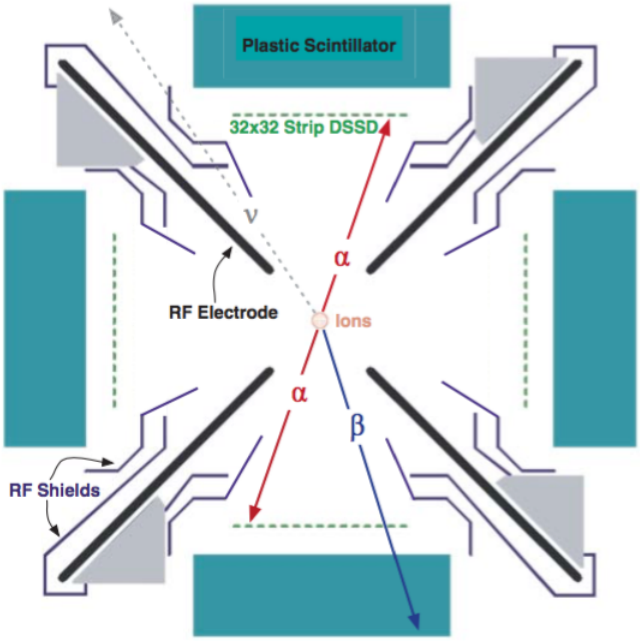

Figure 1.9: The BPT setup used in the 2011 experiment with an illustration of what a "triple" event would look like. The backing plastic scintillators did not produce high enough quality data to use. [95]

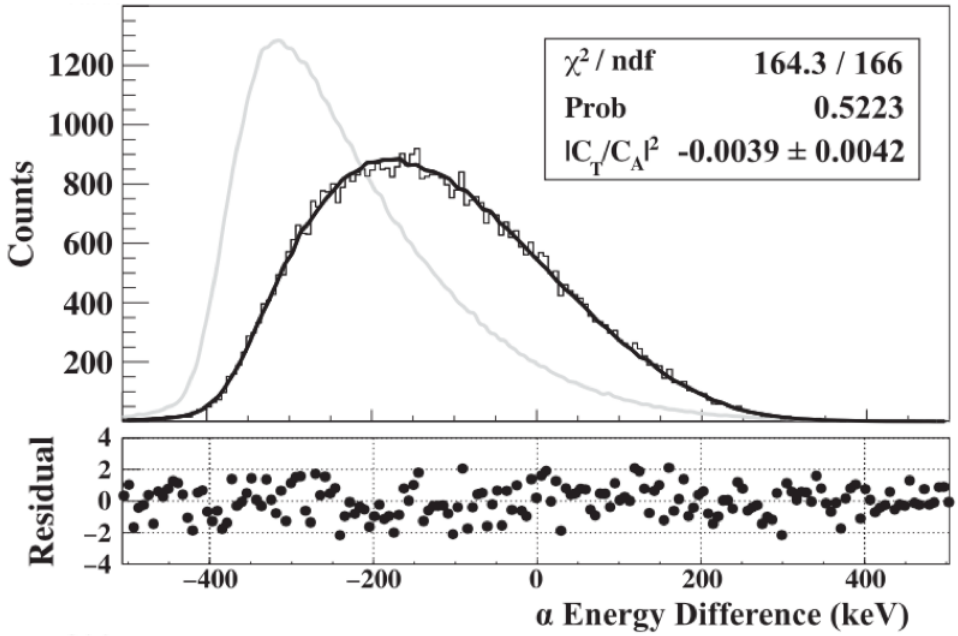

Figure 1.10: Recoil spectrum depicting the difference in energy of the 2 back to back α with the β hitting the same detector as one of the α's. This way, the recoil energy of the ^{8}Be* is most discernable and sensitivity to $a_{\beta\nu}$ is increased. Picture taken from the 2015 ^{8}Li paper. [94]

turous reader may venture further into the appendices for more theory than likely should be in an experimental thesis.

CHAPTER 2

LITHIUM-8 PRODUCTION AND TRANSFER

Since this experiment effectively starts at the ANL ATLAS Accelerator, it is fitting to also start this thesis with the same. Beginning with the ion source, a high temperature oven is used to evaporate and ionize ^{7}Li. Extending ∼100 meters through the Physics 203 building, there are a series of magnets and niobium split-ring resonators that accelerate and steer the ^{8}Li beam to where the BPT is housed. This experiment marks the third time this beamline had been utilized for a set of runs meant to produce ^{8}Li. As there have been minimal changes since the previous iteration, this chapter will be meant only as a summary of the production and transfer methods. More details can be found in the dissertations of my two predecessors, Matt Sternberg [95] and Gang Li [65].

We utilize the ATLAS facility at Argonne National Lab to produce ^{7}Li and have 4 main stages of processing before the ^{8}Li product is delivered to the BPT. A schematic of the production beamline can be seen in Figure 2.1. The 24 MeV ^{7}Li beam impinges on a deuterium (^{2}H) gas target and via a neutron pickup reaction, a small percentage of the particles become ^{8}Li while scattering off the gas. Immediately following the gas target is a large superconducting bore magnet used to re-focus the wide-angled beam into something vaguely linear. The beam eventually passes through a thin metal window and into a gas catcher[1]. There, the ions thermalize in high purity helium while still maintaining their charge, are condensed into a beam, and escorted out using a DC gradient. The ions are insulated from the sides of the gas catcher using an RF carpet, which will be discussed in greater detail in section 2.2.

Once the ^{8}Li^{+} ions are extracted from the gas catcher, they are fed into a RF-quadrupole ion guide (RFQ, a linear Paul trap with conventional cylindrical electrodes). There, the ions are briefly trapped and ejected, resulting in a bunched beam. These ^{8}Li^{+} bunches are periodically fed into the Advanced Penning Trap (APT) where any lithium molecules are

1. Designed by the dark and twisted mind of Dr. Guy Savard.

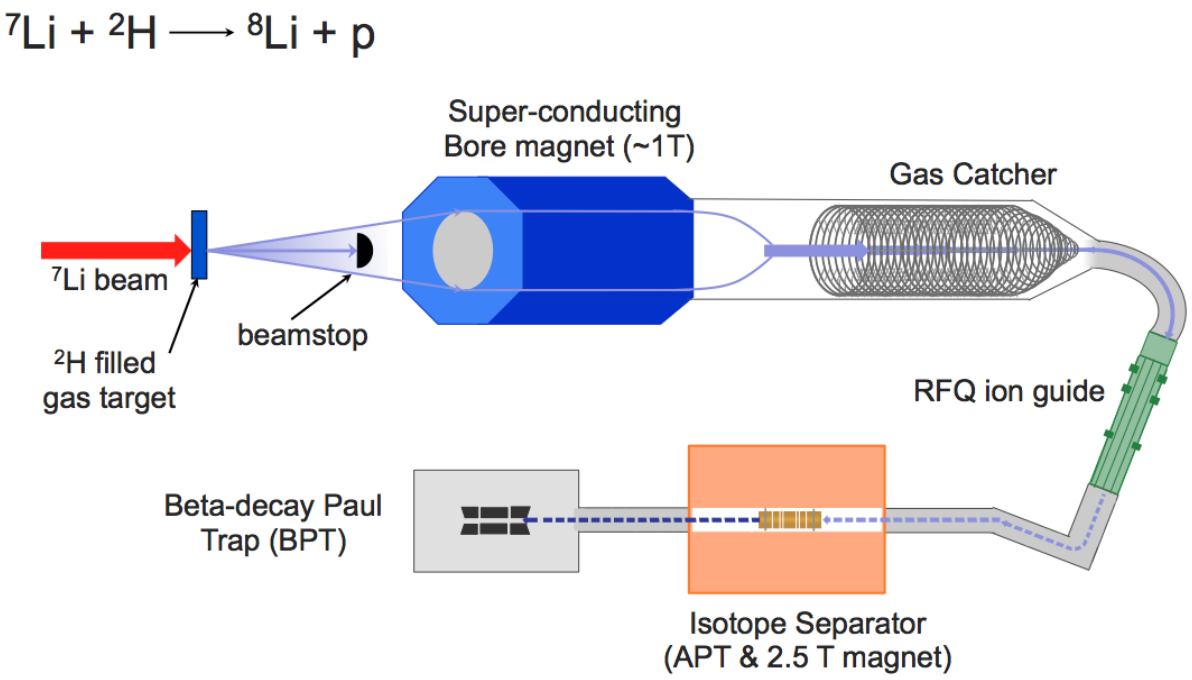

Figure 2.1: An overview of the beamline used to create and transfer ^{8}Li to the BPT

broken up and contaminants are discarded. Upon ejection from the APT, a final, pure $^8Li^+$ bunched beam is delivered to the BPT. More technical details about each stage of the processing are found in the subsequent sections.

2.1 The Reaction

The original ^{7}Li beam is produced by ATLAS via heating a solid stable source in a commercial oven and collecting the evaporated, ionized particles. The beam is then accelerated to 24 MeV and directed to Experimental Area II where the gas target and our production beamline are located. The gas target, pictured in Figure 2.2.A, is 4.5 cm long and holds 550 Torr of liquid nitrogen-cooled deuterium gas. The 2 faces of the cylinder are covered by 1.3 mg/cm^2 titanium windows. The ^{7}Li(d,p)^{8}Li reaction has a total cross section of about 75 mb. [58]

The particles that emerge from the target can roughly be divided into three different categories. The first set, which consists of un-reacted and mostly un-scattered ^{7}Li with angles of less than $\sim 5^o$, is halted by a beamstop made of tantalum mounted on an aluminum

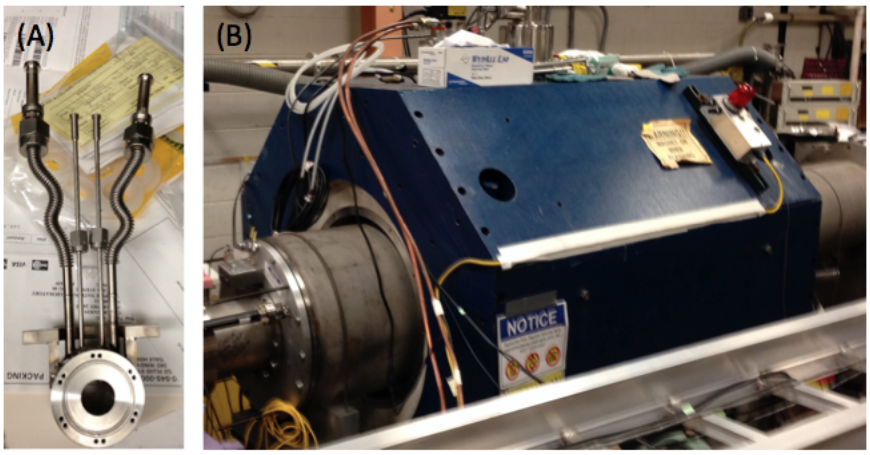

Figure 2.2: A) The target used to form ^{8}Li. The cylindrical space is enclosed by titanium windows and holds about 550 torr of deuterium gas at -180^{o}C. B) The 1 T, 60 cm diameter bore magnet used to focus the scattered products of the ^{8}Li neutron pickup reaction.

rod. The remaining two sets of particles: ^{8}Li reaction products and Coulomb-scattered ^{7}Li, make it around the beamstop and must be separated so that only the ^{8}Li is directed into the gas catcher. This process is accomplished via a large bore magnet (as seen in Figure 2.2.B), which serves as a focusing lens for the scattered particles.[2] The relationship between the focal length and magnetic rigidity (momentum divided by charge) is below:

$$\frac{1}{f} = \frac{e^2}{4p_z^2}\int B_z^2 dz$$

where $p_z = \gamma^2 m^2 v_z^2$ is the momentum along the axis of the solenoid and B_z is the magnetic field in the same direction [59].

Since the charges on both isotopes of lithium are the same, the magnet's separation works best when the discrepancy between ^{8}Li's and ^{7}Li's momentum is large. Figure 2.3 shows the momentum distributions based on the outgoing angle. There is clearly a much wider distance in the isotope's momentum when backward center of mass (COM) angles are selected. Unfortunately, based on angular distribution measurements done by Schiffer et

2. In the previous 2 experiments, a degrader foil was used to further decrease the particles' energy before entering the magnet but has since been removed.

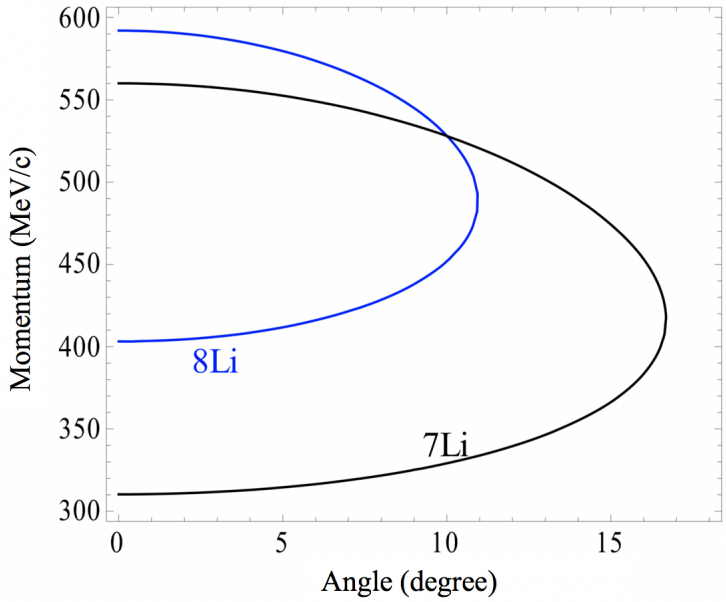

Figure 2.3: Outgoing momentum distribution for ^{8}Li and scattered ^{7}Li in the Lab frame with the incident beam energy equal to 24 MeV. The top (bottom) branches correspond to a forward (backward) angle in the center of mass frame. [65] Slightly downstream from the target is a beamstop that halts all particles within 5 degrees of the normal beam trajectory.

al. using 12 MeV deuterons on ^{7}Li, the reaction cross section for backward COM angles is nearly an order of magnitude less than for forward angles less than 20^{o}.[87] However, based on previous production runs, if the forward COM angle products are selected and focused, there is not enough separation between the 2 isotopes to prevent significant amounts of ^{7}Li from going into the gas catcher. If there are too many ions entering the gas catcher, the ionization transfer with the helium gas will be too high and the resulting He^{+} ions will shield the desired ^{8}Li ions from being directed out by the DC fields, resulting in saturation. Thus, despite the lower cross section, this experiment utilizes the lower momentum branches in Figure 2.3 to extract and focus ^{8}Li from the solenoid magnet into the gas catcher.

2.2 The Gas Catcher

After the solenoid has collected and separated the ^{8}Li, a helium-filled gas catcher (pictured in Figure 2.4) is utilized to return the fast-moving and widely dispersed particles into something

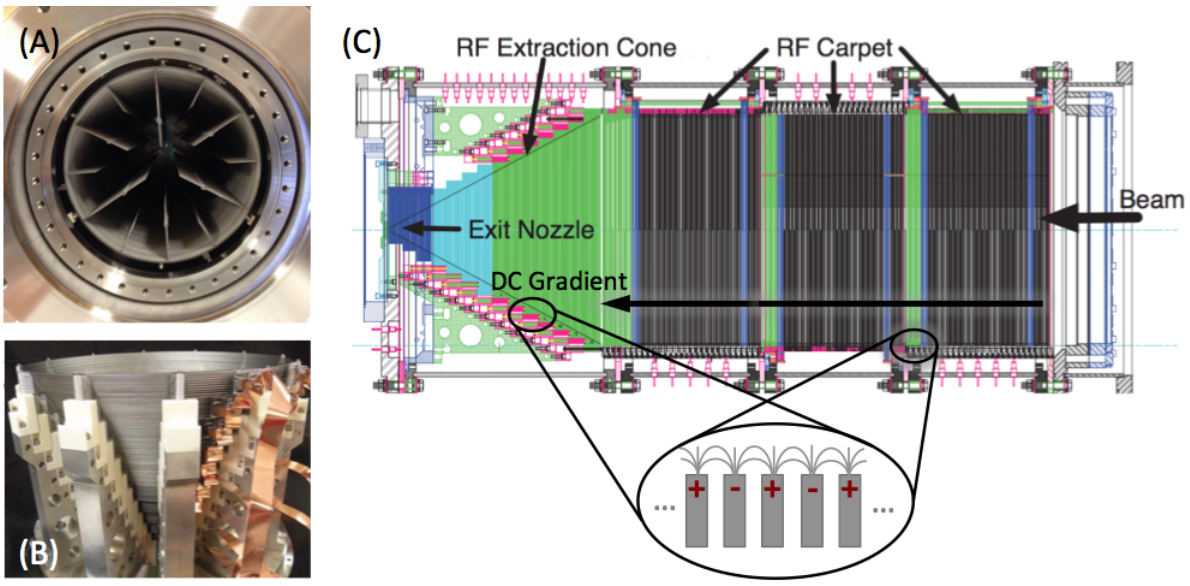

Figure 2.4: A) Radial cross section of the gas catcher installed after the magnet. B) Close-up of the cone section. C) A schematic of a fully assembled gas catcher with a zoomed-in diagram of the RF Carpet (adapted from [86]).

resembling a normal beam again. The particles enter through a thin aluminum window (∼3 mg/cm^2) that contains the helium gas within the chamber and decreases the ^{8}Li's energy to below 2 MeV. Once inside, the ^{8}Li ions are slowed to a near halt, thermalized within the helium, and guided toward the exit nozzle while being condensed into a beam using a DC gradient.

The high-purity helium within the gas catcher is held at 65 torr, which roughly corresponds to the pressure needed to produce a ^{8}Li stopping length of less than the length of the gas catcher (∼70 cm). In the process of thermalizing, the ^{8}Li ions stay within their +1 charge state unless they interact with a contaminant (most likely water). To prevent this, the helium goes through three stages of purification. The first stages flow the helium through two activated cold traps: the first immersed in liquid nitrogen and the second cooled to less than 24 K by a cyro cooler. Finally, the helium is fed through a commercial activated getter system, which brings the level of water contamination to below 1 ppb. This purity is enough to keep the ion lifetime well above 10 ms, which is about how long the ^{8}Li stays in the gas catcher. The dominant form of ^{8}Li leaving the gas catcher in the experiment used for this

thesis was $^{8}LiOH^{+}$.

Four different voltages are applied to the gas catcher to provide a DC gradient for the ions to follow. Beginning at the aluminum window and ending at the cone where the ions leave the gas catcher, the DC gradient values are 100, 56, 54, and 1 V. To prevent the ions from interacting with the electrodes and chamber of the gas catcher, an RF carpet (also called an RF wall or RF cone) is applied to the electrodes. A schematic can be seen in Figure 2.4).C with a close-up of the stacked electrodes in the cone section shown in Figure 2.4).B. By applying an alternating RF ($\sim$ 5 MHz) potential to the electrodes, an effective field is generated close to the electrodes that pushes the ions away. The effective force of the field in cases of high pressure is given by [27].

$$F_{eff} = -m\mu^2 \frac{V_{RF}^2}{r_0^3}\left(\frac{r}{r_0}\right)$$

where μ is the mobility of the ions and r_0 is the half-distance of the electrodes. The physics of this operation will be discussed in further detail in the next chapter since an RF carpet is effectively an unfolded Paul trap and the same principles are used to trap in the BPT. Far from the electrodes, the field averages to 0 and the applied DC gradient dominates. The spokes (seen in Figure 2.4.A) serve to help distribute the DC gradient throughout the chamber. Because of the low mass (which results in a lower F_{eff}) and the limitations of RF field applied to electrodes by the breakdown voltage of the gas, the final efficiency of the gas catcher for transferring ^{8}Li from the aluminum window to the exit nozzle is between 0.1 and 1% (though the efficiency depends deeply on the quality of the beam itself as well). Previous studies indicate that our gas catcher can handle about 10^8 incident ions per second before saturating [93].

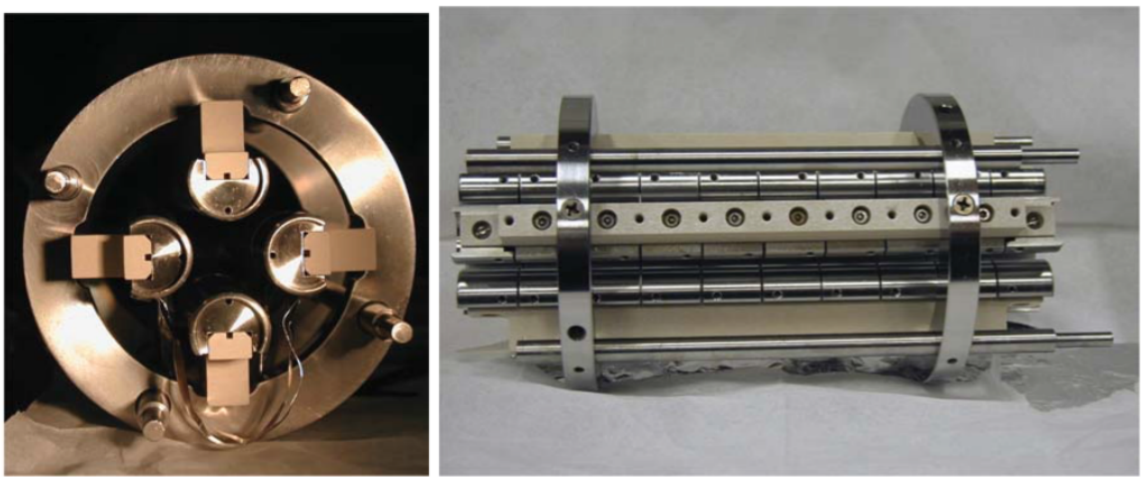

Figure 2.5: Axial and radial cross sections of one portion of the RFQ ion guide. The axially segmented electrodes used to form a DC gradient can be seen on the right.

2.3 Bunching via RFQ ion guide

Upon exiting the gas catcher, the ^{8}Li ions enter the RFQ (radio frequency quadrupole) ion guide. The RFQ is divided up into 3 sections and serves to remove the majority of helium gas that is extracted with the ions from the gas catcher, do some rough mass selection, and "bunch" the ^{8}Li beam into small packets of ions that are accelerated and cycled through the remainder of the beamline. One of the sections is pictured in Figure 2.5. The RFQ electrodes themselves consists of 19 mm diameter steel rods arranged axially with 14 mm of space between the outermost edges. The electrode segments are each 20 mm long and are separated by ceramic insulators. They provide the DC gradient and RF fields that both linearly confine the ions and accelerate them down the beamline. There are two diagnostic detector sets (silicon with a biased foil and MCP for each: one placed after the first section and the second at the end of the RFQ) that are designed to detect radioactivity, monitor what compounds of ^{8}Li come out of the gas catcher, and assist with the mass selection. In addition, the end of each RFQ section is outfitted with a differential pumping apparatus to remove residual helium from the gas catcher (about 20 torr of pressure by the end of the RFQ sections).

The first RFQ section serves simply to transfer ions from the gas catcher to the next RFQ

section and has no special properties. One of the diagnostic detector sets is placed after this section to determine the quantity of ions coming out of the gas catcher. Because of its short half-life, ^{8}Li is easy to identify. After going around a 90 degree bend, the beam enters the second RFQ section and is subjected to the first mass filtering process (though this feature was not used in the run that produced the data for this experiment). Again, the physics of the quadrupole/Paul trap will be discussed in the next chapter, but the combination of DC and RF fields applied to the trap results in the stability of only a narrow range of masses. Thus, by applying a DC offset, only one mass can be selected to continue on to the next section. In this ^{8}Li experiment, the mass selection in section 2 of the RFQ was tuned to the pure ^{8}Li ion.

The final section of the RFQ is devoted to bunching the beam and accelerating it toward the APT. The last three electrodes of the RFQ have a potential well applied to them to briefly confine and cool the particles in about 10^{-3} Torr of purified helium gas. At a rate of 25 Hz (every 40 ms), the downstream electrodes are lowered which ejects the bunched ions from the trap and accelerates them downstream with 1.5 keV of energy. After the mass selection in the previous section, enough of the beam should be filtered to prevent too many ions from reaching the buncher, which results in the particles pushing themselves out of the trap via charge repulsion.

After exiting the RFQ, the bunched beam is sent along the beamline to the triangle room where the APT and BPT both reside. Another MCP/Si diagnostic detector before the APT is used to determine the time of flight of the various lithium compounds coming out of the RFQ compared to when they were ejected. By deflecting the beam except in time ranges where the desired mass resides, we can further filter the beam for a desired mass with resolution of about 2 u. For the data used in this experiment, mass 25 (^{8}LiOH^{+}) was chosen based on high abundance (over 50% of the available molecular forms).

2.4 Advanced Penning Trap Isotope Separator

After exiting the RFQ, the bunched ions are injected into the Advanced Penning Trap (APT). Though the beam had already been filtered for other masses, any remaining contaminants were removed and the $^8LiOH^+$ ions broken up into pure $^8Li^+$. This thesis primarily relies heavily on a Paul Trap. However, an ion trapping thesis would be incomplete without a brief venture into how the Penning trap works as well. What follows is a brief summary of the physics behind Penning traps. For a complete derivation of the equations of motion, see Matt Sternberg's thesis [95], a thorough theory paper by Brown and Gabrielse [15] or any of the work done by my colleagues at the Canadian Penning Trap (CPT)[101][75].

2.4.1 Penning Trap Dynamics

The basic Penning traps consist of a set of electrodes that apply a static quadrupole electric field and a uniform magnetic field (symbol: B, often from a solenoid magnet, ∼2.5 T for the APT). Two different configurations of electrodes can be seen in Figures 2.6.A and B. The APT follows the configuration of B, but has 9 electrodes instead of 3. The quadrupole electric field serves to confine ions along the axis of the magnetic field and creates a hyperbolic harmonic motion with frequency ω_z. The magnetic field provides confinement in the radial place and induces a cyclotron motion ω_c around the axis of the magnetic field. If the equations of motion are solved for the Penning trap, ω_c is actually the sum of 2 other frequencies (magnetron frequency: ω_-, and modified cyclotron frequency: ω_+) that represent the two remaining modes of harmonic particle motion. The motion of all three modes can be seen in Figure 2.6.C and the equations for each of the frequencies are below.

$$\omega_c = \frac{qB}{m} \qquad \omega_z = \sqrt{\frac{qU_{dc}}{md^2}} \qquad \omega\pm = \frac{1}{2}(\omega_c \pm \sqrt{w_c^2 - 2w_z^2})$$

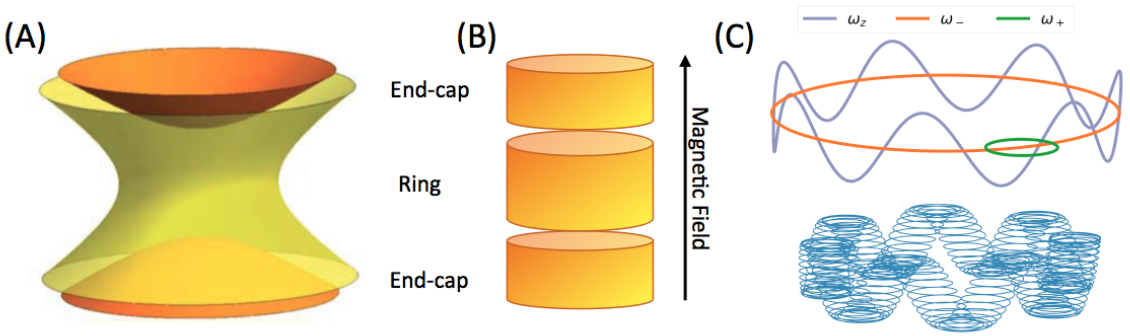

Figure 2.6: A) Basic electrode configuration for a traditional Penning trap. The CPT utilizes 7 electrodes instead of 3 to correct for the hole needed to inject and eject ions. B) Basic electrode configuration for a cylidnrical Penning trap. The APT utilizes 9 electrodes rather than 3. C) Above: motion of an ion in a Penning trap with the 3 eigenmotions labeled. Below: the summation of the 3 motions. [76]

where U_{dc} is the potential difference between the end-cap and ring electrodes and $d^2 = \frac{1}{2}\left(z_0^2 + \frac{\rho_0^2}{2}\right)$.[3]. Each of the three modes can be excited at their resonance by applying dipole fields at the corresponding frequency to the appropriate electrodes. The end-caps are used to excite ω_z. The ring of each Penning trap is also segmented into 4 radial pieces so that both dipole and quadrupole fields can be used to excite $\omega_\pm$. Such manipulations can be used to remove contaminants from the trap or make precision mass measurements via scanning for the resonant ω_c.

Though the CPT is operated at high vacuum, the APT is used with $\sim$3 μTorr of purified helium gas inside. At such pressures, the resident ions collide with the helium and lose energy. The energy of an ion with quantum numbers n_z, n_+, and n_- in a trap is defined by [84]:

$$E_{n_z n_- n_+} = \hbar\omega_+(n_+ + \tfrac{1}{2}) + \hbar\omega_z(n_z + \tfrac{1}{2}) - \hbar\omega_-(n_- + \tfrac{1}{2})$$

The reduced cyclotron and z harmonic motion are both positive terms, so the amplitudes of both decrease as the ions interact with the helium and E decreases. In contrast, the magnetron orbit (a negative term) increases in size as E decreases. An example of the

3. ρ_0 is the inner ring radius and z_0 is the distance from the center of the trap to the bottom of the closest end-cap electrode in Figure 2.6.

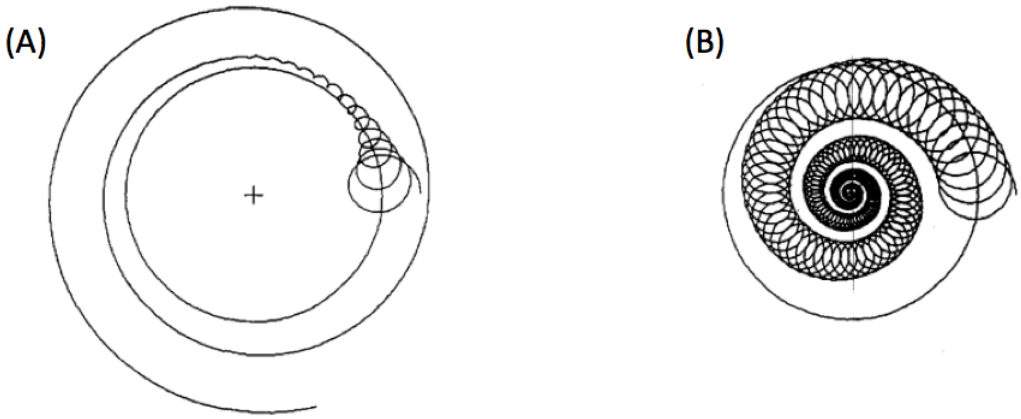

Figure 2.7: Taken from [84]. The cross and circle in both represent a normal magnetron orbit radius with no interactions with a buffer gas. A) The trajectory of an ion in a gas filled trap. Both the magnetron orbit increases and the modified cyclotron orbits decrease as the ion loses energy to the buffer gas. B) The same as (A) except with a quadrupole excitation at ω_c. The ions still lose energy to the buffer gas, but they are directed towards the center of the trap as they cool.

motion can be seen in Figure 2.7.A. Left unchecked, an ion with this motion will eventually hit one of the electrodes of the trap. If a quadrupole excitation from the ring electrode at ω_c (which corresponds to the desired mass) is applied, then both the reduced cyclotron and magnetron motions become coupled. The smaller orbit loses energy faster than the larger and collectively drags both motions toward the center of the trap (Figure 2.7.B).

2.4.2 Advanced Penning Trap Operation

We utilize a combination of the two different motions in Figure 2.7 to clean the APT of contaminants for each injection and break up the $^8LiOH^+$ compounds into pure $^8Li^+$. First, a dipole excitation of the ω_- corresponding to $^8LiOH^+$ is applied to the trap. This energizes the $^8LiOH^+$ and causes it to interact more with the helium gas and eventually be torn apart by the collisions. In addition, the excitation begins driving any other contaminant ions out of the trap. A quadrupole excitation of the ω_c corresponding to the desired mass ($^8Li^+$ in our case) in turn drives the selected mass 8 ions toward the center of the trap while any contaminants and the broken hydroxyl groups continue their outward trajectory until they

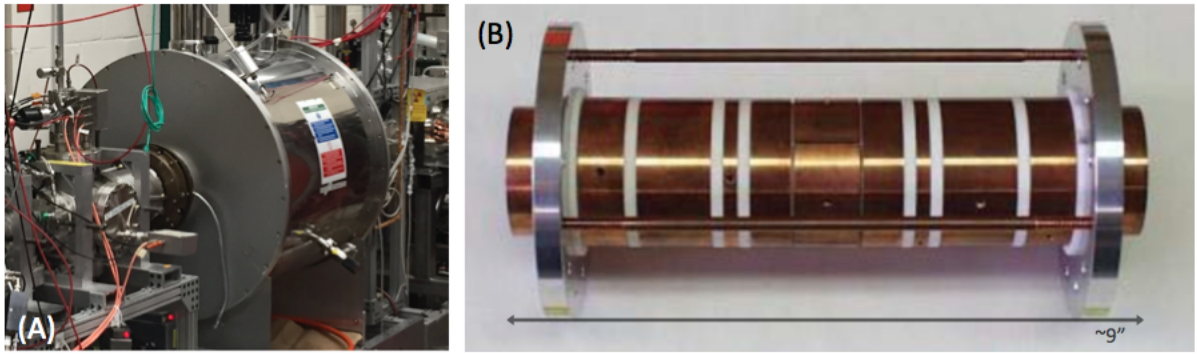

Figure 2.8: A) The isotope separator beamline enclosed by a 2.5 T superconducting magnet. B) Axial view of the electrodes of the Advanced Penning Trap.

leave the trap. The cleaning process typically takes less than 50 ms and the quality of our magnetic field, electronics, etc allow for a mass separation resolution of about 10^{-4}. The molecule breakup efficiency is close to 100%. The 2.5 T solenoid magnet is pictured in Figure 2.8.A and the APT itself with the electrodes visible (separated by ceramic insulators) is seen in 2.8.B.

In sequence with the RFQ buncher, ions are injected into the APT every 40 ms by lowering the upstream electrode and quickly raising it again (> 2 μs) 5 bunches of ions are sent to the APT for cleaning before injecting them into the BPT (every 200 ms).

2.5 Successful Experiments

I led the campaign that resulted in the data for this experiment, which took place in August 2016, spanned two weeks, and resulted in 2.3×10^6 raw triple events (both α particles and the β particle from ^{8}Li were detected) Of the 2.3×10^6, 3×10^5 events had to be discarded at the beginning of the run due to heavy noise contamination from the liquid nitrogen pump attached to the BPT, resulting in 2×10^6 usable raw triples. Even with the discarded events, the resulting statistics were over an order of magnitude larger than our previous experiment.

Leading up to the August 2016 experiment, a production run and data campaign were performed in 2015, resulting in about 5×10^5 raw triples. The data set was compromised by a

higher level of RF noise pickup from the BPT and remains unused. In addition, a production run in preparation for the aforementioned high statistics campaign was performed in June of 2016. 7×10^5 raw triples were collected. However, the top silicon detector began to fail at the start of the experiment and could not be properly biased, resulting in more noise contamination.

Of the experiments listed, the 2×10^6 triples from August 2016 remain the highest quality and largest data set produced so far. All the results of this thesis are drawn from the aforementioned data.

CHAPTER 3

THE BETA DECAY PAUL TRAP

After being ejected from the APT, the ^{8}Li ions are transferred to the Beta decay Paul Trap (BPT), which is a radio-frequency (RF) quadrupole ion trap specifically designed for precision studies of nuclear decay [89]. Utilizing a DC gradient and the oscillating RF electric field, the ^{8}Li or any unstable ion of interest can be held in a small 1-2 mm^3 volume at the center of the trap until it decays essentially at rest. In turn, the decay products can then propagate outward with little interference from the electrodes and fields to ideally hit one of the surrounding detectors. For this particular experiment, the alpha energy, direction, and beta direction were determined using a set of silicon double sided strip detectors (DSSD's), which were backed by a set of plastic scintillator detectors for gathering the beta energy. However, those detectors could be swapped out for a variety of others (MCP, germanium, etc) if a different experiment required it.

This chapter will serve as a summary of the BPT system. It will cover the physics of Paul traps, features of the BPT in particular, including the detection system used in this experiment, some of the noise challenges, and an explanation of how signals are processed by the data acquisition system.

3.1 The Physics of Paul Traps

The radio-frequency quadrupole ion trap was originally designed by Wolfgang Paul, from whom its shortened name is derived. Due to the extreme versatility of such a trap, Paul was given a Nobel Prize in 1989 for his design, which featured hyperbolic-shaped electrodes. Though the BPT itself utilizes thin planar electrodes, which distort the electric field close to the metal, the field within 1 cm of the center of the trap follows the potential produced by the usual hyperbolic electrodes quite closely. For simplicity, the physics and fields that pertain to hyperbolic electrodes will be discussed here. A diagram of the coordinates and

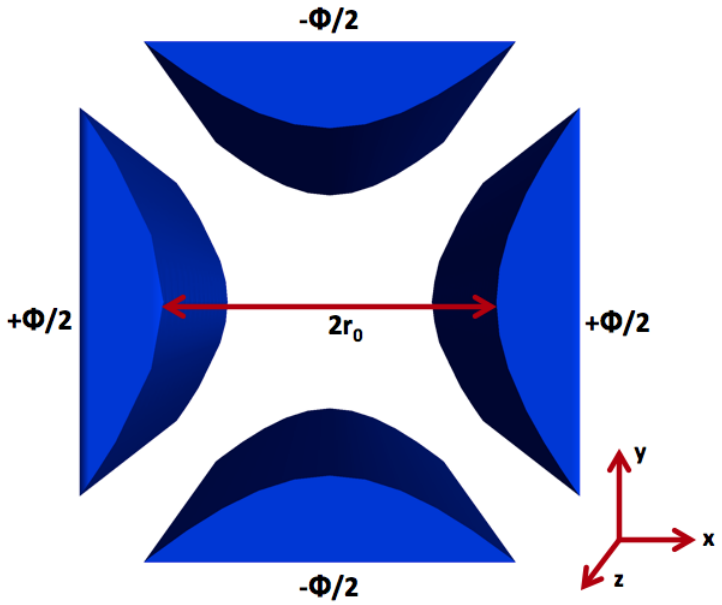

Figure 3.1: Axial view of a linear Paul Trap with hyperbolic electrodes. A voltage of $\pm\frac{\Phi}{2}$ is applied to opposing electrodes. The closest point between each of the electrodes is $2r_0$.

electrodes can be found in Figure 3.1.

Beginning with the hyperbolic potential and corresponding electric fields in the x-y direction, borrowed from Paul's Nobel lecture, we have: [6]

$$\Phi = \frac{\Phi_0}{2r_0^2}(x^2 - y^2), \quad E_x = -\frac{\Phi_0}{r_0^2}x, \quad \text{and} \quad E_y = \frac{\Phi_0}{r_0^2}y$$

where $\pm\Phi_0/2$ is the potential applied to the opposing electrodes. The result is a system that pushes positive ions towards the center of the trap along the x direction but away from the center in the y direction. If the potential is allowed to oscillate with voltage V around a DC offset U, then Φ_0 is replaced with $U + V\cos(\omega t)$. The equations of motions can be constructed by summing forces:

$$m\frac{d^2x}{dt^2} + \frac{e}{mr_0^2}\big(U - V\cos\omega t\big)x = 0, \quad \text{and} \quad m\frac{d^2y}{dt^2} - \frac{e}{mr_0^2}\big(U - V\cos\omega t\big)y = 0 \tag{3.1}$$

where m and e are the mass and charge of the ion in the trap, respectively. If one defines a

few different variables to insert into the equations:

$$t = \frac{2\tau}{\omega}, \quad a_x = -a_y = \frac{4eU}{mr_0^2\omega^2}, \quad \text{and} \quad q_x = -q_y = \frac{2eV}{mr_0^2\omega^2} \tag{3.2}$$

and divides out the m, then the Mathieu equations are produced.

$$\frac{d^2x}{d\tau^2} + \big(a_x - 2q_x\cos 2\tau\big)x = 0, \quad \text{and} \quad \frac{d^2y}{d\tau^2} + \big(a_y - 2q_y\cos 2\tau\big)y = 0 \tag{3.3}$$

Fortunately for our purposes, the Mathieu equations are well-known and can be solved exactly for the trajectories of ions within the trap[1]. According to [24], the solutions are expressed independently for each direction (x, y) as:

$$\frac{d^2u}{d\tau^2} = -(a - 2q\cos 2\tau)u \quad \text{with} \quad u = \alpha' e^{\mu\tau}\sum_{n=-\infty}^{\infty} C_{2n}e^{2in\tau} + \alpha'' e^{-\mu\tau}\sum_{n=-\infty}^{\infty} C_{2n}e^{-2in\tau} \tag{3.4}$$

α' and α'' are integration constants that depend on the ions' initial position, velocity, and τ. C_{2n} and μ are both constants and are dependent on the properties of the trap itself (a_u and q_u), but not the initial conditions. Naturally, for an ion trap system, the desired trajectories would be stable and not increase to infinity. The constant μ defines the stability of the ion's trajectory and must be a purely imaginary non-integer ($i\beta$) in order for the ion to remain in the trap. The boundaries of stability for a_u and q_u are defined by the integer imaginary values. If μ is real or a complex number, the real exponential components will cause the ion's trajectory to diverge. If one were to solve β_u for a and q (not attempted here), the result would be approximated in its simplest form as: $\beta = \sqrt{a + q^2/2}$. Figure 3.2.A shows the numerical space a_u and q_u can occupy in order to have a stable trap. Plugging $\mu = i\beta$ into equation 3.4, we can simplify a bit and pull out the real part, which represents the ions'

1. The Mathieu equations can be solved exactly in the "regions of stability" which will be discussed shortly.

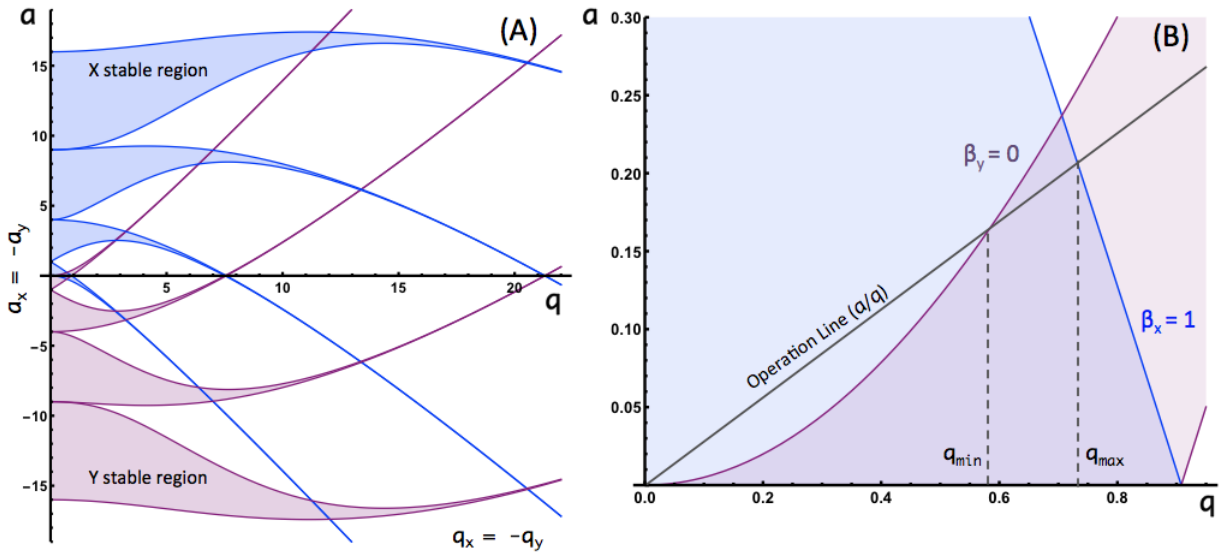

Figure 3.2: A) The first four stability regions (shaded) for the x and y directions in a Paul Trap as defined by a and q. B) A zoomed-in image of the lowest order stability region. Mass-selective traps can use the trap voltages and RF along the operation line to only select masses that fall within q_{min} and q_{max} with the corresponding a values. (Calculated using Mathematica.)

motion.

$$u = \alpha' \sum_{n=-\infty}^{\infty} C_{2n} e^{i(2n+\beta)\tau} + \alpha'' \sum_{n=-\infty}^{\infty} C_{2n} e^{-i(2n+\beta)\tau} \tag{3.5}$$

$$u_{(real)} = (\alpha' + \alpha'') \sum_{n=-\infty}^{\infty} C_{2n} \cos{(2n+\beta)\tau} \tag{3.6}$$

Most ion traps are operated in the lowest overlap region of stability ($a \ll q$ or $a = 0$ and $q_u < 0.908$). For mass-selective ion traps, one can use an operation line such as the one pictured in Figure 3.2.B to only trap masses between the corresponding q_1 and q_2 values. In the regime where $a \ll q$ and $q, \beta \ll 1$, the two first modes of equation (3.6) dominate the ion's motion. An example of an ion's stable 1D motion can be seen in Figure 3.3.

If the two modes are represented by $u = A(n_0) + B(n_1)$, we can assume that $A \gg B$, $\frac{dA}{dt} \ll \frac{dB}{dt}$ and $\int_0^{2\pi} \frac{d^2B}{dt^2} = 0$, which from Figure 3.3 is not unreasonable. By applying these

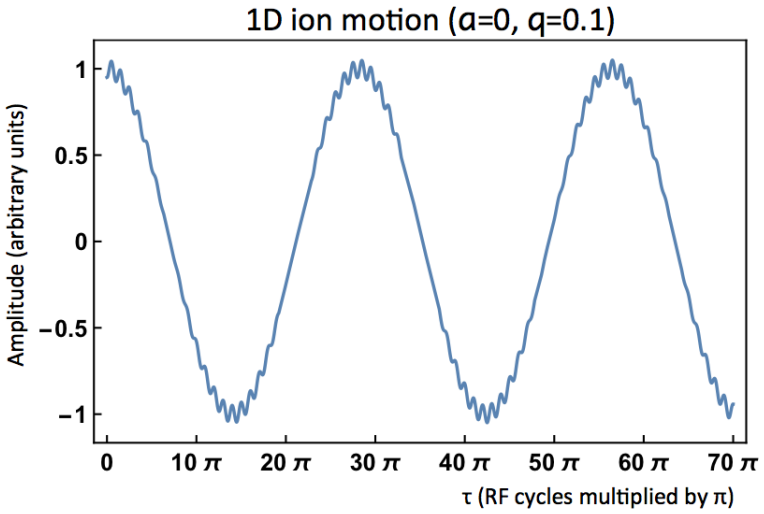

Figure 3.3: Example 1D solution of the Mathieu equation for $a = 0$ and $q = 0.1$. The ion's motion is dominated by a harmonic macromotion with a much smaller high frequency oscillation most easily seen at the peaks. (Calculated using Mathematica.)

assumptions to equation (3.4), we can obtain an approximation of the smaller oscillation, B:

$$\frac{d^2B}{d\tau^2} = -(a - 2q\cos 2\tau)A \tag{3.7}$$

Since we have already assumed $a \ll q$, equation (3.7) can be integrated twice to obtain a new representation of B that can in turn be substituted into $u = A(n_0) + B(n_1)$:

$$B = \frac{-qA}{2}\cos 2\tau \quad \text{which gives} \quad u = A - \frac{qA}{2}\cos 2\tau$$

Putting all this back into the right side of $\frac{d^2u}{d\tau^2}$ in (3.4), we get:

$$\frac{d^2u}{d\tau^2} = \frac{d^2A}{d\tau^2} + \frac{d^2B}{d\tau^2} = -aA + \frac{aqZ}{2}\cos 2\tau + 2qA\cos 2\tau - q^2A\cos^2 2\tau$$

If we average over 1 RF period (2π), then from our previous assumption that the acceleration of the small oscillations over 1 period of the RF is 0, $\frac{d^2B}{dt^2}$ drops out along with all of the

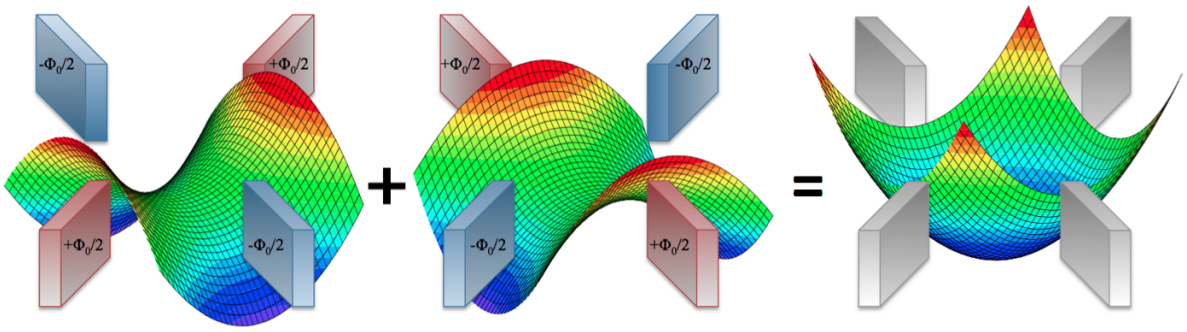

Figure 3.4: With settings $a = 0$ and $q \ll 1$, the radial potential of the trap can be approximated as a harmonic potential when averaged over an RF cycle.

single cosine terms on the right side, leaving:

$$\frac{d^2A}{d\tau^2} = -(a + \frac{q^2}{2})A \quad \text{then, substituting with} \quad \tau = \frac{\omega t}{2}, \qquad \frac{d^2A}{dt^2} = -\frac{\omega^2}{4}(a + \frac{q^2}{2})A$$

If for simplicity, we assume $a = 0$ (which is the case for the BPT and RFQ ion guides), q from equation (3.2) can be substituted in to get a new differential equation that contains our approximate potential $\widetilde{\Phi}$.

$$\frac{d^2A}{dt^2} = -\frac{e^2V^2}{2m^2r_0^4\omega^2}A \quad \text{such that} \quad m\frac{d^2A}{dt^2} = -e\frac{d\widetilde{\Phi}}{dA} \quad \text{where} \quad \frac{d\widetilde{\Phi}}{dA} = \frac{eV^2}{2mr_0^4\omega^2}A. \tag{3.8}$$

Remembering that $u = A + B$ and integrating A from 0 to u, we obtain a well of depth:

$$\widetilde{\Phi}(u) = \frac{eV^2}{4mr_0^4\omega^2}u^2 \tag{3.9}$$

for the 1D approximate ion trap potential. [66] [24] Thus, with the appropriate conditions and assuming the macro oscillation dominates as in Figure 3.3, a Paul trap can be approximated as having a simple static harmonic potential in the radial direction when averaged over the RF period (Figure 3.4).

3.1.1 Buffer Gas Cooling

The BPT system and the RFQ buncher also use a small amount of high-purity helium ($\sim$ 1mTorr in the RFQ and $\sim$15μTorr in the BPT) as a buffer gas to cool the ions and reduce some of their potential energy from the beam injection. As the ^{8}Li ions move about the trap, some of their momentum is transferred to the helium gas until the system comes to thermal equilibrium. The buffer gas can be modeled in the Mathieu equations by adding a damping term to equation (3.1): $\frac{d^2u}{dt^2} = -\frac{e}{K}\frac{du}{dt} + eE$.

$$m\frac{d^2u}{d\tau^2} + 2\kappa\frac{du}{d\tau} + (a_u - 2q_u\cos 2\tau)u = 0 \quad \text{with} \quad \kappa = \frac{e}{mK\omega} \tag{3.10}$$

Here, κ is calculated from the ion mobility (K), which is the proportionality constant between an ion's drift velocity in a gas and the electric field strength ($v_d = KE$). [68] If we make the substitution $v = ue^{-k\tau}$, then

$$\frac{d^2v}{d\tau^2} + (\hat{a_u} - 2q_u\cos 2\tau)v = 0 \quad \text{where} \quad \hat{a_u} = a_u - \kappa^2 \tag{3.11}$$

From a practical standpoint, looking back at equation (3.4), a solution is now a function of $e^{(\mu-\kappa)}$. Thus, as τ approaches infinity, the trap can stay stable until $\mu < \kappa$, which significantly expands the regions of stability.

3.2 BPT Design and Features

Some alternatives to using an ion trap for high-precision kinematic measurements include using ion implantation in foils or the detectors themselves, or using neutral atom magneto-optical traps (MOTs). In the case of ion implantation, understanding the implantation itself well enough to achieve a low systematic error can be extremely difficult. MOTs were successfully used in both the sodium-21 and potassium-38 measurements from section 1.3. They avoid using magnetic fields and electric fields which could alter the trajectories of any

decay products, and despite having very low trapping efficiencies ($\sim 1\%$), still hold a high density of particles without having to deal with Coulomb repulsion. However, MOTS come at the cost of being very ion-specific and require laser-heavy experimental setups, which can prove both expensive and cumbersome.

In contrast, ion traps have close to 100% efficiency and can easily trap a range of different isotopes by varying frequency and voltages. Unfortunately, despite the high efficiency, only about 10^4 ions/mm^3 can be trapped before the repulsion forces become overpowering. In addition, the previously mentioned electric fields and in the case of Penning traps, magnetic fields, can indeed become a systematic error in their own right. Fortunately, in the BPT, the impacts of the RF and DC fields on the decay products' trajectories are less than 1 keV, in contrast to the average beryllium-8 α energy, which is 1.5 MeV and are thus well below our current levels of sensitivity (see section 6.2.9). Even with the high statistics data set used for this experiment, such effects are still beyond our sensitivity. The recoiling beryllium-8 also decays too quickly ($\sim 70fs$) for the electric fields to change the trajectory noticeably.

Though most Paul traps utilize hyperbolic or cylindrical electrodes, the BPT uses thin planar electrodes (separated by $2r_0 = 3.4$ cm and pictured in Figure 3.5) to minimize any scattering of the decay products and increase the solid angle available for detectors to occupy. The planar electrodes were simulated using SIMION software to ensure the approximate harmonic potential in the trap center was preserved. Within 1 cm of the center of the trap, the resulting potential closely matches what would be produced by hyperbolic electrodes with radius $\sim 1.3r_0$. The highest voltage that the electrodes can safely carry is about 1kV$_{pp}$. To separate the remainder of the trap and detectors from the high voltage, the electrodes are also segmented in the radial direction to leave a 2 mm gap. They are held in place using a ceramic brace that can be seen in the upper part of Figure 3.5.B.

The BPT RF was operated at $\omega = 2\pi \times 1.33$ MHz with 400 V$_{pp}$ for lithium-8 with the axially segmented electrodes carrying DC's of 10, -50, and 10 V going from upstream to downstream. Using SIMION modeling, the depth of the harmonic potential ends up being

$\sim$3 V/cm^2 when both the DC gradient from the segmented electrodes in Figure 3.5.B and the RF are taken into account. Supplying such a strong RF and DC at the same time required a custom circuit box constructed by our RF engineer, Tony Levand. The circuit consisted of a center-tapped coil for each segmented electrode set (3 total) coupled across a variable capacitor used for tuning and wound around a common primary coil.The opposite ends of the center-tapped coils provided the opposite RF phases to the radially-adjacent electrodes. The circuit was also equipped with RF chokes designed to keep the RF from feeding into the DC power supplies. The resulting configuration allowed for unique DC offsets on each of the 3 segments of the trap alongside the required 2 RF phases that could be operated at or above the 1kV$_{pp}$ level. The DC offsets could also be pulsed (either of the end electrode sets lowered) for both injection and ejection of ions from the trap as discussed at the end of Chapter 2.

To maintain the stability of the trap for several times longer than the lifetimes of the ions inside, everything in the BPT chamber was designed to ultra-high vacuum standards to reduce possible interactions of the lithium-8 ions with other atoms that might provoke neutralization. However, a small amount of buffer gas (described in section 3.1.2) with high ionization potential, namely ultra-pure helium, was added to the trap to effectively provide a low temperature bath for the hot ions and improve the trapping capability. In addition, while in operation, the trap frame has liquid nitrogen pumped through it to both help cool the buffer gas and ions (to $\sim$90 K), substantially reduce the residual gas (mostly water), and improve the performance of the silicon detectors. The trap itself rests on 4 quartz spheres to thermally isolate it from the rest of the chamber. With liquid nitrogen cooling but without the buffer gas, residual pressure in the chamber can reach 5×10^{-9} Torr. Before cooling with liquid nitrogen, the chamber is pumped down to below 1×10^{-7} Torr to ensure minimal condensation buildup from gas contaminants on the silicon detectors.

Trapping lifetimes for lithium-8 in the BPT are estimated to be longer than 30 seconds. It takes injected ions about 30 ms to be cooled and reach equilibrium with the other trap

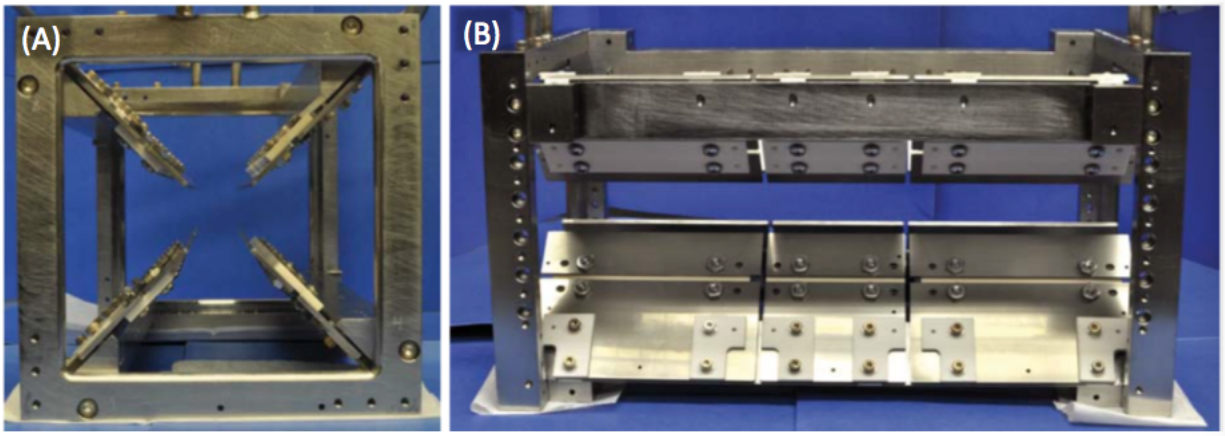

Figure 3.5: A) Radial view and B) axial view of the BPT frame and electrodes. The three axially segmented electrodes that provide the DC well can clearly be seen in B.

occupants. Data recorded before the 30 ms after an ion bunch is injected are not used. [89]

3.3 Detector System

The BPT system is outfitted with 2 sets of detectors: 4 32x32 double sided silicon strip detectors (DSSD's), which were the primary workhorse of this experiment, and 4 plastic scintillator detectors that backed the silicon detectors. The plastic detectors were used as a means to limit beta scattering systematics and calibrate a portion of another experiment to measure the beta spectrum of rubidium-92. The DSSD's collect information on the beryllium-8 α's energy and direction, and the lithium-8 β direction while the plastic detectors collected the β energies. Portions of both detector sets can be seen in Figure 3.6. The individual detectors are referred to as Top, Bottom, Left, and Right based on what orientation they have in the direction of the beam. In Figure 3.6, upstream to downstream runs from right to left.

3.3.1 Double-Sided Silicon Strip Detectors

Part of a larger category of semiconductor detectors (which also includes germanium detectors), silicon crystal detectors are often thin wafers that are operated as a reverse-biased p-n junction, which are commonly found in circuit diodes. This configuration requires 2

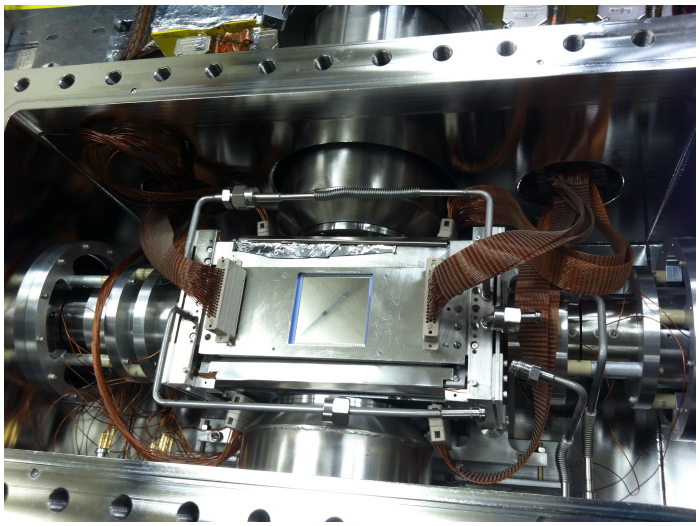

Figure 3.6: The BPT chamber with the trap inside. Two plastic detectors are mounted on each side of the chamber to back the left and right silicon detectors. The top silicon detector can be seen mounted on the trap in the middle of the chamber.

layers of silicon: one doped to produce a "p-type" crystal with an excess of valence band electron holes, and another doped to produce a "n-type" crystal with a surplus of electrons. A "depletion zone" between the 2 layers is created when spare electrons from the edge of the "n-type" side flow into electron holes on the opposite side of the barrier, such that at the interface between the two, there are no charge-carriers and an electric field is created which prevents further movement of ions. When reverse bias is applied (cathode to p-side and anode to n-side), the depletion zone is widened, which further prevents leakage current from passing between the 2 crystals. When charged particles pass through the depletion zone, the liberated electron and hole pairs drift to their respective electrodes, which creates a current that is approximately proportional to the energy deposited by the impinging particle. The current is collected and sent as a signal to be amplified and shaped by subsequent electronics.

Our set of DSSD's were custom-made by Micron Semiconductors Ltd (UK) [1] with design number BB7(DS) 7P/2M and again, are used for collecting the trajectory directions of the α's and β's along with the energy of the α's. When mounted, they cover about 25% of the total solid angle available to the ions at the center of the trap. A picture of one of the detectors mounted on its ceramic board can be seen in Figure 3.7.A, with the strips running

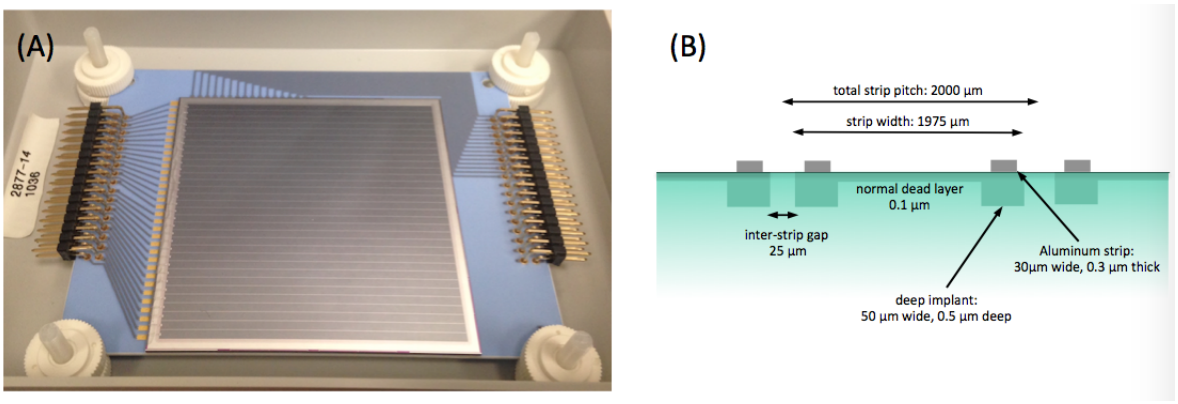

Figure 3.7: A) Double sided silicon strip detector mounted on a ceramic board. B) shows a cartoon of the surface profile. Each of the 32 strips are bookended by a deep implanted "extra" dead layer containing an aluminum strip used for charge collection and biasing the detector. There is a 25 μm gap between each strip. (not to scale)

horizontally. Within a tolerance of $\sim$ 4%, each detector is 1 mm thick[2] and has a 100 nm layer of inactive silicon material called a "dead layer" (discussed with more detail in sections 4.2.2 and 6.2.2). The strips are each 2 mm wide, which covers a span of about 2^o. A profile of what a strip segment would look like is shown in figure Figure 3.7.B. [104]

According to Micron, on each edge of the strip there is a 30 μm wide and 300 nm thick ribbon of aluminum used for biasing and charge collection from events. The aluminum ribbon is implanted on 500 nm of inactive silicon that is 50 μm wide. Our characterization of this "extra" dead layer produced energy losses different from what Micron had specified. Characterization of the two dead layers is covered in Chapter 4. Each strip is separated by a 25 μm gap. Events that enter this gap will not have the charge fully collected by the front face of the detector, so the back and front measurements of the detector will not match within a range for an event to be considered "real," and are thus discarded. During the experiment, the detectors are cooled to liquid nitrogen temperatures to reduce the leakage current and thus improve the possible resolution. The bias voltage was -180 V for all detectors.

2. With 1 mm thickness, β's passing through the detector deposit $\sim$300 keV of energy, which is well-separated from the main α energy peak.

3.3.2 Plastic Scintillator Detectors

Scintillator detectors are fairly common in physics experiments to either measure time-of-flight or the direct energy of particles (for our case, the lithium-8 β energy). When a particle is incident on a scintillator detector, it ideally deposits all of its energy in the scintillation medium if a complete energy measurement is to be made. The scintillation medium absorbs the energy and emits light, which is then detected by a photodiode or photomultiplier tube (PMT) and converted into an electrical signal proportional to the light emitted.

The scintillator detectors in this experiment used organic plastic scintillator media (polyvinyl-toluene) manufactured by Eljen Technology (model EJ-200) that were 6.2" in diameter and 6" in length. Organic plastic scintillator detectors are ideal for having a fast timing (rise time of 1 ns and decay time 2 ns for EJ-200) and high output for the light they produce. The volume was selected to provide sufficiently large coverage to collect all betas that pass through the DSSD's and ideally ensure full energy collection. The light from the scintillators was collected using a Hamamatsu R877-100 PMT, which was operated at -1300 V. [45] The plastic detectors were held under a low vacuum ($\sim$5 mTorr), which was separated from the ultra-high vacuum of the chamber by a thin kapton window. In the preparation stage of the 2016 experiment, I spent a great deal of effort helping to mount them, building the vacuum system around them, and then assembling a portion of the DAQ to collect their data. A schematic of the detectors can be viewed in Figure 3.8. Photos of an unmounted plastic detector and then the top and right mounted on the BPT chamber can be found in Figure 3.9.

3.4 Data Acquisition System

The signals taken from the DSSD's 256 channels are amplified separately by a set of 8 Mesytec MPR-16 preamplifiers (Figure 3.10.B), each capable of taking 32 channels. The amplified signals are then passed via twisted pair ribbon cables to a set of 16 Mesytec MSCF-16-

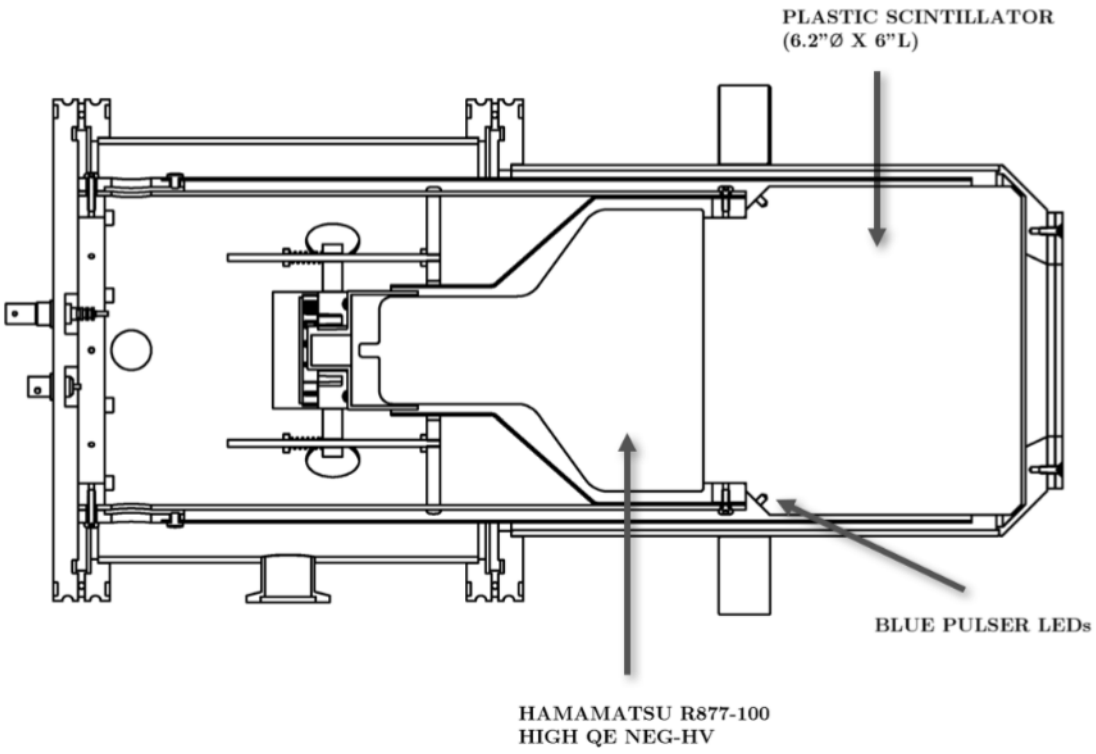

Figure 3.8: Inside schematic of the plastic scintillator detectors used in this experiment.[45]

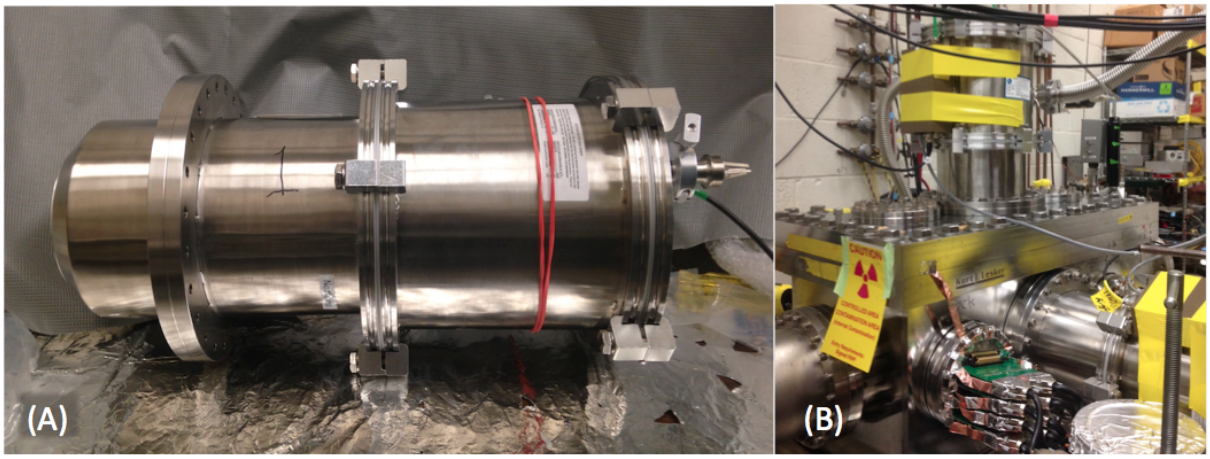

Figure 3.9: A) Unmounted plastic scintillator detector B) The top plastic detector mounted on the BPT chamber.

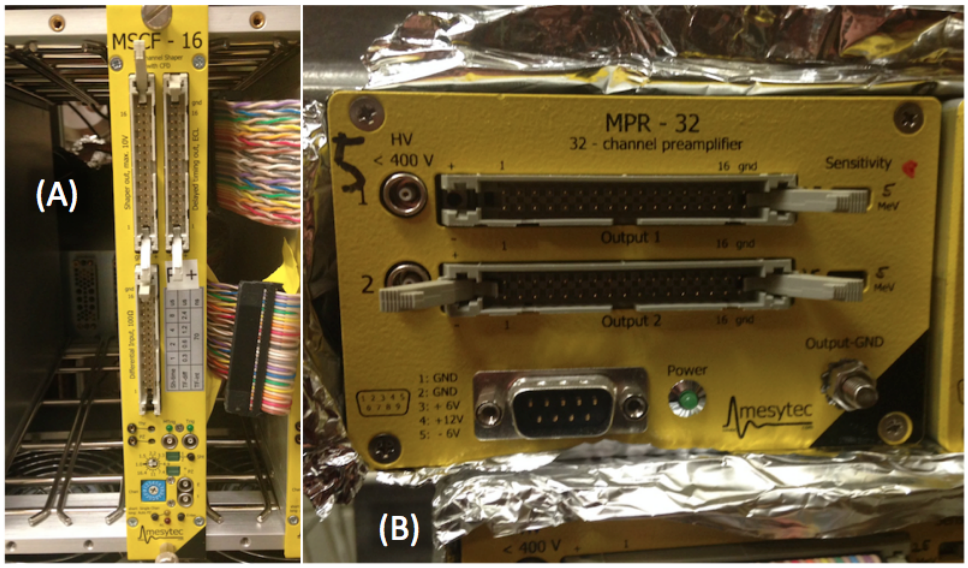

Figure 3.10: The 32 channel preamplifier (B) and shaper (A) used for the silicon strip detectors in the BPT system.

F shapers (Figure 3.10.A), each capable of processing 16 channels. The shapers were made with a custom chip to allow triggering on the leading edge of the shaped output signal rather than using the usual shaper settings for constant fraction discriminators (CFD's). CFD's operate by quickly finding the maximum of the incoming signal to use for the trigger logic and are extremely useful for precision timing. However, in this experiment, the pre-shaped signals are sometimes corrupted by RF picked up by the silicon detectors, which distort the shape of the signal. A high-precision timing is less desirable in this experiment than an uncorrupted trigger, so the trigger is taken from the signals after they have been shaped over a few μs. Alternative chips can be swapped out for the custom chips to return the shapers to a normal CFD operation. All of the Mesytec electronics were procured specifically for the BPT beta-neutrino correlation experiments.

From the shapers, the DSSD signals are transferred via more twisted pair ribbon cables to a mirror set of Philips 7164H peak-sensing ADCs, which are housed in two CAMAC crates. Similar to the DSSD's, the olastic detector signals are put through a preamplifier (Ortec 113 preamp with 1000 pF input capacitance via BNC cable), a Tunnelec TC 244 shaper, and then again through a LEMO cable to a Philips 7164 ADC housed in one of the CAMAC

crates. Other modules used for data acquisition alongside the ADC's are two LeCroy 4208 TDC's that measured the timing between events picked up by the DSSD's, three scalar modules (LeCroy 2551), which recorded the state of the trap (empty or filled), the number of injections, and provided a simple 1 Hz clock. Each event is triggered by any viable signal from any of the 8 front side Mesytec DSSD shapers, which then opens a 15 μs gate for data collection from all modules in the two CAMAC crates. Any events that occur whilst the system is injecting or ejecting ions are rejected to prevent collection of "fake" events due to noise. The data collection and gates are controlled by a driver package, developed in-house by Kenneth Teh of the ANL Physics Division. The package, called SCARLET, also records the data into a readable hex format and archives them on the local computer. [98]

3.5 RF Noise Suppression

Keeping the RF fields required to trap the lithium-8 from being picked up by the highly-sensitive DSSD's has been a challenge since the inception of this experiment. Each person who has assumed responsibility of the BPT has contributed in some way to decreasing the RF pickup and the resulting accumulation of modifications allowed for this experiment to be the first without any RF broadening in the resulting data.

The signature of RF pickup in the data is very distinct from all other noise (such as electronic and mechanical vibrations) picked up by the DSSD's. Unless the RF pickup is exceptionally large, usually only the highest energy signals are heavily affected. As the pulse from the DSSD currents are input into the shapers alongside any 1.33 MHz sinusoidal signal from the RF, the peak height and thus the recorded energy is affected by what position on the phase of the RF the peak appears (the rise and fall time of the current pulse is $\sim$10x smaller than the period of the RF). As a result, the calibration source peaks could appear to be much broader and potentially at lower energy rather than a sharp peak at the correct energy. An extreme example can be seen in Figure 3.11. RF pickup can also be measured via peaks input by a precision pulser (Ortec 448) through the preamplifiers that span the

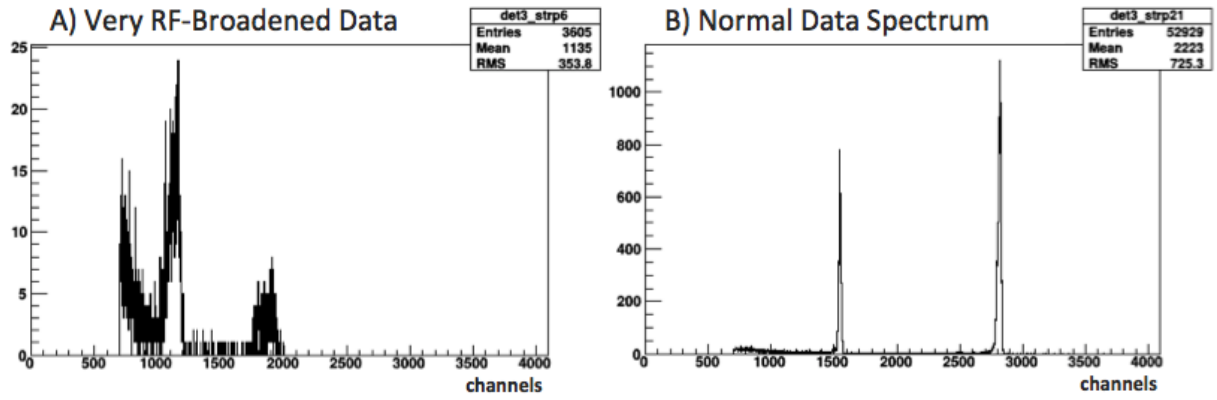

Figure 3.11: A) Example of a data spectrum, including the two mono-energetic peaks from the calibration alpha sources, that has been heavily corrupted by RF pickup. B) For comparison, what the data spectrum in A) would look like with no RF broadening.

full ADC range.

A variety of methods were implemented by my predecessors to reduce the RF pickup on the DSSD's. The current electrodes in use in the trap are updated ones from a previous version. The axial segment of each electrode that actually carries the RF field was shortened such that the field was kept as close to the center of the trap as possible, with the radially outer part of the electrode kept at ground. Later, two layers of stainless steel shielding (pictured in Figure 3.12) were added to serve as a rough Faraday cage. The full Mesytec set of electronics were purchased for all detectors so that their increased shaping ability would filter out more of the pickup. All of the cabling mounted on the trap frame which carries the RF to the electrodes is twisted together so that opposite phases are carried together, reducing the potential of the RF field being picked up by the cabling. In addition, some of the cables that carry the signals from the DSSD's to the wall of the vacuum chamber are twisted together for the same purpose. All of these modifications accumulated to only half of the front strips on both of the left and right detectors being heavily impacted by the RF pickup.

To free the remaining front strips from RF and thus increase the amount of available statistics available to use, in collaboration with Phil Wilt from the ANL Physics Division supporting engineers and Jeffery Klimes, then a masters student at the University of Chicago,

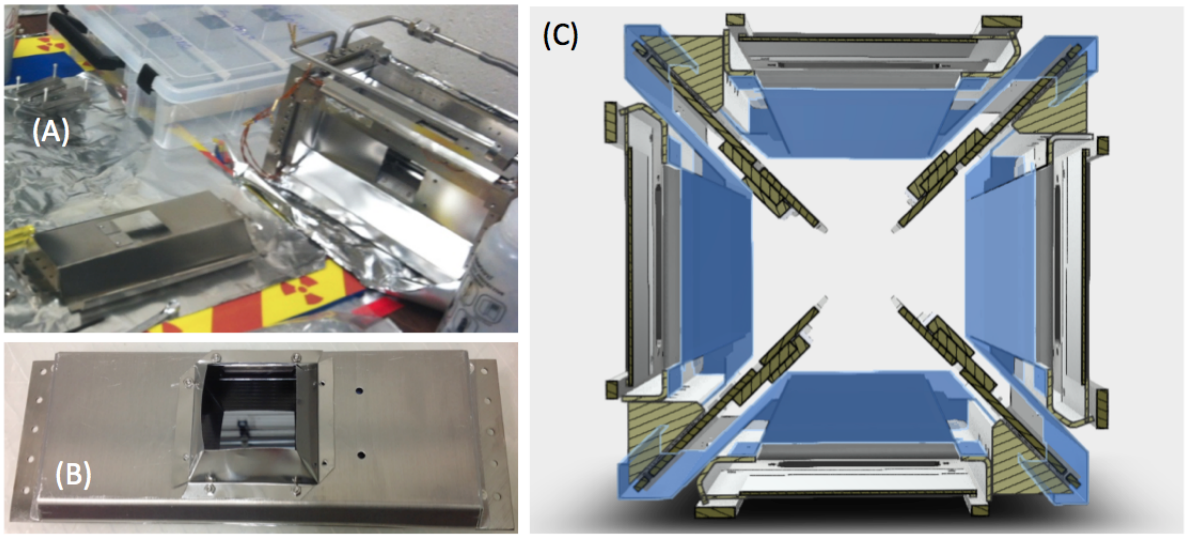

Figure 3.12: A) Inner stainless steel shielding used to prevent RF pickup on the silicon detectors. B) Stainless steel "hoods" attached to the aluminum detector covers also used to reduce RF noise. C) AutoCad schematic (radial cross-section) of the RF shielding placement within the trap. The stainless steel shields are highlighted in blue.

I implemented a set of 128 tunable notch filters on all of the front strip channels for the 4 detectors at a point between the detectors and the preamplifiers. Each filter was designed to filter only frequencies close to the one used for the RF field. The small tunable capacitor was set in place to adjust each of the strips filter to maximize the filtering capabilities for each strip's individual impedance. Eight filter circuits were housed on a small board that could be easily added or removed from a larger circuit board that carried all 32 channels for a detector's front face. A schematic of the circuit, along with pictures of each of the boards can be found in Figure 3.13. Though cumbersome to tune and not versatile in terms of changing frequencies, the filters successfully removed all traces of RF pickup from the data, which allowed us to use a much larger fraction of the statistics that were collected and ensured no systematic uncertainty was introduced because of the RF pickup. Because the rise and fall times of the detector signals were so much smaller than the RF period, the filters had no impact on the data itself either.

There were hopes that the filters would open the opportunity to remove some stainless steel RF shielding in the trap, which is a large contributor to lithium-8 beta scattering during

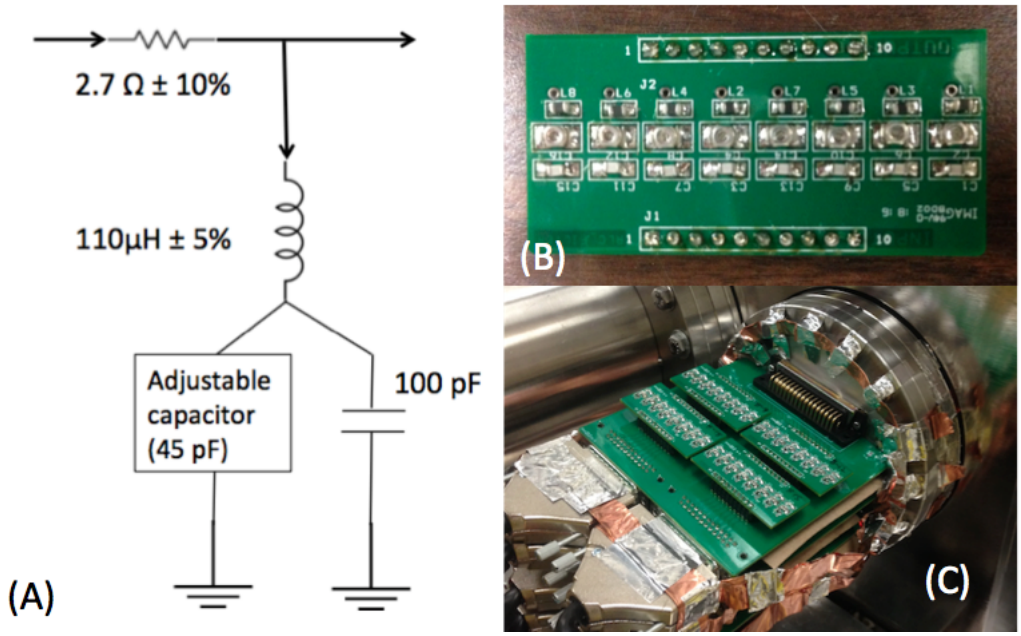

Figure 3.13: A) Simple schematic of the notch filter used for this experiment. B) Photo of the board used to house 8 of the 32 channels for 1 detector. C) Photo of the notch filter boards mounted to the BPT chamber before the preamps. Each large board contains 32 channels corresponding to one face of a silicon detector.

measurements. However, when tested, the boards proved not strong enough to cancel the heightened RF pickup that resulted from removing the shielding. In addition, when the shielding was entirely removed, RF pickup was visible on both the front and back faces of the detector (rather than just the front). However, the detector bias (180 V) is applied to the back side and because notch filter components that can withstand such high voltages do not exist on such a small scale, the same circuits cannot be implemented for the back channels. Currently, some of our colleagues are testing a possible digital data acquisition system where the RF pickup could be removed from signals in post-processing.

CHAPTER 4

CALIBRATION AND DATA PROCESSING

Once all the lithium-8 data have been obtained, they must be calibrated and cleaned before they can be compared to simulation. A high-quality and precise calibration is invaluable for the success of this experiment. We estimate that our calibration is accurate to about 5 keV depending on the strip it corresponds to, which is more than sufficient for the precision level of this measurement. However, since we take the difference between alpha energies in our final spectra, if a calibration mistake is made on all detectors, effects on the final result are suppressed. Over the course of the August 2016 run, there were almost 160 hours of consecutive data-taking where the results were of sufficient quality to be used. After performing an Allan-Variance calculation (to maximize statistics for a fit while minimizing fluctuations between time segments), that total was divided into 16 segments of 10 hours each. Each of the 16 time segments were calibrated independently. It took me 6 months of dedicated effort to complete the full calibration to the precision we desired, as almost every aspect of the calibration from previous experiments had to be re-examined or discarded.

The first sections of this chapter will cover the steps taken to convert ADC channel values to real energies in keV and the corrections that were made to the resulting values. The remaining sections will explain how the data set is sorted and what cuts are applied to eliminate noisy data and background events that could skew the beta-correlation measurement.

4.1 Alpha Calibration Sources

Two mono-energetic alpha sources serve as the centerpiece of our energy calibration. They provide two known anchors to the energy spectrum and serve as a monitor of the system's drift over the course of the experiment. The isotopes are comprised of gadolinium-148 and curium-244 and their energies are given in the table below. [90] [8]

Isotope	Energy (keV)	Intensity	Half-life
^{148}Gd	3182.690(24)	100%	74.6 y
^{244}Cm	5804.77(5)	76.90%	18.11 y
^{244}Cm	5762.64(3)	23.10%	18.11 y

Table 4.1: Calibration source isotopes, α decay energies, and half lives

4.1.1 Sources and Placement

In previous lithium-8 experiments, the calibration sources we utilized were made in-house by John Greene in the Target Lab using dissolved radioactive material dried on a piece of foil. Though they served us well during the previous experiments, the sources came with a deep dead layer and caused some trouble with Health Physics when it became apparent that they were leaking onto other material in the chamber. Before the August 2016 experiment, our group opted to invest in spectroscopy-grade commercial alpha sources. These were purchased from Eckert and Ziegler Isotope Products and were created using electrodeposition onto platinum. The sources themselves were slated to have spectra with less than 20 keV FWHM peak widths. However, the actual width may be much smaller, since strips with low noise indicate a resolution of 20 keV FWHM from the same peaks when all dispersion factors are taken into account (more details discussed in section 5.1.2). Four total sources were purchased (two Gd and two Cm) and those in turn were each cut into four pieces and mounted on small stainless steel squares as seen in Figure 4.1.A. Each stainless steel square housed one Gd source and one Cm source. Combined, our complete set included eight stainless steel source mounts: two for each detector. Two squares were mounted on each outer RF shield as pictured in Figure 4.1.B. so that they could illuminate the opposing detector (almost) completely in between the electrodes in the center of the trap. Axial and radial projections of the sources' illumination of the detectors within the trap can be seen in Figure 4.2. On all detectors, either all or most of the front strips are illuminated by both the Gd and Cm sources. Back strips 9 through 32 on all detectors are illuminated, leaving back strips 1-8 in shadow as a result of the RF hoods. Each front strip receives alphas from

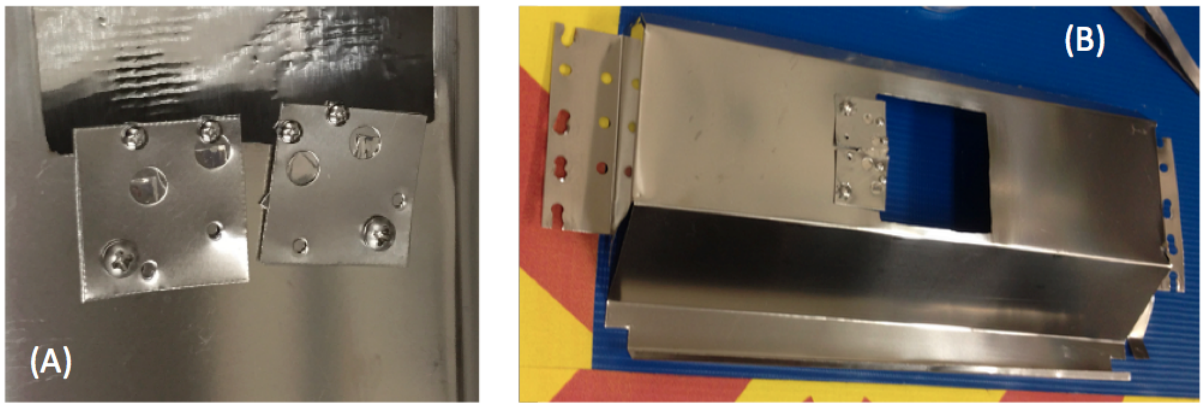

Figure 4.1: A) The Gd and Cm sources are mounted on small stainless steel squares which are screwed into (B) the outer RF shield. There are two of each isotope sources that illuminate each detector, for a total of sixteen alpha sources.

each source at a rate of ∼0.5 Hz.

4.1.2 Spectra Fitting

Examples of the spectra of each of the sources for a single peak can be seen in Figure 4.3 (the smaller peak to the left of the main Gd peak is from the "extra" dead layer. In order to extract a consistent "center-point" of each peak to use as the energy value, a fit was performed on each source spectra of the illuminated strips (both front and back). The function utilized for the fits is an elaborate skewed Gaussian defined by Bortels and Collars in 1987 [13] which includes two different exponential tails. If the spectra in 4.3 were visualized using a logarithmic y scale, the two differing exponential tails would be clearly visible. The fits and corresponding residuals of both peaks are also featured in Figure 4.3. The fits were performed with an automated fitting routine written in the programming library ROOT [16], which was originally developed at CERN for handling large packages of data.

Both peaks were fit using spectra with one channel per bin. The fitting functions for both the Gd and Cm peaks are below.

$$f_{\mathrm{Gd}}(x) = \mathrm{bkgd} + \frac{A_1}{2}\left[\left(\frac{1-\eta}{\tau_1}\right)\exp\left(\frac{x-\mu_1}{\tau_1} + \frac{\sigma_1^2}{2{\tau_1}^2}\right)\mathrm{erfc}\left(\frac{1}{\sqrt{2}}\left(\frac{x-\mu_1}{\sigma_1} + \frac{\sigma_1}{\tau_1}\right)\right)\right.$$

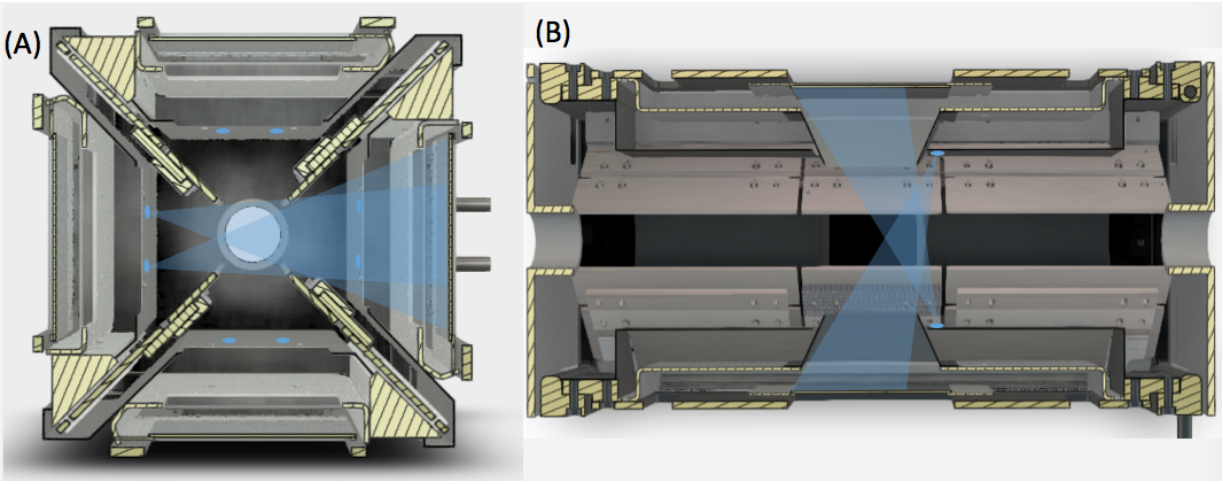

Figure 4.2: The sources are represented by the blue circles and the blue triangles are their projected illumination. A) Radial view of the source placement along with an example illumination of one of the detectors. B) Axial view of the source placement and illumination. 8 of the back strips are prevented from being illuminated by the RF hood shields.

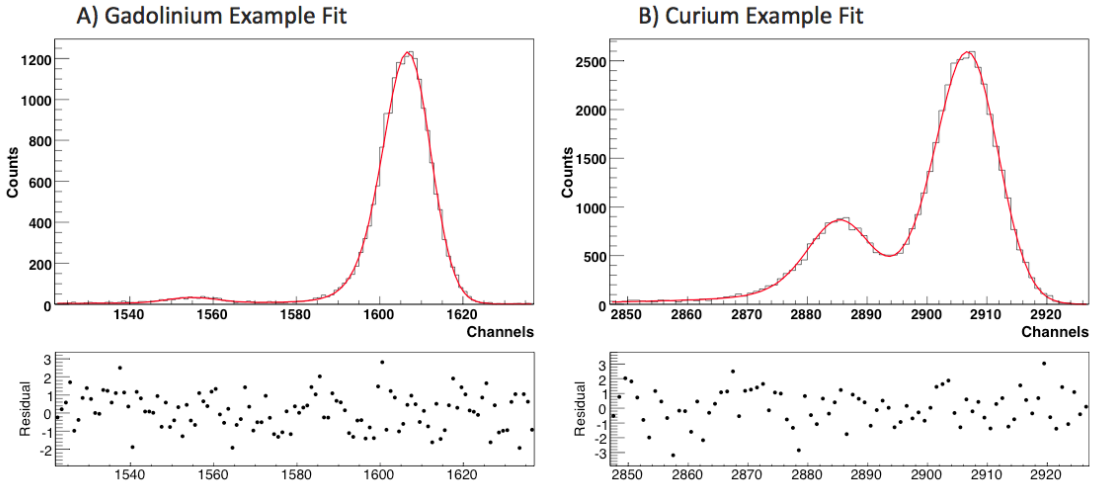

Figure 4.3: A) gadolinium-148 and B) curium-244 alpha energy spectra with a fit to the "Bortels" function. Residuals are below each of the fits. The "x" axis is in units of ADC channels (2 keV/channel). The small "extra" dead layer peak can be seen to the left of the main Gd peak. A similar "extra" dead layer peak exists in the Cm spectra but are not visible to the untrained eye.

$$+\frac{\eta}{\tau_2}\exp\left(\frac{x-\mu_1}{\tau_2}+\frac{\sigma_1^2}{2{\tau_2}^2}\right)\mathrm{erfc}\left(\frac{1}{\sqrt{2}}\left(\frac{x-\mu_1}{\sigma_1}+\frac{\sigma_1}{\tau_2}\right)\right)\Bigg]+A_2\exp\left(-\frac{(x-\mu_2)^2}{2\sigma_2^2}\right)$$

$$f_{\mathrm{Cm}}(x)=\frac{0.769A}{2}\Bigg[\left(\frac{1-\eta}{\tau_1}\right)\exp\left(\frac{x-\mu_a}{\tau_1}+\frac{\sigma^2}{2{\tau_1}^2}\right)\mathrm{erfc}\left(\frac{1}{\sqrt{2}}\left(\frac{x-\mu_a}{\sigma}+\frac{\sigma}{\tau_1}\right)\right)$$

$$+\frac{\eta}{\tau_2}\exp\left(\frac{x-\mu_a}{\tau_2}+\frac{\sigma^2}{2{\tau_2}^2}\right)\mathrm{erfc}\left(\frac{1}{\sqrt{2}}\left(\frac{x-\mu_a}{\sigma}+\frac{\sigma}{\tau_2}\right)\right)\Bigg]+$$

$$\frac{0.231A}{2}\Bigg[\left(\frac{1-\eta}{\tau_1}\right)\exp\left(\frac{x-\mu_b}{\tau_1}+\frac{\sigma^2}{2{\tau_1}^2}\right)\mathrm{erfc}\left(\frac{1}{\sqrt{2}}\left(\frac{x-\mu_b}{\sigma}+\frac{\sigma}{\tau_1}\right)\right)$$

$$+\frac{\eta}{\tau_2}\exp\left(\frac{x-\mu_b}{\tau_2}+\frac{\sigma^2}{2{\tau_2}^2}\right)\mathrm{erfc}\left(\frac{1}{\sqrt{2}}\left(\frac{x-\mu_b}{\sigma}+\frac{\sigma}{\tau_2}\right)\right)\Bigg]+\mathrm{bkgd}$$

To stabilize the fit, the extra dead layer was incorporated into the fit of the Gd peak. The extra dead layer could not be resolved from the Cm peak and was left untouched. Some constant background was allowed in each of the fits to loosely account for lithium-8 alpha backgrounds. The fitting range was from 15 bins above the bin with the highest number of counts to 70 and 35 bins below for gadolinium and curium, respectively.

Once fit, the maximum of each curve was considered the "center-point" of the peak. This point was chosen (over the high-energy FWHM and the actual fitted center of the peak) because it is the easiest to compare to when matching the detector response function or "lineshape" in the simulation (more details in chapter 5). The error of each maximum was taken by sampling 10,000 different fitting curves generated by sampling a Gaussian distribution of each fitting parameter with the sigma representing the error for each fit parameter. The resulting standard deviation of the 10,000 maximums became the fitting error on the maximum of the curve. Distributions of both the χ^2's and errors for the fitted maximum can be seen for both Cm and Gd in figures 4.5 and 4.4 respectively. A strip was only considered usable if it was possible to resolve the two Cm peaks, which are separated by $\sim$40 keV and only the "good strips" are included in these distributions.

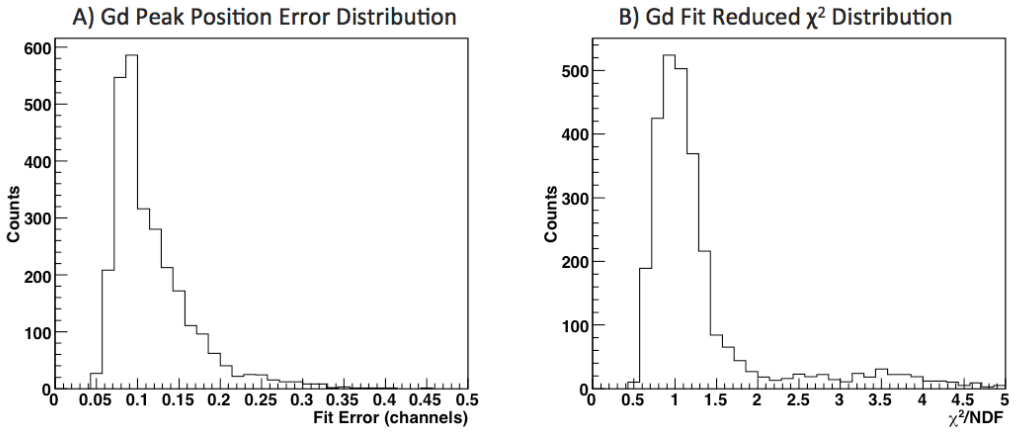

Figure 4.4: A) Errors on all usable gadolinium fits for the position of the peak. The "x" axis is in units of ADC channels (2 keV/channel). B) The reduced χ^2 distribution of usable gadolinium peak fits.

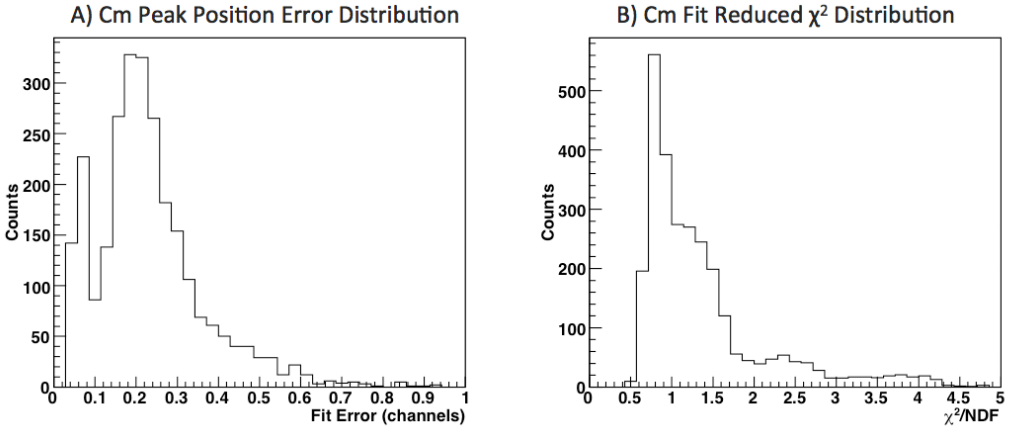

Figure 4.5: A) Errors on all usable curium fits for the position of the peak. The "x" axis is in units of ADC channels (2 keV/channel). B) The reduced χ^2 distribution of usable curium peak fits.

The maximum of the error distributions is about 0.1 channels for Gd (about 0.2 keV) and 0.2 channels for Cm (about 0.4 keV). The high-error tails on the ends of each of the distributions are due to spectra that were not noisy enough to cut completely, but still have some aberrations that the fit was unable to account for. These slight failures could be attributed to high electronic noise or some faster-than-average drifting in the system electronics.

4.2 Energy Calculations

Before the natural energies of the Cm and Gd shown in the previous table can be matched to the maximum of each fit, they must be corrected for a few real effects. The point is to make it such that the energy matches what the silicon detector "sees," so that the calibration is as accurate as possible and corrects for any non-linear effects. In order of the effects felt by the alphas as they exit the source, they are impacted by a source dead layer, the detector dead layer, the nonionizing energy loss in the detector, and then a pulse height defect. Once all of these effects have been accounted for, the energy calibration forms a line with a very small quadratic contribution as a result of the ADC's. This correction was handled using a minimization routine rather than a correction due to the loss of our linearity data. More details are discussed in section 4.4 and a combined plot of all the corrections except for the source dead layer can be found in section 4.5.

4.2.1 Source Dead Layer

While developing the detector response function for our simulations, it became clear that the sources were at least slightly affected by a source dead layer. To account for this, an offline measurement using a passivated implanted planar silicon (PIPS) detector was performed on 2 of the 8 stainless steel square source mounts (4 sources total: 2 Gd and 2 Cm). The measurement and analysis in the following section was performed by Louis Varriano with

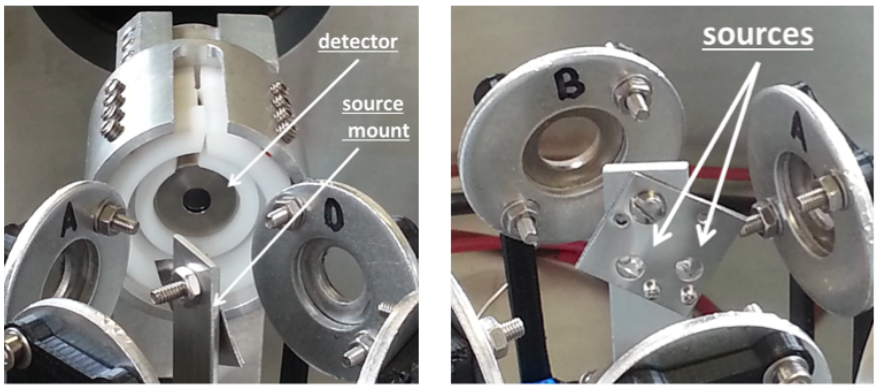

Figure 4.6: Multiple angles of the setup used to measure the dead layer of our calibration sources. The PIPS detector and angle-adjusting mount are both pictured. The other rings that are not labeled were used for a parallel experiment. Photos taken by Louis Varriano.

guidance from myself and Dr. Guy Savard. Several measurements over a couple weeks were taken of each source mount with the angle of the source mount normal to the detector at 0, 45, and 60 degrees in a vacuum chamber. The setup can be seen in Figure 4.6. Once the data were taken, the shift as a result of the source dead layer was calculated using a convolution process similar to how the detector lineshape was constructed in chapter 5. From the sources, Louis found that a skewed "step" function as seen in the black curve of Figure 4.7 matched the data the closest. Accounting for that activity distribution in the source caused the maximum of a Bortels fit to the data to be shifted lower in energy by approximately 4 keV depending on the angle and the electronic noise (all of which was accounted for when making corrections in the calibration). Fortunately, since we are using trapped lithium-8, there is no source dead layer for those alphas to contend with. Thus, this correction is exclusively for the Gd and Cm sources. For the calibration, the calculated energy values of Gd and Cm held only errors attributed to the source dead layer: 0.2 keV for Gd and 0.45 keV for Cm. The remainder of the corrections are simply added back to the data later and their systematic effects are examined separately.

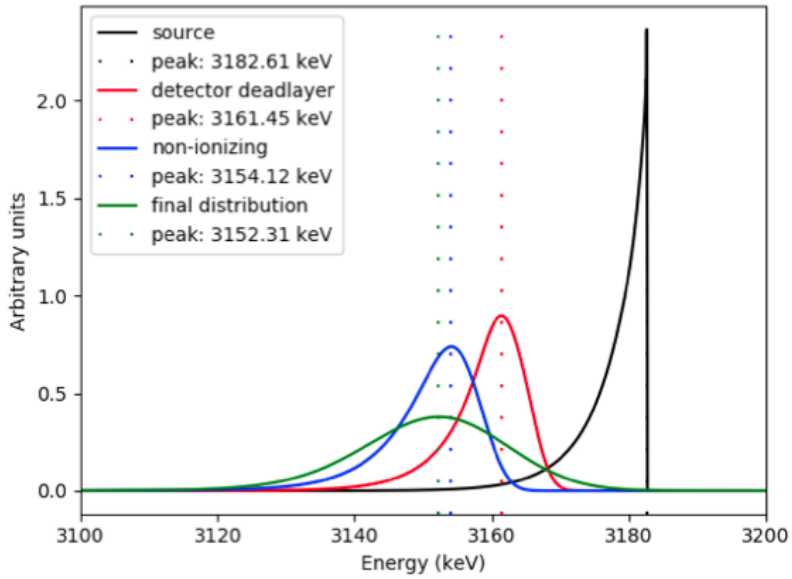

Figure 4.7: Steps for the convolution of a gadolinium source spectrum. Black: energy spectrum of particles emitted from the source before hitting the detector taking into account a skewed depth source dead layer. Red: black spectrum convolved to include widening and energy loss from the detector dead layer. Blue: red spectrum convolved to include the energy loss and widening of the nonionizing energy loss in the detector. Green: blue spectrum convolved with the electronic noise and Fano factor resolution to produce a final spectra. The Green spectrum is closest to what we would expect to see in our data. Graph created by Louis Varriano.

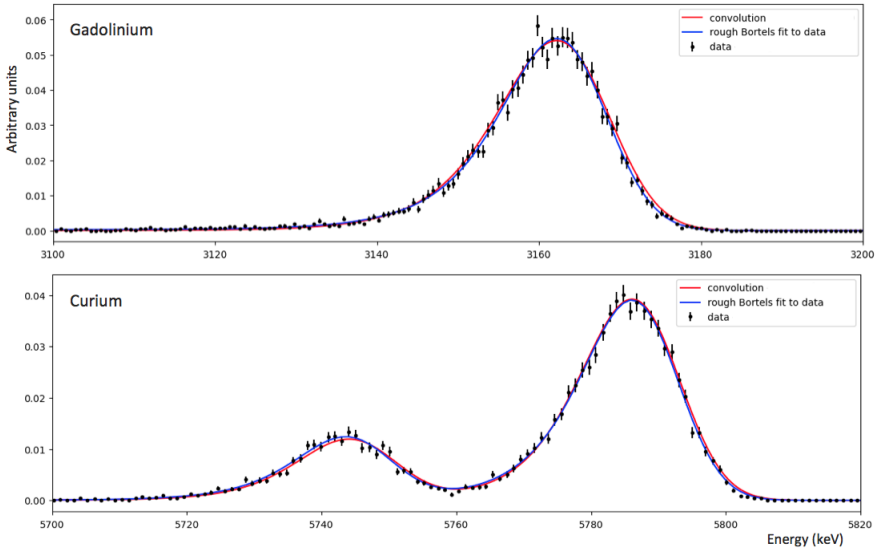

Figure 4.8: Comparison between data taken of the curium-244 and gadolinium-148 by the PIPS silicon detector for the source dead layer measurement compared to fit using the Bortels function (blue) and what the expected convoluted function for the source would look like. All three are in good agreement.

4.2.2 Detector Dead Layer

The next obstruction for the Gd and Cm alphas is a ∼100 nm inactive layer of silicon doped with aluminum on the surface of the silicon detectors. When the alphas pass through this layer, they lose energy through ionization that cannot be collected like the rest of the energy deposited in the active silicon. Based on the angle of incidence and the stopping power of alpha particles in silicon, the energy lost in the dead layer can be reconstructed.

The dead layer was originally measured during an offline experiment with several more in-house made alpha sources. However, since the measurement was performed before we became aware of the extra dead layer, the resulting numbers were in effect the average of the normal dead layer and extra dead layer. This time, the dead layer was measured by exploiting the incident angle difference across the face of the detector (25 degrees from center to edge) using a calibrated lithium-8 alpha spectrum (sans alpha's used to make the $a_{\beta\nu}$ measurement) with all other corrections but the detector dead layer applied compared to the same simulated spectrum. The χ^2 between the two spectra was taken for 64 4-pixel segments with corrections for dead layers of varying thicknesses. The dead layer values for each detector that corresponded to the lowest average χ^2 of the 64 segments was considered the "correct" dead layer value. This technique was used with two different final state distributions in the simulation with the same results coming out of each, which lends some confidence to this method. The Left detector proved a bit too noisy to extract good values from, but it was grown in the same set as both the Bottom and Right detectors, which should imply the same dead layer thickness. The results from this measurement indicated thicknesses of 97 ± 5 nm (Top), 98 ± 5 (bottom), and 111 ± 7 nm (right). Taking the weighted average of these returns the manufacturer's dead layer thickness value of 100 nm with a weighted uncertainty of 3.5 nm. The systematic uncertainties associated with the detector dead layer are discussed in section 6.2.2. The relative uncertainties between the individual detector dead layers are not a consequential source of error compared to the uncertainty introduced if all four detectors are either larger or smaller than 100 nm.

The dead layer energy loss calculations were performed by calculating the secant of the angle between the normal of the source and the normal of the surface of the silicon detector and multiplying it by the measured dead layer thickness and the stopping power of alpha sources in silicon at the energy of the incident alphas. The stopping power was determined using the program SRIM (the Stopping and Range of Ions in Matter) [111] and was confirmed with full Monte Carlo calculations in TRIM (TRansport of Ions in Matter), which is a program contained in SRIM. A graph of the energy correction needed for alphas in a 100 nm silicon dead layer as a function of energy can be seen in Figure 4.18. The energy loss for alphas in 100 nm of silicon is about 19 keV and 13 keV for ^{148}Gd and ^{244}Cm respectively.

4.2.3 Nonionizing Energy Loss

Once the alpha particles enter the detector, not all of the energy they contain is collected in the liberated electron-hole pairs. Some of it is lost through various mechanisms, the most dominant of which is interactions with the silicon nuclei. The distribution of energy lost from mono-energetic alphas can be modeled in TRIM for any alpha energy and most materials. For alphas in silicon at Gd and Cm energies, the spectra of nonionizing energy loss (NIEL) of several thousand alphas would resemble a f-distribution function (something similar to a skewed Gaussian with the tail extending to higher energy). When correcting for NIEL, in order to best match with simulation, the maximum of the NIEL spectra for each energy (Gd: $\sim$ 3159 keV and Cm: $\sim$ 5787 keV after previous corrections) simulated in TRIM were used as the energy corrections for each source energy. The idea behind this choice was that we can use the lineshape of the detector in the simulation to spread out the distribution from the maximum of the peak. A graph of the maximum of the NIEL spectra as a function of energy can be seen in Figure 4.18. The NIEL corrections for ^{148}Gd and ^{244}Cm were $\sim$ 6 keV and 7 keV respectively. As discussed in section 4.5.1, the lithium-8 α's have their NIEL energy loss (and other energy-dependent corrections) added back after the calibration to

return their energies to what they were when the α was emitted from the beryllium-8.

4.2.4 Pulse Height Defect

The last correction that must be accounted for is known as the pulse height defect. It has been well-established that the energy of alpha particles that impinge upon a silicon detector do not create pulses of current that are directly proportional to their energy. This is in part because it takes slightly less energy to create an electron-hole pair in a region where one has already been created. A simple model described by Lennard et al. in a 1986 paper [63] matches all current data that has compared known alpha energies with detector responses. The function for his model is below, where $N(E_0)$ is the relative number of electron-hole pairs produced by projectile of incident energy E_0 and dE/dx is the stopping power of the projectile in silicon.

$$N(E_0) = \int_0^{E_0} \frac{dE}{\epsilon + k(dE/dx)} \tag{4.1}$$

The same model has been used to calculate the pulse height defect correction for both the Gd and Cm sources. A graph that also includes the pulse height defect correction as a function of energy can be seen in Figure 4.18. The final corrected energy values of Gd and Cm that the detector "sees" are ~ 3215 keV and ~ 5874 keV respectively. The systematic uncertainties introduced by the energy corrections to the calibration are discussed in section 6.2.2.

4.3 Lithium-8 DSSD Beta Spectrum

To anchor the silicon detector calibrations in the low-energy regime, the lithium-8 beta minimum ionizing spectrum was used as a known energy point.[1] Alongside the two mono-energetic alpha peaks, the three peaks provided an essentially complete coverage of the

1. Events where an electron scattered and deposited energy over multiple DSSD strips are reconstructed by adding the energy across the affected strips and choosing a single incident strip randomly from the ones containing β energy

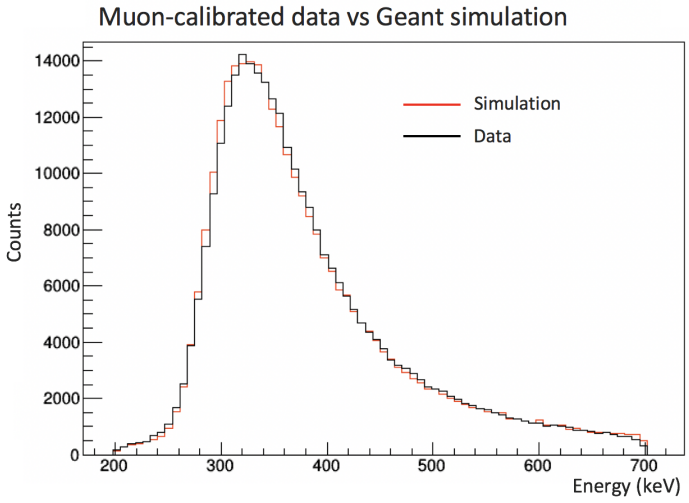

Figure 4.9: Comparison between a lithium-8 β^- spectrum that was calibrated using cosmic muons and a Geant simulation of our lithium-8 β^- spectrum

lithium-8 alpha energy spectrum. This option only became possible for the August 2016 run due to simply having enough beta particle statistics to form spectra that would fit with a low error. The calibration was performed by fitting the beta particle spectra to a simple Landau function (more details below) and comparing the mirror simulations in Geant4 [28] with an identical fit. This method was only used after a calibration was first performed using cosmic muons in the Top-Bottom detector system as a low-energy anchor and comparing that to simulated muons (generated using Cosmic Ray shower generator (CRY) [43] and propagated through Geant4). This method was developed by one of our former postdocs, Dr. Tsviki Hirsh, and is documented in [48]. When correcting for the varying thicknesses of the detectors and comparing simulation to data, the muon-calibrated data spectrum closely matched the Geant4-generated lithium-8 beta spectrum. An example can be seen in Figure 4.9. The fitted Landau peak centers of the muon-calibrated beta spectrum and Geant4 beta spectrum matched within error as well.

This calibration was performed at first using only the original beta spectrum. A better calibration with lower errors from the Landau fits was also completed by angle-correcting the energy of the beta spectrum in both the data and Geant4 spectra. In the following section, the process and results of the Landau fits from both calibrations are discussed.

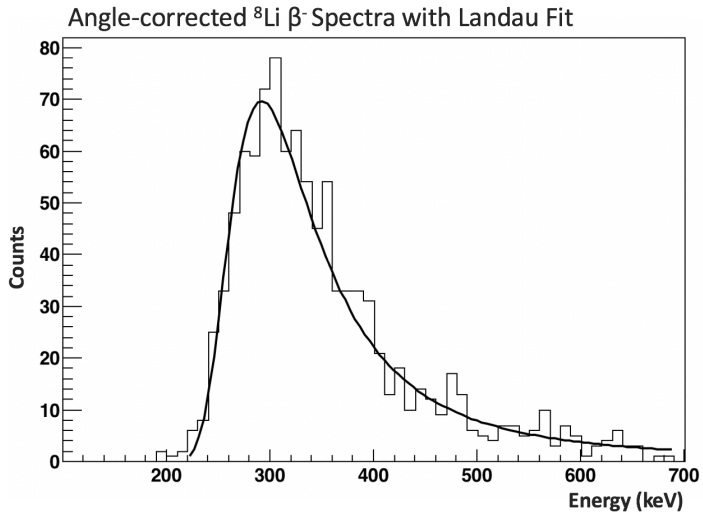

Figure 4.10: Calibrated and angle-corrected lithium-8 β^- minimum ionizing spectrum with a Landau function fit.

4.3.1 Fit Function and Results

As previously mentioned, all minimum ionizing spectra of the lithium-8 betas passing through the silicon detectors were fit using a Landau function (below). The distribution was originally developed and named by Lev Landau for the energy loss of "fast" particles that would obey ionization theory as they pass through a thin layer of material, which exactly describes the lithium-8 betas passing through our silicon detectors. [60]

$$p(x) = \frac{1}{\pi c} \int_0^\infty e^{-t} \cos\left(t\left(\frac{x-\mu}{c}\right) + \frac{2t}{\pi} \log\left(\frac{t}{c}\right)\right) dt \tag{4.2}$$

The fits were performed using an automated routine in ROOT (similar to the routine used for the Gd and Cm sources), where μ in the equation above was the desired parameter. The histogram spectra were created with the data occupying bins of 10 channels and were fit from 70 bins below to 180 bins above the position of the bin with the highest number of counts. An example of a beta spectrum and fit can be seen in Figure 4.10. The results of the fits from all "good" strips can be seen in Figure 4.11. To complete the angle-corrected calibration, the beta spectrum calibrated using the original method was modified such that

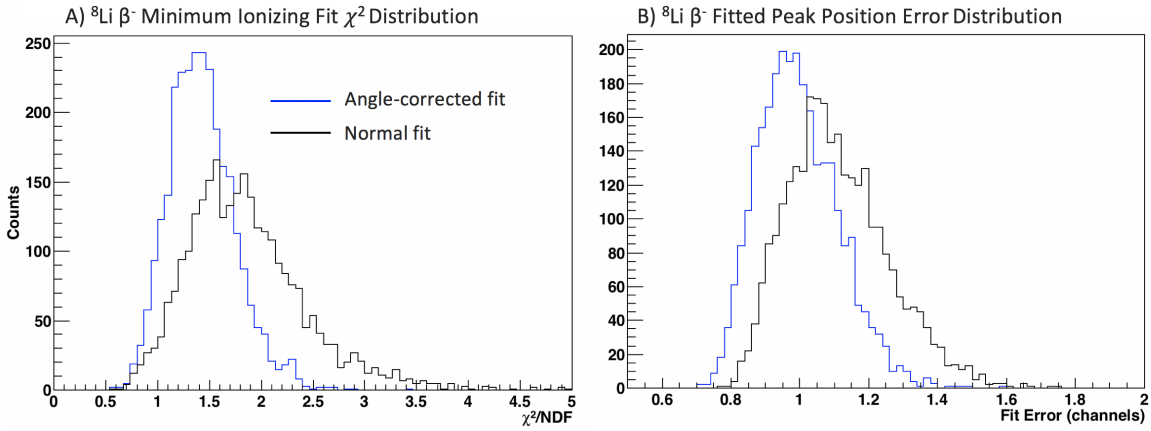

Figure 4.11: A) χ^2 distribution of fits on all usable strips to both the original lithium-8 β^- minimum ionizing peak (black) and the angle-corrected version (blue). B) Distribution of all fitted Landau peak parameter uncertainties. Each uncertainty was applied to the minimum ionizing peak channel value when calculating the calibration.

each beta particle's energy was divided by the secant of the impinging angle. The new, more narrow peak was then fit to a Landau function with more successful results, as can be seen in the blue curves in Figure 4.11. Using the calibration functions from the previous round, the μ and error values could then be returned to units of channels and used in a new calibration. This method was also performed in the same manner using Geant4 simulations for each strip to obtain the reference energy. The resulting fitted μ errors were about 2.2 keV (1.1 channels) from the uncorrected data, and 2 keV (1 channel) from the corrected data. For fits to the Geant4 simulations, both angle-corrected and uncorrected, the fitting error was ~ 0.3 keV (semi-infinite statistics are available in simulations).

4.4 Full Calibration

Once fits to all three known points and the corrected energies were obtained for each strip, a final calibration was performed. A figure of the full energy spectrum from a silicon detector can be seen in Figure 4.12.

Under normal circumstances, the final calibration applied to each strip would have been corrected for the slight quadratic response of the ADC's using linearity data obtained by

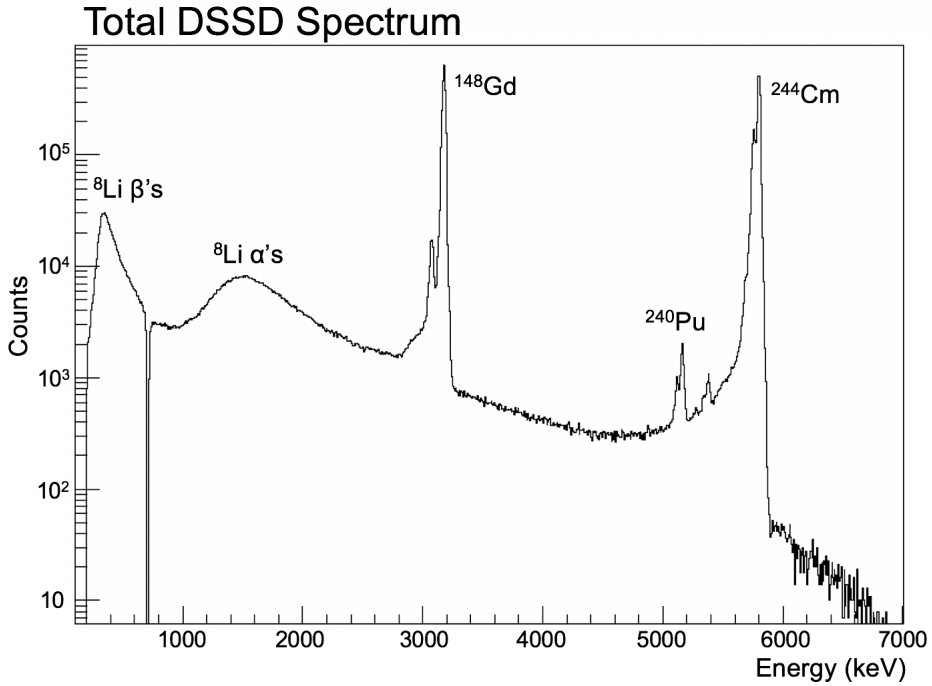

Figure 4.12: Full energy spectrum of events collected by the silicon detectors. At low energy is the minimum ionizing spectrum of the ^{8}Li betas that pass through the detectors (the threshold between β's and α's is set at 700 keV), followed by the broad peak of the ^{8}Li alphas then moving to higher energy with the calibration sources ^{148}Gd and ^{244}Cm, and the small ^{240}Pu peak, which is the daughter of ^{244}Cm.

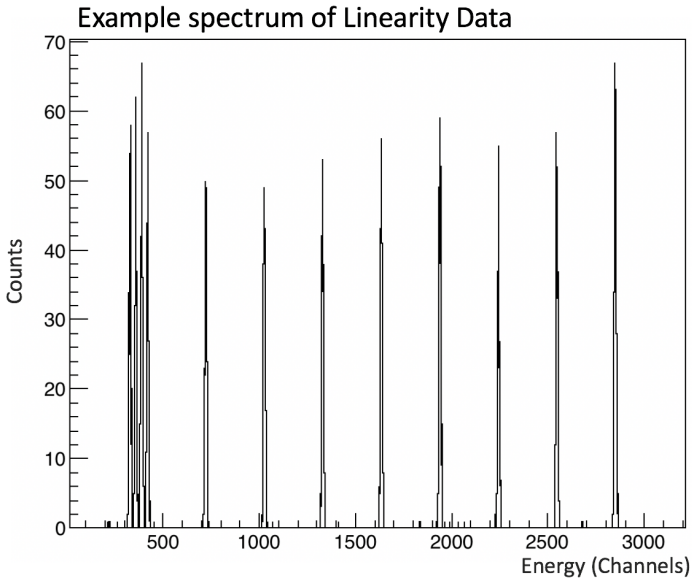

Figure 4.13: Example of the 12 peak precision pulser spectrum spans the full lithium-8 α energy spectrum and is used to determine the quadratic response of the ADC's as well as the electronic noise of the system. The four clustered peaks at the lowest part of the spectrum correspond to the 1.5 MeV lithium-8 α peak, where the linearity must be the most accurate. The "X" axis is in ADC channels, with a conversion to keV=2×Ch

applying 12 signals of varying magnitude from a precision pulser to the preamplifiers every 10-12 hours over the course of the experiment. An example of the spectrum can be seen in Figure 4.13. The centers of the peaks could then be fit to a quadratic to account for the response of the electronics. In previous data campaigns, the results of the quadratic fits were always stable compared to the usual gain drifts of the system electronics. However, the pulser data taken during the August 2016 experiment demonstrated changes over time that were ∼3x as large as the gain drifts of the system and were in turn discarded. The point of failure was attributed to the pulser itself, it having been recently repaired (unsuccessfully) and not to any other malfunction of the electronics. Since this method of calibration using the linearity data was last performed successfully for the most recent data-taking experiment (boron-8 in 2014) with muons, shown in [48], we took it upon ourselves to soldier on with a slightly different method. The linearity data itself is easily removed from the data using a simple cut on the event multiplicity across strips (pulser signals are applied across all 32 strips at once).

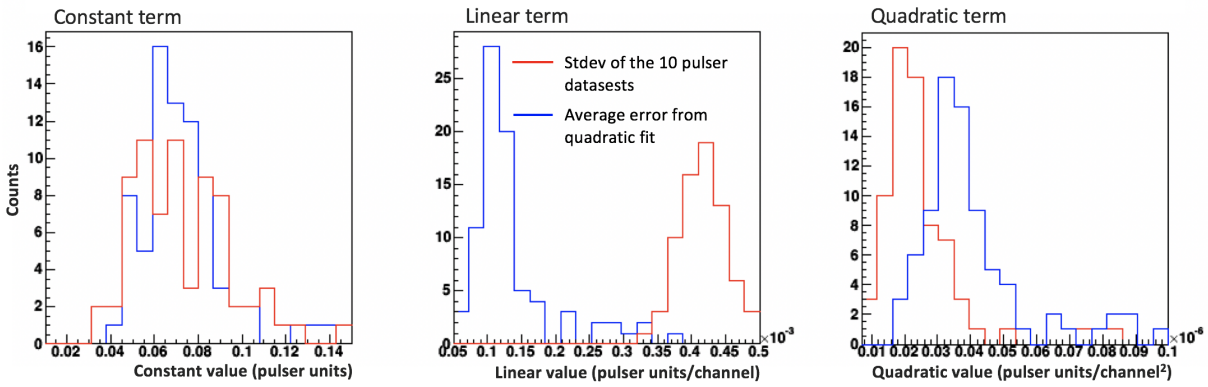

Figure 4.14: A demonstration of the linearity data stability from the 2014 ^{8}B experiment before our pulser was damaged. Effectively the standard deviation of all the terms in the quadratic fit for each of the 10 times the linearity was measured is on the order to the actual average error for each term over the 10 data sets. The constant distributions are about 1% of the actual constant values, with the linear term errors at 0.1% and the quadratic terms at 10%

4.4.1 Method and Linearity

Going from the linearity data taken in the boron-8 experiment in 2014, over 10 samples, the standard deviations each of the 10 quadratic fits for each strip are on the order of magnitude of the actual fit errors themselves (see Figure 4.14). In addition, since the quadratic response is an intrinsic part of the ADC, we came to the conclusion that the quadratic ADC response is constant over the course of an experiment.

With that assumption, the gain drifts that happen to each of the peaks over the course of our 16 time segments (an example can be seen in Figure 4.15) are moving along the same quadratic function for each strip. Thus, the desired results from a strip calibration using the 3 points from each time segment (48 total if the strip has no noise over the course of the entire experiment) would be a constant and linear term for each time segment and then a gain and quadratic common across all time segments to account for the ADC response (a total of $32+2=34$ unknown variables). With such a high ratio of known points to unknown variables, a minimization of this system could easily be performed and be well-constrained. The offset that would have been included in the ADC response was folded into the individual time segment's constant term to stabilize the minimization.

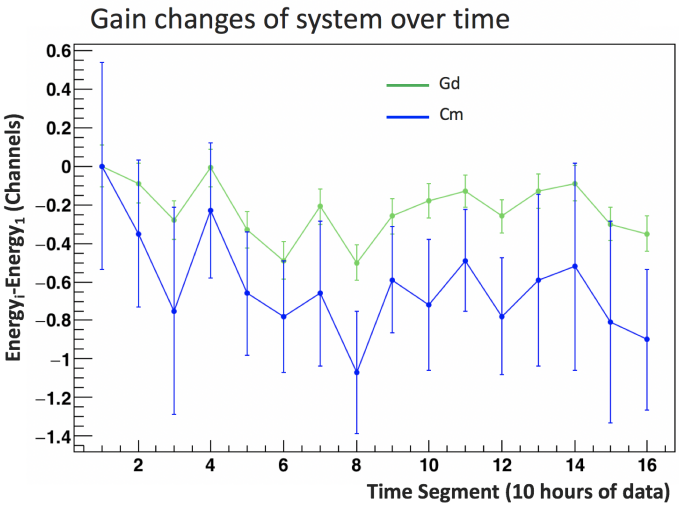

Figure 4.15: Drift in the positions of the mono-energetic alpha sources over the course of the run for an example strip with the fitting uncertainty serving as the error bars. The higher energy values experience the gain drift more drastically than the lower energy values.

The minimization itself was performed by applying ROOT's Minuit2 package (written using C++ but based on the original Fortran Minuit package [53]) to the least squares method for each strip, both front and back. Front strips 1 and 32 as well as back strips 1 through 8 and 32 were excluded. The calibration was performed in 2 rounds. The first round excluded points from strip-time segment combinations that were considered noisy and eliminated strips entirely if there were less than 5 time segments that were not too noisy. The resulting functions were taken as the final calibrations for the strips and time segments that were included in the minimization. A second round of minimizing included all the strips and time segments was used to establish calibrations for the previously excluded data. An example of the residuals of one strip's calibration over the 16 time segments can be seen in Figure 4.16. For the back strips 1-8 where no illumination from the sources was possible, a rough calibration was done by matching front lithium-8 alpha energies to the back ones using the technique described in section 4.9 of Matt Sternberg's thesis. [95]

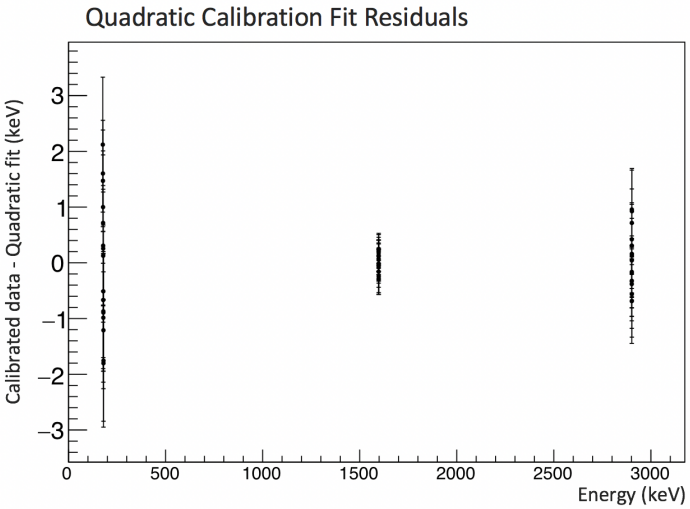

Figure 4.16: Example set of calibration residuals for a single strip across the 16 time segments. The points are minimized to have an offset and gain for each time segment to account for drift, but have a common gain and quadratic that are intrinsic to the ADC channel for the entire experiment. The minimum ionizing peak from the betas has the widest peak and less counts than the two alpha sources, which results in larger fitting uncertainties. Of the alpha sources, with two peaks included in the fit, the curium-244 also has more fitting uncertainty than the gadolinium-148.

4.4.2 Results and Errors

The results from the minimization calibration for all the usable strips are in Figure 4.17. The fitted errors for all three terms in the quadratic allow for an calibration systematic error that is over 10× smaller than our largest systematic uncertainty. The distributions of the actual calibration values do not form a simple Gaussian shape because each individual set of 16 channels within an ADC has its own signature distribution. The calibration values of the back strips are also noticeably different than the front strips, in part because of the difference in charge collection.

4.5 Data Processing

Once a calibration has been completed, it can be applied to the lithium-8 data using a sorting routine that was developed to convert the hex files generated by our DAQ into something easy to manipulate, i.e., ROOT files. Our data were first sorted without a calibration to

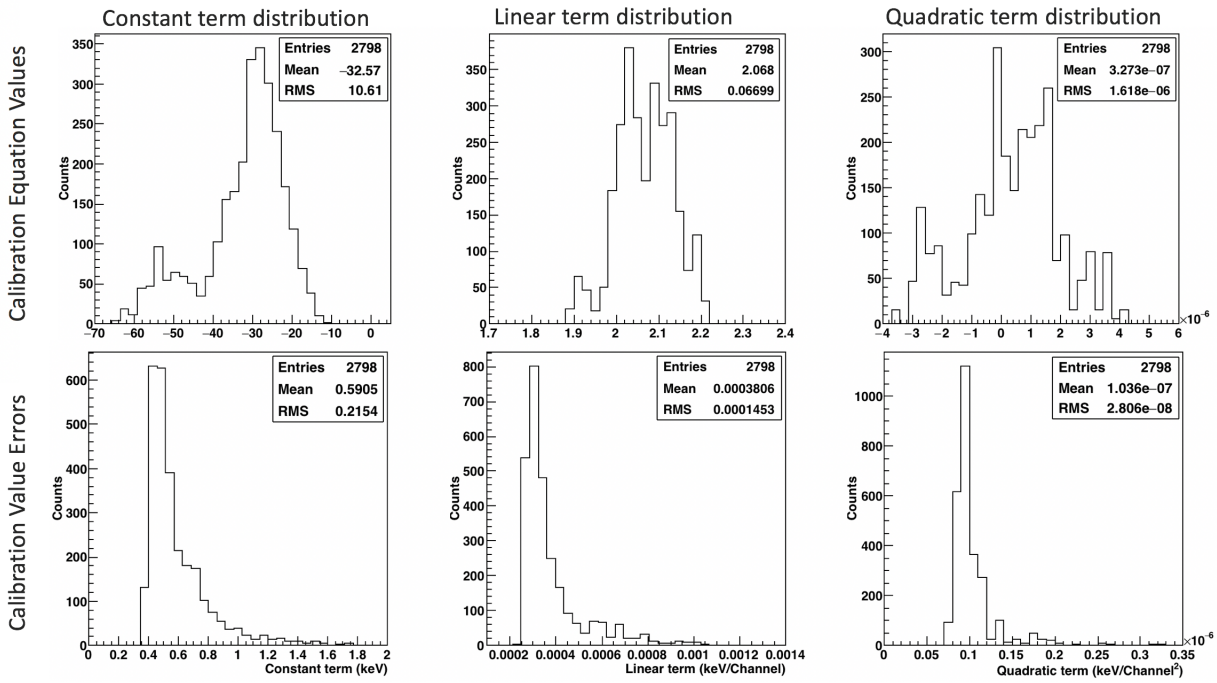

Figure 4.17: Distributions of the quadratic calibration equation terms and the corresponding statistical fitting errors for all usable strips on both front and back of all detectors. The histograms containing the calibration values (top) have some structure, as each set of 16 strips corresponding to a single shaper has its own distinct distribution center.

simply get channel values of the data to perform the calibration. Subsequent sorting was done with a completed calibration applied to the data. To make the sorting easier, some rudimentary cuts to the data were applied inside the routine with more stringent cuts applied later. All of the data-processing steps described in the next two sections were done with the goal of creating a data set of lithium-8 alphas and betas that match what our simulation would be able to create while cleaning it of all background and noisy events that would increase our final systematic errors.

4.5.1 Sorting

The sorting code we use performs a variety of functions after converting data from hex format and applying a calibration. It takes the 1-hour run files taken over the course of the experiment and combines them into the 16 time segments and creates a final ROOT file with data sorted into beta and alpha events. The energy threshold defined as the upper endpoint of the betas and the lower endpoint of alphas was chosen to be 700 keV. Though there is some crossover between the two, 700 keV is at a relative minimum where there are few of each particle (see Figure 4.12).

For alpha particles, an event is considered "real" by the sort code if both the front and back of the detector read an event within the same time gate window and the energies read by the front and back are within 300 keV of each other. A more stringent cut is applied after the sort code to further eliminate noise and background. For events where some of the energy is dispersed across several back strips, the code will search for nearby strips with energy depositions that sum to something within 300 keV of what was measured by the front. If the code is successful, the reconstructed event will be retained and will join others like it to make up 10% of events used in the final analysis.

Once an event has been constructed, the alpha particle energies are returned from what the detector "sees" to what the energy would have been before the alpha hit the detector. This adjustment is completed by correcting the energy in the reverse order of the corrections

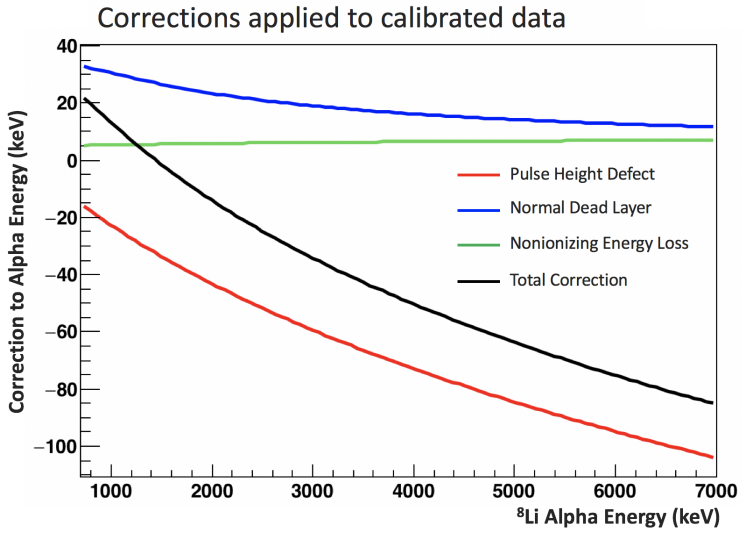

Figure 4.18: Energy corrections applied to the calibrated ^{8}Li alphas to return their energy values back to their real energy coming out of the ion cloud. The black line is the sum of the three individual corrections.

applied to the calibration energies. First, the pulse height defect is removed, then the nonionizing energly loss correction, and finally the dead layer energy loss. A graph of all three corrections as they are applied to the data as a function of the original energy can be seen in Figure 4.18 where the black curve is the combined energy correction of all three. In addition, the calibration files include a rating of each front and back strip based on whether they were either usable or too noisy [2]Z for that particular 10-hour time segment. A "final" energy of each event is prescribed based on the quality of the strips that the particle hit. If in the event a front strip is considered too noisy and the back strip is not, the back energy will be taken instead of the front energy. If both strips are too noisy to be used, the entire event is discarded.

The beta particles are treated slightly differently, since they do not deposit all their energy within the silicon. As a beta can pass between both the front and back interstrip gap and cause scattering within the detector, the code attempts to do a reconstruction using energy deposited in both neighboring front and back strips. After the energy summing has

2. Strips where the two curium-244 peaks could not be resolved, so the resolution was below 20 keV, were considered too noisy and discarded.

been performed, a lower threshold of total energy is taken to be 200 keV, which contains the minimum ionizing peak within the spectra while still cutting out any low-energy noise. No noise-based strip selecting is performed on the beta particle since the distribution is a wide one and the location information is more important than a precise energy.

From there, the events can be divided into four different categories: "singles," where all recorded alphas are defined as a standalone event, "doubles," events where two opposite detectors each have an alpha hit them within a single time gate window, "triples," doubles events in coincidence with a beta event being picked up by any detector, and "backscattered events", or triple events where two opposite detectors record a beta event in coincidence. The primary data used to measure $a_{\beta\nu}$ are triples. Backscattered events are used to set benchmarks for comparing our Geant4 scattering simulation to data.

For triple events, the sorting algorithm also attempts to reconstruct the kinematics of the event, i.e., the final energy of the beta particle and both the energy and direction of the antineutrino. Each of the four outgoing particles has 4 degrees of freedom, though one DOF for each particle can be constrained using principles of energy and momentum conservation. Given that we directly measure the energy and direction of both alpha particles and the direction of the beta particle in the silicon detectors for a triple event, that leaves only 4 degrees of freedom that need to be determined for the system to be reconstructed via energy and momentum conservation. With the addition of the plastic detectors directly measuring the beta energy, the system becomes over-constrained. My predecessor, Gang Li included a full calculation of the kinematic reconstruction in chapter 4 of his thesis, which the reader may explore if they wish. [65] The reconstruction algorithm includes a check to see if the solution to the reconstruction is plausible and conveys a status to the reconstructed event based on this check that is included with the sorted ROOT data.

4.5.2 Selection and Cuts

Once the data have been calibrated, corrected, sorted, cleaned, and reconstructed, some final cuts are applied to the data to make sure only real events are measured and that the background is as low as possible. The list below contains all the major cuts performed post-sorting as well as a brief explanation. All the same applicable cuts are also applied to the simulated data.

- The difference in numbering of front strips and back strips between the two alpha particles must be less than 8 (the difference corresponding to the maximum angle that is allowed by kinematics). Any coincidence greater than 8 would be attributed to a coincidence with some background particle (See Figure 4.19.B).

- The difference in final energy between the two alpha particles must be less than 600 keV. The entire alpha difference spectra is well-contained within 600 keV and anything outside of that range would again be attributed to a background coincidence (See Figure 4.20).

- The difference in energies measured by the front strips and back strips must be less than 60 keV for the α's and 110 keV for the β's. As Figure 4.19.A shows, most of the data are well-contained within 50 keV, though there is a tail from reconstructed back strip events that are lower in energy than their front strip counterparts. This cut ensures the integrity of an event and were chosen based on how well the distribution of particles matched that of the simulation.

- Events recorded within 30 ms after an ion bunch has been injected into the BPT chamber are rejected to ensure that the ion cloud has a chance to cool down and return to its normal size before events are recorded again. 30 ms was recommended by [89], though calculations using the strip difference spectra from the August 2016 experiment indicate that a 15 ms cut would be sufficient.

- Alpha events that occur on the edge strips: front strips 1 and 32 and back strips 1 and 32 are rejected due to potential incomplete charge collection.
- Events where the β and an α both hit either the same back strip or front strip on the same detector are discarded in the event that the DAQ can't easily distinguish which particle was which.
- Any event where there is more than one beta measured in coincidence with a double is discarded from the triples set because it is unclear which beta actually belonged to the decay that occurred. (Depending on the nature of these events, some are sorted into alternate trees to compare with simulation when establishing β-scattering benchmarks.)
- Alpha events with energy above 7 MeV are discarded. This is just to have a consistent upper threshold. This resulted in $\sim$10 rejected events.
- Events with the β energy below 200 keV are discarded. At lower energies, noise-related events begin to dominate.

Upon passing the final cuts, data can then be parsed into spectra that are useful for determining $a_{\beta\nu}$. As was mentioned in the introduction, we have had the most success in terms of sensitivity when using the spectra containing the difference in energy between the two alpha particles in a triple event. Examples of these spectra for the Top-Bottom detector system (similar results for the Left-Right system) with the beta particle going into each of the four detectors are exhibited in Figure 4.20. To obtain the additional sensitivity to $a_{\beta\nu}$ imparted to us by the delayed alpha emission decay rate (discussed in section 1.2.4), we must use events where the beta and one of the alphas are emitted in roughly the same direction. More intuitively, the weight for the beta-neutrino correlation in events can be simplified to something like the equation below:

$$W(\theta_{\beta\nu}) = 1 + a_{\beta\nu}\frac{v_\beta}{c}\cos(\theta_{\beta\nu}) \quad \text{Axial-Vector: } a_{\beta\nu} = -\frac{1}{3}, \quad \text{Tensor: } a_{\beta\nu} = \frac{1}{3} \tag{4.3}$$

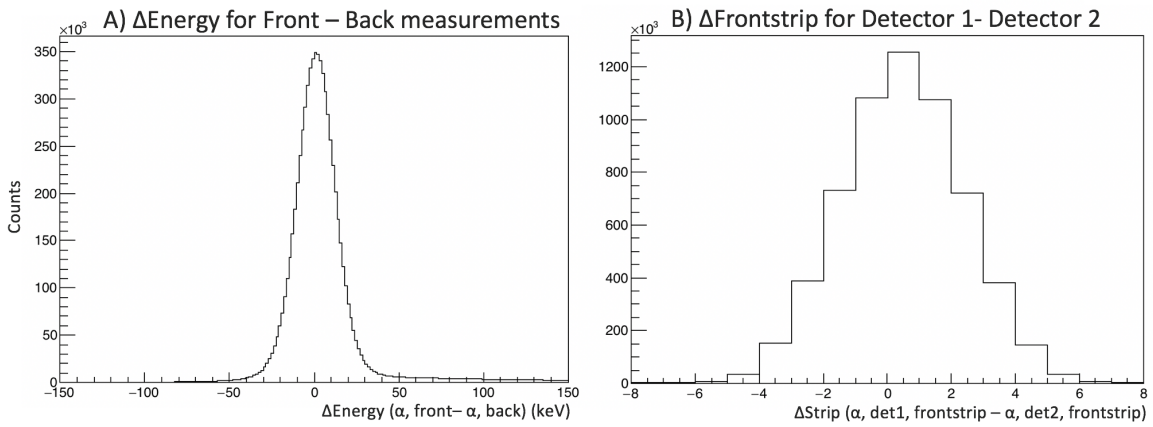

Figure 4.19: A) Difference in energy for all usable strips between the front and back measurements. Events with an energy difference greater than 60 keV are discarded. The tail on the right hand side is due to incomplete charge collection on the back strips or a poor back strip energy reconstruction across strips. B) Difference in strip number between the two alphas when they hit opposite detectors. It is kinematically impossible for an alpha double to have a difference in strip number greater than 8.

If the interaction is axial vector, then it is more favorable for the beta and antineutrino to be emitted in opposite directions. If the interaction is tensor, then the leptons are most likely to be emitted in the same direction. For this reason, if both leptons are emitted in the same direction, the resulting "kick" to the recoiling nucleus would show up most clearly in the alpha difference spectra if the leptons were also emitted in the same direction as one of the alphas. You can already see the "kick" imparted by the beta particle in the skewed shapes of the parallel beta spectra in Figure 4.20. It is the parallel beta spectra that we compare to simulation for determining a final value of $a_{\beta\nu}$. For spectra shown in the results section, they are often combined versions of the spectra seen below. This is accomplished by simply swapping the energy subtraction on one of the spectra to make the shape match the other and summing the two. A total energy difference spectra for the beta hitting the same detector as an alpha can be obtained by summing both the Top-Bottom detector system and Left-Right detector system spectra.

It is also possible to determine $a_{\beta\nu}$ using a spectra containing the reconstructed angles between the beta and antineutrino. However, since the reconstructed kinematics are highly

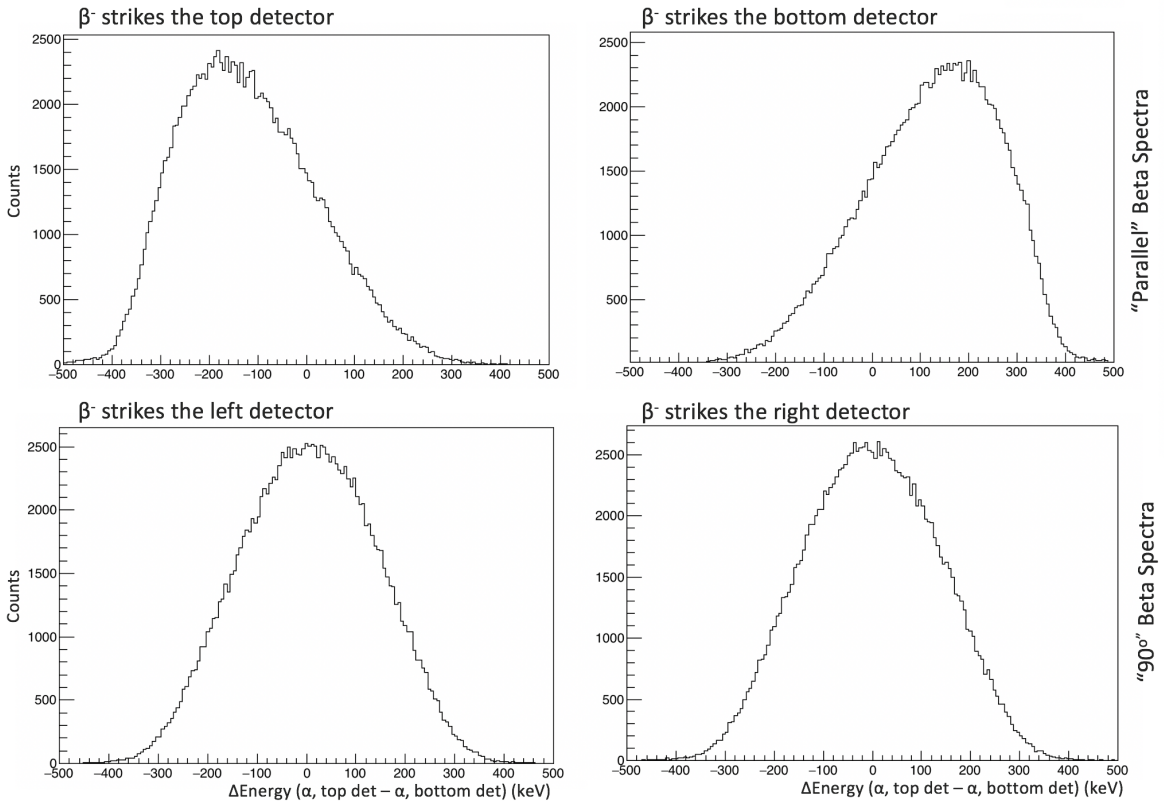

Figure 4.20: A subset (α's in the Top-Bottom detector system, $\sim$50% of the total) of the good-quality experimental "triples" data divided into the four possible alpha energy difference spectra. The "parallel" beta spectra have clear structure and can be used to measure tensor currents. The "90^o" beta spectra have less structure and are used to test various systematics

sensitive to any error in the ion cloud position and are not always successful, this technique is not nearly as powerful.

CHAPTER 5

SIMULATIONS

Once the data set has been calibrated and cleaned, it can be compared to simulation so a value for $a_{\beta\nu}$ can be extracted. Given that this is a high-statistics precision measurement, it is of the utmost importance that the simulation takes into account every relevant detail of the decay and detector system. This goal is accomplished using two different simulation stages. The actual decay and the resulting products with energies and trajectories are created using a Monte Carlo Event Generator code. From there, the generated β^- particles are propagated through a full material model of the BPT and chamber to account for scattering. The simulations are run in both a pure axial vector mode and a pure tensor mode (details discussed in appendix B). Once an alpha difference spectra is constructed for each, splines are fit to each of the spectra and a linear combination of the two splines are fit to the data. The resulting tensor fraction of the total contribution becomes $|C_T/C_A|^2$ and can in turn be plugged into the formula for $a_{\beta\nu}$.

$$a_{\beta\nu} = -\frac{1}{3}\frac{|C_A|^2 - |C_T|^2}{|C_A|^2 + |C_T|^2} \tag{5.1}$$

5.1 β-Decay Event Generator

The β decay Event Generator is the cornerstone of our simulation software and includes all of the necessary components for dealing with the ^{8}Be* α particles. It was originally written by one of our former postdocs, Dr. Nick Scielzo (who is now a staff member at Lawrence Livermore National Lab) for the ^{21}Na MOT experiment discussed in section 1.3.3 [88]. It has since been modified for the mass-8 system and upgraded from C to C++ by Aaron Gallant, one of our postdoc collaborators currently working under Dr. Scielzo.

The event generator code goes through a series of steps to include all possible physics into the generation of the α's, β^-, and $\bar{\nu}$ particles. It begins by first choosing an excitation

energy from the broad ^{8}Be* 2^{+} state. This step is completed using a final state distribution (FSD, from a ^{8}Li decay, specifically) that must be included in the event generator. The one we use is taken from an R-Matrix fit to the spectrum of summed ^{8}Li α energies. The FSD itself is discussed in further detail in the next section.

Once an excitation energy has been selected, there are two possible types of decays that should be accounted for. The first is a normal β^{-} decay that is constructed using a simple Monte Carlo rejection method. The directions for the β^{-}, $\bar{\nu}$ and α breakup axis are randomly generated on a unit sphere (in the rest frame of the recoiling nucleus). The α energies are taken from the resulting ^{8}Be* decay Q value with the chosen excitation energy and the β^{-} energy is chosen at random from a range of 0 to the endpoint energy (also calculated from the excitation energy of the ^{8}Be*). Finally, the $\bar{\nu}$ energy is determined from conservation of energy and momentum. Once everything has a direction and energy, they are boosted into the lab frame and the resulting phase-space amplitude is calculated using Holstein's decay rate expansion for a β decay with delayed α emission where the β and ν energy and momentum are known [49]. The amplitude is compared to the maximum of the phase space over all parameters and either kept or rejected based on the likelihood of it being a real event.

The second possible decay is one where a photon (bremsstrahlung radiation) is emitted from the β^{-} particle as it exits the charge radius of the atomic ^{8}Be*. This process occurs in about $\sim$6.5% of the total decays and can be accounted for by having a set fraction of events with photon emission and using an alternate recoil expansion. The steps for adding photon emission to a Monte Carlo event generator and the corresponding decay rate expansion is described in Glück's 1997 paper [37]. More details on the full decay rate expansion from Holstein's paper and Glück's bremsstrahlung radiation expansion can be found in Appendix B.

For pure axial-vector events, the correlations within each of the decay rate remains as described by both Holstein and Glück. To simulate pure tensor events, we collectively swap

the signs ($\pm$) of each term containing a correlation between the β and ν. This method has been roughly verified through conversations with Holstein. In addition, based on our previous study, the tensor interaction contributes less than 1% to the total events, so only the leading-order terms are important.

Once the decay has either been accepted or rejected based on the phase space, it can be applied to a theoretical rendition of the actual trap and detector setup. The decay's location is assigned based on a random generation using a 3 dimensional Gaussian (determined by comparing α strip difference spectra to simulation). The meV level thermal energies of the ^{8}Li particles are not included as they are much smaller than the 20 keV sensitivity we strive for in our system. The particle trajectories are then used to determine whether or not any of the particles hit a silicon detector. The location of the hits on silicon detectors are recorded based on strip number. At this point, a detector response function or "lineshape" is applied to the alpha particles to take into account a variety of real factors that would spread out the α energy distribution. The code also takes into account whether or not an α hits a strip that would be considered too noisy to use and rejects events based on that criteria as well. More details can be found in section 5.1.2.

The final product of the event generator is a ROOT file filled with information similar to what the sort code would output for the data. This file can then be funneled through a Geant4 simulation to incorporate any effects from β^{-} scattering.

5.1.1 Final State Distribution

The final state distribution (FSD) is a crucial component to the Event Generator simulation as it eventually defines what the single α energy spectrum will look like. In previous works, we have used an R-Matrix fit from a paper in 2006 by Bhattacharya, M. et. al [12]. Their ^{8}Li FSD (blue curve) can be seen in Figure 5.1 (they also performed a similar fit to the ^{8}Be*

FSD for a ^{8}B decay). An example of an R-Matrix fitting function is below.

$$\mathcal{F}(E_X) = \frac{Nt_{1/2}}{\pi B} f_\beta(E_x) P_l(E_x) \times \frac{\left|\sum_\lambda \frac{g_{F,\lambda}\gamma_\lambda}{\mathcal{E}_\lambda - E_x}\right|^2 + \left|\sum_\lambda \frac{g_{GT,\lambda}\gamma_\lambda}{\mathcal{E}_\lambda - E_x}\right|^2}{\left|1 - \left[S_l(E_x) - B_l + iP_l(E_x)\right]\sum_\lambda \frac{\gamma_\lambda^2}{\mathcal{E}_\lambda - E_x}\right|^2} \tag{5.2}$$

where P_l is the penetrability factor, S_l is the shift factor, B_l is the boundary condition, $g_{F,GT}$ is the Fermi or Gamow-Teller matrix element, γ is the partial width, $\mathcal{E}_\lambda$ is the energy level, and E_x is the excitation energy.

The 2006 FSD served us well until this experiment, where there were enough statistics to show a discrepancy. At this point, the Bhattacharya, M. et. al. FSD resulted in simulated α energy spectra with a peak $\sim$6 keV higher in energy than the data ($\mathcal{E}_1 \sim 12$ keV higher for the FSD peak center). However, the error on the 2006 R-matrix $\mathcal{E}_1$ peak fit was $\sim$10 keV. In addition, a similar measurement had been done at IGISOL in Finland in 2012 for ^{8}B that produced a $\mathcal{E}_1$ FSD peak 10 keV lower in energy than the 2006 paper [81]. Bearing that in mind, we came to the conclusion that the 2006 ^{8}Li FSD was not sufficiently precise to use for our simulations. Since it is the lepton correlation that primarily concerns our measurement, we opted to perform our own R-matrix fit to the high-statistics ^{8}Li data. This fitting is being done by Dr. Tsviki Hirsh alongside his own R-matrix fit of our 2014 ^{8}B data and is still in progress. For the moment, we are utilizing a modified R-Matrix fit from [12] with the $\mathcal{E}_1$ term shifted 12 keV lower, which we project will be very similar to the final R-matrix fit. The shifted FSD can be seen in the grey curve of 5.1, and the peak is indeed shifted slightly lower in energy. A comparison of the two single α energy spectra can be found in section 6.2.5. In the end, the difference between tensor contributions when changing between the two final state distributions was roughly half of our statistical uncertainty (more details are discussed in section 6.2.5).

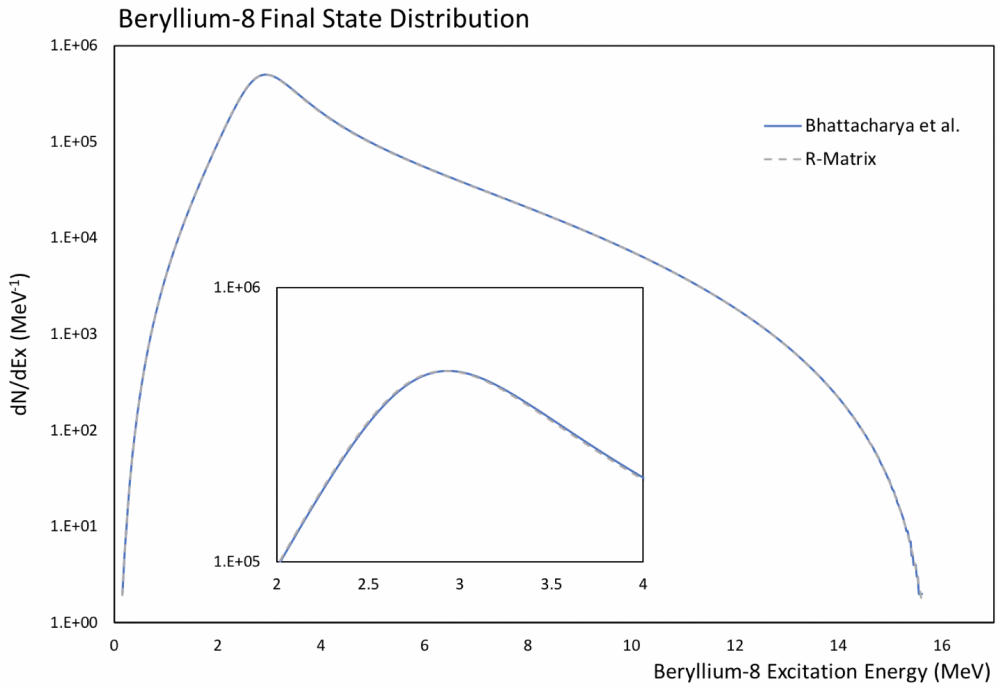

Figure 5.1: Example of the decay from lithium-8 to beryllium-8* final state distribution. The blue curve is taken from an R-matrix fit to measured lithium-8 data by Bhattacharya, M. et. al. in 2006 [12]. The grey dashed line is an R-matrix fit to our lithium-8 data done by Tsviki Hirsh. The peak of the grey line is ∼13 keV lower in energy than the Bhattacharya et al. curve (inset).

5.1.2 α Detector Response Function

Another key attribute of the Event Generator that I gave a great deal of attention is the detector response function or "lineshape." This particular aspect was of great importance in terms of tying in several real effects on the ^{8}Li data to the simulation. The previous ^{8}Li experiment used a skewed Gaussian to represent the lineshape based on noise and the energy of the alphas that was based on a guess from comparing to offline measurements of thin mass-separated ^{148}Gd and ^{244}Cm sources. This time, being aware of the extra dead layer and having spectroscopy-grade ^{148}Gd and ^{244}Cm alpha sources for comparison already in the system, we completed a fully calculated lineshape based on known physics and features within the silicon detectors. This calculated lineshape was in turn added to our Event Generator.

Going according to the formulation described in E. Steinbauer et. al.'s 1994 paper [92], a full lineshape convolution has 4 stages: dispersion through the dead layers, dispersion from nonionizing energy loss (NIEL), and spread from the Fano factor resolution within the detector as well as the electronic noise of the system. Since the calibration was performed with the line centers at the maximum of each alpha peak, the lineshapes were also constructed such that the largest peak of the final convolution had its maximum at 0 keV.

The Extra Dead Layer

The first stage requires fully understanding the normal and extra dead layer (defined in section 3.3.1, see Figure 3.7) dispersion based on both energy and incident angle, as well as the compositions of each layer. The full lineshape had to include two different peaks to account for the normal and extra dead layer effects. The percentage of events going into each dead layer was determined by fitting the ^{148}Gd peak with two Bortels skewed Gaussian functions (one for each peak) and integrating over each individual function. The fitting was done over all doubly-illuminated pixels. The center of the Gaussian distribution of each detector's extra dead layer percentage (and the corresponding error) was used as the final

percentage. Because of the high electronic noise on the Left detector, a precise percentage value could not be determined. However, since the Left and Right detectors were purchased together and therefore the crystals were grown at the same time, we use the Right detector percentage value and error for both detectors. Rudimentary fitting of the Left detector confirmed this result within the precision that was possible. The percentage of α events that interact with the extra dead layer (intrinsic for each detector) with the corresponding errors can be found in table **??**.

Detector	Extra Dead Layer Event %
Top	3.132 ± 0.017
Bottom	3.287 ± 0.017
Left/Right	2.917 ± 0.014

Table 5.1: Percent of measured α events that interact with the extra dead layer by detector as determined by the Gd source peak.

The thickness of the extra dead layer was determined using a linear regression of the energy difference between the two Gd peaks (one for each dead layer) vs incident angle over pixels in the five front strips that were most centrally illuminated by the two Gd sources.[1] The results were remarkably consistent across all detectors: for a Gd alpha normally incident on a detector and factoring in a $\sim$100 nm normal dead layer, the energy loss would be 112 ± 4 keV. The extra dead layer thickness that Micron prescribed us (300 nm of aluminum and 500 nm of silicon) would have produced a much higher energy loss. Less precise fits to the Cm extra dead layer peak corroborated what was found with the Gd peaks. A comparison of the data to SRIM [111] projections of what the energy loss curve would look like with different combinations of materials can be seen in Figure 5.2. We settled upon a dead layer composition with 300 nm of aluminum and 270 nm of inactive silicon with a 3.5% error

1. See Figure 4.2.A. The angle difference between the pixels corresponding to the illuminated edge back-strips is approximately 37 degrees, see Figure 4.2.B. There are 23 illuminated pixels per strip that can be used for the linear regression.

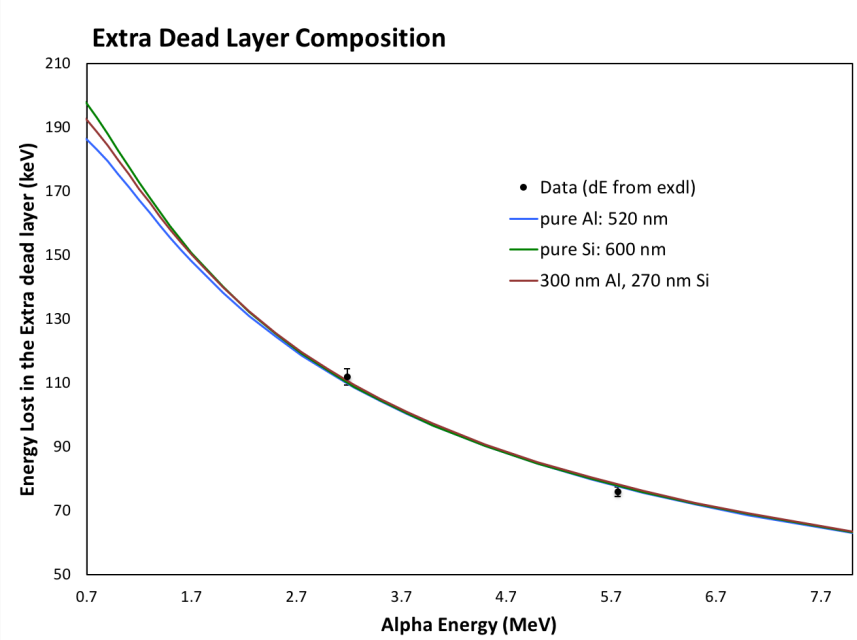

Figure 5.2: Comparison of the energy loss in the extra dead layer for the ^{148}Gd and ^{244}Cm alpha sources (taking into account a ∼100 nm normal dead layer) compared to SRIM [111] stopping power curves for 3 different potential extra dead layer compositions. The mixture of silicon and aluminum was chosen because it best matched what Micron claimed we should have.

(corresponding to 4 keV out of 112). However, in the likely event that our composition estimates are wrong, Figure 5.2 implies there would be up to a 5 keV discrepancy in either direction for a pure silicon or pure aluminum extra dead layer. Such a small change on 3% of the lowest energy events is not a large enough effect for this experiment to be sensitive to it.[2]

Once the size and composition of the extra dead layer had been determined, it was necessary to determine the resulting energy dispersion of alpha energies within each dead layer based on energy and impinging angle. This was accomplished by running a series of simulations in TRIM of 10,000 mono-energetic alphas passing through each of the two dead layers (100 nm of silicon and 300 nm of aluminum with 270 nm of inactive silicon, separately).

2. The composition between silicon and aluminum in the extra dead layer would also have an effect on potential "channeling," or α's passing through potential silicon crystal axes where the electron density is less, [25] thus depositing less energy for a small percentage of events. However, the silicon implants are the same material as the normal dead layer and no channeling was observed through the normal dead layer. This issue is discussed in further detail in section 6.2.9

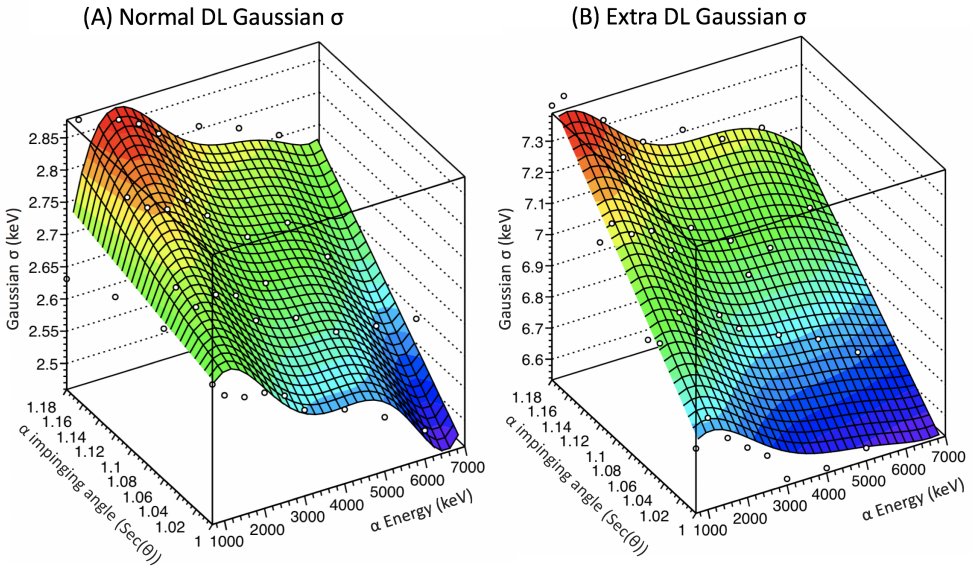

Figure 5.3: Energy dispersion of α particles through the A) normal dead layer and B) the extra dead layer based on impinging angle and α energy used to construct the detector lineshape. Here, the white dots represent the sigma of a Gaussian fit to a dead layer simulation in TRIM and the colored plane is a 2-dimensional polynomial fit to the data.

40 simulations for each dead layer were run: 10 different values of energy spanning 700 keV to 7 MeV with 4 different thicknesses: the original thickness with 106%, 112%, and 118% of the original thickness to simulate different impinging angles. The resulting standard deviations of a Gaussian fit to the energy loss for each 10,000 alphas simulations are plotted in Figure 5.3. The 40 values were fitted to a 2D polynomial, which was incorporated into the lineshape construction.

Thus, the first stage of the lineshape construction was completed by using a random number generator compared to the extra dead layer percentage to determine which dead layer the alpha would "hit." Depending on which dead layer was chosen, the event generator would then determine what the resulting spread from the dead layer using the 2D polynomials with respect to the energy and impinging angle of the alpha. The combined systematic error brought to the detector lineshape from the dead layers was roughly half of the statistical uncertainty, with the extra dead layer thickness being the largest contributor. More details can be found in section 6.2.7.

Nonionizing Energy Loss

After passing through a dead layer, the alpha also loses energy from various interactions within the silicon detector that aren't picked up in the total energy measurement and are primarily from collisions with the silicon nuclei. TRIM is also capable of simulating energy lost through nuclear collisions, thus 6 more simulations of 30,000 α particles implanting in silicon were run at 6 different energies that spanned the ^{8}Li α spectrum. These 6 curves were then fit to a modified F-Distribution function (a function that is often found in statistics). The modifications were imposed such that the resulting function would be the right width, and with the peak centered at 0. An example of the fit can be seen in Figure 5.4, though it was flipped from positive to negative when applied to the lineshape convolution. It is in part the nonionizing energy loss that gives the skewed Gaussian from the Bortels function its skew. The modified function itself is below:

$$f(E_\alpha) = Y\left(\frac{m^{m/2}n^{n/2}(E_\alpha X - 0.818)^{n/2-1}}{\big(m + n(E_\alpha X - 0.818)\big)^{n+m/2}B\big(\frac{1}{2}n, \frac{1}{2}m\big)}\right) \text{ with: } B(p,q) = \frac{(p-1)!(q-1)!}{(p+q-1)!} \tag{5.3}$$

where $n = 10000.0$ and $m = 9.0$. Over the 6 simulations that were run, the X and Y scaling factors were allowed to vary when fitting the resulting nonionizing energy loss curve. The two factors were then fit to a quadratic (also seen in Figure 5.4). The shape of the nonionizing energy loss curve did not noticeably change across the alpha energies. However, whatever small effect there was, it was taken into account and the resulting F-distribution function was convoluted with the Gaussian from the dead layer dispersion.

Fano Factor Resolution

Alongside the nonionizing energy loss, there is some spread attributed to the number of electron-hole pairs created when mono-energetic alphas are measured by silicon detectors, which is loosely known as the Fano factor resolution. This spread is also Gaussian with a

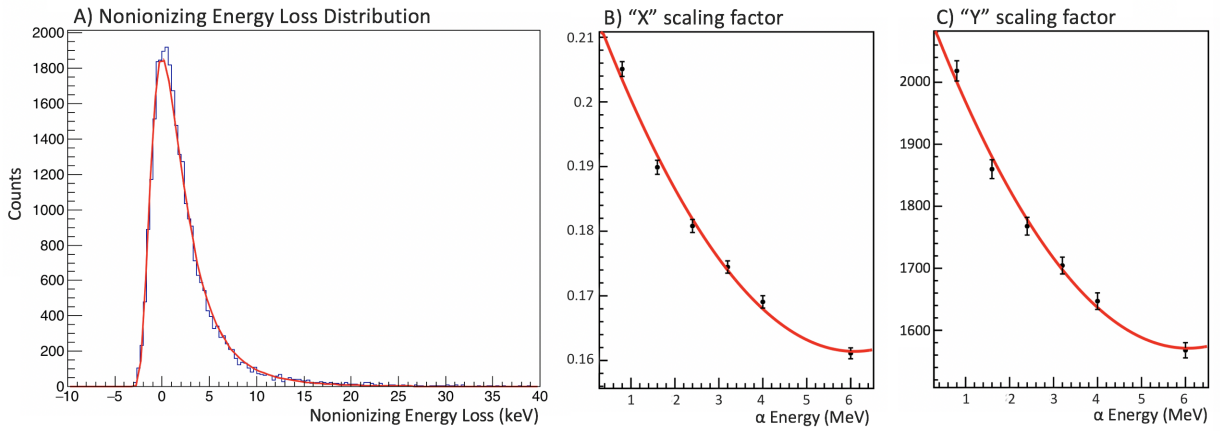

Figure 5.4: A) Example of a nonionizing energy loss distribution for an α particle in silicon fit to a F-Distribution (shifted so that the maximum is at 0 to match with the energy loss correction already applied to the data). The entire distribution will be flipped from positive to negative before being applied to the lineshape. B) and C) are quadratic fits to the F-Distribution fitting parameters for 6 different α energy NIEL distributions.

standard deviation of: [30]

$$\sigma_{FF} = \sqrt{wE_\alpha F} \tag{5.4}$$

where F is the Fano factor, measured to be 0.134 $\pm$ 0.007 [92], E_α is the energy of the α particle and w is the average energy required to create an electron-hole pair. This simple Gaussian distribution is also convoluted into the final lineshape.

Electronic noise

The final component of our lineshape is the individual electronic noise picked up by each strip, both front and back. This "ambient" noise is a result of the cumulative racket that our system makes, both electronically and vibrationally during the course of an experiment. Roughing and turbo pumps must run and be fed power, liquid nitrogen must be pumped through the trap, and various electronics are required to actually perform the measurement. The final result is yet another Gaussian spread to the data that must be incorporated into the lineshape. As it happens, our precision pulser linearity data were still useful for this purpose, if not for actually measuring the linearity. By applying 12 pulses of different energies to the

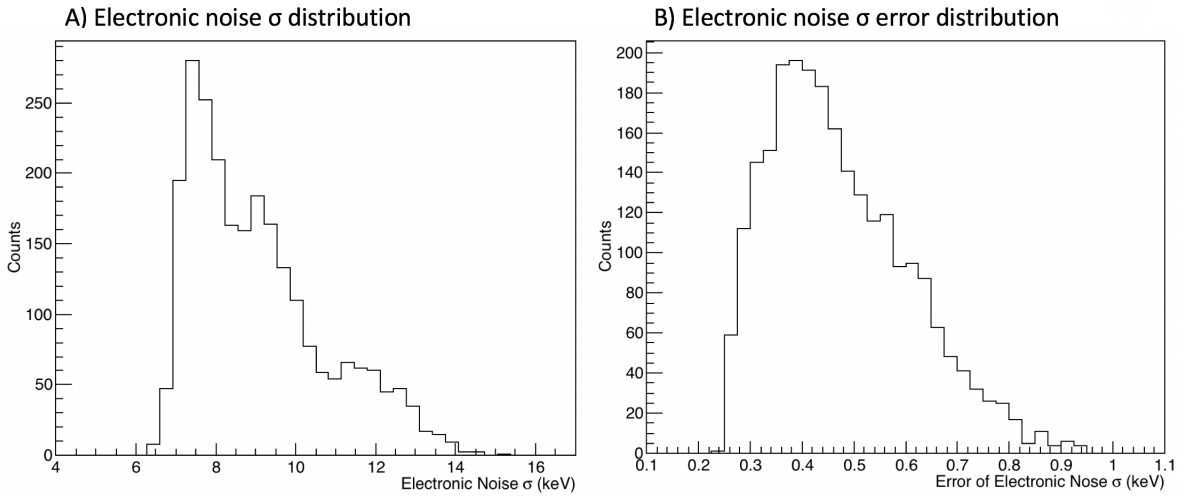

Figure 5.5: A) Distribution of the average Gaussian σ's fit to the precision pulser peaks to measure electronic noise for all usable strips with B) the corresponding errors for each strip.

strips, it was possible to measure the electronic noise spread directly by fitting the pulser peaks to Gaussian fits, and taking the average σ over all 12 pulser peaks. The error for each sigma was either the standard deviation of the 12 σ's or the highest of the 12 errors on the σ in the Gaussian fit, whichever was larger. Distributions for the electronic noise σ's and the corresponding errors can be found in Figure 5.5. In principle, as long as the resolution of the strip is not too compromised, as long as the electronic noise (or the peak widths of the Gd and Cm sources) between the simulation and strip match, the electronic noise does not contribute significantly to the systematic uncertainty (more details in section 6.7.2).

The event generator will choose an electronic noise based on which strip it projects the alpha has hit (while also choosing randomly between the 16 time segments, which each have individual noise contribution to account for fluctuations in time). Mirroring the sort code, if either front strip in the α double is found to be too noisy from the input electronic noise values, it will choose the corresponding back strip noise σ. If both the front and back are too noisy, the event is rejected.

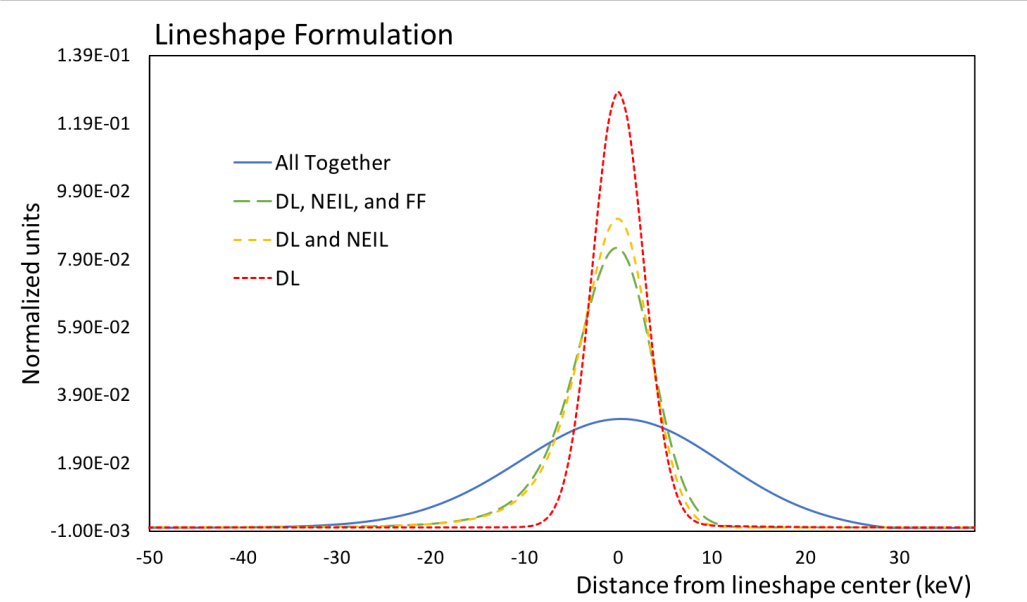

Figure 5.6: The four stages of formulating a lineshape. The first widening factor is the detector dead layer (red), followed by the nonionizing energy loss distribution (orange), then the detector Fano factor resolution (green), and then the general electronic noise from our system measured by a precision pulser. Each stage is a combination of the previous ones. The combination of all effects is in blue.

Final Lineshape

In the event generator, the final spread "value" is selected by choosing between the two dead layers using the detector's percentage value, and then adding together a random number generated from the dead layer Gaussian distribution, the nonionizing energy loss, and then the combined Fano factor and electronic noise Gaussians. A step-by-step look at what a resulting lineshape would look like for a normal dead layer can be seen in Figure 5.6. For the extra dead layer, a similar pattern would be evident, though the distribution would be wider and centered at the energy and incident-angle dependent negative offset that corresponds to the extra energy lost in the thicker dead layer.

When all is calculated and compared to the spectroscopy-grade alpha sources, the results are very consistent. An example lineshape compared to a Gd and a Cm spectrum is seen in Figure 5.7. The high-energy side of each spectra is well-matched, as is the position and size of the extra dead layer peak. The discrepancies between the lineshape and the lower-energy

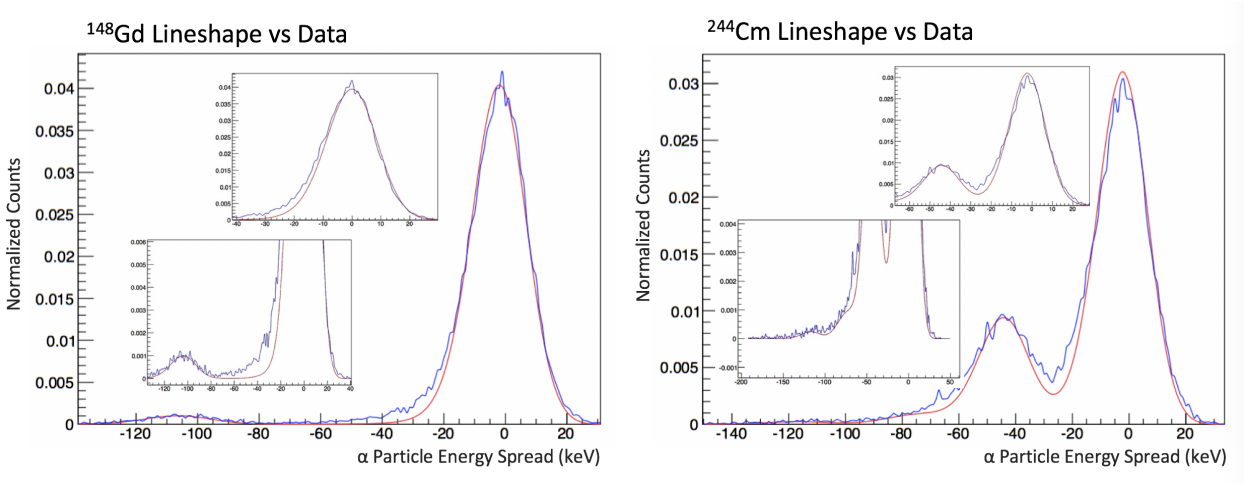

Figure 5.7: A comparison between both ^{148}Gd and ^{244}Cm spectra (blue) with their calculated lineshape (red). They match very well, except for a low-energy tail that results from a source dead layer, which is not present in the ^{8}Li α lineshape.

tails in the spectra are the result of a small source dead layer, as was determined by Louis Varriano in the experiment discussed in section 4.2.1. Since the trapped ^{8}Li ions have no source dead layer, it is not necessary to add a source dead layer to the lineshape.

Depending on the needs of the simulation, the lineshape can be either applied within the event generator or after a simulation has been completed.

5.2 Geant4 Scattering Simulation

The second stage of simulation is a Geant4 [28] program seeded with the β^- particles created by the Event Generator which takes into account scattering off material in and around the trap. As the α particles are simply stopped by any material, their properties remain the jurisdiction of the Event Generator and are unchanged after the Geant4 simulation. The β particles and their energies are fed into the Geant4 simulation as a "beam" and propagated through a full geometry of the trap and chamber. Geant4 registers any scattering that happens to the β's and records any interactions with both the silicon and plastic scintillator detectors. In addition, the simulation is used to determine both detector sets' responses to β interactions and includes a kinematic reconstruction program identical to the one in our

data sort code. From comparing simulation to data, it is estimated that between 85-80% of betas are direct hits to the silicon detector, while the remaining percentage is impacted by some type of scattering. Since our previous experiment, Geant4 has become a much more complete and powerful program for dealing with ion propagation and has been able to keep up with our high-statistics data set. An updated version from the original code used in the 2015 experiment was compiled by Dr. Aaron Gallant for the ^{8}Li August 2016 data analysis and the upcoming high-statistics ^{8}B analysis. The upgraded code included the most recent version of Geant4 (10.03) and corrected some multithreading errors.

5.2.1 Geometry

In order to accurately take into account the scattering, a complete model of the trap and chamber material is required. The model was constructed in Autodesk Inventor utilizing the original engineering designs of the BPT itself for simulations in the 2015 ^{8}Li PRL experiment. 3 different views of the model can be seen in Figure 5.8.

Before use, one of the most important components: the distance between detectors was precisely measured to 0.001" after the model's construction. The measurements matched the Autodesk model to within 0.003" for the Top/Bottom and 0.021" for the Left/Right detector systems, which do not cause a problem for the α difference spectra, but are incorporated into the kinematic reconstructions. In addition, rather than being precisely machined, the RF shielding was cut and folded from stainless steel sheets, which could lead to discrepancies of up to 2 mm between the model and actual trap. None of the cabling surrounding the trap or small screws were included either. However, by observing the β-scattering in Geant4 directly, the vast majority of redirected β's result from interactions with the RF shielding. Similarly, comparing a simulation taking into account scattering to a simulation without, the correction to $|C_T/C_A|^2$ only changes by $<$0.02 for each detector system. Thus, a potential discrepancy of 2 mm on some of the shielding should not pose a problem. β's that are scattered into a detector are usually already heading in the direction of a detector and therefore the scattering

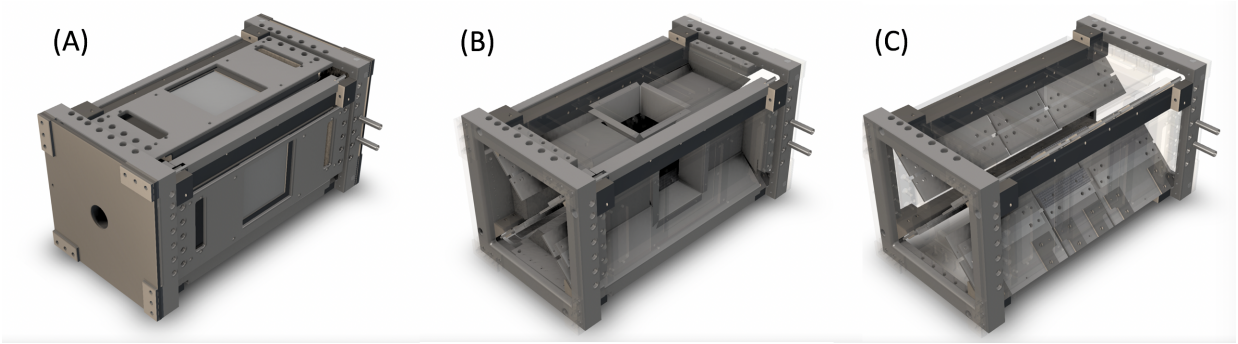

Figure 5.8: The full Autocad rendition of the BPT trap used for the Geant4 geometry. The chamber and plastic detectors are also included, but not shown here. A) A complete version with the silicon detectors and their mounts, B) one where the detectors and mounts are removed so the stainless steel RF shielding is visible, and C) one with only the frame and electrodes.

itself will not have such a large effect.

A complete chamber and the new plastic detectors were added to the model later for the August 2016 run by Dr. Aaron Gallant. The Autodesk file was converted to a Geant4-friendly file format (gdml) using open-source software. [2]

5.2.2 Physics Package

The number of physics packages available for use in the low-energy regime (β energy from 250 eV to 1 GeV) has expanded since our previous experiment from three to over a dozen. The most widely used packages of the current low-energy electromagnetic physics packages are the default, Livermore, PENELOPE, and Options 1 through 4 packages. There is also a DNA physics package primarily used for biological purposes that is not applicable to this research and will not be discussed.

For the purposes of determining which package to use in the updated Geant4 version, Dr. Gallant ran a series of small simulations to measure the scattering fraction in a hemisphere of several relevant materials (stainless steel, silicon, and gold) at the range of energies required for this experiment. The results indicated that the Livermore, PENELOPE, option3, and option4 packages converged for all materials and thus, any would suffice for our analysis.

These results were confirmed using similar scattering fractions discussed in the next section: no statistically significant discrepancy in the scattering fractions between the four models was discernible. Of the four, we opted to use the option3 package, due to being the most simple package available while still having all the necessary physics.

The reason for all of the physics lists having converging results is that elastic Coulomb scattering itself is what dominates the effects that we're looking for and all four use the same Geant4 Urban multiscattering model [51]. This particular model has its foundations in Lewis theory [41] and uses a new "Goudsmit-Saunderson" model that relies on a database of total and transport cross sections of positrons and electrons generated by the ELSEPA code [83]. This database allows for fast sampling of positron and electron angular distributions to find deflections from neutral atoms to model the scattering. [55]. The addition of this new technique allowed Geant4 to become a much more powerful tool for modeling low-energy electron and positron scattering and the accuracy has been well tested in a variety of mediums ([56], though Geant4 keeps a full validation data archive here: [3]). Currently, the best benchmark for backscattering pins accuracy to be within 16% [67]. A variety of other physical processes that do not contribute significantly to our β scattering but are still taken into account in the option 3 package are bremsstrahlung radiation, ionization, and Compton scattering.

The Option 3 physics list comes with a few tunable parameters that have been incorporated into the code, though changing them from the default values has not shown any noticeable change in the results of our simulation. Two parameters: F_R is the "range factor" and F_G is the "geometry factor" are used to determine the maximum number of steps the scattering simulation may take (L).

$$L = \text{Min}(F_R * \text{Max}(R, \lambda), D/F_G)$$

Here, R is the particle range in the material, and λ is the inverse cross section (both are

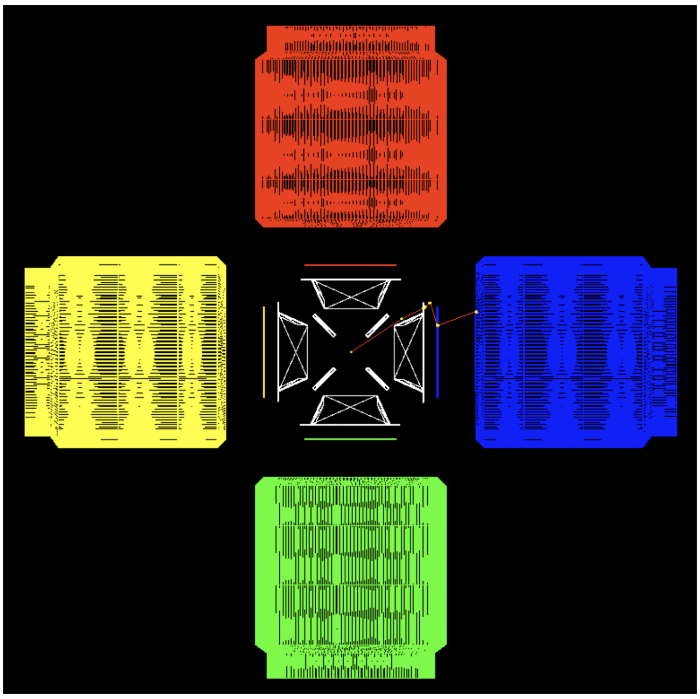

Figure 5.9: An example of an electron's scattering trajectory. Each of the silicon detectors and backing plastic detectors are highlighted in color. The trap electrodes and inner "hood" shields are outlined in white.

dependent on the energy of the particle), and D is the distance to the geometrical boundary. However, if we choose to use the option "fUseDistanceToBoundary" command, (which gives the most accurate results from Option 3) the terms are set to values of $F_R = 0.04$ and $F_G = 2.5$. [51].

5.2.3 Scattering Quality-Checks

In order to ensure that the Geant4 simulation is outputting quality data that is directly comparable to the actual data, a variety of quality-checks or "benchmarks" are used. Some have already been discussed. For this experiment, they include:

- Energy deposited in the silicon detectors
- Fraction of $\beta - \alpha - \alpha$ coincidences to $\alpha - \alpha$ coincidences, or the "triples fraction"
- Fraction of triples where a β is backscattered from one silicon detector to an opposite

silicon detector

- Distribution of β particles in triple events across each detector
- Fraction of triple events where plastic data is measured above threshold
- Stability of the simulation when adjustable parameters are changed

The energy deposition spectrum of the β's passing through the silicon detector was already discussed in the previous chapter, given that the spectrum itself needed to be thoroughly vetted for its integrity using a similar muon spectrum and data before use in the calibration.

The triples fraction and backscattered fraction are both fairly straightforward to calculate for the simulation, though some background (muons, betas from other decays where the alphas aren't detected, etc.) needs to be taken into account when doing the calculations for the data. In the previous experiment, there were not enough statistics to actually use the backscattered fraction as a true benchmark. However, with the current data set, the backscattered fraction in the data can be known to within 16%, which is well within the capabilities of Geant4's accuracy. All of the fractions from both the simulation and data are included at the end of this section.

The distribution of β's over each silicon detector is possibly the best way to determine the quality of the Geant4 simulations as it has the most sensitivity to any significant discrepancies between the model and the actual trap. A simple χ^2 calculation over the detector's pixels can be used to determine the integrity of the scattering simulation. The final systematic error prescribed to β scattering was calculated using artificial changes to the simulation scattering distribution.

In contrast, the plastic detectors are much less reliable in terms of being used as a benchmark. Their calibration is determined by the Geant4 simulation itself rather than independent alpha sources. Thus, the fraction of triples with plastic data vs the total is very much dependent on what threshold defines a plastic event and the quality of the calibration.

Benchmark	Simulation	Data
Triples Fraction	0.2602 ± 0.0005	0.259 ± 0.001
Backscattered Fraction	0.000229 ± 0.000007	0.00019 ± 0.00003
Plastic Fraction	0.69	0.74

Table 5.2: Quality benchmarks for scattering in the Data vs the Geant4 simulation.

That said, for posterity, the "plastic fraction" from both the simulation and data is also included at the end of this section.

In previous experiments, the stability of the triples fraction when the adjustable parameters were changed was considered a benchmark. However, since upgrading to a more recent version of Geant4, the triples fraction has in fact not budged at all across all adjustable parameters in acceptable ranges, though we could see that the speed of the simulation was clearly being affected by the changes. This new Geant4 "feature" now lends some confidence to our final simulation results.

5.3 Comparison to Data

Once the simulations have been generated, the events are cut using the same applicable criteria as the data. This includes:

- The difference in numbering of front strips and back strips between the two alpha particles must be less than 8 (the maximum difference that is allowed by kinematics).
- The difference in energy between the two alpha particles must be less than 600 keV.
- Alpha events that occur on the edge strips: front strips 1 and 32 and back strips 1 and 32 are rejected.
- Alpha events with energy above 7 MeV are discarded.
- Events with the β energy below 200 keV are discarded.

The other cuts to the data: energy differences between the front and back faces of the detector and the trap cycling are not simulated, and therefore not included in the simulation cuts.

Once the cuts are applied, the simulated triples are distributed into the same α energy difference spectra as the data is. Examples of what this would look like for pure axial-vector and pure tensor interactions can be seen in Figure 5.10. There is a very distinct shape difference between the two, which gives us the sensitivity we require to define $a_{\beta\nu}$. Since this is a precision measurement, it is unwise to compare the data to simulations any less than 10x as large as the data. Differences between the two detector systems' spectra can be attributed to geometry: some strips are rejected (mostly based on noise) on the Left-Right are not rejected on the Top-Bottom system and vice versa.

Though the simulated Geant4 spectra aren't directly used for the measurement of $a_{\beta\nu}$, they serve a variety of other purposes (calibration, nailing down systematics, etc.). The two Geant4 simulated spectra: a beta spectrum through a silicon detector and then a plastic scintillator detector are seen in Figure 5.11. The threshold for a plastic event to be considered "real" is 700 keV.

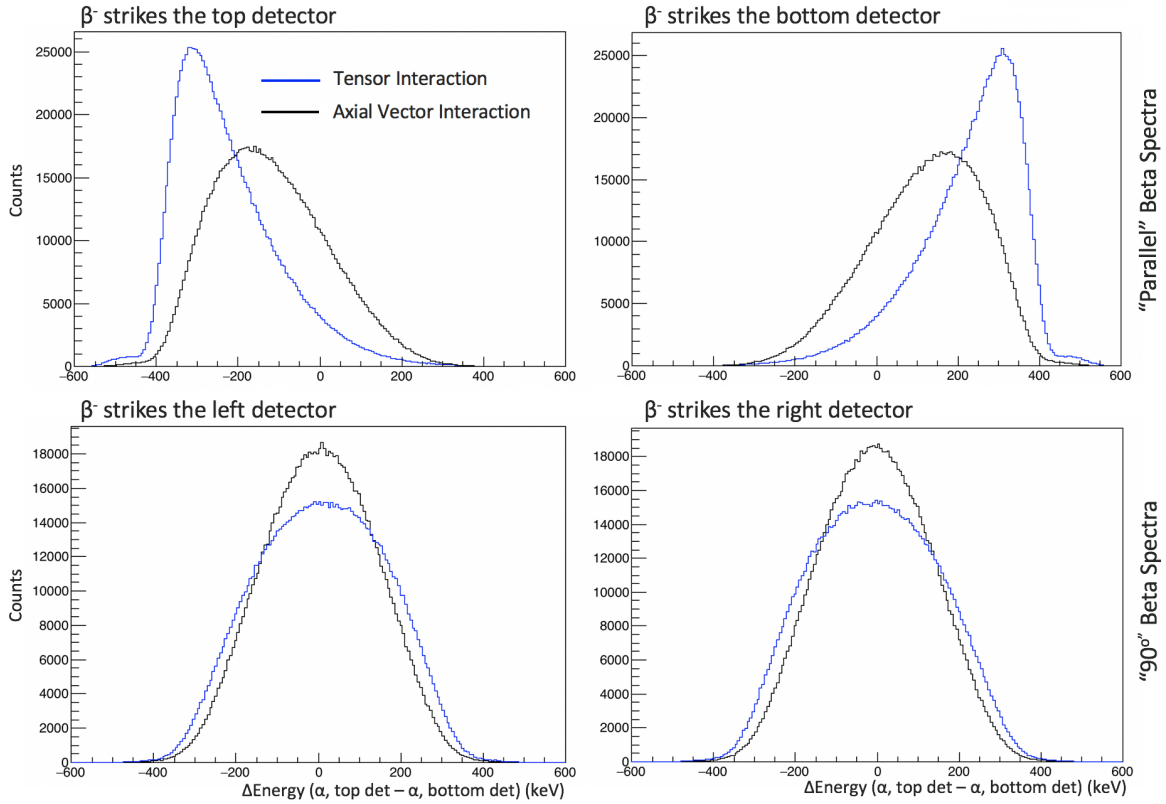

Figure 5.10: The four possible simulated alpha energy difference spectra for the top-bottom detector system to be used for comparison to the data. The blue lines represent what a pure tensor-interaction spectra would look like while the black represents a pure axial vector interaction.

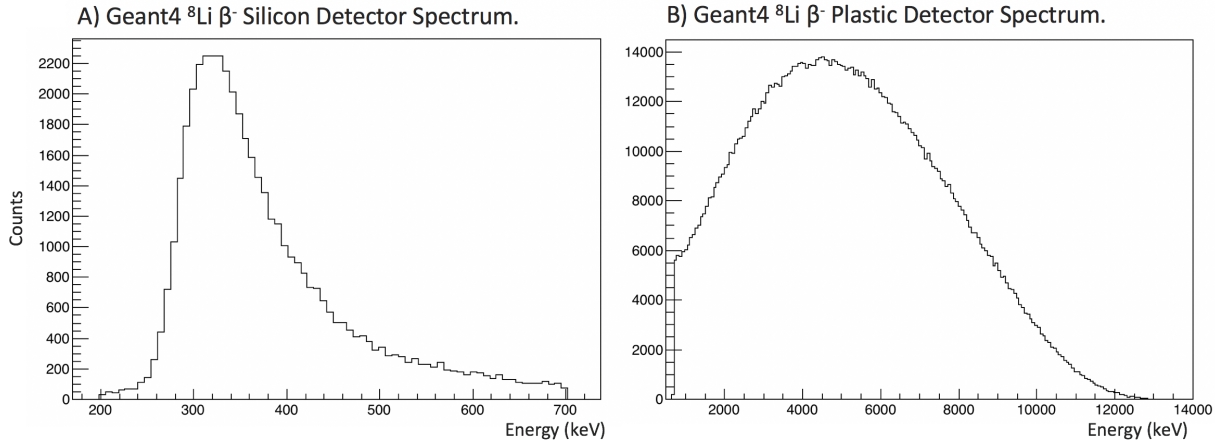

Figure 5.11: Geant4 simulated lithium-8 β^- spectra for A) a silicon detector and B) a plastic scintillator detector.

CHAPTER 6

RESULTS AND SYSTEMATICS

6.1 α Energy Difference Spectra

Once the data processing is complete and an accurate simulation has been assembled, the two can be compared to extract a value of $|C_T/C_A|^2$. As has been mentioned previously, we use only data where both ^{8}Be* α's and the ^{8}Li β are detected. In addition, we require that the β hits one of the same detectors as an α. Going by the rough weighting of the $\beta - \nu$ correlation, $W(\theta_{\beta\nu}) = 1 + a_{\beta\nu}(v/c)\cos(\theta_{\beta\nu})$, where $a_{\beta\nu} = -1/3(+1/3)$ for an axial-vector (tensor) interaction, it is clear that tensor interactions favor the β and $\bar{\nu}$ being emitted in the same direction. Intuitively, such an interaction would give an extra "kick" of momentum that would be very obvious in the α energies for events where the beta is measured to have gone in roughly the same direction as the α's. Furthermore, as was discussed in Appendix B.2, we gain a factor of 3 in sensitivity to $a_{\beta\nu}$ when we use this requirement.

Thus, we use the "parallel" β, α energy difference spectra from both the data and simulation to extract $a_{\beta\nu}$ via $|C_T/C_A|^2$. This process begins with fitting separate α energy difference spectra of pure tensor and pure axial vector simulated events to cubic splines. A linear combination of the resulting functions are then fit to spectra generated from the data: $(c_A\text{Spline}_A + c_T\text{Spline}_T)$ using ROOT's Minuit minimization package with the least squares method [53]. From the fit parameters c_A and c_T the $|C_T/C_A|^2$ value is calculated from $(c_T)/(c_A + c_T)$. More details can be found in Appendix B.

Examples of each of the possible parallel β, α energy difference spectra can be found in Figure 6.1. The detectors each of the particles were measured on are abbreviated as T (Top), B (Bottom), L (Left), and R (Right). The blue lines indicate what the pure tensor simulated spline would look like while the black line is the linear combination of interaction splines fit result. A table containing the extracted $|C_T/C_A|^2$'s and uncertainties is below.

Spectra	$\lvert C_T/C_A\rvert^2$	χ^2/NDF
$\alpha(T/B)\beta(T)$	-0.0104 ± 0.0026	1.13
$\alpha(T/B)\beta(B)$	0.0039 ± 0.0027	1.06
$\alpha(L/R)\beta(L)$	0.0092 ± 0.0030	1.16
$\alpha(L/R)\beta(R)$	-0.0116 ± 0.0029	1.29

Table 6.1: Fitted $|C_T/C_A|^2$'s for each parallel beta α energy difference spectrum.

The relatively large but reversed magnitudes of $|C_T/C_A|^2$ is attributed to a calibration offset between the two Left/Right detector spectra, likely due to the back face energies collected by the silicon detectors being slightly lower than their front counterparts. Due to issues with electronic noise, a substantial number of α events on the Left detector use the back energies. However, when the two spectra are summed together, the large $|C_T/C_A|^2$'s resulting from the offset cancel out and render the calibration offset a non-issue. This insensitivity has been corroborated by numerous systematic tests with the calibration. A similar argument can be made for the Top/Bottom detector system, though on a smaller scale.

In order to obtain a single fit and final statistical error, we can combine the four spectra in Figure 6.1 by reversing the α energy subtraction of two right-skewed spectra and adding each of the data and simulation spectra together before fitting to a spline. The individual simulation spectra are already intrinsically scaled to the data spectra, which is passed to the splines used to fit the total combined data. Figure 6.2 contains the combined spectrum with the fitting results. Despite attempting the analysis in multiple different ways and throughout the process of correcting errors, the inflection in the residuals at ∼-150 in Figure 6.2 has remained stubbornly resilient. Thus, the final statistical error has been inflated by $\sqrt{\chi^2_{red}}$ to account for the poor fit. The resulting fitted $|C_T/C_A|^2$ and adjusted statistical error are below.

$$|C_T/C_A|^2 = -0.0019 \pm 0.0016 \quad \text{or} \quad a_{\beta\nu} = -0.3346 \pm 0.0011 \tag{6.1}$$

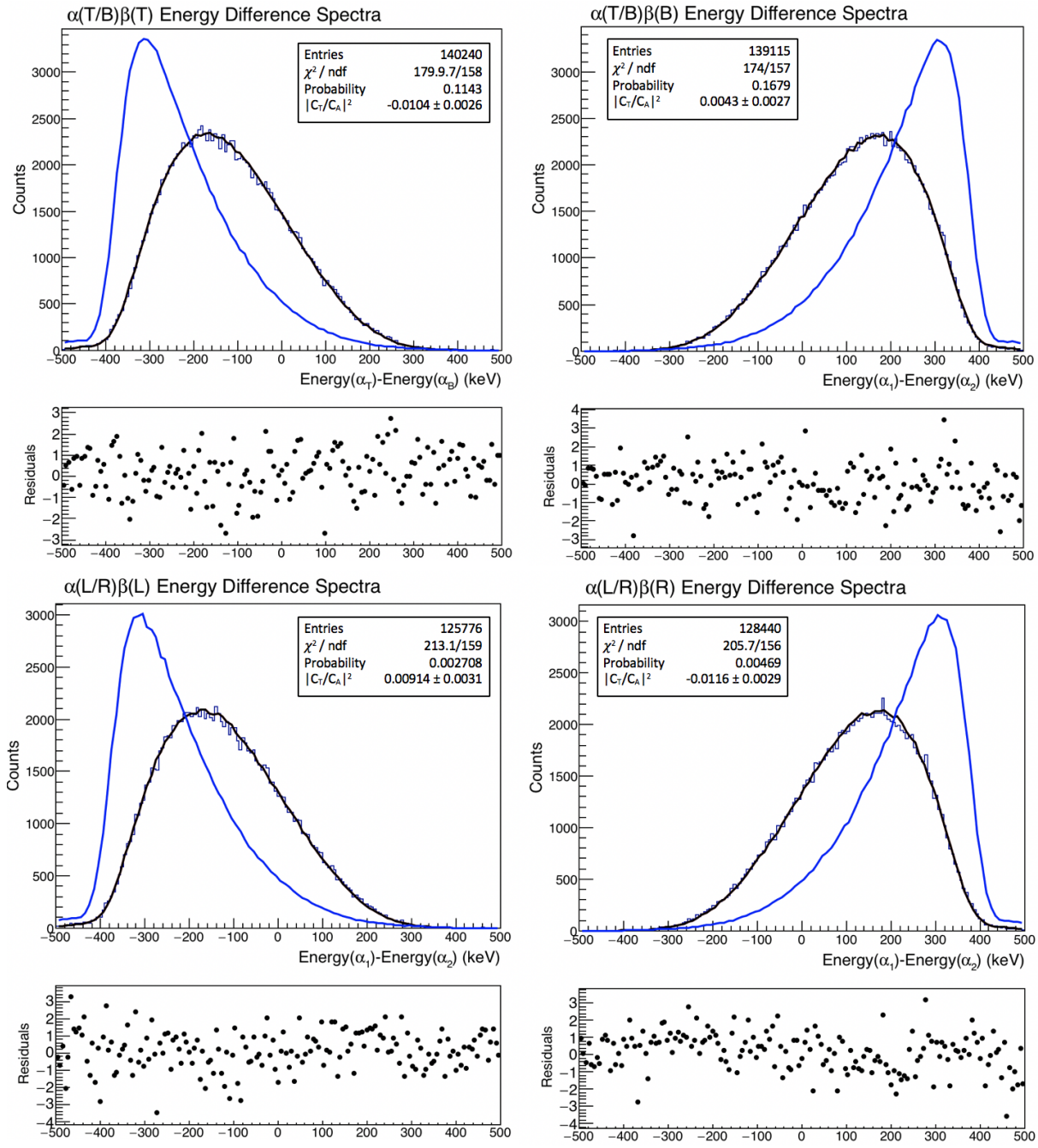

Figure 6.1: The four individual α energy difference spectra with the β's hitting one of the same detectors as the α. Also shown are the fits to simulation with the blue line as pure tensor example and the black line as a fit of both tensor and axial-vector interactions. The title abbreviations refer to the detectors that received the α's and the β.

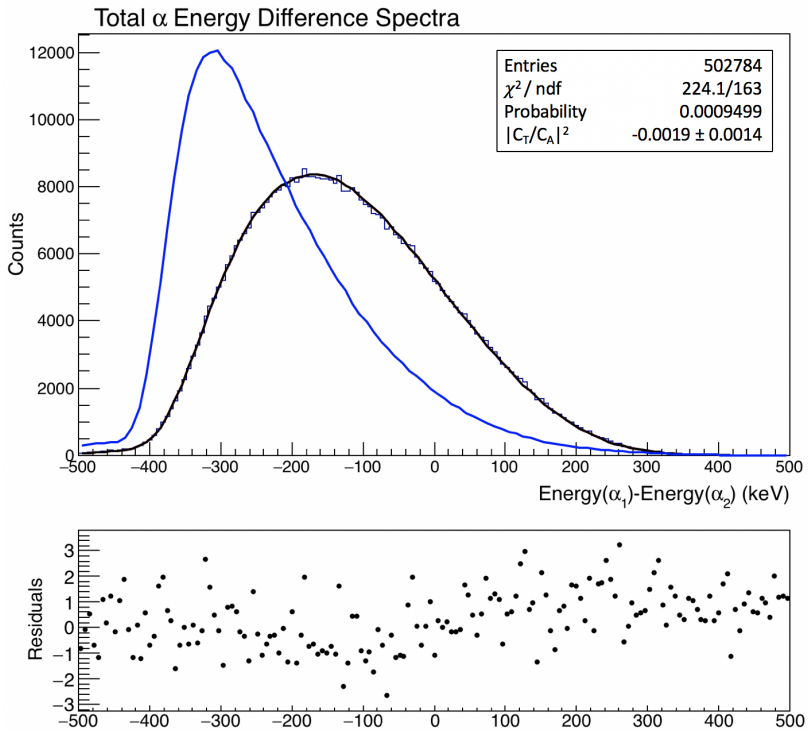

Figure 6.2: Combined spectra of the ones seen in the previous figure. The $\alpha(T/B)\beta(B)$ and $\alpha(L/R)\beta(R)$ spectra are added by reversing the energy difference from $\alpha_T - \alpha_B$ to $\alpha_B - \alpha_T$ and $\alpha_L - \alpha_R$ to $\alpha_R - \alpha_L$. The fitting results of this spectra define the total $|C_T/C_A|^2$ value along with the statistical error.

Finally, it is possible to perform a similar fit to the remaining triples: where the β did not hit the same detector as one of the α's. For completeness, the results are shown in Figure 6.3. The sensitivity to $a_{\beta\nu}$ is 4 times smaller than for the parallel β spectra. However, these spectra are useful to use as a cross-check for the quality of the simulation-data comparison and some systematics.

6.2 Systematics

Once a value of $|C_T/C_A|^2$ and a corresponding statistical uncertainty are defined, the systematic uncertainty must also be calculated. Everything that was used to create the calibration, process the data, construct each simulation, and account for the various physical attributes of the trap comes with its own uncertainty that factors into the final systematic error bar.

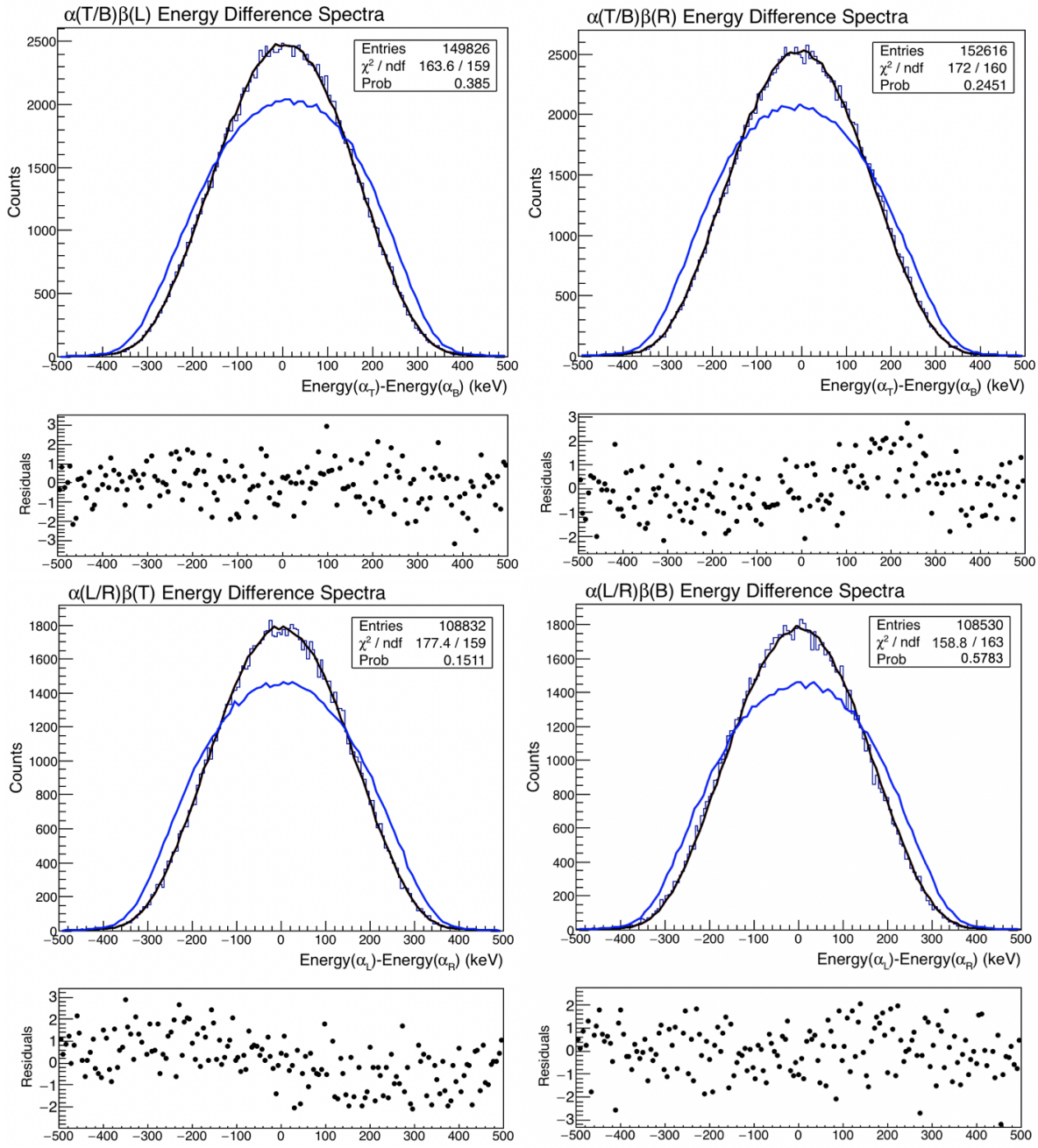

Figure 6.3: The four individual α energy difference spectra with the β's hitting either of the detectors not struck by an α. Also shown are the fits to simulation with the blue line as pure tensor example and the black line as a fit of both tensor and axial-vector interactions. The title abbreviations refer to the detectors that received the α's and the β. Though these spectra are not useful for determining $|C_T/C_A|^2$, they are a good check of the integrity of the spectra and simulation fits.

All known contributions to the systematic uncertainty of this experiment are covered in the remaining sections of this chapter, with a table summarizing the results at the end.

6.2.1 Calibration

The calibration systematic uncertainty was taken into account on a strip-by-strip basis. As each of the silicon front strips and back strips have their own independent quadratic calibration with independent errors on all three of the peak reference points, it was deemed unrealistic to require all strips to have the same error offsets across an entire detector or detectors. Other effects on the calibration, such as the dead layer estimate and other energy corrections are collected in a separate systematic uncertainty in the next section. As such, the calibration systematic error specifically corresponding to the fitting and statistical uncertainty was calculated by generating 5 alternate sets of calibrations for each of the 16 time segments. These alternate sets contained calibration values that were created by generating random, Gaussian distributed numbers with the center at each original calibration value (a, b, and c from $Energy = a+b(Channels)+c(Channels)^2$ with a σ corresponding to the fitted statistical uncertainty on each calibration parameter. These adjusted calibrations were then applied back to the data. Each set produced a shift in $|C_T/C_A|^2$ compared to a fit using the original calibrated data, which are listed in the table below. To err on the conservative side, the maximum absolute value of $\Delta|C_T/C_A|^2$ was taken as the total systematic error contributed by the calibration. Though not listed in the table, the Top/Bottom system produced a calibration $\Delta|C_T/C_A|^2$ of 5×10^{-5} and the Left/Right system, 4×10^{-4}. The Left/Right system was much more noisy than the Top/Bottom system, which contributed to higher uncertainties in each of the strip calibrations. Fit together, the maximum $\Delta|C_T/C_A|^2$ was 1.4×10^{-4}.

Calibration Set	$\Delta\lvert C_T/C_A\rvert^2$
1	3.0×10^{-5}
2	-1.0×10^{-4}
3	6.0×10^{-5}
4	-1.6×10^{-5}
5	-1.3×10^{-4}

Table 6.2: $\Delta|C_T/C_A|^2$'s for 5 different randomly generated calibration sets based on the strip-by-strip error of each quadratic term.

6.2.2 α Energy Adjustments

Some adjustments are applied to each α energy in the calibration based on real effects from the silicon detectors and then subtracted again after the calibration to return the α energy to its value when it was emitted from the ^{8}Be*. These corrections include the normal dead layer, the pulse height defect and the nonionizing energy loss. More details on the nature of the effects can be found in Chapter 4. These corrections are applied collectively to all the data instead of strip-by-strip like the calibration itself, which was covered in the previous section. The systematic uncertainties introduced by each adjustment are covered in the subsequent subsections with the normal dead layer being the largest contribution. The combined uncertainty of the three effects is 1.17×10^{-3}.

Normal Dead Layer

The normal dead layer[1] systematic was calculated by applying a combined (Top/Bottom and Left/Right) 1σ shift in normal dead layer thickness for each of the possible combinations and simply taking the maximum of the resulting $\Delta|C_T/C_A|^2$'s. The 1σ shifts were applied both to the calibration and the energy adjustment made to the α energies after in order

1. The ∼100 nm-thick layer of inactive silicon which covers about 96% of the surface of our DSSD's. The extra dead layer covers about 3% of the DSSD surface and is located on the edges of each strip

to maximize accuracy. The possible shift combinations for each detector set (with "D1" referring to the Top/Left detector and "D2" to the Bottom/Right detector) are: both D1 and D2 shifted up 1σ in thickness, both D1 and D2 shifted down, D1 shifted up with D2 shifted down, and D1 shifted down with D2 shifted up. Each of these combinations must be applied to both detector systems, for a total of sixteen permutations. The weighted uncertainty for the detector normal dead layers was $\sigma = 3.5$ nm. The $\Delta|C_T/C_A|^2$ results for each permutation can be found in the table below, with each detector abbreviated by its first letter. The final normal dead layer systematic uncertainty was taken from the permutation where all the detectors were given a normal dead layer thickness 1σ more than was measured, which produced a $\Delta|C_T/C_A|^2$ of 1.08×10^{-3} (listed in bold on the table).

	T↑B↑	T↑B↓	T↓B↑	T↓B↓
L↑R↑	$\mathbf{1.08 \times 10^{-3}}$	6.3×10^{-4}	6.1×10^{-4}	2.1×10^{-4}
L↑R↓	4.6×10^{-4}	3×10^{-5}	-5×10^{-6}	-4.4×10^{-4}
L↓R↑	3.9×10^{-4}	-6×10^{-5}	-8×10^{-5}	-5.0×10^{-4}
L↓R↓	-1.6×10^{-4}	-6.3×10^{-4}	-6.3×10^{-4}	-1.04×10^{-3}

Table 6.3: $\Delta|C_T/C_A|^2$'s for all possible combinations of normal dead layer shifts of 1σ for each of the detectors.

Pulse Height Defect

The pulse height defect was originally modeled by Lennard et al. [63] and defines the nonlinearity between the number of electron-hole pairs created by an incident α (and other heavy particles) in a silicon detector vs the α's energy. Lennard's model was confirmed in the same paper [63] for ^{1}H, ^{4}He, ^{7}Li and ^{16}0, and then again by Bauer et. al for electrons and α's at using multiple methods at various energies [11] Everything agreed to within statistical uncertainty and both experiments were able to determine a value of k from their data. Many experiments that utilize silicon-detector energy measurements have since used the pulse height defect model to successfully calibrate their data. The function itself (equation 4.1)

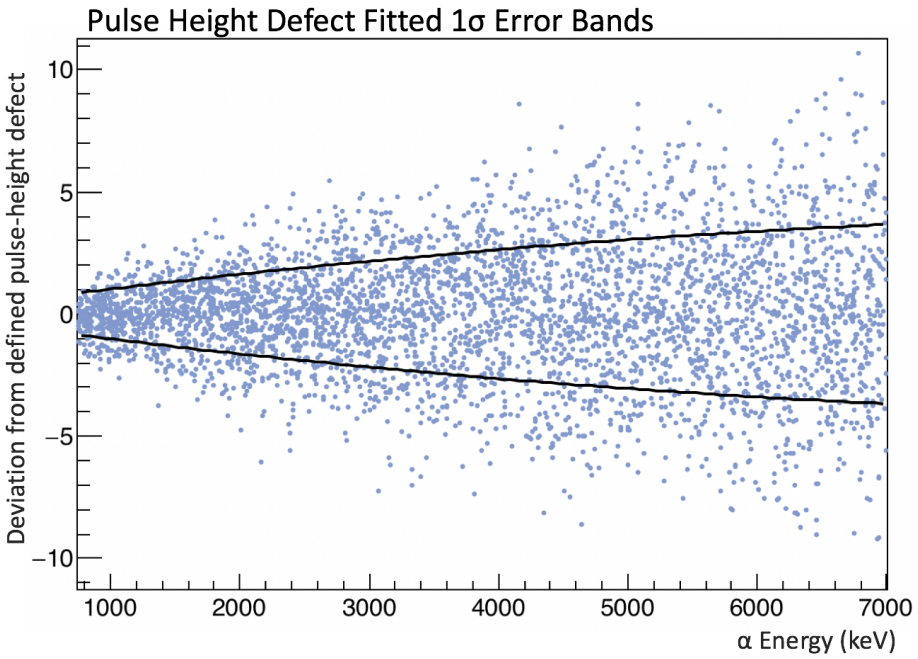

Figure 6.4: Randomly generated pulse height defect deviations in keV using Gaussian distributions of each measured parameter defined by the corresponding error (blue dots). The uncertainty was defined by the 1σ fitted error bands (black)

requires the input of three parameters: k, ϵ, and the stopping power of an α in silicon. The stopping powers are already well-established by SRIM/TRIM with uncertainties of $\sim$3.5% for α's in silicon at our energy range [111]. Thus, the pulse height defect errors are dominated by the uncertainties on k and ϵ_0. Thus far, the best measurement of k was done by Bauer et. al. [11] with $k = (2.8 \pm 0.3) \times 10^{-4}$ nm/electron-hole pair. The measurement currently used for ϵ is 3.67 $\pm$ 0.02 eV from [77]. A distribution of 100,000 randomly generated pulse height defect points with the standard deviations of each measured factor taken into account was fit to an upper and lower sigma band to define the error functions as seen in Figure 6.4. The uncertainty of the pulse height defect ranges from about 1 keV at the lowest ^{8}Li α energies to 4 keV at the highest energies. Applying each of the error-band functions to the calibration and then the data resulted in an average $\Delta|C_T/C_A|^2$ of 4.3×10^{-4}.

Nonionizing Energy Loss

The nonionizing energy loss function was taken from a series of TRIM simulations of energy lost to recoiling atoms at energies from 700 to 7000 keV in increments of 100 keV. Each energy loss distribution was fit to a f-distribution to find the maximum. The error for each fit was about 1% of the maximum value. Similarly, the discrepancy in maximum value between the most accurate full cascade TRIM calculation vs the faster Kinchin-Pease [57] analytic solution was about 2%. Combined with fluctuations when fitting to a polynomial function, a very conservative 5% estimated error for the nonionizing energy loss adjustment was applied to the data with a resulting $\Delta|C_T/C_A|^2$ of 1.6×10^{-4}.

6.2.3 Energy Cuts

A number of cuts are applied to the data in order to decrease the level of background and address potential systematics. The cuts themselves are listed in section 4.5.2. Many of them, such as the cut on the difference in strip number and the time since injection introduce no systematic errors by adjusting the threshold within an appropriate range. However, the energy threshold cuts on the α and β energies with the energy cut between the front and back face of the detectors both reduce systematic errors in terms of background and noise, but also can introduce their own systematic errors if $|C_T/C_A|^2$ changes depending on where the cuts are placed.

Based on the Geant4 simulation, the α energy spectrum extends from $\sim$ 400 keV to $\sim$ 7800 keV and the β DSSD energy spectra, from just above 0 keV to over 3000 keV. We set a lower threshold of 200 keV for the β spectrum, with a 700 keV upper threshold for the data we use. Similarly, the lower and upper energy thresholds we set for our α data are 700 keV and 7000 keV. Adjusting the 700 keV threshold between α's and β's 200 keV higher (where there are roughly half as many β's as there are at 700 keV) resulted in a $\Delta|C_T/C_A|^2$ of 7.7×10^{-4} and adjusting the 700 keV threshold lower by 100 keV (half as many α's as there are at 700 keV) produced a $\Delta|C_T/C_A|^2$ of 9.8×10^{-4}. The 200 keV β

threshold is in an optimal spot to within 100 keV, so will not be adjusted for a $\Delta|C_T/C_A|^2$. 200 keV is positioned at another relative minimum, where going any lower will result in noise contributing false events. $\sim$300 keV is where the peak of the nonionizing energy loss spectrum is located. For the upper α energy threshold, removing it completely only returns less than 10 additional events and moving it lower by 500 keV similarly does nothing to $|C_T/C_A|^2$.

As is pictured back in Figure 4.19, the vast majority of α events have measured DSSD front and back energies within 50 keV of each other (with the exception of a tail where poorly reconstructed back strip events are lower in energy than their front counterparts). A 60 keV difference threshold was chosen based on a χ^2 minimization calculation of the triples α distribution across the face of the detector compared to simulation vs the cut threshold. The difference between the measured front and back energies distribution for the β is effectively the same as the α spectrum (this time with a 110 keV difference threshold also applied based on a similar calculation), except with tails on both sides of the distribution, since both front and back strips are used to reconstruct events, (again, sometimes poorly). Changing these two thresholds (independently) by 15 keV (a $\sim$1% increase in the χ^2) produced an average $\Delta|C_T/C_A|^2$ of 5.5×10^{-4} for the α's and 7.2×10^{-4} for the β's. Adding all these contributions in quadrature results in a total energy cut systematic uncertainty of 1.25×10^{-3}.

6.2.4 Background

Over the course of an experiment, the BPT operates on a cycling basis. Ion bunches are injected from the APT every 200 ms a number of times and eventually the entire cloud is ejected from the trap. After the ejection, the BPT sits idle for some amount of time before ions are again injected. During this trap-empty period, any triple coincidences that are measured and make it past cuts must be a result of untrapped ^{8}Li, which can seriously impact the integrity of the $a_{\beta\nu}$ measurement. Though it is difficult to foresee where such events would originate, the most logical guess for an untrapped event that would pass the

applicable cuts would be one where an ^{8}Li ion is implanted on one of the silicon detectors, thus the actual α energy difference and β direction would not be severely impacted. Other potential background events, such as where a lithium-8 ion might be stuck to an electrode, would most likely not pass the α double-event criteria and then, would be even less likely to pass the strip difference cut.

However, for the 2015 PRL experiment, the trap was mistakenly left empty for too short a time per cycle (120 ms), which meant a reliable limit on the number of untrapped ^{8}Li measured over the course of the experiment could not be defined. An upper limit of 230 triple events from decays via untrapped ions was estimated with a potential $\Delta|C_T/C_A|^2$ of 1.1×10^{-3}. For the August 2016 experiment, the trap-empty cycling time was increased to 800 ms (see Figure 6.5). During this time, a total of 29 triple coincidences were measured (after cuts), which scales to 451 ± 84 over the course of the entire run. Compared to the total number of triple coincidences that were available to use after cuts (both 90^o and parallel β's: $1.1{\times}10^6$ events), this estimate amounts to about 0.04% of the total events, an order of magnitude less than the 2015 PRL estimate and below the sensitivity of this experiment. Thus, the background systematic error is eliminated for this work.

Though it does not impact the systematic errors, there are several other sources of background, namely, random single ^{8}Li α's and β's in coincidence with either calibration source α's or non-^{8}Li β's. The most likely combination of background is a random β in coincidence with two ^{8}Li α's. It is estimated that about 800 of these events were detected over the course of the entire run, which, when scaled by the number of double events, is $3\times$ less than what was measured in the previous ^{8}Li experiment. The background had no noticeable effect on $|C_T/C_A|^2$ when simulated on a larger scale in the previous experiment, so a similar negligible effect is inferred for this one.

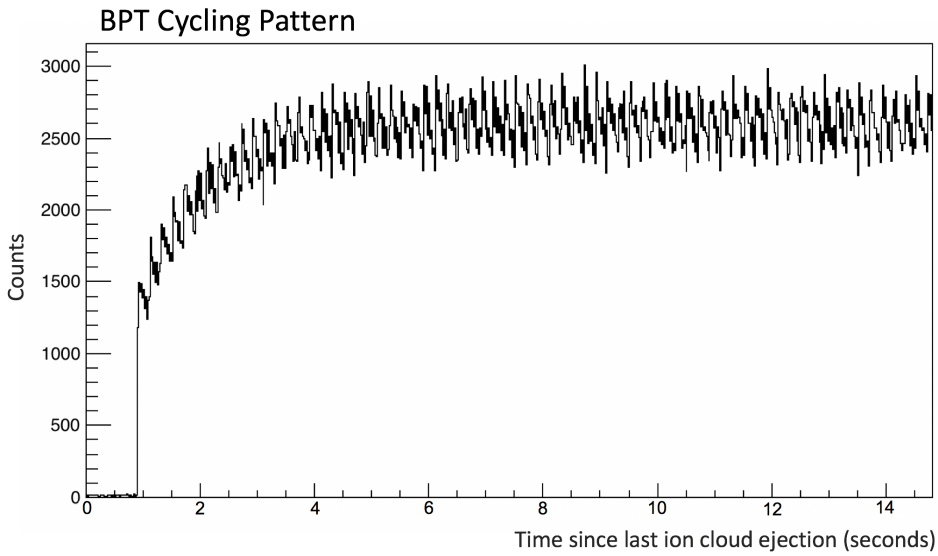

Figure 6.5: The number of triples measured over the course of the August 2016 experiment as a function of the time since the ion cloud was ejected. The cycle begins with 800 ms of background measurement and is followed by 70 ion bunch injections (small peaks) with 200 ms in between each injection. On a larger scale, the number of decays as a function of the total cycle time increases until the half-life of ^{8}Li ($\sim$840 ms) causes the decay rate to level out.

6.2.5 Final State Distribution

The ^{8}Be* Final State Distribution used to sample the excitation energy for our Event Generator is a key component when determining both of the resulting α energies. If there is a discrepancy in the shape of the α energy spectrum between simulation and data, that error can propagate to the actual α energy difference spectra used for determining $a_{\beta\nu}$, particularly if the discrepancy is where the slope is the steepest, close to the peak. The α energy spectrum from ^{8}Li can be seen in Figure 6.6. Currently, we are using a FSD that was created by shifting the R-matrix peak position fitting parameter ($\mathcal{E}_1$) from the 2006 Bhattacharya, M. et. al. paper [12] 12 keV lower to match what the data shows (red curve vs blue curve in Figure 6.6). Given that the $\mathcal{E}_1$ parameter error in [12] has an uncertainty of 10 keV, using a shifted FSD is not unreasonable. Currently in process via one of our collaborators (Dr. Tsviki Hirsh), is a full R-Matrix fit to this high-statistics ^{8}Li data, which will give an even more accurate FSD. In parallel, the uncertainty on $\mathcal{E}_1$ for fits Dr. Hirsh has already

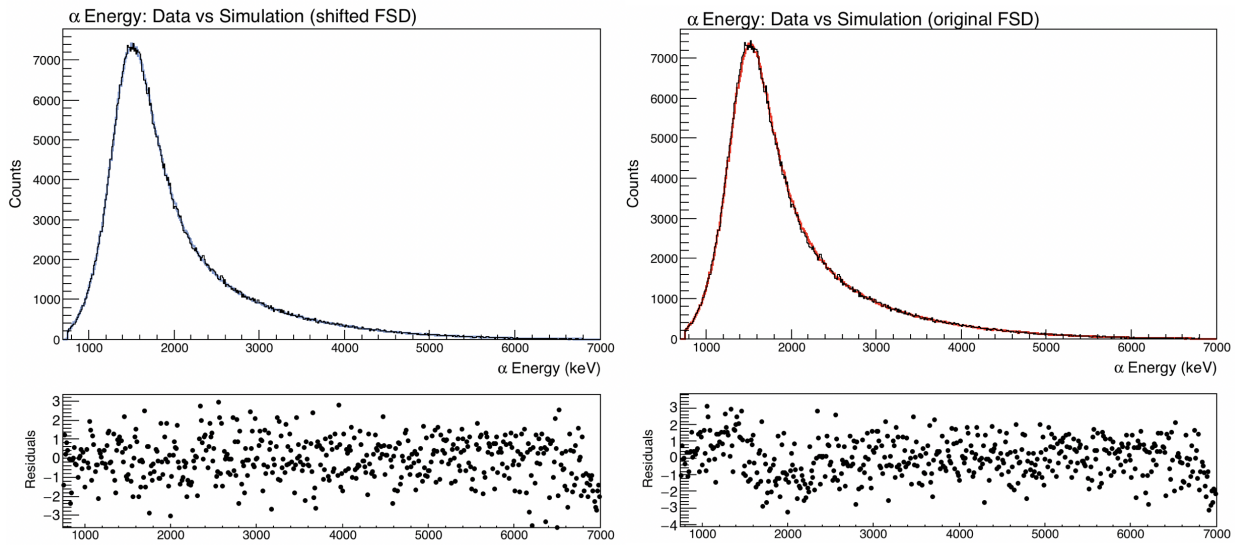

Figure 6.6: Comparison between the Top Detector single α energy spectrum (triple events, black curve) to a simulated one: blue for the $\mathcal{E}_1$-shifted FSD, and red for the original Bhattacharya, M. et al. FSD [12]. The shifted FSD residuals indicate a close match with the data.

done to the ^{8}B data set taken in 2014 (which is 10$\times$ smaller than the 2016 ^{8}Li data set) are already a factor of two smaller than the fit uncertainties from the 2006 R-matrix fit. When the new ^{8}Li FSD R-Matrix fit becomes available, this systematic will be calculated using the uncertainties from the resulting parameters. However, for now, the $\Delta|C_T/C_A|^2$ from changing between the original 2006l FSD and our current, shifted one, is 8×10^{-4}, which is not a substantial amount for so large a shift in $\mathcal{E}_1$. Until the new FSD is finished and can be tested properly for its uncertainty, we will neglect the FSD systematic error.

6.2.6 Radiative Corrections and Recoil Order Terms

The ^{8}Li decay rate within the Event Generator comes with its own set of error contributions. In Holstein's decay rate expansion for a normal decay, there are several experimentally measured terms, second class currents, and form factors, each with their own uncertainties that must be taken into account. A complete list of these terms and (when available) their error bars can be found in Appendix B. Furthermore, when applying the decay rate for the bremsstrahlung radiation, the expansion that Glück provides [37] does not take into

account the delayed alpha emission of ^{8}Be*. This incomplete expansion also introduces some uncertainty.

The terms that primarily contribute to the uncertainty in the Holstein expansion are the second-forbidden form factors in the axial vector current (j_2 and j_3), the weak magnetism term (b), the induced tensor current (d, a result of the delayed α strong force and separate from what we are measuring) and the second-forbidden form factors in the vector current (f and g). Most of these terms were measured experimentally in the mass-8 system by Sumikama, T et. al. [97]. Their effects on $|C_T/C_A|^2$ were determined by running two simulations (with 80× the number of triples in the data) for each term: shifted $+1\sigma$ and -1σ from the original value. These simulations were in turn compared to the $|C_T/C_A|^2$ measured by a simulation with no shifts of the same size. The simulations for f and g were combined into one because g is calculated from f $\left(g = -\sqrt{2/3}(2Mf/E_0)\right)$, where E_0 is the endpoint energy of the β and M is the reduced mass of the ^{8}Li and ^{8}Be* [69]). The resulting $\Delta|C_T/C_A|^2$'s of these simulations are shown in the table below. The induced pseudoscalar form factor (h) and the ^{8}Li nuclear radius shifts to $|C_T/C_A|^2$ were not simulated because their total effect on the decay rate expansion is below our sensitivity ($\leq 0.001\%$).

2nd-class currents & form factors	Value	$\Delta\|C_T/C_A\|^2$
Weak magnetism term, b	60.3 ± 1.5	5.9×10^{-4}
Induced tensor current, d	40 ± 14	1.22×10^{-3}
2nd-forbidden A form factor, j_2	-31000 ± 4000	4.7×10^{-4}
2nd-forbidden A form factor, j_3	-63000 ± 18000	3.01×10^{-3}
2nd-forbidden V form factor, f	8 ± 2.4	5.3×10^{-4}
Total	-	$\mathbf{3.30 \times 10^{-3}}$

Table 6.4: $\Delta|C_T/C_A|^2$'s corresponding to the uncertainty of all non-negligible decay rate recoil order terms.

The largest recoil-order term contributors to the systematic error are clearly j_3 and d. If

one references the decay-rate expansion in Appendix B, the reader will quickly notice that j_3 and d are well-separated in all the g_i terms that they appear in, thus suggesting that they are not correlated. The most likely terms to be correlated are b and d, and then j_2 and j_3. However, since the systematic error contributions of both b and j_2 are 5-6$\times$ smaller than j_3, no simulations were attempted to establish the extent of their correlation on $\Delta|C_T/C_A|^2$.

A full explanation of our treatment of the hard bremsstrahlung radiation in the decay rate can be found in Appendix B. However, in order to account for the $\alpha-\beta-\bar{\nu}$ correlation, the $g_3 - g_{15}$ terms from the Holstein expansion are scaled to the Glück expansion using the leading order terms (g_1) from each rate. This pseudo-decay rate is most likely a mistreatment of what the actual expansion would look like. In order to take into account the resulting uncertainty, a simulation with the explicit Glück rate without the $\alpha - \beta - \bar{\nu}$ correlation was compared to a simulation with the hard bremsstrahlung pseudo-decay rate (the one we normally use, both with $\sim$80$\times$ the number of data triples). The $|C_T/C_A|^2$ difference between the two was 6.0×10^{-4} and is added in quadrature with the total second class current uncertainty to obtain a final radiative and recoil uncertainty of 3.36×10^{-3}. The relatively small error contribution from the hard bremsstrahlung treatment can be attributed to the emitted photon having no effect on the recoiling ^{8}Be* nucleus and the majority of photons having low-energy with a preferred emitted direction in line with the direction the β is already going.

6.2.7 α Silicon Detector Lineshape

The simulated silicon detector lineshape systematic error was calculated by running a 100 million triple simulation with no lineshape applied in the Event Generator. The results of the simulation were then run through a post-processing lineshape application identical to the one used in the Event Generator before having cuts applied. This allowed us to compare a variety of lineshape adjustments very quickly. A "normal" lineshape with no errors applied was run 20 times in order to establish a clear center of the original $|C_T/C_A|^2$ distribution.

The resulting center was then compared to the simulation results with lineshapes containing either $+1\sigma$ or -1σ errors of all applicable uncertainty contributions. The average absolute value of $\Delta|C_T/C_A|^2$ from the $\pm1\sigma$ shifted lineshape was taken as the partial error for each contribution. The total uncertainty was calculated by summing all the partial errors in quadrature. Results from each lineshape uncertainty and the total are shown in the table below.

Detector Lineshape Uncertainty	$\Delta\|C_T/C_A\|^2$
Electronic noise	6.7×10^{-5}
Fano factor resolution	1.2×10^{-4}
Nonionizing energy loss fit	4.2×10^{-5}
Extra dead layer percentage	7.8×10^{-5}
Extra dead layer thickness	5.6×10^{-4}
Normal dead layer thickness	2.3×10^{-4}
Total	$\mathbf{6.3 \times 10^{-4}}$

Table 6.5: $\Delta|C_T/C_A|^2$'s for the uncertainty corresponding to each component of the α DSSD lineshape in the event generator.

The electronic noise $\Delta|C_T/C_A|^2$ was obtained by running 5 lineshape simulations, each with an independent set of files that describe the electronic noise of each strip. The five sets of noise files were generated by adding a random Gaussian-distributed number (centered at 0, with 1σ being the electronic noise error for each strip) to each strip's electronic noise. The absolute value of the average of the 5 $\Delta|C_T/C_A|^2$'s was taken as the electronic noise error contribution.

Taking into account the error on each term in the Fano factor resolution calculation (w, E_α, and F from equation 5.4), it was found that the error of the measured Fano factor itself (F) dominated the other uncertainties. The total error on the Fano factor resolution σ was calculated to be 0.25 keV [92], which was in turn applied to two separate lineshape simulations ($\pm\sigma$)

The nonionizing energy loss error was calculated using the fitting errors of the "X" scaling factor from the F-Distribution fit (equation 5.3). The "Y" scaling factor errors were found to be negligible and were ignored. A $\pm\sigma$ function for the "X" scaling factor was calculated by randomly generating points along the quadratic fit to the "X" scaling factor's α energy dependence with the $+1\sigma$ and then -1σ uncertainty applied. Assuming a Gaussian distribution about the center of the quadratic, the $\pm1\sigma$ were fit to similar quadratics and applied to the lineshape simulation separately.

Each of the dead layer errors were taken into account by applying $\pm\sigma$ to both the Top and Left detectors and then separately applying $\pm\sigma$ to the Bottom and Right detectors. Again, the resulting absolute value average of $\Delta|C_T/C_A|^2$ was taken as the uncertainty contribution.

6.2.8 β-Scattering

According to our simulations, about 20% of the ^{8}Li β's that we measure as triple events are a result of scattering and therefore must be very accurately simulated in order to make a valid comparison to data. The integrity of our Geant4 β scattering simulation has already been briefly covered in sections 5.2.3 and 4.3. To recap, after using cosmic muons to perform a calibration of the top and bottom detector, the resulting ^{8}Li β spectra closely matched the Geant4 simulated ^{8}Li β spectra for the DSSD's (see Figure 4.9). Thus, the matching data and simulated β spectra were used as a low-energy calibration point for all strips. In addition, the more robust scattering benchmark fractions: the triples fraction and backscattered fraction match within 1σ uncertainty even with such high statistics (1σ is 0.4% for the triples fraction and 16% for the backscattered fraction, see section 5.2.3). Finally, the ^{8}Li β hitmap across the pixels of each silicon detector (in comparison to simulation) is also a good gauge for Geant4's accuracy. The results of such a comparison can be seen in Figure 6.7. Though there is slightly more simulated β's on the low front strip vs high front strip side on each detector, the statistical error of each bin is on the order of 5% of the bin's total contents ($\sim$16 counts),

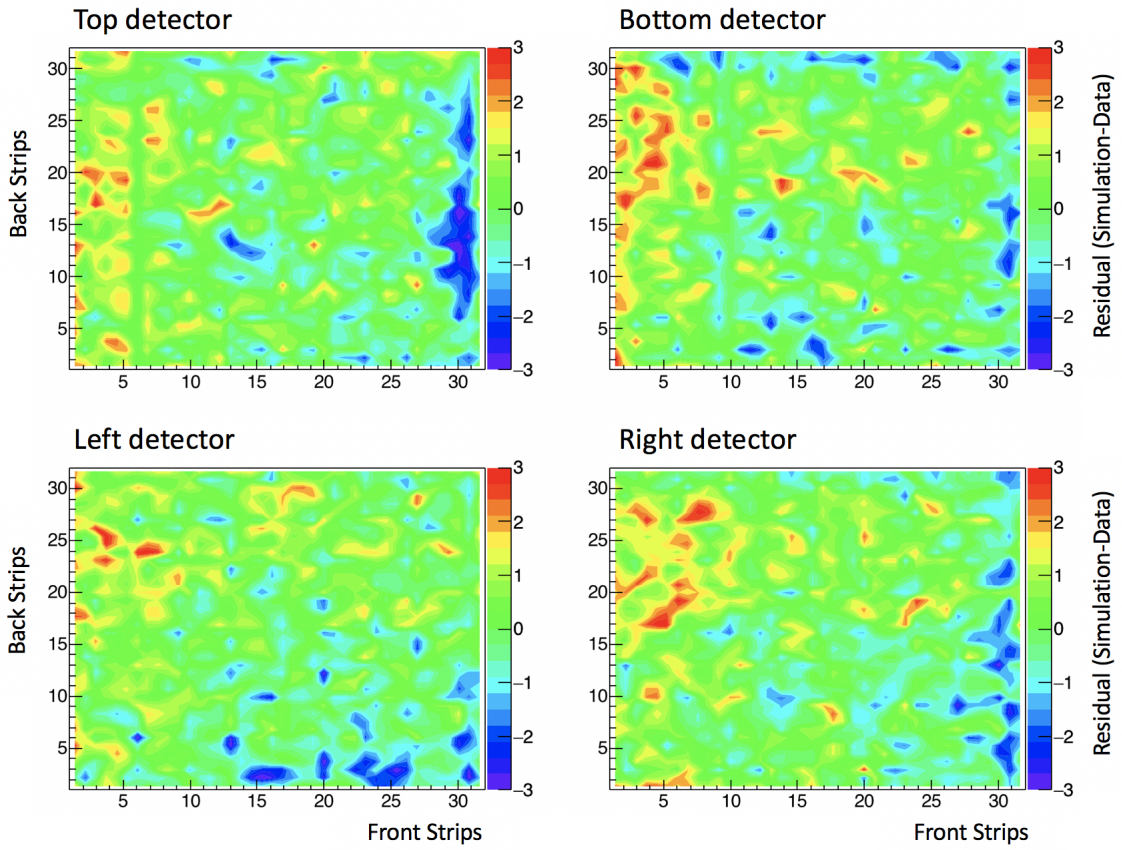

Figure 6.7: The residual differences (measured in 1σ) between the beta distributions across each detector face for simulation and data.

which is a trivial percentage when scaled to the total number of events. It is also very likely that the calibration may be the cause of the discrepancy rather than the scattering. Edge strips are not well-illuminated by the calibration α sources, which often produces a poor calibration and in turn may not match well to the opposite face measurement, resulting in lost events. In order to calculate the β scattering systematic error and in turn take into account the discrepancy described above, a set of randomly collected scattered events corresponding to the magnitude of a 1σ shift from the triples fraction (taken from the data) were removed and then separately added (from a different simulation). This process was also performed for 2σ and 3σ shifts. The resulting changes in the tensor fractions indicated that adding up to 3σ worth of extra random scattering events did not change $|C_T/C_A|^2$ more than 1×10^{-4}. Taking away scattered events did have a noticeable effect, which increased with

each additional σ. When 3σ's worth of scattered events ($\sim$1.5% of the total number of triples and 7.5% of the scattered events) was removed, the $|C_T/C_A|^2$ shift was 5.0×10^{-4}, which we will take as a conservative estimate for the systematic error contributed by β scattering.

6.2.9 Miscellaneous

Though there are undoubtedly more small effects on the sensitivity of this measurement, the most significant known systematics have been covered already in this chapter. However, there are several other real effects that do not affect the current $\beta - \nu$ correlation measurement that are worth mentioning for the purposes of future experiment and completeness.

Ion Cloud Size and Location

One key component of the ion trapping that later must be incorporated into the simulation is the ion cloud size and position. These quantities can be very accurately determined using the difference in strip number between the two ^{8}Li α's. An example of a strip difference spectrum is in Figure 4.19. For this experiment, the ion cloud size (FWHM) was determined within 0.01 mm to be 1.28, 1.26, and 1.96 mm for the radial (x,y) and axial (z) directions, respectively. The corresponding ion cloud center (within 0.001 mm) is 0.053, 0.031, and 0.331 mm in the same order of directions. Both the widths and center are stable to within 4% across the 70 ion injections per cycle.

In the previous ^{8}Li experiment, no impact on $|C_T/C_A|^2$ whatsoever was observed between changing the FWHM of the entire cloud size from 0 to 3 mm (in 0.2 mm steps). A similarly robust study was not attempted for this experiment due to the heightened cost of computation that comes with having more statistics, but no statistically significant change in $|C_T/C_A|^2$ was found when compared to an 80 million triple simulation with ion cloud size (FWHM) of 3 mm. This phenomenon is in part because no cuts requiring the kinematics to make sense is applied to the α energy difference spectra. When we do use our full kinematic data either to determine some of the recoil order terms or make a separate measurement

of $a_{\beta\nu}$, the ion cloud size and position will then become highly sensitive parameters with corresponding systematic uncertainties.

Magnetic Field

Due to the close proximity of the APT, which requires a superconducting magnet to operate, there is a ∼20 Gauss magnetic field aligned along the axis of the BPT that has a very slight effect on the trajectory of the ^{8}Li decay products, particularly the β. At its lowest possible energy (∼1.5 MeV), the β could potentially be displaced about 0.7 mm across the face of the detector. However, this potential effect decreases to 0.2 mm at the 5 MeV β energy peak and continues lower as the β energy increases. Given that our strips are only 2 mm across and the α energy difference $|C_T/C_A|^2$ is not impacted at all by the ion cloud size, this particular contribution to the particle trajectories can for now be ignored. For further studies to determine any recoil order terms or $a_{\beta\nu}$ from the kinematic reconstruction, the effects of the magnetic field will need to be simulated. The trajectory impact on the α's would be $\sim 10\times$ smaller, due to their higher mass-to-charge ratio.

RF Field and Thermal Energy

It is estimated that the RF amplitude was about 400 V_{pp} during this experiment, which implies that even if the α's carried +2 charge, the most energy they could collect from the RF field would still be less than a keV. The same argument applies for a β particle. In addition, it is worth noting that the thermal energy carried by the trapped ^{8}Li ions is on the order of 10 meV, which is far below our level of sensitivity. Thus, the thermal energy of ^{8}Li and the RF field contributions to our systematic uncertainty can also be neglected.

Channeling

Briefly touched on in section 6.2.7, channeling is when a particle, (in this case, an α particle) passes through an axis of the silicon crystal that contains less electron density, and thus deposits less energy in a small percentage of events at certain incident angles. Since all α particles are fully stopped by the 1 mm-thick silicon detectors in this experiment, the only potential source of bias would be if less energy were lost in the normal dead layer. However, a thorough examination of the mono-energetic gadolinium-148 α peak on every single pixel ($\sim$2 degree angle change across a single pixel) on each detector revealed no additional higher energy peak structure that would be associated with a percentage of the α's channeling through the normal dead layer. The incident angles of the lithium-8 α's span 0 to about 35 degrees, while the incident angles from the sources span 14 to 35 degrees. Thus, with a large fraction of the non-perpendicular angles revealing no signs of channeling, it is reasonable to assume that if channeling is occurring, it is not something we are sensitive to. The lack of channeling could be attributed to a high concentration of aluminum doping within the silicon of the normal dead layer.

6.3 Summary

A compilation of all the non-negligible systematic uncertainties discussed in this chapter can be found in Table 6.6 at a 1σ confidence level. The total systematic error was calculated by adding all the individual errors in quadrature, since the six categories were selected in order to minimize correlation between them. Combining the α energy difference fit with the statistical and systematic uncertainties we obtain a final result of $|C_T/C_A|^2 = -0.0019 \pm 0.0016_{stat} \pm 0.0036_{sys}$ or $a_{\beta\nu} = -0.3346 \pm -0.0011_{stat} \pm 0.0024_{sys}$.

Systematic Uncertainty	$\Delta\lvert C_T/C_A\rvert^2$
Calibration	1.4×10^{-4}
α energy corrections	1.17×10^{-3}
Cuts to the data	1.25×10^{-3}
Radiative and recoil order terms	3.36×10^{-3}
α Si detector lineshape	6.3×10^{-4}
β Scattering	5.0×10^{-4}
Total	$\mathbf{3.62 \times 10^{-3}}$

Table 6.6: Summary of systematic errors at 1σ with the total. Contributions from background and the ^{8}Be* FSD used in the Event generator were deemed negligible and not included.

CHAPTER 7

CONCLUSION AND FUTURE ENDEAVORS

7.1 Summary

The final results of this experiment are well within the bounds of the Standard Model and represent a 33% improvement on our previous lithium-8 $\beta - \nu$ correlation measurement. However, there is still substantial room for improvement, particularly in the realm of systematic errors. Though there are a number of enhancements this collaboration can make to both the BPT and our analysis method, we will require a great deal of help from both theorists and other experimentalists to reach further precision.

This experiment is the most precise beta-neutrino correlation measurement ever performed for a Gamow-Teller decay. Our results set the most stringent low-energy limit on tensor currents in the weak interaction to date. In addition, this measurement is sensitive to theoretical corrections that could have been neglected in the analysis of previous experiments. At this point, the largest limitation on our precision are the uncertainties associated with the various second forbidden form factors and second class currents within the theoretical decay rate expansion. Fortunately, this issue is something that we ourselves can potentially address, especially with the upcoming high statistics boron-8 data analysis. However, help from other collaborations (both theoretical and experimental) is always welcome, particularly when it comes to cross-checking results. Given the resiliency of the main residual feature at $\sim$ -150 keV in Figure 6.2 (that was also present, but less visible in the final α difference spectrum from our previous lithium-8 study [94], despite the analysis and calibration being performed very differently), there is reason to question whether or not the issue is related to the simulation decay rate or something in that realm. Having theoretical help to confirm that the second class currents from the Sumikama paper [97] are roughly what was expected and that all approximations are below our level of sensitivity would be invaluable as we attempt proceeding to greater sensitivity. Furthermore, a complete theoret-

ical treatment of hard bremsstrahlung radiation in a delayed alpha-emission system would have the potential to completely eliminate one of our systematic uncertainty contributions. Simply having less uncertainty associated with the measured terms of the pulse-height defect as well as the stopping power of α's in silicon from SRIM would be an immense help as well.

Outside of this collaboration, there are several more low-energy $\beta - \nu$ correlation experiments focused on helium-6 currently in development in France, Israel, and Washington State that will attempt measurements very similar to this one with likely many of the same sources of systematic uncertainty. Furthermore, some of our collaborators at the University of Notre Dame are in the process of developing a Paul trap of their own to measure the Fermi to Gamow-Teller mixing ratio in mirror nuclei via $\beta - \nu$ correlation as well. This list is by no means comprehensive and there will surely be more experiments to follow. As the low-energy physics community continues to chase the limits of precision into the regime that was previously only accessible through high-energy physics, issues we and eventually they encounter will undoubtedly reach the attention of other researchers able to potentially address them.

7.2 System Upgrades and Improvements

Though there are a number of things that we do not currently have the ability to improve on without outside help, there is a still greater list of tasks that we ourselves can do to lower the systematic errors from this experiment. Many of these projects are well underway and there is even another tentative lithium-8 data-taking campaign scheduled for 2019 to increase our store of statistics.

7.2.1 The High-Statistics Boron-8 Measurement

Though it has already been alluded to multiple times in this thesis, it is worth spending some time explaining the boron-8 effort in detail. A much smaller data set of ^{8}B $\beta - \nu$ correlation

data was collected at the BPT in 2014. The analysis is nearing completion and will lead to both a measurement of the neutrino spectrum (useful for astrophysical purposes) as well as $a_{\beta\nu}$. Another data-taking campaign is loosely scheduled for the winter of 2018-19. A number of earlier beamline upgrades have been implemented that have since increased the yield of ^{8}B. In addition, there is also the (limited) possibility of having a molecule breakup section of the beamline installed and operational before the winter campaign. This would allow pure ^{8}B to be passed to the BPT rather than a boron-water quasi-molecule and would further increase our transmission efficiency. The same RF-reducing filters (fitted to the frequency required by ^{8}B) would be applied to the BPT as well.

Once this data set is collected and analyzed, the comparison between our two mirror high-statistics $\beta - \nu$ correlation measurements would be immensely useful for either continuing the search for new physics, or more urgently, to limit our own systematic uncertainties that stem from the decay rate expansion.

7.2.2 Silicon Detector Dead Layer Measurement

One particular curse that seems to follow this experiment is that a precise measurement of the normal dead layer thickness on each silicon detector is always just slightly out of reach. My predecessor, Matt Sternberg, performed his own measurements of the normal dead layer for his set of detectors with a resulting uncertainty of 10 nm for the thickness values. I in turn performed a better dead layer measurement for him to use for his 2015 PRL with uncertainties of 4 nm though with a thicker value. A short while later, we learned of the "extra" dead layer and came to the conclusion that my thicker value for the normal dead layer thicknesses was in fact likely an average of the two dead layers. A re-analysis of the second dead layer data set was attempted, though at that point one of the detectors that had been measured was replaced, making the option of performing yet another measurement become more desirable.

As of yet, no new measurement has been performed, as it was long hoped that the

calibration data from the 2016 experiment would be sufficient to determine the dead layer values alongside the ^{8}Li α's. However as this analysis comes to a close, it is clear that again, a proper normal dead layer measurement (that takes into account the extra dead layer) will be necessary for future analysis. The spectroscopy-grade alpha sources will be an invaluable tool, as high-precision characterization of the extra dead layer can also be obtained at the same time.

7.2.3 Digital Data Acquisition System

Another project currently underway in our collaboration is a digital data acquisition system. A decent portion of the hardware and pre-development has already been done and our colleagues in Israel are eagerly awaiting for one of our DSSD's to be shipped over for testing. This hardware will likely not be implemented for another year at least and it will undoubtedly come with its own set of issues. However, when the digital DAQ is implemented, the option to remove limited RF pickup from our data post-processing will become available. Such a technique could be used in lieu of the notch filters if we needed to change the trapping frequencies by more than a few kHz. Or, provided the pickup does not saturate preamplifiers, (either with the aid of the filters or not) we could potentially remove some or all of the stainless steel shielding that covers the inside of the trap, which causes a great deal of our β scattering headaches.

7.3 Further Areas of Study

Especially with the opportunity to collect more statistics and then when paired with a high statistics data set of boron-8, the data from this experiment will certainly not be left neglected post-$a_{\beta\nu}$. There are still quite a few other opportunities for exploration that can either limit tensor currents in alternative ways or further limit the systematic errors on our current $a_{\beta\nu}$ measurement.

7.3.1 Reconstructed $\cos\theta_{\beta\nu}$ Spectrum

Though the reconstructed $\cos\theta_{\beta\nu}$ spectrum has about $4\times$ less sensitivity to tensor currents than the α energy difference spectra, it is still possible to extract a value of $a_{\beta\nu}$. This alternative measurement is particularly useful for checking systematics, since the reconstruction spectrum has less sensitivity to some of the things the α energy difference spectrum is sensitive to, such as errors in the energy calibration. However, the trade in sensitivity goes both ways, as reconstructing the kinematics requires having a very precise knowledge of the ion cloud size and location, while simulations of the α energy difference spectrum indicate no sensitivity whatsoever to this quantity. Either way, the reconstructed $\cos\theta_{\beta\nu}$ spectrum will undoubtedly be explored in further studies as it shows the true $\beta-\nu$ correlation and other reconstructed angles may required to address some uncertainties from the recoil order terms in the decay rate expansion.

7.3.2 Recoil Order Terms in the Decay Rate Expansion

As the sensitivity of this work is now largely limited by the uncertainties from Sumikama et al's [97] measurements of the second forbidden form factors and second class currents (listed in Table B.1, found in the appendices), we can also explore the possibility of using a portion of the data from this experiment (that was not used to measure $a_{\beta\nu}$, i.e., the 90^o β triples) to perhaps define some smaller errors on the more dominant terms.

At the moment, j_3, a second forbidden axial vector form factor, is by far the largest contributor of the decay rate recoil order uncertainty and the total uncertainty (in part because its error is 30% of the total j_3 value), so therefore is of the most interest. Even a slight improvement on the j_3 error would have a direct impact on the systematic uncertainty of this experiment. A survey of Holstein's decay rate expansion (found in Appendix B) indicates that terms which contain correlation between the α and $\bar{\nu}$ have the highest contributions from j_3 in terms of magnitude. Thus, it could potentially be possible to use the reconstructed $\cos\theta_{\alpha\nu}$ spectrum to extract a value of j_3 with a smaller uncertainty. Figure 7.1 shows what

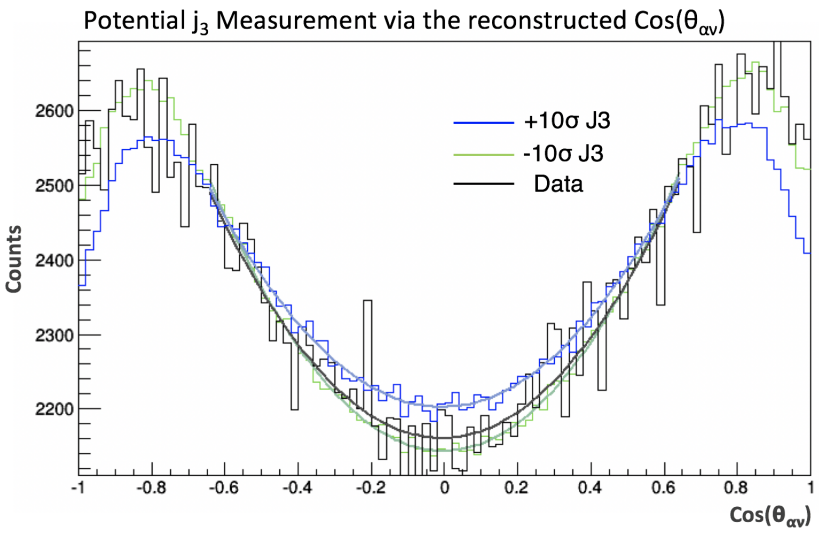

Figure 7.1: An example data (black) reconstructed $\cos\theta_{\alpha\nu}$ spectrum. The blue and green lines represent what a simulated spectra with a $\pm 10\sigma$ shift in j_3 would look like. The discrepancy indicates that this spectrum is indeed sensitive to j_3 and could potentially be used for a successful determination of j3.

this spectrum looks like with examples of simulations containing decay rates with j_3 shifted $\pm 10\sigma$. With enough simulations to compare to, a simple χ^2 calculation between each of the comparing spectra could indicate what value of j_3 is true for our system. In this instance, j_3 would be sensitive to all of the same systematics as an $a_{\beta\nu}$ extracted from the reconstructed $\cos\theta_{\beta\nu}$.

Alternatively, though they do not contribute to our uncertainty on such a large scale, defining better b and f/g terms can also be explored when the high-statistics boron-8 data set becomes available. Each of these terms contribute differently to the decay rate based on the type of beta decay ($\beta^{\pm}$). By comparing spectra sensitive to each of the terms between the two data sets (similar to Sumikama), it should be possible to extract our own values of each of those terms as well, though f/g are small enough that measuring them would test the limits of our sensitivity.

7.3.3 The Fierz Interference Term

Another potential use for this data is searching for left-handed tensor currents through the Fierz interference term (b_{Fierz}). Fortuitously, this particular term is a by-product of the $a_{\beta\nu}$ derivation found in Appendix A, so the adventurous reader can venture there for more information on its origin. The full expansion of b_{Fierz} can be seen below.

$$b_{fierz} = \frac{2\Big(C_S C_V \left|\int 1\right|^2 + C_A C_T \left|\int \boldsymbol{\sigma}\right|^2\Big)}{\Big(|C_S|^2 + |C_V|^2\Big)\left|\int 1\right|^2 + \Big(|C_A|^2 + |C_T|^2\Big)\left|\int \boldsymbol{\sigma}\right|^2} \tag{7.1}$$

By Standard Model conventions, b_{Fierz} would be 0, but if there were tensor currents present, the term would contribute to the $a_{\beta\nu}$ measurement with this relationship:

$$a_{(meas)} = \frac{a_{\beta\nu}}{1 + b_{Fierz}\frac{m_e}{E_e}}$$

where $a_{(meas)}$ is the value that we're actually measuring (a better expansion is in section 1.3). If there were a tensor current, b_{Fierz}, would also be nonzero, though it scales to C_T linearly. Pulling from the simple decay rate result from Appendix A:

$$\Gamma(E_e)dE_e = (2\pi^3 c^5 \hbar^7)^{-1}\xi\left(1 + a_{\beta\nu}\frac{(\boldsymbol{p}\cdot\boldsymbol{q})c^2}{|E||E_\nu|} + b_{fierz}\frac{mc^2}{|E|}\right)pE(E_0 - E)^2 dE \tag{7.2}$$

one could probe for b_{Fierz} directly by simply adding in the appropriate term to the simulated decay rate while keeping the $\beta - \nu$ correlated terms as they are. Such probes for tensor currents in this manner are well within our levels of sensitivity.

Appendices

APPENDIX A

DERIVATION OF THE $\beta - \nu$ CORRELATION COEFFICIENT

Since this work is dedicated to limiting exotic contributions in the $\beta-\nu$ correlation coefficient, the writer would be negligent if there was no explanation of where the term comes from. This appendix is dedicated to a comparatively simple derivation of $a_{\beta\nu}$ and by association, the Fierz interference term, b_{Fierz}.[1] We will begin with the building blocks of an interaction theory:

- The Dirac equation: describes the behavior of relativistic fermions,

$$(E + c\boldsymbol{\alpha} \cdot \boldsymbol{p} + \beta mc^2)\psi = 0 \tag{A.1}$$

- The Dirac matrices: introduced in the Dirac equation and used throughout this derivation. They are normally expressed in 4x4 matrices as: $\gamma_k = -i\beta\alpha_k$ $(k = 1, 2, 3)$, $\gamma_4 = -\beta$, and $\gamma_5 = i\gamma_1\gamma_2\gamma_3\gamma_4$, with the components defined below.[2]

$$1 = \begin{bmatrix} 1 & 0 \\ 0 & 1 \end{bmatrix}, \quad \beta = \begin{bmatrix} 1 & 0 \\ 0 & -1 \end{bmatrix}, \quad \boldsymbol{\alpha} = \begin{bmatrix} 0 & \boldsymbol{\sigma} \\ \boldsymbol{\sigma} & 0 \end{bmatrix}, \quad \boldsymbol{\sigma} = \begin{bmatrix} \boldsymbol{\sigma} & 0 \\ 0 & \boldsymbol{\sigma} \end{bmatrix}$$

- Fermion wave functions: four-component spinors that solve the Dirac equation and will eventually be used for the neutron, proton, antineutrino, and electron wave functions. $\boldsymbol{p}$ and E are the momentum and energy of the particle, respectively.

$$\psi(\boldsymbol{r}, t) = \begin{pmatrix} v \\ u \end{pmatrix} \exp\left(\frac{i(\boldsymbol{p} \cdot \boldsymbol{r} - Et)}{\hbar}\right) \text{ where } u, v = a \begin{pmatrix} 1 \\ 0 \end{pmatrix} + b \begin{pmatrix} 0 \\ 1 \end{pmatrix} \text{ and } (a^2 + b^2 = 1) \tag{A.2}$$

1. Hereafter, a bold symbol will denote a vector.

2. 1 is a shorthand notation for the identity matrix and can be 2x2 as in the defining equation or 4x4 by inserting 1 into itself. In addition, we will also frequently make use of the 2x2 Pauli matrices, which are the 3 components of $\boldsymbol{\sigma}$. They are: $\sigma_x = \begin{bmatrix} 0 & 1 \\ 1 & 0 \end{bmatrix}$, $\sigma_y = \begin{bmatrix} 0 & -i \\ i & 0 \end{bmatrix}$, and $\sigma_z = \begin{bmatrix} 1 & 0 \\ 0 & -1 \end{bmatrix}$.

- The weak interaction Hamiltonian: to eventually be used for calculating $\beta - \nu$. This was first established by Fermi in his "Theory of Beta Decay" [33] and later expanded.

Both the wave functions and Hamiltonian require some extrapolation in order to perform this derivation. Beginning with Fermi's beta decay Hamiltonian, the format was constructed by drawing from an already-in-use Hamiltonian for electromagnetic interaction. In principle, a nucleus emitting a beta and neutrino is not so different from the same nucleus emitting a gamma-ray photon. The two different processes and interactions are compared side by side in equation A.3 using relativistic formalism.

$$\begin{aligned} &(A,Z)^* \longrightarrow (A,Z) + \gamma \quad \text{vs.} \quad (A,Z) + \nu \longrightarrow (A,Z+1) + \beta^- \\ &\mathscr{H}_\gamma = -ei(\bar{\psi}_p \gamma_\mu \psi_p) A_\mu \quad \text{vs.} \quad \mathscr{H}_{\beta^-} = gC_V \big(\bar{\psi}_p \gamma_\mu \tau_+ \psi_n\big)\big(\bar{\psi}_e \gamma_\mu \psi_\nu\big) \end{aligned} \tag{A.3}$$

Here, $(A,Z)^*$ denotes the excited state of the parent nucleus and a beta decay is imagined as the annihilation of a neutrino followed by a β^- emission (and vice versa with their antiparticles) rather than the emission of both a β^- and antineutrino. This makes the beta decay interaction much easier to visualize. Both Hamiltonians are summed over μ. $\mathscr{H}_\beta$ was obtained from $\mathscr{H}_\gamma$ by making 3 changes.[3]

1. A_μ is the vector potential that can either create or annihilate a photon. For the beta decay interaction, it was exchanged for the bilinear wave equations of the beta particle and neutrino: $i(\bar{\psi}_e \gamma_\mu \psi_\nu)$ for β^- decay.

2. The electric current: $i(\bar{\psi}_p \gamma_\mu \psi_p)$ is replaced by the weak current,$(\bar{\psi}_p \gamma_\mu \tau_+ \psi_n)$ where $\boldsymbol{\tau}_\pm$ changes the neutron into a proton (or vice versa), but does not change the spatial or spin state of the nucleon.

3. e, the electric charge, is swapped for a vector coupling constant, which for reasons described later, is called C_V.

3. $\mathscr{H}$ is the Hamiltonian density and is related to the actual Hamiltonian by $\mathscr{H} = \psi_f^\dagger H \psi_i$ (where f and i are final and initial states, respectively)

However, the beta decay Hamiltonian that Fermi introduced postulated only a "vector" interaction (ergo the C_V), but there is no reason to not allow any of the 5 possible Lorentz-invariant interactions (scalar, vector, tensor, axial vector, and pseudoscalar) to contribute. Thus, the most general Hamiltonian for beta decay is:

$$\begin{aligned}\mathscr{H}_\beta = g\big[&C_S(\bar{\psi}_p\psi_n)(\bar{\psi}_e\psi_\nu) + C_V(\bar{\psi}_p\gamma_\mu\psi_n)(\bar{\psi}_e\gamma_\mu\psi_\nu) + C_T(\bar{\psi}_p i\gamma_\mu\gamma_\lambda\psi_n)(\bar{\psi}_e i\gamma_\mu\gamma_\lambda\psi_\nu) \\ &+ C_A(\bar{\psi}_p i\gamma_\mu\gamma_5\psi_n)(\bar{\psi}_e i\gamma_\mu\gamma_5\psi_\nu) + C_P(\bar{\psi}_p\gamma_5\psi_n)(\bar{\psi}_e\gamma_5\psi_\nu)\big] + h.c\end{aligned} \quad \text{(A.4)}$$

where h.c is the Hermitian conjugate and the γ's are the Dirac matrices defined above.

To simplify the next few steps of the derivation, we will assume that the beta decay Hamiltonian is Lorentz, time reversal, and space inversion invariant. Lorentz invariance implies that the Hamiltonian is the same between coordinate frames moving at constant velocity between each other, which is reasonable. Time reversal non-invariance has not yet been completely ruled out, as people are still working to limit its contribution (similar to this work). That said, the most recent limit placed on time reversal symmetry breaking contributions is on the order of 0.01% [73]. If the derivation were to include time reversal symmetry breaking, we would add complex conjugates to the derivation. Conversely, space inversion or parity invariance is maximally violated in beta decay. However, to maintain simplicity, this derivation will not include the parity-nonconserving coupling constants C_i', though they can be easily reintroduced to the derivation at the end simply by exchanging $|C_i|^2$ with $|C_i|^2 + |C_i'|^2$. [109] If $|C_i|^2 + |C_i'|^2$ were introduced, as was discussed in the introduction $C_i \approx \pm C_i'$ assuming a nearly massless neutrino and depending on the helicity of said neutrino. Furthermore, to make better use of the matrices defined above (and their identities), we will move into the "isospin formalism" where the adjoint wave function $\bar{\psi} = \psi^\dagger\beta$, and $\psi^\dagger$ is the Hermitian conjugate. And finally, despite having just introduced it, for the remainder of this derivation, we will be dropping $\tau_\pm$ since the Hamiltonians would

effectively be the same without them.

$$\psi_p^\dagger \tau_+ \psi_n \;=\; (\psi_p^\dagger, 0) \begin{pmatrix} 0 & 1 \\ 0 & 0 \end{pmatrix} \begin{pmatrix} 0 \\ \psi_n \end{pmatrix} \;=\; \psi_p^\dagger \psi_n$$

The final result of all these assumptions and adjustments is an equivalent beta decay Hamiltonian that we can work with.

$$\begin{aligned} \mathscr{H}_\beta = \; & g\big[C_S(\psi_p^\dagger \beta \psi_n)(\psi_e^\dagger \beta \psi_\nu) + C_V\big[(\psi_p^\dagger \psi_n)(\psi_e^\dagger \psi_\nu) - (\psi_p^\dagger \boldsymbol{\alpha} \psi_n)(\psi_e^\dagger \boldsymbol{\alpha} \psi_\nu)\big] \\ & + C_T\big[(\psi_p^\dagger \beta \boldsymbol{\sigma} \psi_n)(\psi_e^\dagger \beta \boldsymbol{\sigma} \psi_\nu) + (\psi_p^\dagger \beta \boldsymbol{\alpha} \psi_n)(\psi_e^\dagger \beta \boldsymbol{\alpha} \psi_\nu)\big] \\ & + C_A\big[(\psi_p^\dagger \boldsymbol{\sigma} \psi_n)(\psi_e^\dagger \boldsymbol{\sigma} \psi_\nu) - (\psi_p^\dagger \gamma_5 \psi_n)(\psi_e^\dagger \gamma_5 \psi_\nu)\big] \\ & + C_P(\psi_p^\dagger \beta \gamma_5 \psi_n)(\psi_e^\dagger \beta \gamma_5 \psi_\nu)\big] + h.c \end{aligned} \tag{A.5}$$

The other puzzle piece that is needed to set up this derivation is a set of wave functions for each of the particles involved. The general form of these wave functions was defined in equation (A.2), but there are a few more details that need to be worked out.

We'll begin with the wave functions for the nucleons. To get rid of some extra variables, we'll insert equation (A.2) into the Dirac equation (A.1):

$(E + c\boldsymbol{\alpha} \cdot \boldsymbol{p} + \beta mc^2) \begin{pmatrix} v \\ u \end{pmatrix} \exp\Big(\dfrac{i(\boldsymbol{p} \cdot \boldsymbol{r} - Et)}{\hbar}\Big) = 0$. Subtracting $E\psi$ and canceling $\exp(r)$:

$\left\{ c \begin{pmatrix} 0 & \boldsymbol{\sigma} \cdot \boldsymbol{p} \\ \boldsymbol{\sigma} \cdot \boldsymbol{p} & 0 \end{pmatrix} + mc^2 \begin{pmatrix} I & 0 \\ 0 & -I \end{pmatrix} \right\} \begin{pmatrix} v \\ u \end{pmatrix} = -E \begin{pmatrix} v \\ u \end{pmatrix}$. Performing the matrix algebra:

$\begin{pmatrix} vmc^2 + cu(\boldsymbol{\sigma} \cdot \boldsymbol{p}) \\ cv(\boldsymbol{\sigma} \cdot \boldsymbol{p}) - umc^2 \end{pmatrix} = -E \begin{pmatrix} v \\ u \end{pmatrix}$. If we choose the lower equation and positive E

$v = \dfrac{-c\boldsymbol{\sigma} \cdot \boldsymbol{p}}{E + mc^2} u$ and assume the nucleons are nonrelativistic ($E \approx Mc^2$):

the nucleon wavefunctions become: $\psi_p^\dagger = \left(-\frac{\boldsymbol{\sigma}\cdot\boldsymbol{p}_p}{2Mc}u_p^\dagger, u_p^\dagger \right)$ and $\psi_n = \begin{pmatrix} -\frac{\boldsymbol{\sigma}\cdot\boldsymbol{p}_n}{2Mc}u_n \\ u_n \end{pmatrix}$ (A.6)

For the lepton wave functions, we cannot assume that the particles are nonrelativistic. Furthermore, there are a great many calculations of the $\sum \psi\psi^\dagger$ matrix forthcoming. Thus, we will take a different approach and turn the previous matrix into a projection operator. In more detail:

$$\sum_\sigma \psi_\pm \psi_\pm^\dagger = D_\pm \quad \text{and} \quad \sum_{\sigma,E} \psi\psi^\dagger = D_\pm$$

where $\psi_\pm$ refers to the wave functions for positive or negative energy states. The $D_\pm$ operators will satisfy these conditions:

$$D_+\psi_+ = \psi_+, \quad D_+\psi_- = 0, \quad D_-\psi_- = \psi_-, \quad D_-\psi_+ = 0, \quad \text{and} \quad D_\pm^2 = D_\pm$$

This operator can be constructed from the Dirac equation if we take $H = -(c\boldsymbol{\alpha}\cdot\boldsymbol{p} + \beta mc^2)$,

so that $\pm E\psi_\pm - H\psi_\pm = 0$, or with some strategic algebra: $\psi_\pm = \frac{1}{2}\left(1 \pm \frac{H}{|E|}\right)\psi_\pm$

Hence, the operator is $D_\pm = \frac{1}{2}\left(1 \mp \frac{(c\boldsymbol{\alpha}\cdot\boldsymbol{p} + \beta mc^2)}{|E|}\right)$ and meets the specified conditions:

$$D_+\psi_+ = \frac{1}{2}\left(1 - \frac{(c\boldsymbol{\alpha}\cdot\boldsymbol{p} + \beta mc^2)}{|E|}\right)\psi_+ = \frac{1}{2}\left(1 + \frac{|E|}{|E|}\right)\psi_+ = \psi_+$$
$$D_+\psi_- = \frac{1}{2}\left(1 - \frac{(c\boldsymbol{\alpha}\cdot\boldsymbol{p} + \beta mc^2)}{|E|}\right)\psi_- = \frac{1}{2}\left(1 - \frac{|E|}{|E|}\right)\psi_- = 0 \qquad \left(\pm E\psi_\pm = H\psi_\pm\right)$$

Finally, if we assume that the energy of our leptons is positive, our operators are defined below for an electron and a antineutrino (where the mass of the antineutrino is considered negligible). To change the operator to a positron, one would swap the sign on the βmc^2

term.

$$D_e = \frac{1}{2}\left(1 - \frac{(c\boldsymbol{\alpha}\cdot\boldsymbol{p} + \beta mc^2)}{|E|}\right) \quad \text{and} \quad D_\nu = \frac{1}{2}\left(1 - \frac{(c\boldsymbol{\alpha}\cdot\boldsymbol{q})}{|E_\nu|}\right) \tag{A.7}$$

where $\boldsymbol{q}$ is the momentum of the antineutrino

Now that everything has been defined, we can calculate $a_{\beta\nu}$ using Fermi's golden rule, $\Gamma(E)dE_e = \frac{2\pi}{\hbar}|H_{fi}|^2\frac{dn}{dE_o}$. Here, $\Gamma(E)dE$ is the probability of transition per unit time, $H_{fi} = \int \mathscr{H}_\beta \, d\mathbf{r}_1 d\mathbf{r}_2 ... d\mathbf{r}_A$, and $\frac{dn}{dE_o}$ is the density of final states with respect to the endpoint energy ($E_0 = E + E_\nu$). Briefly, $\frac{dn}{dE_o}$ can be calculated by taking the product of the number of final states of the antineutrino and electron in momentum space (assuming 1 particle per unit volume) using $E_0 - E = E_\nu = cp_\nu \rightarrow (c\,dp_\nu = dE_0)$ and $c^2 p\,dp = EdE$ from Einstein's equation to obtain:

$$\frac{dn}{dE_o} = \frac{dn_e dn_\nu}{dE_0} = \left(\frac{4\pi p^2 dp}{(2\pi\hbar)^3}\right)\left(\frac{4\pi p_\nu^2 dp_\nu}{(2\pi\hbar)^3}\right)\frac{1}{dE_0} = (4\pi^4\hbar^6 c^5)^{-1} pE(E_0 - E)^2 dE \tag{A.8}$$

However, for our purposes, $|H_{fi}|^2$ is the term that will eventually unearth $a_{\beta\nu}$ but requires substantially more effort to get there. To start, we will simplify equation (A.5) using some of the assumptions we have already made and then some new selection rules, all of which will lead to a more workable $|H_{fi}|^2$. First, we have already assumed that the protons and neutrons are not relativistic ($v/c \approx 0.1$), thus the terms with $\boldsymbol{\alpha}$ can be neglected:

$$\psi_p^\dagger \boldsymbol{\alpha}\psi_n = \left(-\frac{\boldsymbol{\sigma}\cdot\boldsymbol{p}_p}{2Mc}u_p^\dagger, u_p^\dagger\right)\begin{pmatrix} 0 & \boldsymbol{\sigma} \\ \boldsymbol{\sigma} & 0 \end{pmatrix}\begin{pmatrix} -\frac{\boldsymbol{\sigma}\cdot\boldsymbol{p}_n}{2Mc}u_n \\ u_n \end{pmatrix} \approx \frac{\boldsymbol{p}_p}{Mc} + \frac{\boldsymbol{p}_n}{Mc}$$

$$\psi_p^\dagger \beta\boldsymbol{\alpha}\psi_n = \left(-\frac{\boldsymbol{\sigma}\cdot\boldsymbol{p}_p}{2Mc}u_p^\dagger, u_p^\dagger\right)\begin{pmatrix} I & 0 \\ 0 & -I \end{pmatrix}\begin{pmatrix} 0 & \boldsymbol{\sigma} \\ \boldsymbol{\sigma} & 0 \end{pmatrix}\begin{pmatrix} -\frac{\boldsymbol{\sigma}\cdot\boldsymbol{p}_n}{2Mc}u_n \\ u_n \end{pmatrix} \approx \frac{\boldsymbol{p}_p}{Mc} - \frac{\boldsymbol{p}_n}{Mc}$$

Using the same math, one can see that none of the pseudoscalar terms ($\psi_p^\dagger\gamma_5\psi_n$) contribute

either. Taking away all the negligible terms, we have a simplified Hamiltonian.

$$\begin{aligned}\mathscr{H}_\beta = \; & g\big[C_S(\psi_p^\dagger\beta\psi_n)(\psi_e^\dagger\beta\psi_\nu) + C_V(\psi_p^\dagger\psi_n)(\psi_e^\dagger\psi_\nu) \\ & + C_T(\psi_p^\dagger\beta\boldsymbol{\sigma}\psi_n)(\psi_e^\dagger\beta\boldsymbol{\sigma}\psi_\nu) + C_A(\psi_p^\dagger\boldsymbol{\sigma}\psi_n)(\psi_e^\dagger\boldsymbol{\sigma}\psi_\nu)\big] + h.c\end{aligned} \tag{A.9}$$

However, this is still a bit of a debacle. When we take the square of H_{fi} and account for the 3 components of $\boldsymbol{\sigma}$, we end up with several dozen different terms to deal with. We can reduce the number of terms by writing the full nucleon side of the Hamiltonian complete with quantum numbers. If the operating matrices are defined as Λ_k, then we can use the Wigner-Eckart theorem to represent H_{fi} in terms of the already defined Clebsch-Gorban coefficients:

$$H_{fi} \simeq \int \psi_p^\dagger \Lambda_k \psi_n d\boldsymbol{r} = \int \psi^\dagger_{J_f M_f} \Lambda_{LM} \psi_{J_i M_i} d\boldsymbol{r} = (J_i \; L \; M_i \; M \mid J_f \; M_f)\langle J_f \| \Lambda \| J_i \rangle$$

Here, L is the rank of Λ_k. $L = 0$ for β and 1, or "Fermi" interactions, while $L = 1$ for $\beta\boldsymbol{\sigma}$ and $\boldsymbol{\sigma}$, or "Gamow-Teller" interactions. M refers to the magnetic quantum number. When $L = 0$, $M = 0$ and for $L = 1$, $M = \{-1, 0, 1\}$ where $\sigma_0 = \sigma_z$ and $\sigma_{\pm 1} = \mp\sqrt{\frac{1}{2}}(\sigma_x \pm i\sigma_y)$ Moving on, if we evaluate a generic term of $|H_{fi}|^2$, define Λ and Λ' as the operators, sum over the final states, and average the initial states (assume the nucleons are not oriented), then:

$$|H_{fi}|^2 \simeq \sum_{M_i M_f} (J_i \, L \, M_i \, M \mid J_f \, M_f)(J_i \, L' \, M_i \, M' \mid J_f \, M_f) \propto \delta_{LL'}\delta_{MM'}$$

where $\langle L \, M | L' \, M' \rangle = \delta_{LL'}\delta_{MM'}$. Drawing from the kronecker delta terms, we can eliminate any $|H_{fi}|^2$ terms where $L \neq L'$ (i.e, Fermi and Gamow teller terms cannot mix). In addition, terms where $M \neq M'$ can also be eliminated. We are now limited to just 12 terms that must be calculated. With all the simplification mostly done, we can now start to directly calculate

$\Gamma(E_e)dE_e = \frac{2\pi}{\hbar}|H_{fi}|^2 \frac{dn}{dE_o}$. If we write $|H_{fi}|^2$ explicitly:

$$|H_{fi}|^2 = g^2 \sum_{k,l} \sum_{\sigma_e,\sigma_\nu} C_k C_l^* (\psi_e^\dagger \Lambda^k \psi_e)(\psi_e^\dagger \Lambda^l \psi_e)^* \Big(\int \psi_p^\dagger \Lambda_k \psi_n d\boldsymbol{r} \Big) \Big(\int \psi_p^\dagger \Lambda_l \psi_n d\boldsymbol{r} \Big)^* \quad \text{(A.10)}$$

At this point, it is useful to define the nuclear matrix elements and reduce the integral terms in equation (A.10). Using the assumption that the nucleons are nonrelativistic once more, we can assume that both $\frac{\boldsymbol{\sigma}\cdot\boldsymbol{p}}{2Mc}$ terms are small compared to the other pure spinor term in ψ from equation (A.6). In addition, since u_p and u_n are normalized, we end up with these matrix properties:

$$\text{if } -\frac{\boldsymbol{\sigma}\cdot\boldsymbol{p}}{2Mc} = \Omega \ll 1 \text{ then: } \int \psi_p^\dagger \psi_n d\boldsymbol{r} = \int \left(\Omega_p u_p^\dagger, u_p^\dagger\right) \begin{pmatrix} \Omega_n u_n \\ u_n \end{pmatrix} d\boldsymbol{r} = \int u_p^\dagger u_n d\boldsymbol{r} = \int 1$$

$$\int \psi_p^\dagger \beta \psi_n d\boldsymbol{r} = \int \left(\Omega_p u_p^\dagger, u_p^\dagger\right) \begin{pmatrix} I & 0 \\ 0 & -I \end{pmatrix} \begin{pmatrix} \Omega_n u_n \\ u_n \end{pmatrix} d\boldsymbol{r} = \int -u_p^\dagger u_n d\boldsymbol{r} = -\int 1$$

$$\int \psi_p^\dagger \boldsymbol{\sigma} \psi_n d\boldsymbol{r} = \int \left(\Omega_p u_p^\dagger, u_p^\dagger\right) \begin{pmatrix} \boldsymbol{\sigma} & 0 \\ 0 & \boldsymbol{\sigma} \end{pmatrix} \begin{pmatrix} \Omega_n u_n \\ u_n \end{pmatrix} d\boldsymbol{r} = \int u_p^\dagger \boldsymbol{\sigma} u_n d\boldsymbol{r} = \int \boldsymbol{\sigma}$$

$$\int \psi_p^\dagger \beta \boldsymbol{\sigma} \psi_n d\boldsymbol{r} = \int \left(\Omega_p u_p^\dagger, u_p^\dagger\right) \begin{pmatrix} \boldsymbol{\sigma} & 0 \\ 0 & -\boldsymbol{\sigma} \end{pmatrix} \begin{pmatrix} \Omega_n u_n \\ u_n \end{pmatrix} d\boldsymbol{r} = \int -u_p^\dagger \boldsymbol{\sigma} u_n d\boldsymbol{r} = -\int \boldsymbol{\sigma} \quad \text{(A.11)}$$

where we define $\int 1$ as the Fermi nuclear matrix element and $\int \boldsymbol{\sigma}$ as the Gamow-Teller nuclear matrix element. In addition, we'll play some matrix tricks with the lepton summation terms in (A.10) as well to use the infrastructure we've already defined and make life a bit easier. If we take

$$|H_{fi}|^2 \propto \sum_{\sigma_e \sigma_\nu} (\psi_e^\dagger \Lambda^k \psi_\nu)(\psi_e^\dagger \Lambda^l \psi_\nu)^* = \sum_{\sigma_e \sigma_\nu} \psi_e^\dagger \Lambda^k \psi_\nu \psi_\nu^\dagger \Lambda^l \psi_e$$

and define $A = \psi_e^\dagger$, and $B = \hat{\Lambda}_1 \psi_\nu \psi_\nu^\dagger \hat{\Lambda}_2 \psi_e$, then AB (a number) is not commutable as itself,

(BA is a 4x4 matrix) but the trace[4] of AB is:

$$AB = \mathrm{Tr}(AB) = \sum_i \sum_k A_{ik} B_{ki} = \mathrm{Tr}(BA).$$

Since $\psi_\nu \psi_\nu^\dagger$ and $\psi_e \psi_e^\dagger$ are summed over all states we can exchange these terms with the operators that we defined in equation (A.7). Hence, the lepton component version of $|H_{fi}|^2$ that we will be using is:

$$|H_{fi}|^2 \propto \mathrm{Tr}(BA) = \mathrm{Tr}(\Lambda^k \psi_\nu \psi_\nu^\dagger \Lambda^l \psi_e \psi_e^\dagger) = \mathrm{Tr}(\Lambda^l D_\nu \Lambda^l D_e)$$

All that is left to do is compute the non-vanishing terms of $|H_{fi}|^2$ to calculate the transition probability. For future use, it is worth pointing out that the trace of β, $\boldsymbol{\alpha}$ (or α_i), $\boldsymbol{\sigma}$ (or σ_i), and all products of odd numbers of these matrices vanish. We'll begin with the pure scalar term:

$$|H_{fi}|^2 = |C_S|^2 \mathrm{Tr}(\beta D_\nu \beta D_e) \Big(\int \psi_p^\dagger \beta \psi_n d\boldsymbol{r} \Big) \Big(\int \psi_p^\dagger \beta \psi_n d\boldsymbol{r} \Big)^*$$

From (A.11), the integrals simplify to $(\int -1)(\int -1)^* = |\int 1|^2$ and the trace can be calculated. Only the $\beta\beta$ and $\boldsymbol{\alpha}\boldsymbol{\alpha}$ terms have nonzero traces.

$$\begin{aligned}
\mathrm{Tr}(\beta D_\nu \beta D_e) &= \frac{1}{4} \mathrm{Tr} \Bigg(\beta \Big(1 - \frac{(c\boldsymbol{\alpha} \cdot \boldsymbol{p} + \beta m c^2)}{|E|} \Big) \beta \Big(1 - \frac{(c\boldsymbol{\alpha} \cdot \boldsymbol{q})}{|E_\nu|} \Big) \Bigg) \\
&= \frac{1}{4} \mathrm{Tr} \Bigg(\beta\beta + \frac{(\beta\boldsymbol{\alpha} \cdot \boldsymbol{p})(\beta\boldsymbol{\alpha} \cdot \boldsymbol{q}) c^2}{|E||E_\nu|} \Bigg) \\
&= \frac{1}{4} \mathrm{Tr} \left(\begin{pmatrix} I & 0 \\ 0 & I \end{pmatrix} + \frac{c^2}{|E||E_\nu|} \begin{pmatrix} 0 & \boldsymbol{\sigma} \cdot \boldsymbol{p} \\ -\boldsymbol{\sigma} \cdot \boldsymbol{p} & 0 \end{pmatrix} \begin{pmatrix} 0 & \boldsymbol{\sigma} \cdot \boldsymbol{q} \\ -\boldsymbol{\sigma} \cdot \boldsymbol{q} & 0 \end{pmatrix} \right)
\end{aligned}$$

4. The trace of a matrix is formally defined as $\mathrm{Tr}(\Theta) = \sum_i \Theta_{ii}$, which is the sum of the diagonal components of Θ

$$= \frac{1}{4}\mathrm{Tr}\left(\begin{pmatrix} I & 0 \\ 0 & I \end{pmatrix} + \frac{c^2}{|E||E_\nu|}\begin{pmatrix} -(\boldsymbol{\sigma}\cdot\boldsymbol{p})(\boldsymbol{\sigma}\cdot\boldsymbol{q}) & 0 \\ 0 & -(\boldsymbol{\sigma}\cdot\boldsymbol{p})(\boldsymbol{\sigma}\cdot\boldsymbol{q}) \end{pmatrix}\right)$$
$$= 1 - \frac{(\boldsymbol{\sigma}\cdot\boldsymbol{p})(\boldsymbol{\sigma}\cdot\boldsymbol{q})c^2}{|E||E_\nu|}$$

Using a standard $\boldsymbol{\sigma}$ commutation relation, we can rearrange $(\boldsymbol{\sigma}\cdot\boldsymbol{p})(\boldsymbol{\sigma}\cdot\boldsymbol{q})$ to $(\boldsymbol{p}\cdot\boldsymbol{q})+i(\boldsymbol{\sigma}\cdot\boldsymbol{q}\times\boldsymbol{p})$. Since the trace of $\boldsymbol{\sigma}$ is 0, the second term drops out and we have for our total scalar term:

$$|C_S|^2\left(1 - \frac{(\boldsymbol{p}\cdot\boldsymbol{q})c^2}{|E||E_\nu}\right)\left|\int 1\right|^2 \tag{A.12}$$

Next is the pure vector term, which will be similar to the pure scalar term.

$$|H_{fi}|^2 = |C_V|^2\mathrm{Tr}(D_\nu D_e)\Big(\int \psi_p^\dagger\psi_n d\boldsymbol{r}\Big)\Big(\int \psi_p^\dagger\psi_n d\boldsymbol{r}\Big)^*$$

The nucleon integrals simplify in a similar fashion to the scalar term: $(\int 1)(\int 1)^* = |\int 1|^2$ and the lepton trace is again, calculated along the same lines. The only nonzero terms are the identity and $\boldsymbol{\alpha}\boldsymbol{\alpha}$ and since there is no β matrix, the $\boldsymbol{\sigma}\cdot\boldsymbol{p}$ terms are positive instead of negative. In addition, we can use the same $\boldsymbol{\sigma}$ commutation relation as the scalar term to get the final trace in terms of $\boldsymbol{p}\cdot\boldsymbol{q}$.

$$\mathrm{Tr}(D_\nu D_e) = \frac{1}{4}\mathrm{Tr}\left(\left(1 - \frac{(c\boldsymbol{\alpha}\cdot\boldsymbol{p} + \beta mc^2)}{|E|}\right)\left(1 - \frac{(c\boldsymbol{\alpha}\cdot\boldsymbol{q})}{|E_\nu|}\right)\right)$$
$$= \frac{1}{4}\mathrm{Tr}\left(1 + \frac{(\boldsymbol{\alpha}\cdot\boldsymbol{p})(\boldsymbol{\alpha}\cdot\boldsymbol{q})c^2}{|E||E_\nu|}\right)$$
$$= \frac{1}{4}\mathrm{Tr}\left(\begin{pmatrix} I & 0 \\ 0 & I \end{pmatrix} + \frac{c^2}{|E||E_\nu|}\begin{pmatrix} (\boldsymbol{\sigma}\cdot\boldsymbol{p})(\boldsymbol{\sigma}\cdot\boldsymbol{q}) & 0 \\ 0 & (\boldsymbol{\sigma}\cdot\boldsymbol{p})(\boldsymbol{\sigma}\cdot\boldsymbol{q}) \end{pmatrix}\right)$$
$$= 1 + \frac{(\boldsymbol{p}\cdot\boldsymbol{q})c^2}{|E||E_\nu|}$$

Which makes our final pure vector term defined as:

$$|C_V|^2\Big(1+\frac{(\boldsymbol{p}\cdot\boldsymbol{q})c^2}{|E||E_\nu}\Big)\left|\int 1\right|^2 \tag{A.13}$$

The final Fermi interaction term that must be done is the cross term between scalar and vector. Because we are still assuming that time reversal invariance is not broken, $C_i = C_i^*$. With the appropriate integrals already substituted in:

$$|H_{fi}|^2 = C_V C_S\Big(\mathrm{Tr}(\beta D_\nu D_e)\Big(\int -1\Big)\Big(\int 1\Big)^* + \mathrm{Tr}(D_\nu \beta D_e)\Big(\int 1\Big)\Big(\int -1\Big)^*\Big)$$

The integrals again simplify to $(\int 1)(\int -1)^* = -|\int 1|^2$. The trace is calculated below. The only non-vanishing terms in both traces are $\beta\beta mc^2$.

$$\begin{aligned}\mathrm{Tr}(\beta D_\nu D_e) + \mathrm{Tr}(D_\nu \beta D_e) =& \frac{1}{4}\mathrm{Tr}\Big(\beta\Big(1-\frac{(c\boldsymbol{\alpha}\cdot\boldsymbol{p}+\beta mc^2)}{|E|}\Big)\Big(1-\frac{(c\boldsymbol{\alpha}\cdot\boldsymbol{q})}{|E_\nu|}\Big)\Big)\\ &+\frac{1}{4}\mathrm{Tr}\Big(\Big(1-\frac{(c\boldsymbol{\alpha}\cdot\boldsymbol{p}+\beta mc^2)}{|E|}\Big)\beta\Big(1-\frac{(c\boldsymbol{\alpha}\cdot\boldsymbol{q})}{|E_\nu|}\Big)\Big)\\ =& \frac{1}{4}\mathrm{Tr}\Big(-2\frac{\beta\beta mc^2}{|E|}\Big) = \frac{-2mc^2}{|E|}\end{aligned}$$

The negatives on the trace and integrals cancel out and final cross term between vector and scalar is:

$$C_V C_S \frac{2mc^2}{|E|}\left|\int 1\right|^2 \tag{A.14}$$

Now we move on to the Gamow-Teller interactions, which are more important for this work. We can begin with the axial vector terms.

$$|H_{fi}|^2 = |C_A|^2\sum_{i=1}^{3}\mathrm{Tr}(\sigma_i D_\nu \sigma_i D_e)\Big(\int \psi_p^\dagger \sigma_i \psi_n d\boldsymbol{r}\Big)\Big(\int \psi_p^\dagger \sigma_i \psi_n d\boldsymbol{r}\Big)^*$$

Due to the selection rules derived from the quantum numbers earlier, the integrals become: $(\int \sigma_i)(\int \sigma_i) = |\int \sigma_i|^2$. To get the Gamow-Teller matrix element, we can define: $|\int \boldsymbol{\sigma}|^2 =$

$|\int \sigma_x|^2 + |\int \sigma_y|^2 + |\int \sigma_z|^2$ or $|\int \sigma_i|^2 = \frac{1}{3}|\int \boldsymbol{\sigma}|^2$ To calculate the traces, we will perform a few more matrix tricks. as with the scalar calculation, all the terms except for $\sigma_z\sigma_z$ and $\boldsymbol{\alpha}\boldsymbol{\alpha}$ vanish.

$$\sum_{i=1}^{3} \mathrm{Tr}(\sigma_i D_\nu \sigma_i D_e) = \frac{1}{4}\mathrm{Tr}\Big(\sum_{i=1}^{3} \sigma_i \Big(1 - \frac{(c\boldsymbol{\alpha}\cdot\boldsymbol{p} + \beta mc^2)}{|E|}\Big)\sigma_i \Big(1 - \frac{(c\boldsymbol{\alpha}\cdot\boldsymbol{q})}{|E_\nu|}\Big)\Big)$$
$$= \frac{1}{4}\mathrm{Tr}\Big(\sum_{i=1}^{3} \sigma_i\sigma_i + \frac{(\sigma_i\boldsymbol{\alpha}\cdot\boldsymbol{p})(\sigma_i\boldsymbol{\alpha}\cdot\boldsymbol{q})c^2}{|E||E_\nu|}\Big)$$

For the time being, we will ignore the neutrino momentum and only look at $\sigma_i\boldsymbol{\alpha}\cdot\boldsymbol{p}\sigma_i$. Since $\boldsymbol{p}$ is only a vector, we'll pull it out and examine what happens if you have $\sigma_i\boldsymbol{\alpha}\sigma_i$. For the x component of $\boldsymbol{\alpha}$:

$$\sum_{i=1}^{3} \sigma_i\alpha_x\sigma_i = \begin{pmatrix}\sigma_x & 0\\ 0 & \sigma_x\end{pmatrix}\begin{pmatrix}0 & \sigma_x\\ \sigma_x & 0\end{pmatrix}\begin{pmatrix}\sigma_x & 0\\ 0 & \sigma_x\end{pmatrix} + \begin{pmatrix}\sigma_y & 0\\ 0 & \sigma_y\end{pmatrix}\begin{pmatrix}0 & \sigma_x\\ \sigma_x & 0\end{pmatrix}\begin{pmatrix}\sigma_y & 0\\ 0 & \sigma_y\end{pmatrix}$$
$$+ \begin{pmatrix}\sigma_z & 0\\ 0 & \sigma_z\end{pmatrix}\begin{pmatrix}0 & \sigma_x\\ \sigma_x & 0\end{pmatrix}\begin{pmatrix}\sigma_z & 0\\ 0 & \sigma_z\end{pmatrix}$$

$$= \begin{pmatrix}0 & 1\\ 1 & 0\end{pmatrix}\begin{pmatrix}\sigma_x & 0\\ 0 & \sigma_x\end{pmatrix} + \begin{pmatrix}0 & -i\sigma_z\\ -i\sigma_z & 0\end{pmatrix}\begin{pmatrix}\sigma_y & 0\\ 0 & \sigma_y\end{pmatrix} + \begin{pmatrix}0 & i\sigma_y\\ i\sigma_y & 0\end{pmatrix}\begin{pmatrix}\sigma_z & 0\\ 0 & \sigma_z\end{pmatrix}$$
$$= \begin{pmatrix}0 & \sigma_x\\ \sigma_x & 0\end{pmatrix} + \begin{pmatrix}0 & -\sigma_x\\ -\sigma_x & 0\end{pmatrix} + \begin{pmatrix}0 & -\sigma_x\\ -\sigma_x & 0\end{pmatrix}$$
$$= \alpha_x - \alpha_x - \alpha_x \tag{A.15}$$

If we do the same matrix multiplication on the other components, we get similar results. In this way: $\sum_i \sigma_i\boldsymbol{\alpha}\sigma_i = -\boldsymbol{\alpha}$, or $\sum_i \sigma_i\boldsymbol{\alpha}\cdot\boldsymbol{p}\sigma_i = -(\boldsymbol{\alpha}\cdot\boldsymbol{p})$. Resuming the derivation, exchanging $\sigma_i\sigma_i$ for 1, and noticing that the second term in the trace is effectively the same as was

calculated in the pure vector instance, we have:

$$\sum_{i=1}^{3}\mathrm{Tr}(\sigma_i D_\nu \sigma_i D_e) = \frac{1}{4}\mathrm{Tr}\bigg(3 + \frac{-(\boldsymbol{\alpha}\cdot\boldsymbol{p})(\boldsymbol{\alpha}\cdot\boldsymbol{q})c^2}{|E||E_\nu|}\bigg)$$
$$= \bigg(3 + \frac{-(\boldsymbol{p}\cdot\boldsymbol{q})c^2}{|E||E_\nu|}\bigg)$$

Adding the trace to the rest of the axial vector term the result is:

$$|C_A|^2\bigg(3 + \frac{-(\boldsymbol{p}\cdot\boldsymbol{q})c^2}{|E||E_\nu|}\bigg)\frac{1}{3}\bigg|\int \boldsymbol{\sigma}\bigg|^2 \tag{A.16}$$

Moving on to the pure tensor component of $|H_{fi}|^2$, we shall employ some similar tricks as the axial vector:

$$|H_{fi}|^2 = |C_T|^2\sum_{i=1}^{3}\mathrm{Tr}(\beta\sigma_i D_\nu \beta\sigma_i D_e)\Big(\int \psi_p^\dagger \beta\sigma_i\psi_n d\boldsymbol{r}\Big)\Big(\int \psi_p^\dagger \beta\sigma_i\psi_n d\boldsymbol{r}\Big)^*$$

For the integrals, we know from equation (A.11) and the axial vector calculation that $(\int \beta\sigma_i)(\int \beta\sigma_i)^* = (\int -\sigma_i)(\int -\sigma_i)^* = |\int \sigma_i|^2 = \frac{1}{3}|\int \boldsymbol{\sigma}|^2$. For the tensor trace, in a similar fashion to the axial vector trace, all the terms except for the $\beta\sigma\beta\sigma$ and $\boldsymbol{\alpha\alpha}$ vanish, leaving only 2 terms.

$$\sum_{i=1}^{3}\mathrm{Tr}(\beta\sigma_i D_\nu \beta\sigma_i D_e) = \frac{1}{4}\mathrm{Tr}\bigg(\sum_{i=1}^{3}\beta\sigma_i\Big(1 - \frac{(c\boldsymbol{\alpha}\cdot\boldsymbol{p} + \beta mc^2)}{|E|}\Big)\beta\sigma_i\Big(1 - \frac{(c\boldsymbol{\alpha}\cdot\boldsymbol{q})}{|E_\nu|}\Big)\bigg)$$
$$= \frac{1}{4}\mathrm{Tr}\bigg(\sum_{i=1}^{3}\beta\sigma_i\beta\sigma_i + \frac{(\beta\sigma_i\boldsymbol{\alpha}\cdot\boldsymbol{p})(\beta\sigma_i\boldsymbol{\alpha}\cdot\boldsymbol{q})c^2}{|E||E_\nu|}\bigg)$$

In this case, the matrices we are working with now are:

$$\beta\sigma_i = \begin{pmatrix}1 & 0\\ 0 & -1\end{pmatrix}\begin{pmatrix}\sigma_i & 0\\ 0 & \sigma_i\end{pmatrix} = \begin{pmatrix}\sigma_i & 0\\ 0 & -\sigma_i\end{pmatrix}, \quad \text{and} \quad \beta\sigma_i\beta\sigma_i = \begin{pmatrix}1 & 0\\ 0 & 1\end{pmatrix} = I$$

The matrix algebra used to achieve $\sum_{i=1}^{3}\sigma_i\alpha_x\sigma_i$ in the axial vector derivation is the same here, except the signs for each term will be flipped, producing $+\boldsymbol{\alpha}$ instead of $-\boldsymbol{\alpha}$. In this way, we end up with:

$$\begin{aligned}\sum_{i=1}^{3}\mathrm{Tr}(\sigma_i D_\nu \sigma_i D_e) &= \frac{1}{4}\mathrm{Tr}\bigg(3+\frac{(\boldsymbol{\alpha}\cdot\boldsymbol{p})(\boldsymbol{\alpha}\cdot\boldsymbol{q})c^2}{|E||E_\nu|}\bigg)\\ &= \bigg(3+\frac{(\boldsymbol{p}\cdot\boldsymbol{q})c^2}{|E||E_\nu|}\bigg).\end{aligned}$$

Which, after plugging in the integrals and C_k terms, makes the total pure tensor contribution to $|H_{fi}|^2$:

$$|C_T|^2\bigg(3+\frac{(\boldsymbol{p}\cdot\boldsymbol{q})c^2}{|E||E_\nu|}\bigg)\frac{1}{3}\bigg|\int\boldsymbol{\sigma}\bigg|^2 \tag{A.17}$$

The final term we must calculate is the mixed tensor and axial vector contribution. We'll begin in the same way as all the others, except with the integrals already simplified:

$$|H_{fi}|^2 = C_A C_T\bigg(\sum_{i=1}^{3}\mathrm{Tr}(\beta\sigma_i D_\nu\sigma_i D_e)+\mathrm{Tr}(\sigma_i D_\nu\beta\sigma_i D_e)\bigg)\bigg(-\frac{1}{3}\bigg|\int\boldsymbol{\sigma}\bigg|^2\bigg)$$

The trace calculation is similar to the scalar-vector cross term. All of the products in the trace vanish except for the $\beta\sigma\beta\sigma$ term, which we already know to be the identity matrix.

$$\begin{aligned}\sum_{i=1}^{3}\mathrm{Tr}(\beta\sigma_i D_\nu\sigma_i D_e)+\mathrm{Tr}(\sigma_i D_\nu\beta\sigma_i D_e) =&\\ =&\sum_{i=1}^{3}\frac{1}{4}\mathrm{Tr}\bigg(\beta\sigma_i\Big(1-\frac{(c\boldsymbol{\alpha}\cdot\boldsymbol{p}+\beta mc^2)}{|E|}\Big)\sigma_i\Big(1-\frac{(c\boldsymbol{\alpha}\cdot\boldsymbol{q})}{|E_\nu|}\Big)\bigg)\\ &+\frac{1}{4}\mathrm{Tr}\bigg(\sigma_i\Big(1-\frac{(c\boldsymbol{\alpha}\cdot\boldsymbol{p}+\beta mc^2)}{|E|}\Big)\beta\sigma_i\Big(1-\frac{(c\boldsymbol{\alpha}\cdot\boldsymbol{q})}{|E_\nu|}\Big)\bigg)\\ =&\sum_{i=1}^{3}\frac{1}{2}\bigg(\mathrm{Tr}\bigg(-\frac{\beta\sigma_i\beta\sigma_i mc^2}{|E|}\bigg)\\ =&\frac{-6mc^2}{|E|}\end{aligned}$$

Plugging everything in, the final cross term between tensor and axial vector is:

$$C_A C_T \frac{2mc^2}{|E|} \left| \int \boldsymbol{\sigma} \right|^2 \tag{A.18}$$

With all calculated, we can now find the transition probability. Collecting equations (A.12) to (A.18), the total $|H_{fi}|^2$ is:

$$\begin{aligned} |H_{fi}|^2 = g^2 \Bigg[& \Big(|C_S|^2 + |C_V|^2 \Big) \left| \int 1 \right|^2 + \Big(|C_A|^2 + |C_T|^2 \Big) \left| \int \boldsymbol{\sigma} \right|^2 \\ & + \frac{(\boldsymbol{p} \cdot \boldsymbol{q}) c^2}{|E||E_\nu|} \Bigg(\Big(-|C_S|^2 + |C_V|^2 \Big) \left| \int 1 \right|^2 + \frac{1}{3} \Big(-|C_A|^2 + |C_T|^2 \Big) \left| \int \boldsymbol{\sigma} \right|^2 \Bigg) \\ & + \frac{2mc^2}{|E|} \Bigg(C_S C_V \left| \int 1 \right|^2 + C_A C_T \left| \int \boldsymbol{\sigma} \right|^2 \Bigg) \Bigg] \end{aligned}$$

If we rearrange a bit and define $\xi = (|C_S|^2 + |C_V|^2) \left| \int 1 \right|^2 + (|C_A|^2 + |C_T|^2 \left| \int \boldsymbol{\sigma} \right|^2$ then:

$$|H_{fi}|^2 = g^2 \xi \left(1 + a_{\beta\nu} \frac{(\boldsymbol{p} \cdot \boldsymbol{q}) c^2}{|E||E_\nu|} + b_{Fierz} \frac{mc^2}{|E|} \right) \tag{A.19}$$

$$a_{\beta\nu} = \frac{\Big(-|C_S|^2 + |C_V|^2 \Big) \left| \int 1 \right|^2 + \frac{1}{3} \Big(-|C_A|^2 + |C_T|^2 \Big) \left| \int \boldsymbol{\sigma} \right|^2}{\Big(|C_S|^2 + |C_V|^2 \Big) \left| \int 1 \right|^2 + \Big(|C_A|^2 + |C_T|^2 \Big) \left| \int \boldsymbol{\sigma} \right|^2} \tag{A.20}$$

$$b_{Fierz} = \frac{2 \Big(C_S C_V \left| \int 1 \right|^2 + C_A C_T \left| \int \boldsymbol{\sigma} \right|^2 \Big)}{\Big(|C_S|^2 + |C_V|^2 \Big) \left| \int 1 \right|^2 + \Big(|C_A|^2 + |C_T|^2 \Big) \left| \int \boldsymbol{\sigma} \right|^2} \tag{A.21}$$

And so, we have what we sought out to derive, the $\beta\nu$ correlation coefficient ($a_{\beta\nu}$). To finish calculating the transition probability, which will appear at other points in this document, one simply substitutes equation (A.8) and (A.19) into Fermi's golden rule.

$$\Gamma(E_e) dE_e = (2\pi^3 c^5 \hbar^7)^{-1} \xi \left(1 + a_{\beta\nu} \frac{(\boldsymbol{p} \cdot \boldsymbol{q}) c^2}{|E||E_\nu|} + b_{fierz} \frac{mc^2}{|E|} \right) pE(E_0 - E)^2 dE \tag{A.22}$$

At this point, it is worth reminding the reader that this is a very simplified derivation that ignores a great deal of known and potential physics. A full expansion including parity non-

conservation, time reversal non-invariance, proper wave functions for the leptons, Coulomb interactions with the nucleus, and a vast list of other effects is beyond this work and best left to experts such as Barry Holstein, as will be seen in subsequent appendices. [72][109]

APPENDIX B

THE TRANSITION PROBABILITY EXPANSION OF LITHIUM-8

The ^{8}Li beta decay results in the emission of delayed alpha's, so the resulting transition probability expansion has quite a few additional terms to account for the correlation between the alphas, beta, and neutrino. The complete expansion can be found in section IV.C of Barry Holstein's 1974 Review of Modern Physics [49] and is copied below:

$$
\begin{aligned}
d^7\Gamma =& F_{\mp}(Z,E)\frac{G_\nu^2\cos^2\theta_c}{2(2\pi)^6}(E_0-E)^2pE\; dEd\Omega_e d\Omega_\nu d\Omega_n \times \Bigg(g_1(E) + g_2(E)\left[\frac{\boldsymbol{p}}{E}\cdot\hat{k}\right] \\
&+ g_3(E)\left[\left(\frac{\boldsymbol{p}}{E}\cdot\hat{k}\right)^2 - \frac{1}{3}\frac{\boldsymbol{p}^2}{E^2}\right] + \delta_1\big(E,v^*,\tau_{J',J''}(L)\big)\left[\frac{\hat{n}\cdot\boldsymbol{p}}{E}\right] \\
&+ \delta_2\big(E,v^*,\tau_{J',J''}(L)\big)\left[\hat{n}\cdot\frac{\boldsymbol{p}}{E}\;\frac{\boldsymbol{p}}{E}\cdot\hat{k}\right] + \delta_3\big(E,v^*,\tau_{J',J''}(L)\big)\left[\hat{n}\cdot\hat{k}\right] \\
&+ \delta_4\big(E,v^*,\tau_{J',J''}(L)\big)\left[\hat{n}\cdot\hat{k}\;\frac{\boldsymbol{p}}{E}\cdot\hat{k}\right] + \frac{1}{10}\tau_{J',J''}(L)T^{(2)}(\hat{n})\Bigg\{ g_{10}(E)\big[\boldsymbol{p}/E,\boldsymbol{p}/E\big] \\
&+ g_{11}(E)\big[\boldsymbol{p}/E,\boldsymbol{p}/E\big]\left(\frac{\boldsymbol{p}}{E}\cdot\hat{k}\right) + g_{12}(E)\big[\boldsymbol{p}/E,\hat{k}\big] + g_{13}(E)\big[\boldsymbol{p}/E,\hat{k}\big]\left(\frac{\boldsymbol{p}}{E}\cdot\hat{k}\right) \\
&+ g_{14}(E)\big[\hat{k},\hat{k}\big] + g_{15}(E)\big[\hat{k},\hat{k}\big]\left(\frac{\boldsymbol{p}}{E}\cdot\hat{k}\right) + g_{16}(E)\left[\frac{\boldsymbol{p}}{E},\frac{\boldsymbol{p}}{E}\times\hat{k}\right] + g_{17}(E)\left[\hat{k},\frac{\boldsymbol{p}}{E}\times\hat{k}\right]\Bigg\} \\
&+ \delta_8\big(E,v^*,\tau_{J',J''}(L)\big)T^{(3)}(\hat{n})\big[\boldsymbol{p}/E,\boldsymbol{p}/E,\hat{k}\big] + \delta_9\big(E,v^*,\tau_{J',J''}(L)\big)T^{(3)}(\hat{n})\big[\boldsymbol{p}/E,\hat{k},\hat{k}\big] \\
&+ \frac{1}{10}\omega_{J',J''}(L)T^{(4)}(\hat{n})\Bigg\{ g_{25}(E)\big[\boldsymbol{p}/E,\boldsymbol{p}/E,\boldsymbol{p}/E,\hat{k}\big] + g_{26}(E)\big[\boldsymbol{p}/E,\boldsymbol{p}/E,\hat{k},\hat{k}\big] \\
&+ g_{26}(E)\big[\boldsymbol{p}/E,\hat{k},\hat{k},\hat{k}\big]\Bigg\}\Bigg)
\end{aligned}
\tag{B.1}
$$

The top(bottom) sign of the $\pm$ or $\mp$ corresponds to the $\beta^-(\beta^+)$ decay. Holstein gives detailed explanations of the δ_i and g_i terms in his paper. This discussion will only include the simplified, "final" versions of these terms. Useful numbers and some defined terms are found in the chart below.

Name	Variable	Value	Ref
e^- energy	E	∼1-13 MeV	[99]
Endpoint of e^- energy spectrum	E_0	∼13 MeV[a]	[99]
e^- mass	m_β	0.511... ± 3.1×10^{-9}	[71]
e^- momentum (vector, magnitude)	$\boldsymbol{p}$, p	∼1-13 MeV	[99]
Reduced mass $(M_{8Li} + M_{8Be^*})/2$	M	∼7466 MeV[a]	[105]
Mass Difference	Δ	∼ 13.1 MeV[a]	[105]
^{8}Li Nuclear Radius	R	0.0119 ± 0.0002 MeV^{-1}	[10]
^{8}Be* Spin	J'	2	[99]
α Spin	J''	0	-
α angular momentum	L	2	-
α direction unit vector	$\hat{n}$	-	-
α velocity in ^{8}Be* COM frame	$v*$	-	-
ν direction unit vector	$\hat{k}$	-	-
1st Order GT matrix element	c_1	1[b]	-
2nd Order GT matrix element	c_2	<0.025	[100]
Weak magnetism term	b	60.3 ± 1.5	[97]
Induced tensor current	d	40 ± 14[c]	[97]
2nd forbidden V form factor	f	8 ± 2.4	[97]
2nd forbidden V form factor	g	∼-3800[a]	[69]
Induced pseudoscalar form factor	h	∼11000	[50]
2nd forbidden A form factor	j_2	-31000 ± 4000	[97]
2nd forbidden A form factor	j_3	-63000 ± 18000	[97]
Fine structure constant	α	0.007297... ± 1.7×10^{-12}	[71]

Table B.1: Variables and terms used in the lithium-8 decay rate expansion.

a. Varies depending on the excitation energy of ^{8}Be*

b. c_1 is normalized to 1 in our Monte Carlo Event Generator

c. The induced tensor current is actually broken down into a first and second class current $d = d_I + d_{II}$. d_I is the number listed, while d_{II} has been measured to be 0 with uncertainty below that of d_I.[20]

B.1 The Monte Carlo Event Generator $d^7\Gamma$

The construction of the Monte Carlo Event generator that was used to simulate ^{8}Li decay (both tensor and axial-vector) in this experiment rested heavily upon the decay transition in equation B.1. The fully expanded terms (alongside approximate magnitudes) are listed below. For the actual simulation, all the terms containing c_2 (with intensities on the scale of $10^{-7} - 10^{-8}$) are deemed negligible and dropped. In addition, for simplicity, all the $(\Delta/2M)h$ terms were dropped for similar reasons.

The Monte Carlo simulation can be used to generate both axial vector and tensor events. Because we only use betas emitted in roughly the same direction as the alphas and there are correlations between the beta, neutrino, and alphas in all of the terms except for g_1, we simply multiply said terms (g_{2-15}) by -1 to make a simulated decay via the tensor interaction.

g_1 term:

$$|c_1|^2 + \underbrace{\frac{2\mathrm{Re}c_1^* c_2}{9M^2}\left(11m_\beta^2 + 20EE_0 - 2\frac{m_\beta^2}{E}E_0 - 20E^2\right)}_{10^{-8}} - \underbrace{\frac{2E_0}{3M}\mathrm{Re}c_1^*(c_1 + d \pm b)}_{0.1}$$

$$+ \underbrace{\frac{2E}{3M}\Big[\mathrm{Re}c_1^*(5c_1 \pm 2b)\Big]}_{0.1} - \underbrace{\frac{m_\beta^2}{3ME}\Big[2|c_1|^2 + \mathrm{Re}c_1^*(d \pm 2b) - \mathrm{Re}c_1^* h\frac{E_0 - E}{2M}\Big]}_{10^{-4}}$$

$$\underbrace{\mp\frac{8\alpha|c_1|^2 R}{35}\left[28E - E_0 + \frac{9m_\beta^2}{E}\right]}_{10^{-3}}$$

g_2 term:

$$\Big\{ -\frac{1}{3}|c_1|^2 - \underbrace{\frac{2\mathrm{Re}c_1^* c_2}{3M^2}(m_\beta^2 + 8EE_0 - 8E^2)}_{10^{-7}} + \underbrace{\frac{2E_0}{3M}\mathrm{Re}c_1^*(c_1 + d \pm b)}_{0.1} - \underbrace{\frac{4E}{3M}\mathrm{Re}c_1^*(3c_1 \pm b)}_{0.1}$$

$$\pm \underbrace{\frac{24\alpha R}{35}|c_1|^2\Big(4E-E_0\Big)}_{10^{-4}}\Bigg\}\left(\frac{p}{E}\right)\cos\theta_{\beta\nu}$$

g_3 term:

$$\Bigg\{\underbrace{\frac{E}{M}|c_1|^2}_{10^{-3}}+\underbrace{\frac{4}{3}\mathrm{Rec}_1^* c_2\frac{EE_0-E^2}{M^2}}_{10^{-8}}\Bigg\}\Bigg[\cos\theta_{\beta\nu}{}^2-\frac{1}{3}\Bigg]\frac{p^2}{E^2}$$

g_{10} term:

$$\Bigg(-\underbrace{\frac{E}{2M}\mathrm{Rec}_1^*(c_1+d\mp b_{wm})}_{10^{-2}}-\underbrace{\left(\sqrt{\frac{1}{14}}\right)\frac{E}{2M}\mathrm{Rec}_1^*\Bigg[\pm 3f\pm\sqrt{\frac{3}{2}}g\frac{E_0-E}{M}+3j_2\frac{E_0-2E}{2M}\Bigg]}_{10^{-2}}$$

$$-\underbrace{\left(\frac{3}{70}\sqrt{\frac{5}{7}}\right)\mathrm{Rec}_1^* j_3\frac{2EE_0+5E^2}{M^2}}_{10^{-2}}\Bigg)\times\frac{p^2}{E^2}(\cos\theta_{\beta\alpha}{}^2-1/3)$$

g_{11} term:

$$\underbrace{\mathrm{Rec}_1^*\frac{E^2}{2M^2}\Bigg[\sqrt{\frac{1}{14}}\Big(\mp\sqrt{\frac{3}{2}}g-j_2\Big)+\frac{1}{7}\sqrt{\frac{5}{7}}j_3\Bigg]}_{10^{-3}}\times\frac{p^3}{E^3}(\cos\theta_{\beta\alpha}{}^2-1/3)\cos\theta_{\beta\nu}$$

g_{12} term:

$$\Bigg[-\mathrm{Rec}_1^*\Bigg(c_1+\underbrace{\frac{2c_2}{M^2}(m_\beta^2+2EE_0-2E^2)}_{10^{-8}}-\underbrace{\frac{E_0}{2M}(c_1+d\pm b)}_{0.1}+\underbrace{\frac{E}{M}(3c_1\pm b)}_{10^{-2}}-\underbrace{\frac{m_\beta^2}{2M^2}\Big(1+\frac{\Delta}{2M}\Big)h}_{10^{-5}}\Bigg)$$

$$-\sqrt{\frac{1}{14}}\mathrm{Rec}_1^*\Bigg(\pm\underbrace{3f\frac{E_0-2E}{2M}}_{10^{-3}}\pm\underbrace{\sqrt{\frac{3}{2}}g\frac{E_0^2-2EE_0+m_\beta^2}{2M^2}}_{10^{-5}}-\underbrace{j_2\frac{-E_0^2+8EE_0-8E^2+m_\beta^2}{4M^2}}_{10^{-3}}\Bigg)$$

$$-\underbrace{\frac{1}{35}\sqrt{\frac{5}{7}}\mathrm{Re}c_1^* j_3 \frac{E_0^2+9EE_0-m_\beta^2-9E^2}{M^2}}_{10^{-2}} \mp \underbrace{\frac{216\alpha R}{35}|c_1|^2 E}_{10^{-3}}\Big] \times \frac{p}{E}(\cos\theta_{\alpha\beta}\cos\theta_{\alpha\nu}-\frac{1}{3}\cos\theta_{\beta\nu})$$

g_{13} term:

$$\Big[\mathrm{Re}c_1^*\Big(\underbrace{3c_1\frac{E}{M}}_{10^{-3}}+\underbrace{4c_2\frac{EE_0-E^2}{M^2}}_{10^{-8}}\Big)+\underbrace{\frac{9}{35}\sqrt{\frac{5}{7}}\mathrm{Re}c_1^* j_3\frac{EE_0-E^2}{M^2}}_{10^{-2}}\Big]$$

$$\times\frac{p^2}{E^2}(\cos\theta_{\alpha\beta}\cos\theta_{\alpha\nu}-\frac{1}{3}\cos\theta_{\beta\nu})\cos\theta_{\beta\nu}$$

g_{14} term:

$$\Big[\underbrace{-\frac{E_0-E}{2M}\mathrm{Re}c_1^*\Big(c_1+d\pm b+\frac{m_\beta^2}{2ME}\Big(1+\frac{\Delta}{2M}\Big)h\Big)}_{10^{-2}}$$

$$-\frac{3}{2}\sqrt{\frac{1}{14}}\mathrm{Re}c_1^*\Big(\underbrace{\pm f\frac{E-E_0}{M}}_{10^{-3}}\pm\underbrace{\sqrt{\frac{1}{6}}g\frac{E^2-EE_0-m_\beta^2+E_0(m_\beta^2/E)}{M^2}}_{10^{-3}}$$

$$\underbrace{-j_2\frac{2E^2-3EE_0-m_\beta^2+E_0^2+E_0(m_\beta^2/E)}{2M^2}}_{10^{-4}}\Big)$$

$$\underbrace{-\frac{3}{70}\sqrt{\frac{5}{7}}\mathrm{Re}c_1^* j_3\frac{5E^2-12EE_0+2m_\beta^2+7E_0^2-2E_0(m_\beta^2/E)}{M^2}}_{10^{-2}}\mp\underbrace{\frac{24\alpha R}{35}|c_1|^2(E_0-E)}_{10^{-4}}\Big]$$

$$\times(\cos\theta_{\alpha\nu}{}^2-\frac{1}{3})$$

g_{15} term:

$$\Big[\underbrace{\mathrm{Re}c_1^*\frac{E_0^2-2EE_0+E^2}{2M^2}\Big(-\sqrt{\frac{1}{14}}\Big(\mp\sqrt{\frac{3}{2}}g+j_2\Big)+\frac{1}{7}\sqrt{\frac{5}{7}}j_3\Big)}_{10^{-3}}\Big]\times\frac{p}{E}(\cos\theta_{\alpha\nu}{}^2-\frac{1}{3})\cos\theta_{\beta\nu}$$

δ_1 **term:**

$$\frac{-2c_1^2}{Mv*}\Big(E + \frac{E_0 - E}{10}\Big) \times \frac{p}{E}\cos\theta_{\alpha\beta}$$

δ_2 **term:**

$$\frac{18Ec_1^2}{30Mv*} \times \frac{p^2}{E^2}\cos\theta_{\alpha\beta}\cos\theta_{\beta\nu}$$

δ_3 **term:**

$$\frac{-2c_1^2}{Mv*}\Big((E_0 - E + \frac{p^2}{10E}\Big) \times \cos\theta_{\alpha\nu}$$

δ_4 **term:**

$$\frac{18(E_0 - E)c_1^2}{30Mv*}\Big(E + \frac{E_0 - E}{10}\Big) \times \frac{p}{E}\cos\theta_{\alpha\nu}\cos\theta_{\beta\nu}$$

δ_8 **term:**

$$\frac{4Ec^2}{Mv*} \times \frac{p^2}{E^2}\big(\cos\theta_{\alpha\beta}{}^2\cos\theta_{\alpha\nu} - \frac{1}{5}(\cos\theta_{\alpha\nu} + 2\cos\theta_{\alpha\beta}\cos\theta_{\beta\nu})\big)$$

δ_9 **term:**

$$\frac{4(E_0 - E)c^2}{Mv*} \times \frac{p}{E}\big(\cos\theta_{\alpha\beta}\cos\theta_{\alpha\nu}{}^2 - \frac{1}{5}(\cos\theta_{\alpha\beta} + 2\cos\theta_{\alpha\beta}\cos\theta_{\beta\nu})\big)$$

The reader may notice that g_{16}, g_{17}, and $g_{>20}$. The $g_{>20}$ terms were not included in the simulation and are currently proving to be a puzzle for both us and a growing community of theorists. They will be discussed separately in section B.4. Both g_{16} and g_{17} are collec-

tively multiplied by the imaginary component of c_1. Because we assume that time reversal invariance is not violated, Im(c_1)=0 and thus g_{16}=g_{17}=0.

B.2 Extracting $|C_T|^2/|C_A|^2$ from $d^7\Gamma$

Of the terms listed above, g_2 comes the closest to the traditional $a_{\beta\nu}$ that was derived in Appendix A. However, this experiment is particularly powerful because the additional terms governing correlations with the delayed α emission offer an opportunity for extra sensitivity. Of the above listed terms, the 3 that have magnitude closest to 1 are:

$$\overbrace{|c_1|^2}^{g_1} - \overbrace{\frac{1}{3}|c_1|^2}^{g_2}\frac{p}{E}\cos\theta_{\beta\nu} - \overbrace{|c_1|^2}^{g_{12}}\frac{p}{E}(\cos\theta_{\alpha\beta}\cos\theta_{\alpha\nu} - \frac{1}{3}\cos\theta_{\beta\nu}) \tag{B.2}$$

By definition, $a_{\beta\nu} \equiv g_2/g_1 = -1/3$. However, if the data is selected in such a way that the β's are emitted in the same direction as an α, then the $\cos\theta_{\alpha\beta}\cos\theta_{\alpha\nu}$ factors in g_{12} can be approximated as $\cos\theta_{\alpha\beta} \approx 1$ and $\cos\theta_{\alpha\nu} \approx \cos\theta_{\beta\nu}$. Under these circumstances, equation (B.2) becomes:

$$\overbrace{|c_1|^2}^{g_1} - \overbrace{\frac{1}{3}|c_1|^2}^{g_2}\frac{p}{E}\cos\theta_{\beta\nu} - \overbrace{\frac{2}{3}|c_1|^2}^{g_{12}}\frac{p}{E}\cos\theta_{\beta\nu} = \overbrace{|c_1|^2}^{g_1} - \overbrace{|c_1|^2}^{g_2+g_{12}}\cos\theta_{\beta\nu} \tag{B.3}$$

Thus, with the combination of g_2 and g_{12}, this experiment has a 3× higher sensitivity to $a_{\beta\nu}$ than others without the delayed alpha.

$$3a_{\beta\nu} = \frac{|C_T|^2 - |C_A|^2}{|C_T|^2 + |C_A|^2} = \frac{g_2 + g_{12}}{g_1} \tag{B.4}$$

The actual $|C_T|^2/|C_A|^2$ fraction is calculated by fitting a linear combination of a pure tensor spectra and pure axial-vector spectra to the data. The fraction of the contributions from each spectrum then becomes $|C_T|^2/|C_A|^2$ and can be inserted into equation (B.4).

B.3 Bremsstrahlung Radiation

In the event that the β emits a bremsstrahlung photon, the relationship between the β and the recoiling nucleus is altered and must be taken into account in the simulation. Adjustments for such events are introduced in the Monte Carlo event generator via a method described in detail by Glück in his 1997 Computer Physics Communications Paper [37] using calculations made by Sirlin. [91] More details about the actual implementation can be found in Chapter 5. There are two different kinds of adjustments that must be made to the g_i terms above, depending on what kinds of photons were emitted.

The first correction deals with virtual and soft bremsstrahlung photons. Virtual photons are emitted and then reabsorbed into the reaction, while soft photons are emitted throughout the reactions, but their energy is small enough to either not be detected or to not have a significant impact on the recoiling particles. The corrections are defined by equations 2.12, 3.2, 3.9, and 3.10 in [37]. They are implemented in our Monte Carlo simulation via two different functions.

$$z_{VS} = \frac{\alpha}{\pi}\left[\frac{3}{2}\ln\left(\frac{m_{p^+}}{m}\right) + 2\left(\frac{N}{\beta} - 1\right)\ln\left(\frac{2\omega}{m}\right) + 2\frac{N}{\beta}(1-N) + \frac{2}{\beta}L\left(\frac{2\beta}{1+\beta}\right) - \frac{3}{8}\right]$$

$$z_{\widetilde{M}} = \frac{\alpha}{\pi}\frac{\beta^2-1}{\beta}N \quad \text{with} \quad g_{(1,corr)} = g_1\times(1+z_{VS}+z_{\widetilde{M}}) \quad \text{and} \quad g_{(i\neq 1,corr)} = g_{i\neq 1}\times(1+z_{VS})$$

where $\beta = \sqrt{1-m^2/E^2}$, $N = \frac{1}{2}\ln((1+\beta)/1-\beta))$, and L is the Spence function. g_1 and $g_{i\neq 1}$ refer to the Holstein expansion terms listed in section B.1. As described by equation 2.12 and 3.1 in [37], the z_{VS} correction is applied to all the g_i terms used in our Monte Carlo and $z_{\widetilde{M}}$ is applied only to g_1.

The second correction pertains to when a high-energy bremsstrahlung photon is emitted and is applied very similarly to the virtual, soft corrections above. The necessary terms can be found in equations 4.4-4.8 in [37] and their expanded form is below. Here (in contrast to Holstein's equation above, but keeping with Glück's notation), K and $\boldsymbol{k}$ refer to the

bremsstrahlung photon's energy and momentum respectively. The neutrino energy is in turn defined as: $E_\nu = E_0 - E - K$.

$$H0 = E_\nu \Big[-(E+K)\bigg(\frac{1}{K^2} + \frac{m^2}{(EK - \boldsymbol{p}\cdot\boldsymbol{k})^2} - \frac{2E}{K(EK-\boldsymbol{p}\cdot\boldsymbol{k})}\bigg) + \frac{K}{(EK-\boldsymbol{p}\cdot\boldsymbol{k})}\Big]$$

$$\begin{aligned} H1 = \boldsymbol{p}_\nu \cdot \boldsymbol{p} \Big[\bigg(\frac{1}{K^2} + \frac{m^2}{(EK-\boldsymbol{p}\cdot\boldsymbol{k})^2} - \frac{2E}{K(EK-\boldsymbol{p}\cdot\boldsymbol{k})}\bigg) + \frac{1}{(EK-\boldsymbol{p}\cdot\boldsymbol{k})}\Big] \\ + \boldsymbol{p}_\nu \cdot \boldsymbol{k} \Big[\frac{E+K}{K(EK-\boldsymbol{p}\cdot\boldsymbol{k})} - \frac{m^2}{(EK-\boldsymbol{p}\cdot\boldsymbol{k})^2}\Big] \end{aligned}$$

Both of these terms are multiplied by the Fermi function, $F(\beta E)$ and $\frac{\alpha}{2\pi^2} K E_\nu N(EK - \boldsymbol{p}\cdot\boldsymbol{k})$ to complete the transition probability. In addition, $H0$ is multiplied by $-\frac{1}{3}$ to account for $a_{\beta\nu}$. The remaining $g_{i>2}$ terms are handled by scaling them to $H0$. This is only an approximation, since what happens in the hard bremsstrahlung emission for beta decay has only been calculated for the most dominant $g_{1,2}$ terms by theorists. The error associated with this uncertainty is discussed in chapter 5.

B.4 The g_{25}, g_{26}, and g_{27} Mystery

One as yet unresolved problem has to do with the g_{25}, g_{26}, and g_{27} terms. Under most circumstances, it isn't unreasonable to assume that higher order terms are on average smaller than their predecessors. However, in the case of this expansion, such an assumption may or may not be valid. In the eyes of our research group, the problem lies in the ambiguous definition of the factor τ, which only appears in the offending terms. Holstein calls $\tau_{u=2,v=2}$ term with no reference to an angular momentum (L) that is necessary to calculate it in the $g_{>20}$ terms. If we assume the α angular momentum $L = 2$ that was used to calculate the better-defined tau in the remainder of the terms, then for $u = v$:

$$\tau_{u=2,v=2} = \frac{-10}{7u(u+1)}(2u+5)(2u-3) = -\frac{15}{7} \quad \text{(equation 55a in [49])}$$

If this is the case, then the combined contribution of the 3 terms below is about 3× the size of the leading order term (with magnitude 1) and obviously has a significant impact on the simulated spectrum. As can be seen from Figure B.1, the results have virtually no agreement with the data. Given that simulations with the $g_{>20}$ set to zero match the data quite nicely, this presents a bit of a conundrum.

g_{25} **term:**

$$\left(\tau_{2,2}\mathrm{Rec}_1^* j_3 \frac{35E^2}{4M^2}\right)\frac{p^3}{E^3}\Big(\cos^3\theta_{\alpha\beta}\cos\theta_{\alpha\nu} - \frac{3}{7}\Big(\cos\theta_{\alpha\beta}\cos\theta_{\alpha\nu} + \cos\theta_{\beta\nu}\cos^2\theta_{\alpha\beta}\Big) + \frac{3}{35}\cos\theta_{\beta\nu}\Big)$$

g_{26} **term:**

$$\tau_{2,2}\mathrm{Rec}_1^* j_3 \frac{35(EE_0 - E^2)}{2M^2}\left(\frac{p^2}{E^2}\right)\Big[\cos^2\theta_{\alpha\beta}\cos^2\theta_{\alpha\nu} - \frac{1}{7}\Big(\cos^2\theta_{\alpha\nu} + 4\cos\theta_{\beta\nu}\cos\theta_{\alpha\beta}\cos\theta_{\alpha\nu} + \cos^2\theta_{\alpha\beta}\Big) + \frac{1}{35}\Big(1 + 2\cos^2\theta_{\beta\nu}\Big)\Big]$$

g_{27} **term:**

$$\tau_{2,2}\mathrm{Rec}_1^* j_3 \frac{35E_0^2 - 70EE_0 + 35E^2}{4M^2}\left(\frac{p}{E}\right)\Big[\cos\theta_{\alpha\beta}\cos^3\theta_{\alpha\nu} - \frac{3}{7}\Big(\cos\theta_{\beta\nu}\cos^2\theta_{\alpha\nu} + \cos\theta_{\alpha\nu}\cos\theta_{\alpha\beta}\Big) + \frac{3}{35}\Big(\cos\theta_{\beta\nu}\Big)\Big]$$

One solution that our group has proposed is that τ could simply be misinterpreted. The τ in Holstein's equation 55a is defined in terms of the ^{8}Be* spin (J'), the α spin (J''), and the α angular momentum (L) and reads $\tau_{J',J''}(L)$. However, when τ is called in the $g_{>20}$ terms as $\tau_{u,v}$, u and v refer to the spins of ^{8}Be* and ^{8}Li, respectively. If we instead assume the unspecified L refers to either of the previous nuclei, then $L = 0$ and $\tau_{u,v} = 0$, thus effectively removing the problem.

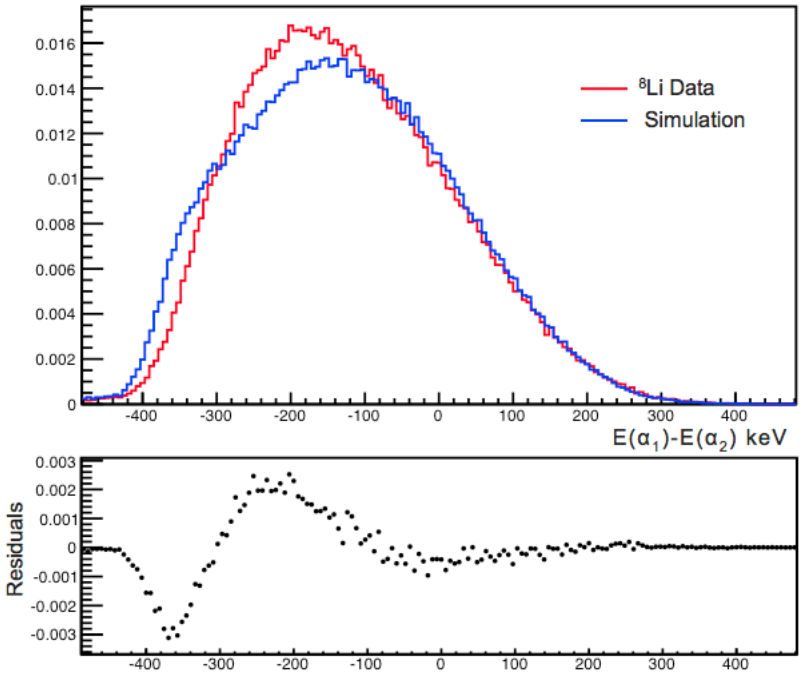

Figure B.1: A comparison between the α difference spectrum (with the β hitting one of the same detectors as the α's) produced by the ^{8}Li data and a simulation in which g_{25}, g_{26}, and g_{27} are allowed to be nonzero with the value of $\tau_{2,2}(L = 2) = -15/7$ input into the calculation. The residuals of ^{8}Li data - Simulation are below the histograms. There is clearly a vast discrepancy between the two spectra.

We have reached out to a number of theorists in hopes of reaching some form of closure to this problem. The most committed few at the Soreq institute have implied that Holstein's expression is complete, but that there may be some mixing with a Fermi transition. Since the closest Fermi transition is 13 MeV away, it seems very unlikely that such mixing would result in a 300% deviation. Even some communication with Barry Holstein himself did not put the issue to rest. However, given the clear disagreement with our data, the g_{25}, g_{26}, and g_{27} terms will all be set to zero for this work.

REFERENCES

[1] http://www.micronsemiconductor.co.uk/.

[2] http://cad-gdml.in2p3.fr/.

[3] https://twiki.cern.ch/twiki/bin/view/Geant4/EMValidation.

[4] Nobel prize in physics 1903.

[5] Nobel prize in physics 1979.

[6] Nobel prize in physics 1989.

[7] E. G. Adelberger, C. Ortiz, A. García, H. E. Swanson, M. Beck, O. Tengblad, M. J. G. Borge, I. Martel, H. Bichsel, and the ISOLDE Collaboration. Positron-neutrino correlation in the $0^+ \to 0^+$ decay of ^{32}Ar. *Phys. Rev. Lett.*, 83:1299–1302, Aug 1999.

[8] Y.A. Akovali. Review of alpha–decay data from doubly–even nuclei. *Nuclear Data Sheets*, 84(1):1 – 114, 1998.

[9] J. S. Allen, R. L. Burman, W. B. Herrmannsfeldt, P. Stähelin, and T. H. Braid. Determination of the beta-decay interaction from electron-neutrino angular correlation measurements. *Phys. Rev.*, 116:134–143, Oct 1959.

[10] I. Angeli and K.P. Marinova. Table of experimental nuclear ground state charge radii: An update. *Atomic Data and Nuclear Data Tables*, 99(1):69 – 95, 2013.

[11] P. Bauer and G. Bortels. Response of Si detectors to electrons, deuterons and alpha particles. *Nuclear Instruments and Methods in Physics Research Section A: Accelerators, Spectrometers, Detectors and Associated Equipment*, 299(1):205 – 209, 1990.

[12] M. Bhattacharya, E. G. Adelberger, and H. E. Swanson. Precise study of the final-state continua in ^{8}Li and ^{8}B decays. *Phys. Rev. C*, 73:055802, May 2006.

[13] G. Bortels and P. Collaers. Analytical function for fitting peaks in alpha-particle spectra from si detectors. *International Journal of Radiation Applications and Instrumentation. Part A. Applied Radiation and Isotopes*, 38(10):831 – 837, 1987.

[14] L. M. Brown. The Idea of the Neutrino, includes translated reprint of Pauli's letter. *Physics Today*, 31:23–28, September 1978.

[15] Lowell S. Brown and Gerald Gabrielse. Geonium theory: Physics of a single electron or ion in a Penning trap. *Rev. Mod. Phys.*, 58:233–311, Jan 1986.

[16] Rene Brun and Fons Rademakers. Root — an object oriented data analysis framework. *Nuclear Instruments and Methods in Physics Research Section A: Accelerators, Spectrometers, Detectors and Associated Equipment*, 389(1):81 – 86, 1997. New Computing Techniques in Physics Research V.

[17] E. Rutherford M.A. B.Sc. Viii. uranium radiation and the electrical conduction produced by it. *The London, Edinburgh, and Dublin Philosophical Magazine and Journal of Science*, 47(284):109–163, 1899.

[18] M. T. Burgy, V. E. Krohn, T. B. Novey, G. R. Ringo, and V. L. Telegdi. Measurements of asymmetries in the decay of polarized neutrons. *Phys. Rev.*, 110:1214–1216, Jun 1958.

[19] CMS Collaboration. Search for leptonic decays of W' bosons in pp collisions at sqrt(s)=8 TeV. 2013.

[20] Jennifer Couture. *A Search for Second Class Currents in the A=8 System*. PhD thesis, University of Notre Dame, 2007.

[21] I. Curie and F. Joliot. Un nouveau type de radioactivite. *Acad. Sci.*, 198:254, 1934.

[22] R.H. Dalitz. Cxii. on the analysis of τ-meson data and the nature of the τ-meson. *The London, Edinburgh, and Dublin Philosophical Magazine and Journal of Science*, 44(357):1068–1080, 1953.

[23] G. Darius, W. A. Byron, C. R. DeAngelis, M. T. Hassan, F. E. Wietfeldt, B. Collett, G. L. Jones, M. S. Dewey, M. P. Mendenhall, J. S. Nico, H. Park, A. Komives, and E. J. Stephenson. Measurement of the electron-antineutrino angular correlation in neutron β decay. *Phys. Rev. Lett.*, 119:042502, Jul 2017.

[24] P.H. Dawson. *Quadrupole Mass Spectrometry and Its Applications*. Elsevier Scientific Publishing Company, 1976.

[25] G. Dearnaley. The channelling of ions through silicon detectors. *IEEE Transactions on Nuclear Science*, 11(3):249–253, June 1964.

[26] M. Bychkov et. al. New precise measurement of the pion weak form factors in $\pi^+ \to e^+\nu\gamma$ decay. *Phys. Rev. Lett.*, 103:051802, Jul 2009.

[27] Michiharu Wada et al. Slow ri-beams from projectile fragment separators. *Nuclear Instruments and Methods in Physics Research Section B: Beam Interactions with Materials and Atoms*, 204:570 – 581, 2003. 14th International Conference on Electromagnetic Isotope Separators and Techniques Related to their Applications.

[28] S. Agostinelli et. al. Geant4—a simulation toolkit. *Nuclear Instruments and Methods in Physics Research Section A: Accelerators, Spectrometers, Detectors and Associated Equipment*, 506(3):250 – 303, 2003.

[29] S. Chatrchyan et. al. Search for leptonic decays of w bosons in pp collisions at sqrt(s) = 7 Tev. *Journal of High Energy Physics*, 2012(8):23, Aug 2012.

[30] U. Fano. Ionization yield of radiations. ii. the fluctuations of the number of ions. *Phys. Rev.*, 72:26–29, Jul 1947.

[31] T. Fazzini, G. Fidecaro, A. W. Merrison, H. Paul, and A. V. Tollestrup. Electron decay of the pion. *Phys. Rev. Lett.*, 1:247–249, Oct 1958.

[32] E. Fermi. Tentativo di una Teoria Dei Raggi β. *La Ricerca Scientifica*, 2, 1933.

[33] E. Fermi. Tentativo di una Teoria Dei Raggi β. *Il Nuovo Cimento*, 11:1–19, January 1934.

[34] E. Fermi. Versuch einer Theorie der β-Strahlen. I. *Zeitschrift fur Physik*, 88:161–177, March 1934.

[35] R. P. Feynman and M. Gell-Mann. Theory of the Fermi interaction. *Phys. Rev.*, 109:193–198, Jan 1958.

[36] G. Gamow and E. Teller. Selection rules for the β-disintegration. *Phys. Rev.*, 49:895–899, Jun 1936.

[37] F. Glück. Order-α radiative correction calculations for unoriented allowed nuclear, neutron and pion β decays. *Computer Physics Communications*, 101(3):223 – 231, 1997.

[38] F. Glück. Order-α radiative correction to 6He and 32Ar β decay recoil spectra. *Nuclear Physics A*, 628(3):493 – 502, 1998.

[39] M. Goldhaber, L. Grodzins, and A. W. Sunyar. Helicity of neutrinos. *Phys. Rev.*, 109:1015–1017, Feb 1958.

[40] A. Gorelov, D. Melconian, W. P. Alford, D. Ashery, G. Ball, J. A. Behr, P. G. Bricault, J. M. D'Auria, J. Deutsch, J. Dilling, M. Dombsky, P. Dubé, J. Fingler, U. Giesen, F. Glück, S. Gu, O. Häusser, K. P. Jackson, B. K. Jennings, M. R. Pearson, T. J. Stocki, T. B. Swanson, and M. Trinczek. Scalar interaction limits from the beta-neutrino correlation of trapped radioactive atoms. *Phys. Rev. Lett.*, 94:142501, Apr 2005.

[41] S. Goudsmit and J. L. Saunderson. Multiple scattering of electrons. *Phys. Rev.*, 57:24–29, Jan 1940.

[42] H.E. Haber, G.L. Kane, and T. Sterling. The fermion mass scale and possible effects of higgs bosons on experimental observables. *Nuclear Physics B*, 161(2):493 – 532, 1979.

[43] C. Hagmann, D. Lange, and D. Wright. Cosmic-ray shower generator (cry) for monte carlo transport codes. In *2007 IEEE Nuclear Science Symposium Conference Record*, volume 2, pages 1143–1146, Oct 2007.

[44] J. C. Hardy and I. S. Towner. Superallowed $0^+ \to 0^+$ nuclear β decays: A new survey with precision tests of the conserved vector current hypothesis and the standard model. *Phys. Rev. C*, 79:055502, May 2009.

[45] Elizabeth Heckmaier. *Addressing the Reactor Antineutrino Anomaly with a New Detector Array for Fission Fragment Beta-Spectroscopy*. PhD thesis, University of California, Irvine, 2018.

[46] P. Herczeg. Beta decay beyond the standard model. *Progress in Particle and Nuclear Physics*, 46(2):413 – 457, 2001.

[47] W. B. Herrmannsfeldt, D. R. Maxson, P. Stähelin, and J. S. Allen. Electron-neutrino angular correlation in the positron decay of argon 35. *Phys. Rev.*, 107:641–643, Jul 1957.

[48] T.Y. Hirsh et al. The use of cosmic-ray muons in the energy calibration of the beta-decay paul trap silicon-detector array. *Nuclear Instruments and Methods in Physics Research Section A: Accelerators, Spectrometers, Detectors and Associated Equipment*, 887:122 – 127, 2018.

[49] Barry R. Holstein. Recoil effects in allowed beta decay: The elementary particle approach. *Rev. Mod. Phys.*, 46:789–814, Oct 1974.

[50] Barry R. Holstein. Electromagnetic effects and weak form factors. *Phys. Rev. C*, 19:1467–1472, Apr 1979.

[51] V.N. Ivanchenko, O. Kadri, M. Maire, and L. Urban. Geant4 models for simulation of multiple scattering. *Journal of Physics: Conference Series*, 219(3):032045, 2010.

[52] J. D. Jackson, S. B. Treiman, and H. W. Wyld. Possible tests of time reversal invariance in beta decay. *Phys. Rev.*, 106:517–521, May 1957.

[53] F. James and M. Roos. Minuit - a system for function minimization and analysis of the parameter errors and correlations. *Computer Physics Communications*, 10(6):343 – 367, 1975.

[54] C. H. Johnson, Frances Pleasonton, and T. A. Carlson. Precision measurement of the recoil energy spectrum from the decay of Helium-6. *Phys. Rev.*, 132:1149–1165, Nov 1963.

[55] O. Kadri, V. Ivanchenko, F. Gharbi, and A. Trabelsi. Incorporation of the goudsmit–saunderson electron transport theory in the geant4 monte carlo code. *Nuclear Instruments and Methods in Physics Research Section B: Beam Interactions with Materials and Atoms*, 267(23):3624 – 3632, 2009.

[56] O. Kadri, V.N. Ivanchenko, F. Gharbi, and A. Trabelsi. Geant4 simulation of electron energy deposition in extended media. *Nuclear Instruments and Methods in Physics Research Section B: Beam Interactions with Materials and Atoms*, 258(2):381 – 387, 2007.

[57] G. H. Kinchin and R. S. Pease. REVIEW ARTICLES: The Displacement of Atoms in Solids by Radiation. *Reports on Progress in Physics*, 18:1–51, January 1955.

[58] A.J. Koning. Calculation and analysis of d+^{7}Li reaction. *ENDF/TENDL-15*, MAT 328, NOV 2015.

[59] Vinit Kumar. Understanding the focusing of charged particle beams in a solenoid magnetic field. *American Journal of Physics*, 77(8):737–741, 2009.

[60] L. Landau. On the energy loss of fast particles by ionization. *J. Phys.*, 8:201, 1944.

[61] T. D. Lee and C. N. Yang. Question of parity conservation in weak interactions. *Phys. Rev.*, 104:254–258, Oct 1956.

[62] T. D. Lee and C. N. Yang. Parity nonconservation and a two-component theory of the neutrino. *Phys. Rev.*, 105:1671–1675, Mar 1957.

[63] W.N. Lennard, H. Geissel, K.B. Winterbon, D. Phillips, T.K. Alexander, and J.S. Forster. Nonlinear response of si detectors for low-z ions. *Nuclear Instruments and Methods in Physics Research Section A: Accelerators, Spectrometers, Detectors and Associated Equipment*, 248(2):454 – 460, 1986.

[64] G. Li et al. Tensor interaction limit derived from the $\alpha-\beta-\overline{\nu}$ correlation in trapped ^{8}Li ions. *Phys. Rev. Lett.*, 110:092502, Mar 2013.

[65] Gang Li. *Electron-Neutrino Angular Correlation Measurement in the Decay of ^{8}Li*. PhD thesis, McGill University, 2013.

[66] R. E. March and J. F. Todd. *Quadrupole Ion Trap Mass Spectrometry, 2nd Edition*. John Wiley and Sons, INC. Publishing, 2005.

[67] J. W. Martin, J. Yuan, M. J. Betancourt, B. W. Filippone, S. A. Hoedl, T. M. Ito, B. Plaster, and A. R. Young. New measurements and quantitative analysis of electron backscattering in the energy range of neutron β-decay. *Phys. Rev. C*, 73:015501, Jan 2006.

[68] Edward A Mason and Homer W Schamp. Mobility of gaseous lons in weak electric fields. *Annals of Physics*, 4(3):233 – 270, 1958.

[69] R. D. McKeown, G. T. Garvey, and C. A. Gagliardi. Beta-alpha angular correlations in mass 8. *Phys. Rev. C*, 22:738–749, Aug 1980.

[70] missmj. Standard model of elementary particles, 2017. Online; accessed October 1, 2017, usage under cc-by-sa-3.0.

[71] Peter J. Mohr, David B. Newell, and Barry N. Taylor. Codata recommended values of the fundamental physical constants: 2014. *Rev. Mod. Phys.*, 88:035009, Sep 2016.

[72] M. Morita. *Beta Decay and Muon Capture*. W.A. Benjamin, Incorporated, Advanced Book Program, 1973.

[73] H. P. Mumm, T. E. Chupp, R. L. Cooper, K. P. Coulter, S. J. Freedman, B. K. Fujikawa, A. García, G. L. Jones, J. S. Nico, A. K. Thompson, C. A. Trull, J. F. Wilkerson, and F. E. Wietfeldt. New limit on time-reversal violation in beta decay. *Phys. Rev. Lett.*, 107:102301, Sep 2011.

[74] Oscar Naviliat-Cuncic and Martín González-Alonso. Prospects for precision measurements in nuclear β decay in the lhc era. *Annalen der Physik*, 525(8-9):600–619, 2013.

[75] R. Orford, N. Vassh, J. A. Clark, G. C. McLaughlin, M. R. Mumpower, G. Savard, R. Surman, A. Aprahamian, F. Buchinger, M. T. Burkey, D. A. Gorelov, T. Y. Hirsh, J. W. Klimes, G. E. Morgan, A. Nystrom, and K. S. Sharma. Precision mass measurements of neutron-rich neodymium and samarium isotopes and their role in understanding rare-earth peak formation. *Phys. Rev. Lett.*, 120:262702, Jun 2018.

[76] Rodney Orford. private communication.

[77] R.H. Pehl, F.S. Goulding, D.A. Landis, and M. Lenzlinger. Accurate determination of the ionization energy in semiconductor detectors. *Nuclear Instruments and Methods*, 59(1):45 – 55, 1968.

[78] M.E. Peskin and D.V. Schroeder. *An Introduction to Quantum Field Theory*. Advanced book classics. Avalon Publishing, 1995.

[79] Planck Collaboration and Ade, P. A. R. et. al. Planck 2013 results. i. overview of products and scientific results. *A&A*, 571, 2014.

[80] Stefano Profumo, Michael J. Ramsey-Musolf, and Sean Tulin. Supersymmetric contributions to weak decay correlation coefficients. *Phys. Rev.*, D75:075017, 2007.

[81] T. Roger et al. Precise determination of the unperturbed ^{8}B neutrino spectrum. *Phys. Rev. Lett.*, 108:162502, Apr 2012.

[82] Brice M. Rustad and Stanley L. Ruby. Correlation between electron and recoil nucleus in He^6 decay. *Phys. Rev.*, 89:880–881, Feb 1953.

[83] Francesc Salvat, Aleksander Jablonski, and Cedric J. Powell. Elsepa—Dirac partial-wave calculation of elastic scattering of electrons and positrons by atoms, positive ions and molecules. *Computer Physics Communications*, 165(2):157 – 190, 2005.

[84] G. Savard, S.T. Becker, G. Bollen, H.-J. Kluge, R.B. Moore, Th. Otto, L. Schweikhard, H. Stolzenberg, and U. Wiess. A new cooling technique for heavy ions in a Penning trap. *Physics Letters A*, 158(5):247 – 252, 1991.

[85] Guy Savard. private communication.

[86] Guy Savard. Large radio-frequency gas catchers and the production of radioactive nuclear beams. *Journal of Physics: Conference Series*, 312(5):052004, 2011.

[87] J. P. Schiffer, G. C. Morrison, R. H. Siemssen, and B. Zeidman. Study of the (d, p) reaction in the $1p$ shell. *Phys. Rev.*, 164:1274–1284, Dec 1967.

[88] N. D. Scielzo, S. J. Freedman, B. K. Fujikawa, and P. A. Vetter. Measurement of the $\beta - \nu$ correlation using magneto-optically trapped ^{21}Na. *Phys. Rev. Lett.*, 93:102501, Aug 2004.

[89] N.D. Scielzo et al. The β-decay paul trap: A radiofrequency-quadrupole ion trap for precision β-decay studies. *Nuclear Instruments and Methods in Physics Research Section A: Accelerators, Spectrometers, Detectors and Associated Equipment*, 681:94 – 100, 2012.

[90] Balraj Singh and E. Browne. Nuclear data sheets for a = 240. *Nuclear Data Sheets*, 109(10):2439 – 2499, 2008.

[91] A. Sirlin. General properties of the electromagnetic corrections to the beta decay of a physical nucleon. *Phys. Rev.*, 164:1767–1775, Dec 1967.

[92] E. Steinbauer, P. Bauer, M. Geretschläger, G. Bortels, J.P. Biersack, and P. Burger. Energy resolution of silicon detectors: approaching the physical limit. *Nuclear Instruments and Methods in Physics Research Section B: Beam Interactions with Materials and Atoms*, 85(1):642 – 649, 1994.

[93] M. Sternberg and G. Savard. A study of the cyclotron gas-stopping concept for the production of rare isotope beams. *Nuclear Instruments and Methods in Physics Research Section A: Accelerators, Spectrometers, Detectors and Associated Equipment*, 596(3):257 – 268, 2008.

[94] M. G. Sternberg et al. Limit on tensor currents from ^{8}Li β decay. *Phys. Rev. Lett.*, 115:182501, Oct 2015.

[95] Matthew Sternberg. *Limits on Tensor Currents from ^{8}Li Beta Decay.* PhD thesis, University of Chicago, 2013.

[96] E. C. G. Sudarshan and R. E. Marshak. Chirality invariance and the universal Fermi interaction. *Phys. Rev.*, 109:1860–1862, Mar 1958.

[97] T. Sumikama, K. Matsuta, T. Nagatomo, M. Ogura, T. Iwakoshi, Y. Nakashima, H. Fujiwara, M. Fukuda, M. Mihara, K. Minamisono, T. Yamaguchi, and T. Minamisono. Test of the conserved vector current hypothesis by a β-ray angular distribution measurement in the mass-8 system. *Phys. Rev. C*, 83:065501, Jun 2011.

[98] Kenneth Teh. Scarlet. https://www.phy.anl.gov/.

[99] D.R. Tilley, J.H. Kelley, J.L. Godwin, D.J. Millener, J.E. Purcell, C.G. Sheu, and H.R. Weller. Energy levels of light nuclei a=8,9,10. *Nuclear Physics A*, 745(3):155 – 362, 2004.

[100] R. E. Tribble and G. T. Garvey. Induced weak currents and $\beta^{\pm} - \alpha$ angular correlations in $a = 8$. *Phys. Rev. C*, 12:967–983, Sep 1975.

[101] J. Van Schelt, D. Lascar, G. Savard, J. A. Clark, S. Caldwell, A. Chaudhuri, J. Fallis, J. P. Greene, A. F. Levand, G. Li, K. S. Sharma, M. G. Sternberg, T. Sun, and B. J. Zabransky. Mass measurements near the r-process path using the canadian penning trap mass spectrometer. *Phys. Rev. C*, 85:045805, Apr 2012.

[102] P. A. Vetter, J. R. Abo-Shaeer, S. J. Freedman, and R. Maruyama. Measurement of the $\beta-\nu$ correlation of ^{21}Na using shakeoff electrons. *Phys. Rev. C*, 77:035502, Mar 2008.

[103] K. K. Vos, H. W. Wilschut, and R. G. E. Timmermans. Symmetry violations in nuclear and neutron β decay. *Rev. Mod. Phys.*, 87:1483–1516, Dec 2015.

[104] Susanne Walsh. Micron semiconductor, ltd. private communication.

[105] Meng Wang, G. Audi, F.G. Kondev, W.J. Huang, S. Naimi, and Xing Xu. The ame2016 atomic mass evaluation (ii). tables, graphs and references. *Chinese Physics C*, 41(3):030003, 2017.

[106] F. L. Wilson. Fermi's Theory of Beta Decay. *American Journal of Physics*, 36:1150–1160, December 1968.

[107] Fred L. Wilson. Fermi's theory of beta decay. *American Journal of Physics*, 36(12):1150–1160, 1968.

[108] Robert Wiringa. private communication.

[109] C. Wu and S.A. Moszkowski. *Beta decay*. Interscience monographs and texts in physics and astronomy. Interscience Publishers, 1966.

[110] C. S. Wu, E. Ambler, R. W. Hayward, D. D. Hoppes, and R. P. Hudson. Experimental test of parity conservation in beta decay. *Phys. Rev.*, 105:1413–1415, Feb 1957.

[111] James F. Ziegler, M.D. Ziegler, and J.P. Biersack. SRIM – the stopping and range of ions in matter (2010). *Nuclear Instruments and Methods in Physics Research Section B: Beam Interactions with Materials and Atoms*, 268(11):1818 – 1823, 2010. 19th International Conference on Ion Beam Analysis.